



HAL
open science

Precision tube production : influencing the eccentricity, residual stresses and texture developments : experiments and multiscale simulation

Farzad Foadian

► To cite this version:

Farzad Foadian. Precision tube production : influencing the eccentricity, residual stresses and texture developments : experiments and multiscale simulation. Physics [physics]. Université de Strasbourg; Technische Universität Clausthal (Allemagne), 2018. English. NNT : 2018STRAE003 . tel-02155136

HAL Id: tel-02155136

<https://theses.hal.science/tel-02155136>

Submitted on 13 Jun 2019

HAL is a multi-disciplinary open access archive for the deposit and dissemination of scientific research documents, whether they are published or not. The documents may come from teaching and research institutions in France or abroad, or from public or private research centers.

L'archive ouverte pluridisciplinaire **HAL**, est destinée au dépôt et à la diffusion de documents scientifiques de niveau recherche, publiés ou non, émanant des établissements d'enseignement et de recherche français ou étrangers, des laboratoires publics ou privés.

ÉCOLE DOCTORALE 182

Institut de Physique et Chimie des Matériaux de Strasbourg

UMR 7504 UDS-CNRS

THÈSE présentée par :

Farzad FOADIAN

soutenue le : **09.02.2018**

pour obtenir le grade de :

Docteur de l'université de Strasbourg

Discipline / Spécialité : Physique

**Precision Tube Production
Influencing the Eccentricity, Residual
Stresses and Texture Developments:
Experiments and Multiscale Simulation**

THÈSE dirigée par :

**Mme Adele CARRADÒ
M Heinz PALKOWSKI**

Prof. Dr. habil., Université de Strasbourg
Prof. Dr.-Ing., TU Clausthal

PRESIDENT DU JURY :

M Karl-Heinz SPITZER

Prof. Dr.-Ing., TU Clausthal

RAPPORTEURS :

**Mme Birgit AWISZUS
M Erman TEKKAYA**

Prof. Dr.-Ing., TU Chemnitz
Prof. Dr.-Ing., TU Dortmund

EXAMINATEUR :

M Volker WESLING

Prof. Dr.-Ing., TU Clausthal

**Precision Tube Production
Influencing the Eccentricity, Residual
Stresses and Texture Developments:
Experiments and Multiscale Simulation**

Doctoral Thesis
(Dissertation)

to be awarded the degree
Doctor of Engineering (Dr.-Ing.)

submitted by

Farzad Foadian

from Tabriz / Iran

approved by the Faculty of
Natural and Materials Science,
Clausthal University of Technology and
Université de Strasbourg, Ecole doctorale :
Physique et chimie physique

Date of oral examination:
09.02.2017

Bibliografische Information der Deutschen Bibliothek

Die Deutsche Bibliothek verzeichnet diese Publikation in der Nationalbibliografie; detaillierte Bibliografische Daten sind im Internet über <http://dnb.ddb.de> abrufbar.

Bibliographic information published by the Deutsche Nationalbibliothek

The Deutsche Nationalbibliothek lists this publication in the Deutsche National-bibliografie; detailed bibliographic data are available by Internet at <http://dnb.dnb.de>.

Zugl.: Clausthal, Technische Uni., Diss., 2018

„Dissertation Technische Universität Clausthal“

Vorsitzender der Promotionskommission: Prof. Dr.-Ing. Karl-Heinz Spitzer

Hauptberichterstatler: Prof. Dr.-Ing. Heinz Palkowski
Prof. Dr. habil. Adele Carradó

Mitberichterstatler: Prof. Dr.-Ing. Heinz Palkowski
Prof. Dr.-Ing. Volker Wesling
Prof. Dr.-Ing. Birgit Awiszus
Prof. Dr.-Ing. Erman Tekkaya

D 104

© Verlag
Adresse

Dieses Werk ist urheberrechtlich geschützt.

Alle Rechte, auch die der Übersetzung, des Nachdruckes und der Vervielfältigung des Buches, oder Teilen daraus, vorbehalten. Kein Teil des Werkes darf ohne schriftliche Genehmigung des Verlages in irgendeiner Form reproduziert oder unter Verwendung elektronischer Systeme verarbeitet, vervielfältigt oder verbreitet werden.

This document is protected by copyright law.

No part of this document may be reproduced in any form by any means without prior written authorization of the publisher.

1. Auflage 2018

Printed in Germany.

Bezugsadresse: Prof. Dr.-Ing. Heinz Palkowski
Werkstoffumformung
Institut für Metallurgie (IMET)
Technische Universität Clausthal
Robert-Koch-Str. 42
D-38678 Clausthal-Zellerfeld

*This thesis is lovingly dedicated to the memory
of my mother, **Masoumeh Asadzadeh**, who I
miss every day.*

Acknowledgment

First and foremost, I would like to express my sincere gratitude to my advisor, **Prof. Heinz Palkowski**, for the continuous support of my PhD study and related research, for his patience, motivation, and immense knowledge. His guidance helped me in all the time of research and writing of this thesis. I could not have imagined having a better advisor and mentor for my PhD study. It has been an honor to do my PhD with him.

Besides of Prof. Palkowski, I want to thank my advisor from Strasbourg University, **Prof. Adele Carradó**. She has taught me, both consciously and unconsciously, how good science is done. I appreciate all her contributions of time and ideas to make my PhD experience productive and stimulating. The joy and enthusiasm she has for her research was contagious and motivational for me, even during tough times in the PhD pursuit. I am also thankful for the excellent example she has provided as a successful woman physicist and professor.

I would like to extend my sincere thanks to my reading committee members, **Prof. Birgit Awiszus** from TU Chemnitz, **Prof. A. Erman Tekkaya** from TU Dortmund, and **Prof. Volker Wesling** from TU Clausthal for accepting reviewing of my thesis.

I would like to thank also **Prof. Heinz-Günter Brokmeier** for his scientific assistants on this project, for his insightful comments and encouragement, and also for the hard questions and discussions inciting me to view my research from different perspectives.

I am appreciative of the people of the department of Surfaces and Interfaces at IPCMS-Unistra; **Dr. Christine Goyhenex**, **Mr. Jacques Faerber**, **Mr. Gilles Morvan** for their intensive support. The group has been a source of friendship as well as good advice and collaboration.

My time at Clausthal was made enjoyable in large part due to the many friends and groups that became a part of my life. My special thanks therefore go to the members of the department of Metal Forming and Processing at TU Clausthal the technical staff of the Institute of Metallurgy and the scientific colleagues of the department for their support, continuous help, friendship, and delivering a good atmosphere.

I like to express further greatest appreciations for their care and very kind help with my work our dear secretaries Mrs. Roswitha Schubert, Ms. Marina Kratzin,

and Ms. Katharina Bednarsky who always gave a helping hand when necessary. Especially, I would like to thank Dr. Mohamed Soliman, Dr. Jan Orend, Dr. Somayeh Khani, Dr. Mohamed Harhash, Dipl.-Ing. Mithat Akdesir, M.Sc. Hossam Ibrahim, M.Sc. Jürgen Nietsch, and M.Sc. Viktoria Harms for their support and friendship.

This Dr. thesis would not have been possible without a financial support: Therefore, I gratefully acknowledge the funding sources of **DFG** (German Research Foundation under contract Nr. PA-837-38-1) and **AiF** (Community of Industrial Research).

Furthermore, I would thank my students and trainees supporting me during my activities at Clausthal, especially Johann Naumann, Sebastian Hinke, Shunyu Li, Alex Asselin, Ansheng Li, Sun Yue.

Regarding residual strain and texture measurements, I thank the Institute Laue Langevin in Grenoble and DESY in Hamburg with special thanks going to Dr. Thilo Pirling for his support in day and night measurements and Dr. Zhengye Zhong, M.Sc. Mohammad Masafi, and Dr. Nowfal Alhamdany for their support of synchrotron measurements at DESY.

Last but not the least, I would like to thank my dear father, **Mohammad**, my sister, **Farzaneh**, and my brother, **Ali** for supporting me spiritually throughout my PhD and also writing this thesis as well as supporting me in my life in general.

Farzad Foadian
Clausthal University of Technology
February 18

Table of contents

Acknowledgment	7
Table of contents	I
Nomenclature	VII
Abstract	XV
Zusammenfassung	XIX
Résumé	XXV
Chapter 1 Introduction	1
Chapter 2 Theoretical background	7
2.1 Introduction.....	7
2.2 Tube drawing.....	7
2.2.1 Mechanics of drawing.....	9
2.2.1.1 Strain and stress.....	9
2.2.1.2 Drawing force.....	9
2.2.2 Analytical study of tube drawing.....	10
2.2.3 Imperfections arising from tube drawing	11
2.3 Eccentricity	12
2.4 Residual stresses	14
2.4.1 Measurement methods.....	16
2.4.1.1 Hole-drilling method.....	17
2.4.1.2 Neutron diffraction method	18
2.5 Texture	21
2.5.1 Description of orientation.....	23
2.5.2 Texture measurement	25
2.5.2.1 Texture measurement by synchrotron radiation	26
2.5.2.2 Texture measurement by scanning electron microscopy	26
2.5.2.3 Texture measurement by neutron diffraction	28

2.6	Multiscale simulation	29
2.6.1	Integrated computational material engineering	29
2.6.2	Macroscale analysis	33
2.6.3	Mesoscale analysis	33
2.6.3.1	Elasticity and crystal rotation	34
2.6.3.2	Dislocation dynamics	35
2.6.4	Atomistic modeling method	35
2.6.4.1	Modified embedded atom method	36
2.6.5	Electronic scale calculation	38
2.6.6	Structure scale simulation; FEM	38
Chapter 3	Experimental and simulation procedures.....	41
3.1	Introduction	41
3.2	Tube drawing and materials.....	41
3.2.1	Drawing machine	41
3.2.2	Materials.....	41
3.3	Eccentricity	43
3.4	Tilting and offset principles.....	44
3.4.1	Laboratory solution.....	44
3.4.2	Industrial solution	46
3.5	Evaluation of RSs.....	46
3.5.1	Residual strain measurement by hole drilling	46
3.5.2	Residual strain measurement by neutron diffraction.....	47
3.6	Analysis of texture development	50
3.6.1	Texture measurements by neutron diffraction.....	50
3.6.2	Texture measurements by synchrotron diffraction	51
3.6.3	Texture measurements by electron diffraction	52
3.7	Multiscale simulation	52
3.7.1	Bridge 1, DFT calculation.....	54
3.7.2	Bridge 2, MEAM and MD calibration	54
3.7.3	Bridge 3, DD simulation	54
3.7.4	Bridge 4, CPFEM simulation	55

Chapter 4	Eccentricity	57
4.1	Introduction	57
4.2	Copper	57
4.2.1	Tilting	57
4.2.2	Offset	62
4.2.3	Combination of tilting/offset	63
4.3	Other materials	64
4.4	Conclusion	66
Chapter 5	Residual stresses	69
5.1	Introduction	69
5.2	Hole drilling	69
5.2.1	Copper	69
5.2.2	Other materials	74
5.3	Neutron diffraction	74
5.3.2	After first drawing step	74
5.3.3	After second drawing step	80
5.4	Conclusion	81
Chapter 6	Texture development	83
6.1	Introduction	83
6.2	Macro-texture data	84
6.2.1	As-received tube and tubes after the first drawing step	84
6.2.2	After second drawing step	92
6.3	Micro-texture	93
6.4	Conclusion	97
Chapter 7	Multiscale simulation	99
7.1	Introduction	99
7.2	Electronic scale simulations	100
7.2.1	Simulation setup at the electronic scale	100
7.2.2	Electronic scale simulation results	100
7.2.3	Electronic scale to atomic scale bridging	103
7.3	Atomic scale simulations	104

7.3.1	Material parameters at atomic scale	104
7.3.2	Results of atomic simulations.....	105
7.3.2.1	Modified embedded atom method	105
7.3.2.2	Molecular dynamics.....	106
7.3.2.3	Bridging to the next microscale simulation scale.....	108
7.4	Microscale simulations	108
7.4.1	Material parameter at microscale.....	108
7.4.2	Results	108
7.4.3	Bridging to the CPFEM	110
7.5	Meso- and structural scale (CPFEM).....	110
7.5.1	CPFEM, first drawing step	111
7.5.2	CPFEM, second drawing step.....	112
7.5.3	Results of CPFEM simulations.....	112
7.5.3.1	Mesh modeling and mesh convergence study	113
7.5.3.2	Energy validation	113
7.5.3.3	Eccentricity	114
7.5.3.4	RSs and stress-strain diagram	115
7.5.3.5	Sensitivity study of m and γ_0	116
7.5.3.6	Texture	117
7.6	Conclusion	121
Chapter 8	Summary and outlook	123
Chapter 9	Résumé de thèse en Français.....	128
Chapter 10	Annexes	142
Annex A	Pole figure	142
Annex B	Kinematics of deformation and strain.....	144
Annex C	Crystal plasticity	146
a.	Kinematic of crystal plasticity	147
b.	Kinetic of crystal plasticity	147
Annex D	Dislocation dynamics	150
a.	Dislocation motion and plastic strain	150
b.	Modeling discrete dislocations	151

Annex E	Embedded atom method	153
Annex F	Density functional theory	154
Annex G	Finite element method	156
Indices	159
Figure captions	159
Table captions	168
Subject indices	169
Chapter 11	References	171
Curriculum vitae	193
Publication list	197

Nomenclature

Greek symbols

Symbol	Definition	Unit
α	Die's semi-angle	[°]
α, β	PF angles	[°]
α_i	Kinematic hardening effects resulting from backstress at the slip system level	[-]
γ_{int}	Intrinsic stacking fault energy	$\frac{J}{m^2}$
γ_{us}	Extrinsic or unstable stacking fault energy	$\frac{J}{m^2}$
γ_{ut}	Unstable twinning stacking fault energy	$\frac{J}{m^2}$
$\dot{\gamma}_i$	Plastic slip (shearing) rate on i_{th} slip system	[-]
δ	Inhomogeneity factor	[-]
δ	Differential energy change	[-]
{ Δ }	Global vector of nodal variables	[-]
Ω	Total energy per atom in the bulk	eV
ε_{11}	Element of the strain tensor along axis 1	[-]
ε_{12}	Off-diagonal element in the (1,2) plane	[-]
ε_d	Strain in diameter	[-]
$\varepsilon_{i,j}$	Strain tensor	[-]
ε^{hkl}	Lattice strain	[-]
ε_s	Strain in wall-thickness	[-]
θ_{hkl}^0	Bragg angle for the stress-free material	[°]
2θ	Diffraction angle	[°]
κ_i	Designator for associated isotropic hardening	[MPa]
κ_i^a	Associated isotropic hardening (athermal)	[MPa]
κ_i^t	Associated isotropic hardening (thermal)	[MPa]
κ_0	Initial slip system strength	[MPa]
κ_s	The saturation strength	[MPa]
λ	Wavelength	[μ m]
μ	Friction coefficient	[-]

μ_1	Friction coefficient between the drawing die and the tube	[-]
μ_2	Friction coefficient between the drawing die and the plug	[-]
v	Mobility of dislocations	$\left[\frac{m^2}{ps}\right]$
\underline{v}	First - rank tensor (vector)	[-]
v_i	First - rank tensor in the einsteinian indicial notation	[-]
ν	Poisson's ratio	[-]
ξ_s	Line sense of the dislocation segment	[-]
ρ	Density	$\left[\frac{Kg}{m^3}\right]$
ρ_i	Dislocation density	$\left[\frac{1}{m^2}\right]$
σ	General stress field; stress field created by the dislocation segment	[MPa]
σ_{ave}^d	Average flow stress	[MPa]
σ_d	Draw stress	[MPa]
σ_{fm}	Average flow stress during deformation	[MPa]
$ \tau_i $	Resolved shear stress	[MPa]
τ_i^a	Applied shear stress needed to overcome the athermal (long range) barriers to dislocation motion	[MPa]
τ_i^t	Applied shear stress needed to overcome the thermal (short range) barriers to dislocation motion	[MPa]
φ and κ	Rotating axis of x-ray texture goniometer	[-]
ϕ_1, ϕ, ϕ_2	Euler's angles	[°]
Ψ	Angle between the scattering vector and the x_3 axis	[°]

Latin symbols

Symbol	Definition	Unit
a_0	Equilibrium lattice constant	[Å]
A_0 and A_f	Initial and final cross-sectional area of tube	[m]
b	Burgers vector	[Å]
b_s	Burgers vector of dislocation segment	[Å]
B	Drag coefficient	[Pa.s]
$\underline{\underline{C}}$	Anisotropic elasticity tensor	[-]
C_h	Hardening constant	[-]
C_r	Recovery constant	[-]

d_0	Reference lattice parameter	[Å]
d_0 and d_{i0}	Outer and inner diameters of the tube before drawing	[m]
d_1 and d_{i1}	Outer and inner diameters of the tube after drawing	[m]
d_{hkl}^0	Interplanar distance of the stress-free sample	[Å]
d_{hkl}	Interplanar distance	[Å]
D_0 and D_f	Initial and final outer diameters	[m]
mE	Young's modulus	[GPa]
E_t	Total energy of a system of atoms	[eV]
E	Eccentricity	[%]
ΔE	Relative change of the eccentricity	[%]
\underline{E}	The green elastic strain tensor or lagrangian strain tensor	[-]
E_0	Eccentricity of the tube before drawing	[%]
E_1	Eccentricity of the tube after drawing	[%]
E_{atom}	Total energy of an isolated atom	[eV]
E_{coh}	Cohesive energy	[eV]
E_{FD}	Frictional dissipation	[J]
E_{hkl}	Diffractional elastic constant	[-]
E_i	Atomic energy	[eV]
E_I	Internal energy	[eV]
E_{KE}	Kinetic energy	[eV]
E_{PW}	Internal work by penalty contact	[eV]
E_{tot}	Total energy of the system (bulk atoms)	[eV]
E_{VD}	Viscous dissipation energy	[eV]
E_W	External work	[J]
\underline{F}	Second-rank tensor; deformation gradient	[-]
$\dot{\underline{F}}$	Rate of change of the corresponding deformation gradient	[-]
F^e	Elastic deformation gradient	[-]
\underline{F}^p	Plastic deformation gradient	[-]
\underline{F}^v	Volumetric deformation gradient	[-]

F_{ij}	Second-rank tensor in the einsteinian indicial notation	[-]
F_N	Drawing force required to perform the pure deformation work	[kN]
F_R	Drawing force required to overcome friction	[kN]
F_{Sh}	Drawing force required to carry out the shear work	[kN]
F_s	Net force	[kN]
$f(g)$	Resultant ODF	[-]
g	Probability density function of orientations	[-]
G	Bulk modulus	[GPa]
h_0	Initial hardening rate	[MPa]
h_i^0	Initial hardening rate due to dislocation accumulation	[MPa]
J_3	Third invariant in terms of the deviatoric stress	[MPa]
κ_i	Designator for associated isotropic hardening	[MPa]
κ_i^a	Associated isotropic hardening (athermal)	[MPa]
κ_i^t	Associated isotropic hardening (thermal)	[MPa]
K_0	Initial slip system strength	[MPa]
K_A	Coordinate systems of crystal	[-]
K_B	Sample coordinate system	[-]
K_i	Internal elastic strain	[-]
$K_{i,s}$	Saturation internal strain-like quantity	[-]
k_m	Average deformation resistance	[-]
K_s	Saturation strength	[MPa]
$K_{s,s}$	Saturation strength	[MPa]
[K]	Global stiffness matrix	[-]
[K] ⁱ	Coefficient matrix of the element expressed in the global form	[-]
l_s	The segment length	[-]
L	Velocity gradient	[-]
\underline{L}^e	Elastic velocity gradient	[-]
\underline{L}^p	Plastic velocity gradient	[-]
L^p	Plastic strain	[-]

L_{max}	Expansion	[-]
m	Rate sensitivity	[-]
m_s	Effective mass	[-]
m_i^0	Unit normal vector to the slip plane	[-]
Q	Scattering vector	[-]
L_1	Contact surfaces of the drawing die	[-]
L_2	Contact surfaces of the drawing plug	[-]
Q-value	Ratio of the strain in wall-thickness	[-]
\underline{R}	Rotation matrix	[-]
{R}	Global right side vector	[-]
R_0	Reference configuration	[-]
R_a	Current configuration	[-]
$ R_i $	Slip resistance	[-]
R_i^a	Slip resistance of the athermal obstacles to dislocations gliding on the i-slip plane	[-]
R_i^t	Slip resistance of the thermal obstacles to dislocations gliding on the i-slip plane	[-]
S_{i0}	Slip direction vector	[-]
t_0 and t_f	Initial and final wall-thicknesses of the tube	[m]
t_{max} , t_{min} , and t_{avg}	Maximum, minimum, and average wall-thicknesses	[m]
T	Transpose of tensor	[-]
u	Approximated primary variable	[-]
v	Mobility of dislocations	$\left[\frac{m}{ps}\right]$
\underline{v}	First - rank tensor (vector)	[-]
v_i	First - rank tensor in the einsteinian indicial notation	[-]
dV	Volume of all crystallites i	$[\text{\AA}^3]$
dV/V	Volume fraction	[-]
V_i	Volume of grain i	$[\text{\AA}^3]$
\underline{x}	Motion of particle	[-]
x_1, x_2	Coordinates of two nodes	[-]
\underline{x}	Initial position of particle	[-]

Abbreviations

Symbol	Definition	Unit
bcc	Body-centered cubic	[-]
(Bs)	Brass orientation	[-]
CP	Crystal Plasticity	[-]
CPFEM	Crystal Plasticity Finite Element Method	[-]
(Cu)	Copper Orientation	[-]
DD	Dislocation Dynamic	[-]
DESY	German Electron Synchrotron	[-]
DFT	Density Function Theory	[-]
dg	Orientation Range	[-]
EAM	Embedded Atom Method	[-]
EBSD	Electron Backscatter Scanning Diffraction	[-]
fcc	Face-centered cubic	[-]
FEM	Finite Element Method	[-]
FSD	Forward Scattered Detector	[-]
GSFE	Generalized Stacking Fault Energy	$\left[\frac{J}{m^2}\right]$
hcp	Hexagonal close-packed	[-]
hkl	Miller indices	[-]
ICME	Integrated Computational Material Engineering	[-]
IDT	Interrupted Drawn Tube	[-]
IGV	Instrument Gauge Volume	[-]
ILL	Institut Laue-Langevin	[-]
LAMMPS	Large-scale Atomic/Molecular Massively Parallel Simulator	[-]
MD	Molecular Dynamic	[-]
MDDP	Multiscale Dislocation Dynamics Plasticity	[-]
MEAM	Molecular Embedded Atom Method	[-]
mrd	Multiples of random distribution	[-]
ND	Normal Direction	[-]
NIST	National Institute of Standards and Technology	[-]

ODF	Orientation Distribution Function	[-]
OVITO	Open Visualization Tool	[-]
PE	Perkin Elmer Detector	[-]
PF	Pole Figure	[-]
RD	Rolling Direction	[-]
RS	Residual Stress	[MPa]
RSs	Residual Stresses	[MPa]
RVE	Representative Volume Element	[-]
SALSA	Stress Analyzer for Large Scaled Engineering Applications	[-]
SEM	Scanning Electron Microscopy	[-]
SFE	Stacking Fault Energy	[-]
SGV	Sample Gauge Volume	[-]
TD	Transverse Direction	[-]
UBM	Upper Bound Method	[-]
UMAT	User subroutine	[-]

Abstract

Tubes are produced for various demands in aerospace, nuclear, automotive and medical fields. Nevertheless, the industries face some challenges to produce high quality tubes with required dimensions and tolerances in a cost effective and productive way. These challenges are the main motivations for the new developments in tube manufacturing industries, in terms of new material, sizes and shapes, manufacturing process and quality control.

The key and foremost aim of this work was to optimize the standard tube drawing process in a way that the wall-thickness variation (eccentricity) of the drawn tubes can be controlled during the tube drawing process. "Eccentricity control" refers to either reducing or increasing the eccentricity. Being able to control the eccentricity is especially interesting for high priced materials as well as tubes with tight tolerance requirements (precision tubes). To be able to control it, the standard drawing method was optimized and tilting of the die or offset (shifting) of the tube was introduced. To perform the tube drawing with tilting/offset, initially the required tools were built for the existing tube drawing machine in the Institute of Metallurgy at Clausthal University of Technology and all tests were performed on this machine on laboratorial scale. To find a general rule for the tubes' behavior concerning eccentricity, different drawing steps and materials (copper, aluminum, brass, and steel) with different tube dimensions were investigated varying the tilting angles, offset values, or a combination of tilting and offset.

After analyzing the effect of tilting/offset on the eccentricity of the drawn tubes, to know in which way tilting and/or offset influence the developed Residual Stresses (RSs), the evolution of the RSs due to the introduced tilting and/or offset was investigated. For analysis hole drilling and neutron diffraction methods were chosen. Hole drilling is a fast and quite inexpensive method, but the results are limited to the surface of the tube. In contrary, using the neutron diffraction method, the whole wall-thickness of the tube can be measured (the measurements were done using SALSA instrument at ILL in Grenoble/France); however, it is an expensive method. The measurements done with neutron diffraction were used also to prepare required data (as input as well as validation data) for the simulation.

The anisotropic behavior and the crystallographical evolution of the tubes drawn with tilting were investigated to make sure that their final properties are not being significantly directionally dependent of the crystallographical directions. Considering anisotropy and mass flow, it was decided to analyze the texture evolution of the tubes before and after drawing with tilting, to state whether tilting creates significant different textures (crystallographical orientations) and/or affect the mass flow in a detectable way. To study these

parameters, the macro- and micro-texture of the tubes were investigated. Using macro-texture, different crystallographical orientations can be compared before and after drawing and it can be investigated, whether the tilting creates different texture. Micro-texture was studied to be able to detect possible inhomogeneities over wall-thickness of the tubes.

For macro-texture analyses, synchrotron and neutron diffraction methods were used. The reason for choosing two different methods was the coarse grain size of the as-received tubes, not possible to be measured by synchrotron method, and therefore neutron method was used. Synchrotron and neutron diffraction measurements were done using HEMS instrument at PETRA III in Hamburg/Germany and STRESS-SPEC instrument at FRM II in Munich/Germany, respectively. Moreover, these results were used as input for the simulations as well as validation data. The micro-texture evolution of the as-received and drawn tubes was measured using the electron backscattering diffraction method (EBSD).

The achieved results have shown the possibility of controlling the eccentricity during drawing for copper, aluminum, and brass in a same way. Depending on the application, it is possible to produce tubes with lower or higher eccentricity. In case of copper, tilting the die about 5° and putting the minimum wall-thickness of the tube in the direction of tilting resulted in approx. 48% eccentricity reduction (compared to 18% average eccentricity reduction by standard drawing) for one pass. By using the same tilting angle and placing the maximum wall-thickness of the tube in the direction of tilting, the eccentricity was considerably increased, which is interesting for applications in which the local thickening is required. The average eccentricity increase achieved by this tilting angle was about 50%. Shifting the tube about 6 mm and placing the minimum side of the tube in the direction of shifting reduced the eccentricity about 46% in one pass.

Comparing RSs results for standard and tilted drawn tubes show the possibility of influencing the RSs clearly, as well. The macro- and micro-texture of the tubes drawn with tilting have shown the development of same orientation, which were developed by standard drawing. However, the density of the pole figure and Orientation Distribution Function (ODF) in case of tilting was significantly higher, which shows the developed texture in tubes with tilting was sharper.

Performing various tube drawing investigations on different materials with different as-received RSs and different initial textures, having different tilting/offset values, are very expensive (from time and experimental method point of views) and not all combination can be studied experimentally. Therefore, to be able to study different parameters, also to have a better understanding of the process, it was decided to develop a simulation model, which takes into account properties of the as-received materials – such as

eccentricity, RSs, initial texture, mechanical – and therewith analyzes more complex situations. For this goal, a multiscale simulation approach based on the Integrated Computational Material Engineering (ICME) was used.

To develop such a model, a FEM approach, in this case a structural scale simulation, was used. Therewith it was possible to simulate the eccentricity, RSs, and mechanical behavior of the drawn tube. However, in order to be able to simulate texture developments, a Crystal Plasticity (CP) approach – which is a mesoscale simulation - was used. This approach was integrated in the FEM simulations using UMAT subroutine. In studying texture evolutions, it is important to consider the anisotropic elastic and plastic behaviors of the material. The anisotropic hardening behavior was calculated using the Dislocation Dynamics (DD) theory (microscale simulation). One important parameter in DD calculations is the dislocation mobility, been calculated by a Molecular Dynamics (MD) approach, which is an atomistic scale simulation. The proper potential, necessary for MD calculations, was created by a Molecular Embedded Atom Method (MEAM) approach, which is an atomistic scale approach, as well. Moreover, by MEAM calculations, the elastic constants of copper have been calculated. C_{11} , C_{12} , and C_{44} were identified to be 169.20, 123.19 and 77.20 GPa, respectively. Finally, the required data for the creation of the above-mentioned potential was calculated by using the Density Function Theory (DFT) – an electronic scale simulation.

Zusammenfassung

Bei der Herstellung von Rohren ermöglicht die Verringerung von Wanddickenschwankungen, beschrieben durch die Rohrexzentrizität, Materialeinsparungen und damit – für materialkostenintensive Werkstoffe - deutliche Kosteneinsparungen. Je höher man die Anforderungen an die Maßhaltigkeit stellt und je weiter man in den Toleranzvorgaben eingeschränkt wird, desto stärker müssen korrigierende Mechanismen in Anspruch genommen werden, die sich direkt auf die Homogenität der Werkstoffeigenschaften und nicht zuletzt auf die lokale Eigenspannungsverteilung auswirken, desto stärker lokalisieren sich ihre Auswirkungen und umso wichtiger wird ihre Quantifizierung. Das Resultat ist eine verbesserte Materialeffizienz, die zu einer Einsparung von Rohstoffen führt. Des Weiteren ist es für bestimmte konstruktive Anwendungen wünschenswert, lokale Inhomogenitäten zu erzeugen. Als Beispiel hierfür sei eine angepasste Wanddickenverteilung zur Fertigung gebogener Rohrabschnitte genannt, bei denen eine Verdickung der Wandung im Außenbereich der Biegung ein frühzeitiges Ausdünnen verhindert. Außerdem kann eine lokale Variation der Wanddicke und Exzentrizität über die Rohrlänge ebenfalls wünschenswert sein.

Ziel des Vorhabens war es deshalb, eine qualitative und quantitative Erfassung der Möglichkeiten zur lokalen Beeinflussung der Rohrwanddicke - in erster Linie um vorhandene Dickenabweichungen über den Rohrumfang zu reduzieren – vorzunehmen. Dazu wurde der Effekt der Matrizenkipfung und/oder der Verschiebung des Rohres (Versatz) auf die Exzentrizität untersucht. Dabei waren nicht nur die Einstellung der Exzentrizität und der Eigenspannungen das Ziel, sondern auch die Kontrolle dieser beiden Parameter. Die gewählte Vorgehensweise war eine Kombination aus Simulation und experimentellem Teil. Diese beiden Ansätze wurden weitestgehend parallel durchgeführt.

Rohrziehuntersuchungen unter Variation des Kippwinkels und Versatzes für unterschiedliche Werkstoffe mit unterschiedlichen Ausgangseigenschaften sind zeit- und kostenintensiv. Darüber hinaus können nicht alle Kombinationen experimentell untersucht werden. Um dieses Problem zu überwinden und das Verfahren besser zu verstehen, wurde ein Simulationsmodell entwickelt, das wesentliche Eigenschaften der Ausgangsmaterialien - Exzentrizität, Eigenspannungen, Textur, und mechanische Eigenschaften – berücksichtigen kann und damit in der Lage ist, komplexere Prozesssituationen zu analysieren. Darüber hinaus bietet das Modell die Möglichkeit, auch die Texturentwicklung im Rohr mit und ohne Kippung zu beschreiben, ohne dass aufwändige Neutronen-, Synchrotron- oder Elektronenmessungen durchgeführt werden müssen. Zur Zielerreichung wurde ein Multiskalen-Simulationsansatz,

basierend auf das Integrated Computational Material Engineering (ICME), verwendet. Seine Entwicklung stellt den zweiten wesentlichen Fokus dieser Arbeit dar.

Die Messung der Wandstärken von Rohren unterschiedlicher Materialien - Kupfer, Aluminium, Messing und Stahl - sowie die Messung und Berechnung der Exzentrizität wurden vorrangig durchgeführt. Die Basisuntersuchungen wurden an Kupferrohren durchgeführt. Zur Erweiterung und Validierung der Ergebnisse wurden die anderen Sorten herangezogen. Es wurden unterschiedliche Kippwinkel und Versatzeinstellungen an den Rohren gewählt. Die rekristallisierend geglähten Kupferrohre wurden mehrfach gezogen, um den Effekt der Kaltverfestigung auf die Exzentrizitätsänderung zu erfassen.

Die Ergebnisse der Kippung haben gezeigt, dass es möglich ist, die Exzentrizität kontrolliert zu beeinflussen und die Rohrwanddicke lokal sowohl zu reduzieren wie auch aufzudicken. Eine Kippung von -5° - das negative Vorzeichen bedeutet, dass die minimale Wandstärke des Rohres in der Kipprichtung lag - führte beim ersten Ziehen zu einer Reduzierung der Exzentrizität um ca. 50%. Im Vergleich dazu führte der Standardziehprozess (0°) lediglich zu einer Exzentrizitätsabnahme von ca. 1%, ein Kippwinkel von $+5^\circ$ führte zu einer Exzentrizitätserhöhung (Aufdickung) von ca. 50% im Max-Bereich. Die Einführung eines Kippwinkels in den Ziehprozess ändert die benötigte Ziehkraft nicht wesentlich. Ein ähnliches Verhalten konnte bei einer Verschiebung (Versatz) des Rohres aus der Ziehachse beobachtet werden. Ein Versatz von -6 mm führt zu einer Reduzierung der Exzentrizität um ca. 25%. Kippung und die Verschiebung wurden außerdem in Kombination untersucht. Neben den Kupferrohren wurden stichprobenartig auch die übrigen Werkstoffe Ziehversuchen mit Kippung unterworfen; Versatz wurde bei ihnen nicht untersucht. Aluminium und Messing zeigten ein dem Kupfer sehr ähnliches Verhalten, die Untersuchungen an Stahlrohren jedoch zeigten deutliche Unterschiede.

Zur Untersuchung des Einflusses von Kippung/Versatz beim Rohrzug auf die Ausbildung von Eigenspannungen wurden diese überwiegend mittels der Bohrlochmethode (zerstörend, oberflächennah) und – an ausgewählten Proben – mit Hilfe der Neutronenstrahlung (zerstörungsfrei, lokal über die Wandstärke) untersucht. Die Ergebnisse zeigten für alle Werkstoffe, dass bei einem Kippwinkel von 5° (sowohl positiv als auch negativ) die erreichten Eigenspannungen im Bereich des ersten Auftreffens des Rohres auf die Matrize (gegenüber der Kipprichtung der Matrize) geringer als im Standardziehverfahren sind. Um die Entwicklung der Eigenspannungen während des Rohrziehens zu verfolgen wurden Stecker (Interrupted drawn tube) gezogen und präpariert und am SALSA Instrument in Grenoble, Frankreich, untersucht. Der Vorteil einer solchen Probe ist, dass die Bedingungen im Anlieferungszustand, im Ziehbereich und am gezogenen Rohr

innerhalb einer Messung erfasst werden können. Die Daten des Rohres im Ausgangszustand wurden als Eingangsgröße für die Simulation genutzt. Die Betrachtung der Umformzone bei -5° -Kippung zeigte, dass sich die Umfangseigenstressungen im Gegensatz zu den axialen Eigenstressungen signifikant änderten (im Bereich des ersten Kontakts), was auf den Massenfluss in Umfangsrichtung zurückgeführt werden kann. Dieser Massenfluss ist der Schlüssel zur Kontrolle der Entwicklung der Exzentrizität beim Rohrziehen.

Parallel zur Untersuchung der Exzentrizität und der Eigenstressungen wurden die Anisotropie der gezogenen Rohre und deren kristallographische Entwicklung untersucht. Damit sollte zum einen das Verständnis zum Einfluss der Kippung auf das anisotrope Verhalten des Rohres verbessert werden und zum anderen bestätigt werden, dass nach dem Rohrziehen mit Kippung keine wesentlich geänderte Richtungsabhängigkeit der Eigenschaften vorliegt. Dazu wurden die Makro- und Mikro-Texturen vor und nach dem Ziehen und mit und ohne Kippung untersucht. Die Makro-Textur ermöglicht den Vergleich verschiedener kristallographischer Orientierungen vor und nach dem Ziehen. Die Mikrostruktur wurde bestimmt, um mögliche Inhomogenitäten der Textur über die Wanddicke der Rohre erkennen zu können.

Die Makrotextur der Stecker wurde sowohl am Synchrotron als auch mittels Neutronenstrahlung am HEMS und dem STRESS-SPEC Instrument gemessen. Eine Analyse der Hauptorientierungen erfolgte durch Darstellung der PF- und ODF-Ergebnisse. Es lässt sich festhalten, dass die ODF- und PF-Intensitäten bei Kippung leicht reduziert waren. Jedoch gab es keinen signifikanten Unterschied zwischen den ohne und mit Kippwinkel gezogenen Rohren! Die Mikrotextur der Rohre wurde mittels Elektronenbeugung mit der EBSD-Methode untersucht.

Die experimentelle Durchführung des Rohrziehens unter Verwendung unterschiedlicher Werkstoffe mit unterschiedlichen Eigenstressungen und Texturen, mit unterschiedlichen Kippwinkeln und Versätzen, ist sehr zeitaufwändig und teuer, besonders dann, wenn eine Vielzahl an Kombinationen untersucht werden sollen. Um hier eine Variabilität zu gewährleisten und um das Prozessverständnis zu verbessern, wurde ein Simulationsmodell entwickelt. Die Eingabewerte des Modells sind die Eigenschaften des Ausgangsrohres wie die Exzentrizität, Eigenstressungen, die Textur und die mechanischen Kennwerte. Zur Entwicklung des Modells wurde eine Multiskalen-Simulationsmethode mit ICME-Ansatz genutzt.

Um die für die Simulation erforderlichen Eingaben zu erhalten, wurden unterschiedliche Simulationslängen genutzt. In der „Electronic Scale“-Simulation, wurde die Density Function Theory (DFT) verwendet und der Gitterparameter und der Kompressionsmodul bestimmt. Die Berechnung dieser beiden Parameter ermöglichte die Ermittlung des optimalen k -Punktes (Netz)

für die DFT Simulationen. Da Versetzungen ein sehr wichtiger Parameter bei Definition des Härtungsverhaltens eines Materials sind, wurden außerdem anteilige und perfekte GSFEs bestimmt. Die genannten Parameter wurden der atomar skalierten Simulation zugeführt. Um das für die MD-Kalkulationen benötigte Potential zu erreichen, wurde MEAM¹ verwendet. Darüber hinaus wurden mittels MEAM-Kalkulationen die elastischen Konstanten von Kupfer berechnet. C_{11} , C_{12} , und C_{44} wurden zu 170.20, 127.19 und 80.20 GPa bestimmt. Die MEAM Kalkulationen wurden mit Hilfe der DFT-Ergebnisse kalibriert. Nach der Kalibrierung der MEAM-Ergebnisse wurde das Potential von Kupfer erstellt und für die MD-Kalkulationen importiert. Die MD-Berechnungen wurden dazu verwendet, die Versetzungsbewegungen bei unterschiedlichen aufgetragenen Schubspannungen zu berechnen. Für jede Geschwindigkeit wurde außerdem der Widerstandsbeiwert (drag coefficient) berechnet, der sich zu 2.56×10^{-10} Pa.s ergab.

Die elastischen Konstanten und Widerstandsbeiwerte wurden direkt auf die FEM-Simulationen übertragen, während die Versetzungswanderungen auf eine größere Skala, mittels DD, auf mikroskalierte Simulationen übertragen wurden. Unter Nutzung der DD-Simulationen wurden die Härtungskenngrößen des Palm-Voce-Härtens bestimmt. κ_s , h_0 , und κ_0 wurden zu 148, 180 und 16 MPa berechnet. In der meso-skalierten Simulation wurde der CP-Ansatz in Form einer UMAT²-Subroutine angewendet. Ein FEM-Modell wurde mittels Abaqus Software entwickelt. Die folgenden Größen wurden in das Modell importiert:

- Messwerte des äußeren Rohrdurchmessers
- Messwerte der Wandstärken der Rohre und Exzentrizität
- Mittels Neutronenstrahlung gemessene Eigenspannungen
- Mittels Neutronenbeugung gemessene global (global-gesamte, umfassende) Makrotextur
- Anisotroper elastischer Tensor von Kupfer, berechnet mittels MEAM (atomar skalierte Simulation)
- Drag coefficient, berechnet mittels MD (Atomskalen-Simulation)
- Härtungsparameter, berechnet mittels DD (Mikroskalen-Simulation)
- Parameters of slipping rate (Literaturwerte)

Mittels berechneter und gemessener Exzentrizität, Eigenspannungen, Spannungs-Dehnungs-Diagrammen und Texturen konnten die Ergebnisse des FEM-Modells erfolgreich validiert werden. Damit liegt ein Simulationstool vor, das den Rohrziehprozess bei Einsatz unterschiedlicher Kippwinkel und

¹ Modified Embedded-Atom Method

² User-Material

Versätze für unterschiedliche Werkstoffe und Ausgangsbedingungen (Eigenspannungen und Texturen) hinsichtlich seiner Auswirkungen auf das Endprodukt zuverlässig beschreibt.

Résumé

Les tubes de précision sans soudure sont utilisés pour diverses applications mécaniques telles que plomberie, automobile, architecture... et généralement sont produites par extrusion, suivie de plusieurs étapes d'étirage à froid pour atteindre les dimensions finales.

Dans le processus d'étirage des tubes, la déformation s'effectue par une combinaison de contraintes de traction et de compression - créées par la force de traction appliquée à la sortie de la matrice et par sa configuration géométrique.

Les tubes étirés présentent des contraintes résiduelles qui sont souvent un point négatif pour leur utilisation finale. De plus, à cause des vibrations du mandrin il peut produire des tolérances de positionnement de la matrice ainsi que des différences de température potentielles dans le tube, des variations d'épaisseur sur la longueur et la circonférence causant l'excentricité (E) et l'ovalité. Les dernières sont généralement causées par un fluage non symétrique du matériau et étant présent pendant le processus d'étirage à froid, provoquant une déformation non homogène sur la circonférence.

Le processus de fabrication de tubes sans soudure entraîne souvent des variations d'épaisseur de la paroi qui, d'une part, augmentent le poids des produits finis et, d'autre part, entraînent des coûts inutiles pour la fabrication. Ainsi, le coût du matériau d'un tel tube ayant une épaisseur de paroi variable dépasse celui d'un tube ayant une épaisseur de paroi uniforme. Pour cette raison, il était nécessaire d'optimiser le processus d'étirage des tubes standards pour contrôler leur excentricité lors du tirage d'une manière reproductible.

Dans ce travail de thèse, une nouvelle méthode a été développée, dans laquelle une valeur spécifique d'inclinaison et / ou de décalage (l'inclinaison et le décalage seront décrit au chapitre 3 a été introduite respectivement dans la matrice et / ou le tube. Différents tubes de matériaux différents tel que : le cuivre, l'aluminium, le laiton et l'acier, avec différentes dimensions ont été étudiés en utilisant cette méthode. En plus d'influencer et de contrôler l'excentricité, il était crucial de prendre en compte ces paramètres. pour comprendre l'évolution des contraintes résiduelles à la surface et à travers l'épaisseur de la paroi du tube dans cette méthode.

La modification du processus d'étirage de tube et l'introduction de l'inclinaison et / ou du décalage ont fortement influencé le flux du matériau, et pour appréhender ce phénomène dans le processus, les développements des orientations cristallographiques tel que la texture cristallographique sont également nécessaires. Ainsi ce travail a été concentré sur l'étude de

l'excentricité, des contraintes résiduelles et des évolutions de la texture lors du processus d'étirage de tube avec des matrices inclinées et / ou décalées.

Parallèlement aux enquêtes expérimentales et afin de pouvoir mieux comprendre le processus et d'analyser des situations plus complexes, on a utilisé une approche de simulation multi-échelle basée sur l'Ingénierie des matériaux intégrés (ICME) et un modèle FEM universel a été développé et vérifié. La responsabilité de ce modèle était d'obtenir l'excentricité, les contraintes résiduelles et la texture des tubes avant le processus d'étirage et de simuler les mêmes paramètres et leurs variations pendant l'étirage avec et sans inclinaison / décalage. Tous les paramètres nécessaires pour les simulations, telles que les valeurs de durcissement, le coefficient de traînée, les constants élastiques, etc. ont été calculés dans différentes échelles de simulation.

Outre les expériences en laboratoire, l'utilisation industrielle de cette méthode a été considérée dès le début et pour cette raison, une construction industrielle du nouveau bloc d'étirage (y compris les outils d'inclinaison et de décalage) a été conçue. En d'autres termes, une solution industrielle a également été conçue dans ce projet.

Les principales étapes de ce travail pourraient être résumées telles que :

- Fournir des options d'inclinaison et de décalage en créant de nouvelles matrices en laboratoire (solution laboratoire),
- Concevoir un nouveau bloc d'étirage pour des applications industrielles impliquant des concepts inclinés et décalés (solution industrielle)
- Étudier l'évolution de l'excentricité des tubes avant et après l'étirage et comparer le changement d'excentricité pour différentes configurations d'étirages (inclinaison de l'angle, décalage de la matrice et combinaison de ces deux), différentes conditions matérielles (d'abord un traitement thermique et ensuite un matériau durci) et différents matériaux, à savoir le cuivre, l'aluminium, le laiton et l'acier,
- Étudier l'évolution des contraintes résiduelles pendant le processus d'étirage en utilisant :
 - Méthode de forage à trous (pour tous les tubes étudiés),
 - Méthode de diffraction des neutrons (dans les tubes de cuivre)
- Étudier l'évolution de la texture. Les mesures de la texture ont été effectuées ex-situ en utilisant des rayonnements de synchrotron, neutrons et électrons,
- Développer un modèle de simulation 3D pour simuler tous les paramètres mentionnés ci-dessus. Pour la simulation d'échelle

structurelle (simulation de tube, excentricité et simulations des contraintes résiduelles) et des simulations de méso échelle (développements de texture), les approches de la plasticité FEM et de la plasticité cristalline (CP) ont été respectivement utilisées. Pour obtenir des paramètres de durcissement, on a utilisé le croisement des théories de la fonction de densité (DFT), la méthode Molecular Embedded Atom Method (MEAM) et la simulation Dynamic Dislocation (DD).

Les résultats obtenus ont montré la possibilité de contrôler l'excentricité pendant l'étirage pour le cuivre, l'aluminium et le laiton de la même manière. Selon l'application, il est possible de produire le tube avec une excentricité inférieure ou supérieure. Pour l'acier, le comportement n'était pas identique aux trois autres matériaux. Dans le cas du cuivre, l'inclinaison de la matrice d'environ 5 ° et la fixation du côté minimum du tube dans le sens de l'inclinaison ont entraîné une réduction de l'excentricité moyenne de 40% (par rapport à l'amélioration de l'excentricité moyenne de 18% par étirement standard). Le décalage du tube d'environ 3 mm et le placement du côté minimum du tube dans le sens de décalage améliorent l'excentricité d'environ 30%. La comparaison des résultats de contraintes résiduelles pour les tubes étirés standard et inclinés montre la possibilité d'influencer les contraintes résiduelles aussi bien. La texture des échantillons de cuivre a été mesurée avec succès en utilisant les trois méthodes de diffraction. Une texture de cuivre pointue a été créée après le processus d'étirage. L'approche de simulation multi-échelle a été développée avec succès et tous les paramètres ainsi que les paramètres d'entrée ont été importés au modèle FEM à l'aide d'un sous-programme UMAT. Le modèle développé est capable d'obtenir et de simuler l'excentricité, les contraintes résiduelles, le comportement mécanique et les évolutions de la texture du processus d'étirage pour les étirages standard ou incliné / décalé.

Dans cette thèse, le chapitre 1 présente les principaux objectifs et les étapes prises dans ce projet. Le chapitre 2 fournit un bref aperçu des antécédents théoriques et des travaux existants sur le dessin par tube, le RS, la texture et les méthodes de simulation relatives au processus de dessin. Le chapitre 3 comprend les matériaux utilisés également dans la procédure expérimentale utilisée dans ce travail. Les résultats des variations d'excentricité pour des matériaux variés sont présentés au chapitre 4. Le chapitre 5 et le chapitre 6 fournissent les RS et les développements de texture et la simulation à grande échelle et ses résultats sont discutés au chapitre 7. Les conclusions sont présentées dans le chapitre 9.

Chapter 1 Introduction

Tubes have a very wide range of applications, so being used in automotive and aerospace industries, medical services, plumbing as well as structural elements in buildings or bridges. Long lasting copper tubes are a favorite choice for plumbing, heating, cooling and other systems [1]. Industries utilize the qualities of copper tube and fittings to maximize performance, cost, and ease of installation [2]. Steel tubes are very common components in industrial machines and in the transport sector. They are used in conveyor belt systems, hydraulic lifts, mills, production lines, for transporting fluids as well as powders, gases, and liquid wastes throughout industrial complexes. Aircraft, aerospace, automotive, and military industries require tubular steel made with tough alloys, preciseness and high resistance to extreme conditions [3]. The medical industry uses tubular steel in equipment and patient assistance applications.

Due to their lower density, aluminum tubes are an obvious choice when the weight is a critical factor. They are used in fields for aerospace, automotive, electronics and marine accessories [4]. Beside metallic tubes, non-metallic materials have also recently turned the attention of manufacturers to produce precision tubes for biomedical applications including catheters, endotracheal, and tracheostomy tubes [5].

Tubes can be produced with a seam or seamless. Tubes with a seam are produced out of sheet material shaped to the desired geometry and finally welded using various welding techniques [9]. Most seamless tubes start as round billets or ingots, which are produced mostly by continuous casting for smaller and larger diameters, respectively. For large diameters, block casting is preferred. Using continuous casting has some benefits such as reduced porosity and cracking in the center of the round, reduced segregation, more uniform properties in a given heat, and high productivity [6]. After casting, the hot round goes to a piercing mill to be pierced at elevated temperatures, e.g. using the Mannesmann process (see [7]) or by extrusion. To achieve the final required dimension, the pre-tube can be hot rolled and downstream cold drawn. Annealing, straightening, forming, coating, cutting and bending are some of the operations which the tube is processed after pre-forming to make it suitable for any end application [8].

Although the process is mostly computer-operated with high precision, some eccentricity – see 2.3 - is introduced to the hollow during piercing or extrusion. This wall-thickness variation over the circumference of the tube remains in

some magnitude in the final or semi-final product, which on one hand increases the weight of the products unnecessarily and therewith increases the costs for the manufacturer. Moreover, designing based on the minimum wall-thickness of such a tube, more metal is needed to reach the required minimum wall-thickness or the minimum required property of the part, respectively.

The key and foremost aim of this work was the understanding and controlling of the tube drawing process with regard to controlling eccentricity, either reducing or increasing it. Being able to control the eccentricity is especially interesting for high-priced materials as well as tubes with very tight tolerance requirements (precision tubes). As an example, in case of copper with a price of approx. 5000 €/t, this material is going to be replaced by some cheaper variations such as plastics or stainless steels. Therefore, being able to reduce the costs of copper tubes by reducing the eccentricity – and therewith the weight per meter, is a key factor. Even for steelmakers weight saving in precision tube production is not negligible. As an example, having a steel tube with an eccentricity of 3% (5%) results in a weight increase of approx. 1.5% (2.5%) for a tube 10x1 mm. The yearly production of precision steel tubes in Germany was about three Mio t in 2015. A weight saving of only 1% results in a reduction of 30,000 t, a saving potential of 90 Mio €, even with a moderate steel price of 3,000 €/t.

Fig. 1.1-a shows the motivation and aims of this work. To be able to control the eccentricity, the standard drawing method was optimized and tilting of the die or offset (shifting) in tube was introduced. To perform the tube drawing with tilting/offset, initially the required tools were built for the existing tube drawing machine at the Institute of Metallurgy, Clausthal University of Technology, and all tests were performed on this machine in a laboratorial scale.

Beside laboratory experiments the industrial usage of this method was considered from the beginning and, for this reason, an industrially suitable construction of a new drawing block (including tilting and offset tools) was designed.

As shown in Fig. 1.1-b, the general approach of this work was as following – which are discussed in Chapter 3:

- Design the tools for the laboratorial scale investigations, as well as design an industrial tool.
- Choose the materials and the drawing steps.
- Investigate the eccentricity, residual stresses (RSs), and texture of the tubes before and after the drawing.
- Develop an FEM model, to study the tube drawing process with all relevant properties of the as-received materials – such as eccentricity, RSs, initial texture, mechanical properties – and therewith analyzing more complex situations.

(a)	Motivation and aim
	<p>Motivation:</p> <ul style="list-style-type: none"> - Influencing the eccentricity in tube drawing process without affecting residual stresses and mechanical properties in a destructive way. <p>Method:</p> <ul style="list-style-type: none"> - Introducing tilting and offset (shifting) to the die/tube. <p>Aim:</p> <ul style="list-style-type: none"> - Controlling the eccentricity of the tubes during tube drawing process by using a tilted die and/or shifting the tube. - Developing an FEM model for simulating the process having real properties.
(b)	Approach - Chapter 3
	<ul style="list-style-type: none"> - Provide tilting/offset possibilities in an existing laboratorial drawing machine by designing and building new tools. - Select different tubes made of different materials and dimensions. - Investigate the eccentricity, RSs, and texture of the tubes before and after the drawing. - Develop an FEM model, which is able to simulate the process to analyze the process in a complex way. - Designing an industrial tool, to be used in industrial tests.
(c)	Experimental methodology - eccentricity - Chapter 4
	<ul style="list-style-type: none"> - Investigate the variation of the eccentricity by applying tilting, offset, and combination of these two. - Find a general rule for the tubes' behavior concerning eccentricity
(d)	Experimental methodology - RSs - Chapter 5
	<ul style="list-style-type: none"> - Study the effects of tilting and offset on the RSs, and be sure of having no negative effect on the RSs. - Hole drilling measurements on the surface (up to 0.7 mm) of the copper, aluminum, brass, and steel tubes. - Neutron diffraction measurements on copper tubes. - The measured RSs by neutron were used in the simulation model, as well.
(e)	Experimental methodology - texture - Chapter 6
	<ul style="list-style-type: none"> - Investigate the texture in drawing with tilting. - Study the macro-texture in drawn tubes by neutron and synchrotron diffractions. - Investigation of the micro-texture by EBSD method. - The measured textures were used in the developed simulation model.
(f)	Simulation methodology - Chapter 7
	<ul style="list-style-type: none"> - Develop an FEM model, which is able to get the eccentricity, RSs, texture, and the anisotropic elastic and plastic properties, a multiscale simulation approach was used. Different simulation scales; electronic, atomic, micro, meso, and structural scales, were used. - Tube drawing was simulated using FEM modelling. - To be able to simulate the texture by FEM, crystal plasticity approach was used (mesoscale simulations). - Hardening parameters were achieved by dislocation dynamic approach (microscale simulations). - Anisotropic elastic matrix was calculated using molecular dynamics (atomic scale modeling). - Density function theory was used to provide required results for developing proper potentials for molecular dynamics simulations (electronic scale).

Fig. 1.1 (a) Motivation of this work along with the aim. (b) to (f) Different methodologies used in this work.

To find a general rule for the tubes' behavior concerning eccentricity, different drawing steps and materials (copper, aluminum, brass, and steel) with different tube dimensions were investigated varying the tilting angles and/or offset values (Fig. 1.1-c). The results are discussed in Chapter 4.

After analyzing the effect of tilting/offset on the eccentricity of drawn tubes, its influence on the developed RSs, as described in Fig. 1.1-d, and the evolution of the RSs due to the introduced tilting and/or offset was investigated using hole drilling and neutron diffraction methods. Hole drilling, as a fast and quite cheap method, is limited to surface-near results. With neutron diffraction the whole wall-thickness of the tube can be measured (measurements were done with SALSA instrument at ILL, Grenoble/France); however, it is an expensive method. The measurements done with neutron diffraction were used also to gain required data (input as well as validation data) for the simulation. The results of the RS evolutions are discussed in Chapter 5.

Tilting and/or offset of the dies clearly influences the mass flow in the tube. This mass flow, which itself is resulting from interactions between temperature, microstructure, time, and deformation, is the decisive factor in texture development in the tube drawing process [9]. The anisotropic behavior and the crystallographical evolution of the tubes drawn with tilting were investigated to make sure that their final properties are not being significantly directionally dependent of the crystallographical directions, (see Fig. 1.1-e). Considering anisotropy and mass flow, it was decided to analyze the texture evolution of the tubes before and after drawing with tilting, to state whether tilting creates significant different textures (crystallographical orientations) and/or affect the mass flow in a detectable way. To study these parameters, the macro- and micro-texture of the tubes were investigated. Using macro-texture, different crystallographic orientations were compared before and after drawing and texture was analyzed. Micro-texture was studied for through-wall-thickness analyses.

For macrotexture analyses synchrotron and neutron diffraction methods were applied. The reason for choosing two methods was the coarse grain size of the as-received tubes, not being possible to be measured by synchrotron use and therefore a neutron source was used. Synchrotron and neutron diffraction measurements were done using HEMS instrument at PETRA III in Hamburg/Germany and STRESS-SPEC instrument at FRM II in Munich/Germany, respectively. Moreover, these results were also used as input data for the simulations as well as for validation. The micro-texture evolution of the as-received and drawn tubes was measured using EBSD (electron backscattering diffraction).

Tube drawing investigations with different tilting/offset values on materials of different qualities with different starting RSs and initial textures are time and

cost intensive. Moreover, not all combination can be studied experimentally. To overcome this problem and also to have a better understanding of the process, it was decided to develop a simulation model containing all relevant properties of the as-received materials – such as eccentricity, RSs, initial texture, mechanical properties – and therewith analyzing more complex situations (as described in Fig. 1.1-f). Moreover, using the developed model, it was possible to compare the texture evolution of the drawn tubes with and without titling, without performing time consuming neutron, synchrotron, or electron measurements. For this goal, a multiscale simulation approach based on Integrated Computational Material Engineering (ICME) was used. To develop such a model, a FEM approach, in this case a structural scale simulation, was used. With this model, the eccentricity, RSs, and the mechanical properties of the tubes were simulated. However, in order to be able to simulate the texture development, the Crystal Plasticity (CP) method (mesoscale simulation) was used. In case of studying texture evolution it is important to consider the anisotropic elastic and plastic behaviors of the material. The anisotropic hardening behavior was calculated by using the Dislocation Dynamics (DD) theory (microscale simulation). One important parameters for these calculations is the dislocation mobility, which was computed by a Molecular Dynamics (MD) approach, which is an atomistic scale simulation. The proper potential, necessary for MD calculations, was created by a Molecular Embedded Atom Method (MEAM) approach being an atomistic scale approach as well. Finally, the required data for the creation of the above-mentioned potential was calculated using the Density Function Theory (DFT) - electronic scale simulation. All these steps are discussed in detail in Chapter 7.

In case of copper, it was not mandatory to calculate and achieve all the parameters relating to the simulations, using different simulation scales. However, focusing in future on a model being usable for other metal materials as well, this approach was taken and all – then necessary - different simulation scales were considered. Moreover, it gave a good possibility to verify the achieved results with existing ones for copper.

The main aims of this work along the most important steps are summarized in **Fig. 1.2.**

In this thesis, beside this chapter, which was an introduction to the main aims and the taken steps in this project, Chapter 2 provides a brief review of the theoretical background and existing works on tube drawing, RSs, texture, and simulation methods relating to the drawing process. Chapter 3 includes the materials which were used also the experimental procedure which was taken in this work, as well as the used solvers and software packages, used in simulation. The results of eccentricity variations for varied materials are presented in Chapter 4. Chapter 5 and Chapter 6 provide the results of RSs and texture developments and the multiscale simulation and its results are

discussed in Chapter 7. A brief summary and outlook are presented in Chapter 8. In Chapter 9 main results of this work are presented in French and a general conclusion is also presented at the end of this chapter.

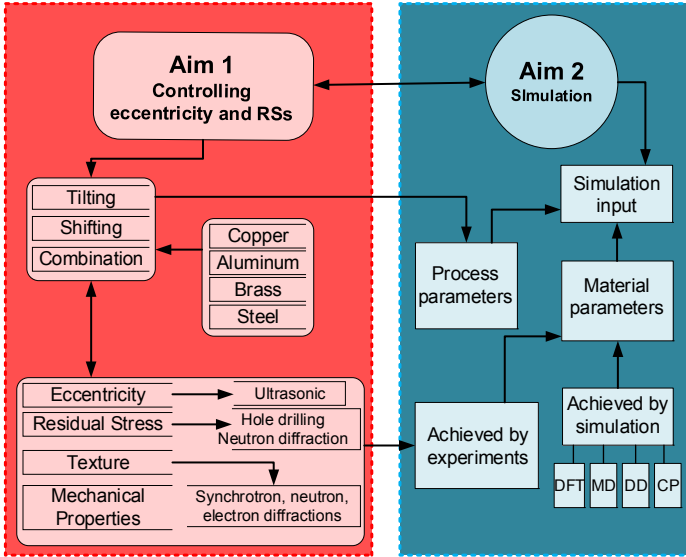


Fig. 1.2 Main aims of this work.

Chapter 2 Theoretical background

2.1 Introduction

The objective of this chapter is to present - as far as necessary - the theoretical background and state of the art on the tube drawing process and the different simulation approaches in different length-scales used. Initially, the principle of the tube drawing process is shortly described and the mechanics of tube drawing - the phenomena mostly at the basis of the drawing process which are investigated numerically - are discussed. Imperfections arising during tube drawing - eccentricity and RSs - were introduced, as well. Crystallographical orientations (crystallographical texture) are briefly familiarized. Finally, the simulation approaches used in this work are introduced and the state of the art regarding this matter is presented.

2.2 Tube drawing

To deliver the desired diameter and wall-thickness of the final product, after producing the very first tube, these tubes will be (hot rolled and) cold drawn. Cold drawing gives the possibility of an excellent surface finishing, closely controlled dimensions, and wanted mechanical properties [10]. The deformation is accomplished by a combination of tensile and compressive stresses that are created by the pulling force applied at the exit of the die and its configuration [11].

There are four distinct types of tube drawing, which are presented in **Fig. 2.1** and introduced shortly:

- **Sinking** (Fig. 2.1-a) is the closest (technology) to wire drawing, where the tube is drawn through a die without a plug. The tube is reduced in the outside diameter, while the wall-thickness and the tube length are increased. The magnitude of thickness increases and tube elongation depends on the flow stress of the drawn part, the die geometry, and the interface friction [12]. Sinking is the least costly drawing method and is advantageous in applications where the inner surface quality or small thickness deviations are of minor importance. Excessive sinking with wall thickening can have an adverse effect on surface quality [13].
- **Drawing over a fixed plug** (Fig. 2.1-b) is used for drawing large to medium diameter straight tubes. To hold the plug in the correct position and avoid movement of the tube caused by friction, the plug

must be fixed by a bar. In addition to the diameter, the wall-thickness can also be reduced defined by the plug diameter [14]. Although the operation is slow and the area reduction is limited, no other drawing process has the capability of producing comparable inside surfaces [13].

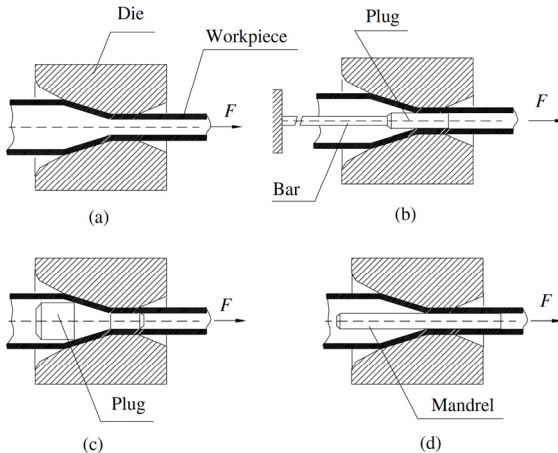


Fig. 2.1 Tube drawing processes: (a) tube sinking, (b) drawing with a fixed plug, (c) floating plug, and (d) drawing on a mandrel [14].

- Drawing with a floating plug** (Fig. 2.1-c) is performed for drawing tubes of small diameters in higher scale. The setup is the same as with plug drawing, however, the plug is not attached to a bar. The plug is designed with higher angles to be fixed in the deformation zone [15]. Proper lubrication is important to avoid stick-slip movement of the plug. Tooling is more critical for this operation than for any of the others. The bearing must be long enough to permit the plug to sit stable in the tube's inside diameter but not so long that friction becomes a problem. In addition to tool design, lubrication and the cleanliness of the tube are critical to successful floating plug drawing [13].
- Mandrel drawing** (Fig. 2.1-d) process draws the tube over a long-hardened mandrel passing the die together with the tube. As the mandrel clamps tightly onto the tube, unpinning is necessary for a second operation. Moreover, removing the mandrel by a rolling operation - called reeling - expands the diameter slightly. However, mandrel drawing creates less friction and needs lower drawing forces than any of the plug drawing operations, so it enables higher area reductions in one pass. Tube producers use mandrel drawing primarily for sizes not suitable for plug drawing, such as heavy-wall tubing. Mandrel drawing requires less set-up time, so it is suitable for small runs [13].

2.2.1 Mechanics of drawing

2.2.1.1 Strain and stress

Assuming no friction and no redundant work, true strain in tube drawing is given as the fractional cross-sectional area where ideal deformation happens. This strain embraces two components, one in wall-thickness (ε_s) and the other in diameter (ε_d). These strains and also the stress resulting from an ideal deformation can be calculated using Eqs. (2.1) to (2.3).

$$\varepsilon_s = \ln \frac{t_f}{t_0}, \quad (2.1)$$

$$\varepsilon_d = \ln \left(\frac{D_f - t_f}{D_0 - t_0} \right), \quad (2.2)$$

$$\sigma = \sigma_{f_m} \ln \frac{A_0}{A_f}. \quad (2.3)$$

where D_0 and D_f are the initial and final outer diameters and t_0 and t_f are the initial and final wall-thicknesses of the tube, respectively (as shown in **Fig. 2.2**). In Eq. (2.3) A_0 and A_f are the initial and final cross-sectional area of tube and σ_{f_m} is the average flow stress during deformation.

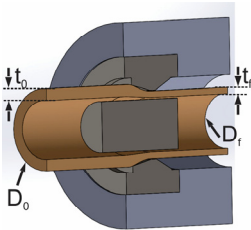


Fig. 2.2
Schematic of the wall-thickness and diameter of the tube before and after drawing.

However, considering friction results in a higher true stress than what is calculated by Eq. (2.3). Alexander predicted the draw stress using Eq. (2.4) where σ_d is the draw stress, μ the friction coefficient, δ the inhomogeneity factor [calculated with Eq. (2.5)] and α is the die's semi-angle [16].

$$\sigma_d = \sigma_{f_m} (1 + \mu \cot \alpha) \delta \ln \frac{A_0}{A_f} \quad (2.4)$$

$$\delta = 0.88 + 0.12 \left(\frac{d_0 + d_f}{d_0 - d_f} \sin \alpha \right) \quad (2.5)$$

2.2.1.2 Drawing force

There are different approaches to calculate the drawing force in tube drawing. In the case of tube drawing with a fixed plug, Geleji [17] and Anke and Vater

[18] are the most used approaches, being worth mentioned here. Geleji divided the drawing force into three constituent forces; F_N , the drawing force required to perform the pure deformation work, F_R , the drawing force required to overcome friction, and F_{Sh} the drawing force required to carry out the shear work. These forces are calculated with the following equations:

$$F_N = k_m \times (A_0 - A_1) \quad (2.6)$$

$$F_R = k_m \times (Q_1 \times \mu_1 + Q_2 \times \mu_2) \quad (2.7)$$

$$F_{Sh} = 0.58 \times \alpha \times \bar{\sigma}_{ave} \times A_1 \quad (2.8)$$

where k_m is the average deformation resistance in MPa that can be calculated with Eq. (2.9), L_1 and L_2 are the contact surfaces of the drawing die and plug, respectively, to be calculated by Eqs. (2.10) and (2.11), μ_1 and μ_2 are the coefficients of friction between the drawing die and the tube and between the plug and the tube, respectively, and $\bar{\sigma}_{ave}$ is the average flow stress.

$$k_m = \frac{\bar{\sigma}_{ave}}{1 + \frac{(A_0 - A_1) + (\mu_1 \times L_1 + \mu_2 \times L_2)}{2 \times A_1}} \quad (2.9)$$

$$Q_1 = \frac{(d_0^2 - d_1^2) \times \pi}{4 \times \sin(\alpha)} \quad (2.10)$$

$$Q_2 = \frac{d_{i1} \times \pi \cdot [(d_0 - d_1) - (d_{i0} - d_{i1})]}{2 \times \tan \alpha} \quad (2.11)$$

where d_0 and d_{i0} are the outer and inner diameters of the tube before drawing and d_1 and d_{i1} are the outer and inner ones after drawing.

Anke and Vater suggested Eq. (2.12) to calculate the drawing force for tube drawing with a fixed plug. The coefficients X_1 and X_2 depend on the internal tool; in case of tube drawing with a plug, both values are set to 1.

$$F_z \approx 1.1 \times A_1 \times \bar{\sigma}_{ave} \times |\varepsilon_s| \times \left[1 + X_1 \times \frac{\mu}{\alpha} + X_2 \times \frac{\alpha}{2 \times |\varepsilon_s|} \right] \quad (2.12)$$

For more information on calculating drawing forces for tube drawing see Gummert [12] or Grote and Antonsson [19].

2.2.2 Analytical study of tube drawing

In one of the first studies performed on analytically studying the tube drawing process, Siebel and Weber (1935) [20] studied the mass flow and the distribution of tensions in tube drawing processes. In the middle of the 40th,

Hoffman and Sachs (1953) [21] directed a series of works about the diminution of diameter and thickness of wires and tubes and calculated the necessary stress to draw tubes using different internal tools. Swift (1949) [22] made also a notable contribution to his mathematical treatment of the process of tube sinking. At the beginning of the 50th, Hill (1948) [23] analyzed - from an industrial point of view - the requirements necessary to predict the change in the wall-thickness and drawing force. Elion and Alexander (1961) [24] carried out an industrial research for the optimization of variables in tube drawing processes. The works of Green (1960) [25], Blazynski and Cole (1983) [26] as well as Johnson and Mellor (1986) [27] are in the same line of that one originated by Sachs. Moore and Wallace [28] studied the tube sinking process numerically using the approximation theory assuming ideal-plastic behavior and a smooth conical die. In their study, they included the Coulomb friction law and strain hardening in their analyses of stresses and strains.

The rapid development of computer techniques made using a more complex approach to solve problems of deformability and plasticity of metals possible. In the 90th first works of tube drawing analyses by numerical methods appeared, in particular, by the *FEM* described in "2.6.6 – *Structure scale simulation; FEM*"; the contributions to the subject that deserve a special mention are those of Avitzur [29], who experimentally analyzed the main processes related to tubes drawing, of Collins and Williams, who proposed an axisymmetric slide-lines field analogous to Hill's one. Um and Lee [30] obtained an Upper Bound Method (*UBM*) for tube drawing with a fixed tapered plug. Using this method, they obtained the optimum die angle minimizing the drawing stress. This optimum die angle was mainly determined by using the internal shear and the friction. Rubio et al. [31, 32] analyzed the tube drawing with a fixed plug by means of the *UBM*. They assumed a plain stress condition considering the Coulomb friction law. The results were validated by comparing them with those obtained by the slab method, the *FEM* and the experimental data found in the literature.

2.2.3 Imperfections arising from tube drawing

Due to the ever-increasing competition with the advent of globalization, it has become highly important to keep on improving the process' efficiency in terms of product quality, precision, and optimized use of resources. The factors that determine the choice of the forming or for that matter any other process are maximum utilization of resources with high-quality output [33]. In cold drawing, like any other forming processes, drawn tubes have also some imperfections, which influence their quality and performance. It is critical to understand the relationships between the individual steps in the production of tubes: casting, extrusion, hot rolling and cold drawing, and connect them into one continuous process. Each step should be initially considered on its own to understand the degree of impact of an individual change and imperfections within that step. If

a billet, for instance, is extruded into a poor-quality tube preform, which has even a moderate level of eccentricity, it will be hard to eliminate its eccentricity during drawing process [34]. Moreover, due to vibrations of the mandrel, tolerances in the positioning of the die and the billet, as well as potential temperature differences within the billet, variations of thickness can occur along the tube's length and around its circumference causing eccentricity and ovality [35]. These differences can lead to an undesirable increase in the tube volume and weight, which, which is of special interest for high-cost materials, making eccentricity potentially an imperfection for produced drawn tubes [36].

On the other hand, tubes produced by tube drawing have a defined tensile RS state over length and thickness of the tube, which can cause failure during its application. Also, the eccentricity influences the circumferential material flow during drawing and generates a complex RS pattern on the surface of the tube, which together with the RS created by drawing can significantly affect its final mechanical and fatigue behavior [37]. Generally, RSs have a noteworthy influence on materials' performance and counts as another imperfection in tubes.

2.3 Eccentricity

Eccentricity (E) is defined as the percentage of the maximum variation in tube wall-thickness from their sum (or from an average value) within the same tube's cross-section, as described by Eq. (2.13) or (2.14) and shown in **Fig. 2.3**. In this work, Eq. (2.13) was used for eccentricity calculations. Tube eccentricity can be measured in two ways: on-line monitoring on a continuous basis during tube production, commonly performed using ultrasonic techniques [38], and off-line by analyzing an adequate number of cross-cuts from tubes sampled from the production [39].

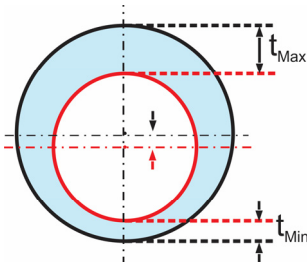


Fig. 2.3
Deviating of wall-thickness from an ideal form (eccentricity).

$$E = \frac{t_{max} - t_{min}}{t_{max} + t_{min}} \quad (2.13)$$

$$E = \frac{t_{max} - t_{min}}{t_{avg}} \quad (2.14)$$

where t_{max} , t_{min} and t_{avg} are the maximum, minimum, and average wall-thicknesses, respectively. The accepted industrial eccentricity for copper and steel tubes is approximately 2 to 10% (DIN EN 12449:2012 [40] and DIN EN 2413:2011-06 [41]) and it is about 3% for aluminum (DIN EN 13957:2008 [42]). Another definition of the eccentricity is the distance between the centers of the external and internal circular profiles of the tube walls [39].

The zones of maximum and minimum wall-thicknesses are often substantially diametrically opposite each other. These zones in the case of extruded tubing, generally extend longitudinally, whereas, in the case of rotary pierced tubing, such zones may follow a helix along the tube [43]. For many applications of tubing, such variation in wall-thickness, despite its disadvantages, is ignored. However, certain applications require tubes having not less than a specified or pre-set minimum wall-thickness. When the inner and outer peripheries are not concentric, the actual minimum wall-thickness must equal the required minimum thickness. In turn, the maximum wall-thickness will then be thicker than the required wall-thickness. Consequently, the weight of the tube will be higher than what is required. This is an excess metal cost which can run into a generous sum of mass production of tubing. Accordingly, there is a substantial saving in metal cost if the tubes can be produced with a uniform, constant wall-thickness, as less weight of metal would be required for such tubes [44].

A very few studies on the dimensional accuracy of tubes in the cold drawing have been reported. Randall and Prieur [45] discussed the effects of the side relief on the dimensional accuracy of finished tubes. The tool design, particularly the side relief, has been thought to be critical for dimensional accuracy. However, in actual operation, tube manufacturers have struggled to achieve the process conditions required for high dimensional accuracy [45]. Tetley [46] discussed some of the factors which are assumed to influence eccentricity during drawing. He analyzed the alignment of the tube to the axis of the draw and its influence on the eccentricity. He compared the distribution of eccentricity in the extruded and drawn copper tubes (**Fig. 2.4**). He stated that the two distributions are almost identical except that the mean of eccentricity for an extruded stock is at about 17 % and for finished tubes about 5 % eccentricity. This would seem to indicate that there was a definite improvement in eccentricity during drawing. Although it was amongst a vast number of mill technicians that "eccentricity cannot, in fact, be improved during drawing, the best that can be achieved is to maintain it at a constant level", his results showed it to be possible to decrease the eccentricity significantly.

Xu et al. [47] developed a plug for the drawing process for achieving higher accuracy in aluminum tubes with rectangular cross-sections. Based on this new plug, they reduced the deviation in wall-thickness. Huml et al. [48] investigated the precision tube production in cold pilger rolling with the aim of optimization

the process and material parameters based on a computer assisted process model. Abe et al. [49] studied the dimensional accuracy of tubes in cold pilgering under different process conditions.

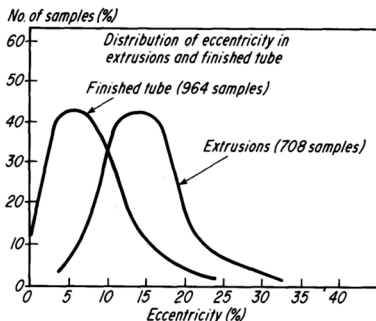


Fig. 2.4
Distribution of eccentricity in extruded and drawn copper tubes [46].

Not only the reduction of the eccentricity is important, but the increase of the eccentricity can also be of interest in special cases. In heat exchangers, controlling the eccentricity (decreasing or increasing) is one important parameter for optimization of the maximum heat transfer under a fixed volume constraint. Matos et al. [50] studied this effect for copper tubes. They showed that the variation of eccentricity allows the heat transfer performance of elliptic tubes to be compared with flat plates and circular tubes. Some structural components found in cars, aircraft and other vehicles require bent or hydro-formed tubes of lower weight. It is of interest to have tubes of varying axial or circumferential thickness so that to reduce overweight on low stressed areas and reinforce it otherwise. In such an application, it is crucial to be able to increase the eccentricity. Bihamta et al. [51, 52] introduced a new method for producing aluminum tubes with variable wall-thicknesses, which could produce tubes with locally increased and decreased eccentricity. They used a conical plug with a supplied movement system to this conical plug. This method was called position-controlled plug method. Negendanka [53, 54] also did investigations on aluminum tubes with axially varied wall-thicknesses and studied the variation of wall-thickness in their production with variable wall-thicknesses. There are also some other methods such as indentation forging (swage autofrettage) [55] or radial forging [56] methods, which have some limitations in producing thin wall tubes. Moreover, their tools are quite expensive compared to standard ones.

2.4 Residual stresses

Stresses remaining in the material or body without an external load (applied force, displacement or thermal gradient) are called residual stresses (RSs). These kinds of stresses originate during manufacturing and processing of

materials mostly due to heterogeneous plastic deformations, thermal contraction and phase transformations [57]. RSs can be classified according to the objective. A classification well suited to purpose of this work is given in **Fig. 2.5** showing the origin of all stresses as mechanical, thermal, or chemical ones [58].

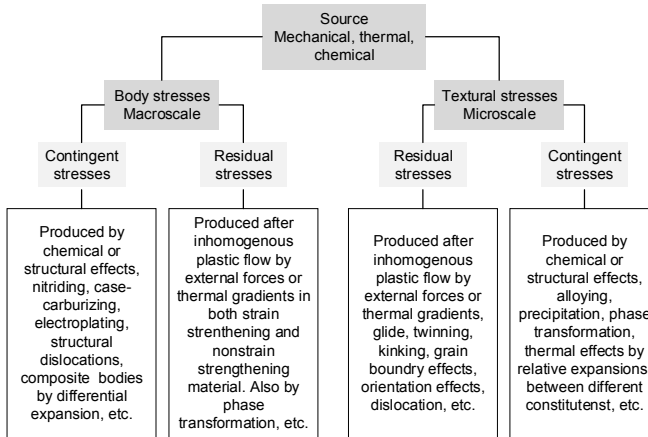


Fig. 2.5 Various sources of RSs in metals [58].

Stresses may be further divided by the length scale over which they equilibrate, namely large-scale (macro-scale) and small scale (micro-scale) RSs as follow:

- **Type I, macro-scale:** these RSs vary within the body of the component over a range much larger than the grain size. For technical applications, one normally focuses only on RSs Type I.
- **Types II and III, micro-scale:** these kinds of RSs result from differences in the microstructure of a material. Whether they are on the scale of an individual grain (type II) - expected to exist in single phase materials because of anisotropy in the behavior of each grain, or within a grain (type III), which results from the presence of dislocation and other crystalline defects [59].

RSs affect the properties and the life time of the final products. Because of their self-equilibrating character, the presence of RSs may not be readily apparent and so they may be overlooked or ignored during engineering design. Their presence in a proper manner could significantly improve the design criterion of the strength-to-weight ratio and reduce final costs. However, RSs are often associated with warping and distortion after heat treatment or machining, and early service failures of tools, dies, machine parts, and welded members.

Tensile stress which exceeds the elastic limit helping cracking in surface coatings. Compressive stress, on the other hand, is considered desirable under these conditions as it closes surface cracks and improves fatigue properties. However, excessive compressive stress can cause cohesive failure and adhesive failure in the case of coating [60]. RSs in a body are in static equilibrium, thus, the total force acting on any plane through the body and the total moment of forces on any plane is zero [61].

Heyn and Bauer (1911) [62] illustrated the spring analogy in their research on RSs in cold-drawn metals to show how the RSs behave in metals. Timoshenko (1941) [63, 64] presented a review of the early literature of manufactured parts such as guns and turbine rotors. Hetenyi (1963) [65] claimed that RSs in an elastic solid arise from three distinct sources, namely, misfit, change in specific volume, and non-uniform distortion. Elices [66] discussed that RSs - due to cold-drawing - are known to be detrimental to the mechanical performance particularly as regards to creep, fatigue, and ductility. Nakashima et al. (2008) [67] proposed a method to produce seamless tubes in such a way that the RSs generated during the stage of correction after cold working could be lowered. Kuboki et al. [68] examined the effect of the plug on RS in tube drawing. They compared the gradient of the RSs through the wall-thickness of the drawn tube with and without plug.

2.4.1 Measurement methods

The “locked-in” character of RSs makes them very challenging to evaluate. Classically, strain or displacement is measured, from which the stresses are subsequently interpreted. Several methods are available to measure residual strains, destructive and nondestructive ones, each having its advantages and disadvantages [69]. Some of the most important destructive methods of measuring residual strains are as follows:

- Bauer and Hayn method, see [70]
- Sachs Boring-out method, see [71]
- Hole-Drilling method, see “2.4.1.1 - *Hole-drilling method*”
- Treuting and Read method, see [72]

In all these methods, the stress-containing material is destroyed and therefore measurements must be made on the adjacent remaining material, which makes these approaches complicated. This separation of stress and measurement locations creates mathematical challenges that require specialized stress evaluation methods [73–75].

For non-destructive measurement methods, since no material is removed, one must use some identification of a “stress-free” reference state for interpreting

the measurements. Nevertheless, achieving such a “stress-free” state can be quite challenging to do reliably. All these challenges cause inaccuracy in measurements of RSs. However, the various RS measurement methods are nowadays quite mature and the accuracy gap is often quite small [76]. Some of the most important non-destructive methods are as follow [77]:

- Diffraction methods (x-ray, neutron, synchrotron)
- Ultrasonic, see [78]
- Photoelastic, see [69]
- Acoustic wave propagation, see [79]

Different parameters such as objective of measurements, specimen damage and dimension, measurement environment (lab or field use), nature of the RS, materials and accuracy and spatial resolution¹ play role in choosing the suitable measurement method [81].

Fig. 2.6 summarizes several methods in terms of their spatial resolution and their ability to penetrate into the specimen. It is evident that several factors need to be carefully considered and balanced to make an appropriate choice of an RS measurement method for a given application [76]. As in this work, the hole drilling and neutron diffraction methods were used to determine RSs, they will be described briefly in sections 2.4.1.1 and 2.4.1.2.

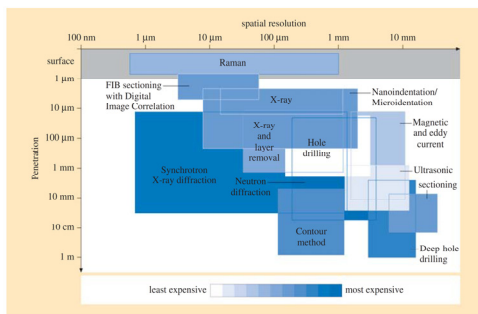


Fig. 2.6 Measurement penetration vs. spatial resolution for various residual stress measurement methods [82].

2.4.1.1 Hole-drilling method

The pioneering work of Mathar in the 1930s [83] is the basic of the hole-drilling method. Since this method is relatively simple, cheap, quick and versatile, it is one of the most widely used general-purpose techniques for measuring RSs. This method can be portable or laboratory-based and can be used for a wide

¹ Angular resolution or spatial resolution describes the ability of any image-forming device such as an optical or radio telescope, a microscope, a camera, or an eye, to distinguish small details of an object, thereby making it a major determinant of image resolution [80].

range of materials and components. It is convenient to use, has standardized procedures and it has acceptable accuracy and reliability. This method is sometimes called “semi-destructive”, since the damage, introduced during the test, is often tolerable or repairable [84]. This technique is well-established with an ASTM Standard Test Procedure - ASTM E837 [85] - and extensive instructional literature (see [86–89]).

The principle of this technique involves the creation of a small hole in a component containing RSs and subsequent measurement of the locally relieved surface strains. **Fig. 2.7** schematically illustrates the deformations around a hole drilled into the material with tensile RSs. The consequent stress release causes an elastic springback that slightly expands the hole edge, with a small local surface rise due to Poisson strain. The opposite happens with compressive stresses. For experimental evaluations, strain gages or optical techniques are available to quantify the surface deformations of the surrounding material, from which RSs originally existing within the hole can be determined [86].

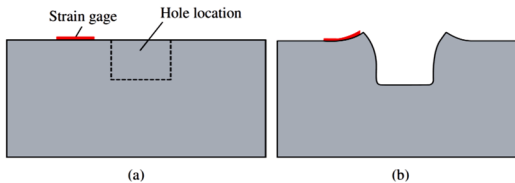


Fig. 2.7 Schematic cross-sections around a hole drilled into tensile RSs. (a) Before and (b) after hole drilling [84].

The measured strains are used to calculate the stresses [90]. Since any RSs which has produced by the drilling process could have affect the results, it is important that a suitable drilling method is chosen. These include the use of conventional drilling, abrasive jet machining, and high-speed air turbines. In practical terms, there is no point making measurements beyond a depth equivalent to the drill diameter, since no additional strain can be measured and accordingly the sensitivity will be too much decreased [91].

2.4.1.2 Neutron diffraction method

Neutron diffraction along with X-ray and synchrotron diffractions forms a family of RS evaluation methods based on diffraction. All these methods involve directing a beam of the chosen radiation on the sample material and measuring the angular distribution of the radiation diffracted from the material [92]. Diffraction methods of RS determination basically measure the angles at which the maximum diffracted intensity occur when a crystalline sample is irradiated

with a beam. From these angles, one then obtains the spacing of the diffracting lattice planes by using Bragg's law, Eq. (2.15) [93].

$$\lambda = 2d_{hkl} \sin \theta \quad (2.15)$$

where d_{hkl} is the interplanar distance of the stress-free sample and subscripts hkl are the Miller indices that specify the planes of the atomic lattice. The interplanar distance d_{hkl} is calculated using the scattering angles [94].

The wavelength (λ) and direction of travel of the neutrons emerging from the beam source are selected either by a single crystal or by time-of-flight through a known distance. The beams of defined wavelength impinge on the sample set up on the instrument and are scattered by the sample. The sharp peaks permit strain measurements through the use of the Bragg relationship, as shown in Eq. (2.15). Both, the incident neutron beam falling on the sample and the diffracted beam may be defined in height and width by slits in the beams as indicated schematically in **Fig. 2.8**. The overlap of the incident and diffracted beams is known as the gage volume and is fixed in space at the center of rotation of the instrument [82]. The basic features of a monochromatic beam diffractometer are shown in Fig. 2.8, as well.

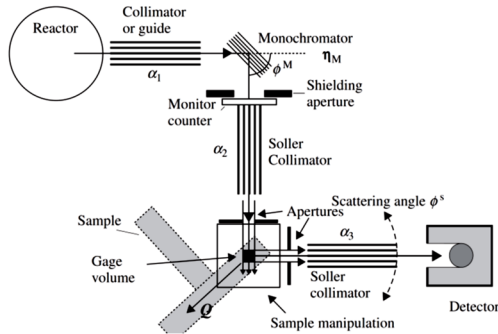


Fig. 2.8 Monochromatic beam diffractometer showing diffraction from the monochromator to the right and diffraction from the sample to the left resulting in focusing [95].

The lattice strain, ε^{hkl} , is defined by Eq. (2.16), in which the lattice spacings - corresponding to the macroscopic stress- (and strain-) free values for the material - are denoted by d_{hkl}^0 . The Bragg angle for the stress-free material is given by θ_{hkl}^0 .

$$\varepsilon^{hkl} = \frac{(d_{hkl} - d_{hkl}^0)}{d_{hkl}^0} = \frac{\Delta d_{hkl}}{d_{hkl}^0} = \frac{\sin \theta_{hkl}^0}{\sin \theta_{hkl}} - 1, \quad (2.16)$$

Three orthogonal stresses may always be obtained from three orthogonal strains. In three dimensions, the stress-strain relationship can be written as following equations:

$$\sigma_{11} = \frac{E_{hkl}}{(1 + \nu_{hkl})(1 - 2\nu_{hkl})} [(1 - \nu_{hkl})\varepsilon_{11} + \nu_{hkl}(\varepsilon_{22} + \varepsilon_{33})], \quad (2.17)$$

$$\sigma_{22} = \frac{E_{hkl}}{(1 + \nu_{hkl})(1 - 2\nu_{hkl})} [(1 - \nu_{hkl})\varepsilon_{22} + \nu_{hkl}(\varepsilon_{11} + \varepsilon_{33})], \quad (2.18)$$

$$\sigma_{33} = \frac{E_{hkl}}{(1 + \nu_{hkl})(1 - 2\nu_{hkl})} [(1 - \nu_{hkl})\varepsilon_{33} + \nu_{hkl}(\varepsilon_{11} + \varepsilon_{22})]. \quad (2.19)$$

where E_{hkl} and ν_{hkl} are the diffracted elastic constant and the Poisson's ratio. These values can be calculated following Kröner [96]. **Table 2.1** and **Table 2.2** show these parameters for four different materials [97]. The presence of a strong texture will modify the constants. Then it is appropriate measuring them on the material of interest.

Table 2.1 Diffraction elastic constant, E_{hkl} (GPa) calculated from using the Kröner model [97].

{hkl}	200	311	420	531	220	422	331	111
Al	67.6	70.2	70.3	71.2	71.9	71.9	72.3	73.4
Cu	101.1	122.0	122.5	131.5	139.1	139.1	144.3	459.0
Ni	160.0	185.0	185.6	195.6	203.9	2033.9	209.5	224.6
304L	152	184	185	199	211	211	219	242

Table 2.2 Diffraction Poisson's ratio, ν_{hkl} , calculated from the Kröner model [97].

{hkl}	200	311	420	531	220	422	331	111
Al	0.35	0.35	0.35	0.35	0.35	0.35	0.35	0.35
Cu	0.38	0.35	0.35	0.34	0.33	0.33	0.32	0.31
Ni	0.36	0.33	0.33	0.33	0.33	0.33	0.31	0.30
304L	0.33	0.294	0.293	0.278	0.265	0.265	0.256	0.23

The Sample Gage Volume (*SGV*) is the part of the sample in the Instrument Gage Volume (*IGV*) from which a measurement of the diffraction peak is obtained. It is the volume of sample over which the strain measurement is averaged, and affected by [98]:

- Partial filling of the gauge volume
- Wavelength distribution of neutrons across the incident beam
- Attenuation of neutrons within the sample
- A high gradient in texture in the sample

Existing each of these causes an irregular shift in Bragg peak angles, not being attributed to stresses or strains, and should be considered in the calculation of the RSs. This matter is discussed in Chapter 5.

2.5 Texture

The microstructures of materials are traditionally characterized by the morphology and distribution of constituent phases and the traditional description of microstructure of a crystalline material specifies a number of parameters, such as the dislocation substructure (overall density and distribution), grain structure (size, size distribution, and shape), second phase content (volume fraction, size, and distribution), and interface characteristics (grain boundaries and interphase boundaries). Nonetheless, this does not suffice to provide a complete description of microstructure. An elaborate and complete description of microstructure of a crystalline material must also include the knowledge about crystallographic orientations of the constituent grains [99].

As stated by Bunge (1987) [100], the influence of texture on material properties in many cases can be 20%–50% of the property values. As an example, **Fig. 2.9** shows the three-dimensional description of the anisotropy of the elastic modulus in crystals of four varied materials. Clearly, the elastic properties strongly differ depending on the crystallographic direction [101]. Mechanical, electric and magnetic properties depend on the average texture of a material as described in [102].

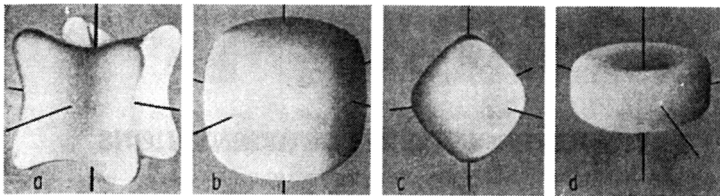


Fig. 2.9 Three-dimensional description of the anisotropy of elastic modulus in crystals of (a) gold, (b) aluminum, (c) magnesium and (d) zinc [101].

It is worth mentioning, that the alignment of the grains or the preferred distribution of second phases in an alloy, which normally is revealed by metallography, is not to be confused with the crystallographic nature of texture. Although equiaxed grain structures frequently exhibit textures, for an elongated grain structure it is very possible to be nearly randomly oriented. Since texture is a statistical concept, the material will be called strongly textured, if 30–40% of the grains have similar orientations. In processes, in which the plastic strain differs near the surface from that in the interior, especially during rolling and drawing, a texture gradient could emerge through thickness, causing texture inhomogeneity [99].

Texture can have either macroscopic meaning, which refers to a statistical measure of the orientations of the constituent grains in a material without regard to the spatial location, or microscopic meaning involving the determination of

the orientation of each grain in a population of grains in a material, as well as the nature and degree of its misorientation with respect to its direct neighbors [103]. The two situations are depicted in **Fig. 2.10**. Micro- and macro-texture are also called as local and global texture respectively.

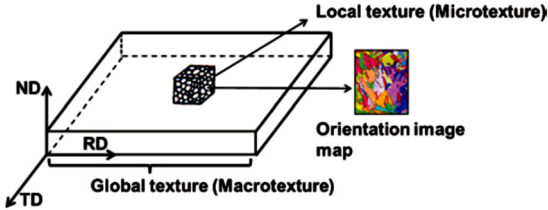


Fig. 2.10 Schematic of the differences in local or microtexture and global or macrotexture [99].

Textures could be classified into four different types: (1) one which develops during melting and casting, solidification texture; (2) deformation texture, which develops during the various deformation processes; (3) recrystallization and grain growth textures; and (4) transformation textures, which are exclusively the texture components that originate as a result of crystallographic transformations from a parent to a product phase and are solely dependent on the texture present in the parent phase different types of texture [104].

There are many different studies on different materials in drawing processes (wire and tube). Truszkowski et al. (1982) [105] analyzed the flow characteristics and their effects on the heterogeneity of texture in rolling of aluminum, 70/30 brass, and silver tubes. They stated a strongly significant dependency of the inhomogeneity on the yield strength and the work hardening exponent (flow characteristics). The higher the yield strength and/or the work hardening exponent are, the less the shear deformation and consequently the texture heterogeneity is. In another work, texture inhomogeneity in cold drawn wires at different locations – moving from its central axis to outer surface – was analyzed by Schläfer and Bunge (1974) [106] using the neutron diffraction method. They showed, that the wires had a rolling type texture near to the outer surface, however, at the center of the wires the texture was an axially symmetric one. Brokmeier et al. (2015) [107] investigated the texture gradient in a copper tube drawn with the sinking process and compared the texture gradient differences in the maximum and minimum wall-thicknesses of the tube. They have shown that strongest texture was at the outer surface of the tube, while in the central region a much weaker one existed. Moreover, Brokmeier et al. (2000) [108] analyzed the texture gradient in drawn $Cu - Fe$ composite wires and studied the effect of the initial texture on the deformation behavior. Park and Lee (2001) [109] studied the deformation and annealing textures in $Al -$

Mg – Si alloy tubes. For this aim, they used the EBSD method. Based on their observation, the tubes with 30% reduction in thickness and 10% reduction in diameter had the $\{111\} \langle 001 \rangle$ and $\{112\} \langle 111 \rangle$ orientations. Cho et al. (2002) [110] also investigated the texture of the deformation in hot extruded and subsequently cold drawn Al tubes and they had a severe texture gradient from the wall surfaces to the mid-plane. However, this gradient was reduced after cold drawing.

Global texture evolution of cold drawn copper wires was studied by Jian et al. (2011) [111] using diffractometry and EBSD. As a result, $\langle 111 \rangle$ and $\langle 100 \rangle$ duplex fiber texture form and with increasing strains the intensities of $\langle 111 \rangle$ and $\langle 100 \rangle$ increase. Alhamdany et al. (2012) [112] analyzed the inhomogeneity of the texture through the wall-thickness of a drawn copper tube, similar to rolled sheets in tubes drawn with a high value of deformation. Carradó et al. (2013) [37] studied the development of RSs and texture in drawn copper tubes using neutron and synchrotron diffraction methods, respectively. Brokmeier et al. (2015) [107] evaluated copper tubes drawn by a sinking drawing process. They stated the variation of the flow conditions during tube processing with the changing of the asymmetry of the Cu-texture component and the texture sharpness.

2.5.1 Description of orientation

Texture is commonly represented as $\{hkl\} \langle uvw \rangle$, which means that most of the grains in the sheet material are such that their $\{hkl\}$ planes are nearly parallel to the rolling plane and the $\langle uvw \rangle$ directions of the grains are nearly parallel to the process direction [113]. There are two ways of representing texture: The Pole Figure (PF) method and the Orientation Distribution Function (ODF) method.

In a PF the positions and also the intensities of a specific orientation, $\{hkl\}$, are plotted regarding the specimen geometry. It is a two-dimensional stereographic projection [103]. To understand the PF, it is essential to realize the stereographical projection. A brief description of PF is given in Annex A. For further information see “*The basics of crystallography*” written by Hommond [114] or “*Crystallography*” written by Borchartd [115]. Presenting results using PF, however, outcomes in a loss in information, which is due to the projection of the 3D orientation distribution onto a 2D projection plane. Hence, in order to describe the orientation density of grains in a polycrystal in an appropriate 3D representation and also evaluate the texture in a quantitative way ODF is used.

Before discussing ODF, it is helpful to get some information about the Euler’s angles. To define the Euler’s angle, as shown in **Fig. 2.11**, two coordinates are necessary to know: the crystal (K_B) and the sample coordinate (K_A). Choosing the sample coordinate system, in principle, is optional. However, the external

shape of the sample will suggest to be used as the coordinate system [116] and often the rolled sample having three directions of rolling direction (RD), transmission direction (TD), and normal direction (ND) are favorable to be chosen. The Euler's angles are three angles, $\varphi_1, \Phi, \varphi_2$ which are necessary to know in order to be able to bring the sample coordinate into the crystal coordinate system. The crystal coordinate system is then first rotated about the Z' -axis through the angle φ_1 then about the X' -axis (in its new orientation) through Φ and, finally, once again about the Z' -axis (in its new orientation) through the angle φ_2 (**Fig. 2.12**). Based on these three angles, $\varphi_1, \Phi, \varphi_2$, the rotation g is accordingly represented. In the most general case, the Euler's angles are defined in the range $0^\circ \leq \varphi_1, \varphi_2 \leq 360^\circ$, and $0^\circ \leq \Phi \leq 180^\circ$.

$$g = \{\varphi_1 \Phi \varphi_2\} \quad (2.20)$$

$$K_A \rightarrow g \rightarrow K_B \quad (2.21)$$

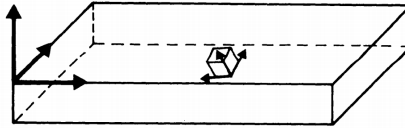


Fig. 2.11 Orientation g of the crystal coordinate system K_B with respect to the sample coordinate system K_A [100].

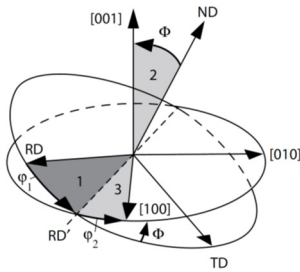


Fig. 2.12 Euler's angle: (a) Coordinate system is presented as Z -axis and its X - Y plane for the sample; Z' and $X' - Y'$ plane for crystal [116].

The ODF, $f(g)$, is defined as a probability density function of orientations g which is expressed in the form of the, typically, Euler's angles φ_1, Φ , and φ_2 (Fig. 2.12). In general, this function is assumed to be the volume fraction of the crystallites having the crystallographic orientation g with respect to the sample's fixed coordinate system. In an element consisting of different grains i of volume V_i with different orientations (**Fig. 2.13**) - grains of similar orientations g within an orientation range dg are color coded with the same color - the ODF $f(g)$ is defined by Eq. (2.22):

$$\frac{dV}{V} = f(g)dg, \text{ with } dg = \sin \Phi d\varphi_1 d\Phi d\varphi_2 \text{ and } \oint f(g)dg = 1. \quad (2.22)$$

where V is the sample's volume and dV is the volume of all crystallites i with the orientation g , represented in Eq. (2.20) in the angular element dg [116].

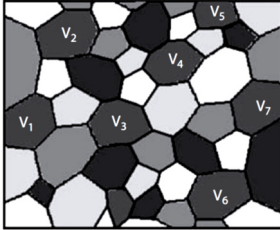


Fig. 2.13
Schematic representation of a microstructure consisting of different grains i of volume V_i with different orientations. Similar orientations g within an orientation range dg are coded with the same gray value [103].

PF measurements are usually the experimental input for ODF computation. Mathematically, the PF is defined by the volume fraction dV/V of crystals having their crystal direction h parallel to the sample direction y - typically given by the two PF angles α and β - where $y = \{\alpha, \beta\}$:

$$\frac{dV}{V} = \frac{1}{4\pi} P_h dy \text{ with } dy = \sin \alpha d\alpha d\beta \quad (2.23)$$

Different methods exist to calculate ODF from PF, such as the series expansion method, Ghosts method, or direct methods such as WIMV or ADC algorithms. Kallend presented a good review of the different determination methods of ODF [117]. In this work, the series of expansion was used. This method was proposed by Pursey and Cox (1954) [118] and a complete scheme for texture analysis by series expansion has been developed independently by Bunge (1965) [119] and Roe (1965) [120]. Although their methods are conceptually identical, the formalism used by Roe and Bunge is different. Bunge and Esling (1985) described this method thoroughly in [121]. Moreover, more details could be found in Bunge and Morris [116], Kallend [117], and Engler and Randle [122].

2.5.2 Texture measurement

The most important task in texture measurement is to know what these orientations are, and in what proportions are they present in the material. The next task is to know where are these orientations located physically in the specimen, which provides an insight into microtexture. Although almost all the diffraction techniques can be used to measure crystallographic texture, most popularly this is carried out using synchrotron, neutrons, or electrons.

2.5.2.1 Texture measurement by synchrotron radiation

Modern electron synchrotrons are using energies of 60 keV and more, yield a white spectrum of x-rays with intensities of six to seven orders of magnitude higher than conventional x-ray tubes, which are combined with a minimum angular divergence of less than 2 mrad. This unique combination of high photon flux, small beam size, and free choice of wavelength opens a wide range of possibilities for texture analysis. Short-wavelength synchrotron x-rays have similar penetration depths as neutrons, which allow global textures of big centimeter-sized specimens to be measured similarly as in neutron diffraction [123]. The main drawback of the synchrotron techniques is the very limited availability of synchrotron sources in large-scale research facilities [124].

By employing an area detector in transmission, full Debye–Scherrer rings are recorded simultaneously so that a significant reduction of the measuring time and high angular resolution are obtained [125, 126]. For this aim, a narrow beam of monochromatic x-rays is required. To achieve monochromatic radiation, the beam first passes a cooled copper plate that absorbs radiation with long wavelengths, and then a monochromator crystal selects the desired wavelength in the range of 0.01–0.1 nm [127]. Finally, the monochromatic beam is collimated to the desired size and falls onto the sample, where the Debye–Scherrer patterns are generated in transmission geometry (**Fig. 2.14**). Nowadays, the diffraction patterns are recorded either with image plates or with a CCD camera [128].

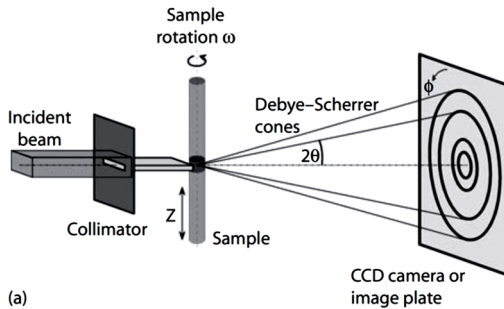


Fig. 2.14 Texture analysis by the Debye–Scherrer method with monochromatic synchrotron radiation. Schematic view of the experimental setup. 2θ is the scattering angle, ω describes the sample rotation, and ϕ denotes the angle along the Debye–Scherrer ring [128].

2.5.2.2 Texture measurement by scanning electron microscopy

The most widely used technique for the determination of microtexture is by EBSD in a SEM [129]. In this method, the orientation information of a sample is

achieved by the backscattered electrons, which are created by the interaction of the electron beam with the uppermost surface layer of the sample (Fig. 2.15-a). The cones can, therefore, be considered as flat. When projected on a suitably placed screen, these cones appear as a pair of parallel straight lines, the so-called Kikuchi lines. A Kikuchi band typically consists of two such mutually parallel lines relating to one particular diffracting lattice plane in the material (Fig. 2.15-d). The intersection of such bands corresponds to a zone axis (pole), and the major zone axes are recognized from the intersection of several bands. The so-obtained Kikuchi pattern contains all the angular relationships between planes in a crystal. The Kikuchi pattern, therefore, contains information about the crystal symmetry [99].

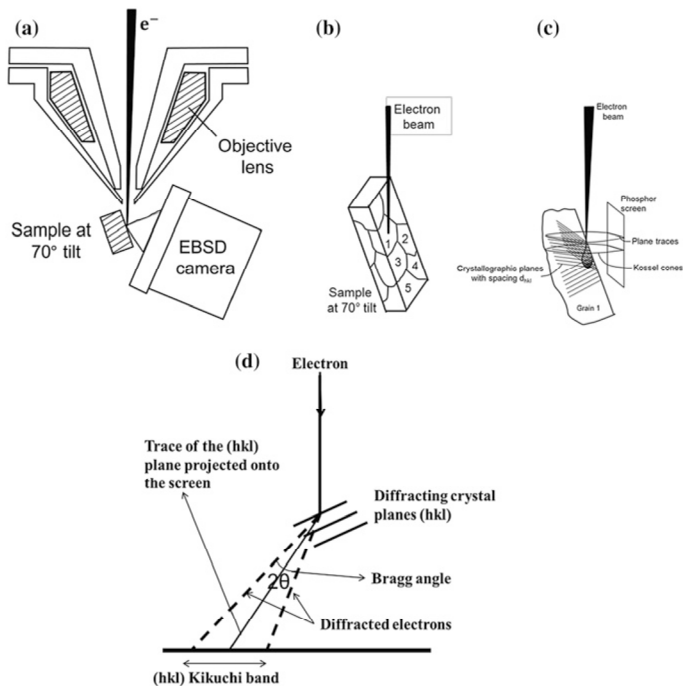


Fig. 2.15 Schematic of Kikuchi pattern formation in SEM-based EBSD technique. (a) Schematic of SEM-EBSD set-up, (b) incidence of electron beam on a polycrystalline material, (c) interaction of incident electron beam and generation of Kikuchi lines, (d) schematic showing diffraction of electron beam from atomic planes [99].

Tilting of the sample is necessary to allow a far greater proportion of electrons to experience diffraction and escape from the specimen before being absorbed.

Producing a detectable diffraction in conventional SEM, which the specimen is flat, is not possible because of the longer path length and hence higher absorption of the backscattered electrons. **Fig. 2.16** shows how the electron–specimen interaction volume is modified from the well-documented “tear drop” shape to a volume having a very small depth when the specimen is tilted [130]. More details on the physics of EBSD can be found in Venables and Bin-Jaya, 1977 [131] or Randle [132].

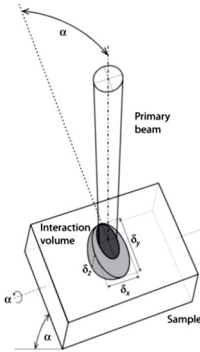


Fig. 2.16
The specimen-beam interaction volume in a specimen tilted for EBSD [130].

2.5.2.3 Texture measurement by neutron diffraction

Another powerful technique for global texture measurement is the neutron diffraction method. High penetration and low absorption make neutrons suitable for bulk texture investigations of large sample volumes and also for samples with coarse grain sizes, which could not be measured by the small synchrotron diffraction beam. This method has the same principle as the synchrotron method for measuring PF and a similar broad spectrum with a peak at 1–2 Å. One drawback of neutron diffraction is that even in high flux reactors the intensity is much lower compared to synchrotron experiments so that counting statistics become an important consideration. A conventional PF scan takes 6–48 h, compared to approximately 10–30 min in synchrotron diffraction [133]. Apart from the high penetration and no need of defocusing correction, neutron diffraction is the most appropriate method for texture measurement in anisotropic polyphase materials, since there is no anisotropic absorption effect for neutrons [134]. The neutron detector is set to the corresponding Bragg angle 2θ for the selected lattice planes $\{hkl\}$. The pole densities of that lattice plane in different sample directions are scanned with a goniometer by rotating the sample around two axes, φ and χ , corresponding to the PF angles β and α , to cover the entire orientation range [135].

2.6 Multiscale simulation

2.6.1 Integrated computational material engineering

“The way a scientist looks at the materials world is changing dramatically. Advances in the synthesis of nanostructures and in high-resolution microscopy are allowing us to create and probe assemblies of atoms and molecules at a level that was unimagined only a short time ago – the prospect of manipulating materials for device applications, one atom at a time, is no longer a fantasy. Being able to see and touch the materials up close means that we are more interested than ever in understanding their properties and behavior at the atomic level [136].”

The idea of multiscale modeling, which nowadays symbolizes the developing field of computational materials research, is to link the micro-to-macro length and time scales across simulation models and techniques, with the aim of controlling and analyzing the critical materials processes. **Fig. 2.17** shows an example of multiscale simulation in materials science, in which the computational and experimental techniques for a variety of length and time scales are presented [137]. In this paradigm, quantum mechanical calculations are used to treat the electronic structure, molecular dynamics simulations for analyzing atomistic processes, dislocation dynamics and crystal plasticity methods for micro- and mesoscale microstructure evolution and finite element methods for structural scale modeling. The vision of multiscale modeling is to deal with complex problems combining these different scales and methods in a much more comprehensive manner than when the methods are used individually [138]. McDowell and Olson (2008) [139] gave a comprehensive summary of computational materials with respect to multiscale modeling. Horstemayer (2012) [140] also discussed Integrated Computational Material Engineering (ICME) for metals and did a broad study on the different scale of simulations.

This simulation-based design paradigm has been created based on the ICME concept. In this methodology, the material models, as well as structure - property relationships, are integrated, with their properties gained from experiments and simulations [140]. The ICME approach can reduce product development time and eases the costly trial and error physical design iterations (design cycles) and facilitates far more cost-effective virtual design optimization. Moreover, it increases product quality and performance by providing more accurate predictions of response to design loads [141]. These benefits, which are now being realized, are the drivers for such an explosion of multiscale modeling into various industrial sectors [142]. Moreover, different scale features result in different scale properties.

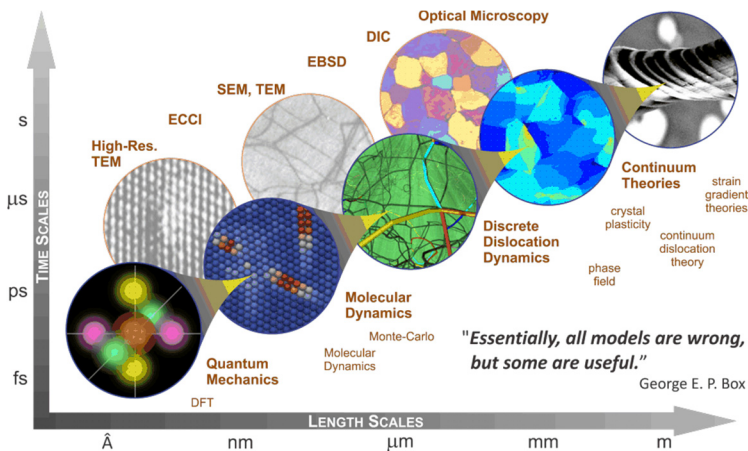


Fig. 2.17 Computational and experimental techniques for a variety of length and time scales [137].

The multiscale simulation starts typically at the atomistic level, in the atomic rearrangement is intimately related to various types of dislocations. Different studies were done at this simulation scale trying to analyze different materials properties. Orowan, Taylor, Polyani, and Nabarro [143], developed a relationship for dislocations that related stress to the inverse of a length scale parameter, and also Burgers vector [144], which laid the foundation for all plasticity theories. Furthermore, Brown (1964) [145], Bacon (1967) [146] and Foreman (1967) [147] established the framework to characterize the curvature of a line of dislocation under an applied stress. Other important contribution in this field was done by Hall (1951) [148] and Petch (1953) [149], who related the work hardening rate to the grain size of poly-crystalline materials. Another researchers made a huge impact on this field by their studies, such as work done by Ashby (1971) [150], who found that the dislocation density increases with decreasing of the second - phase size. Frank (1949) [151, 152], and Read (1953) [153], showed a relation with dislocation bowing as a function of spacing distance and size, and Hughes et al. (1994) [154], discovered that the geometrically necessary boundary spacing decreases with increasing strain. In the late 1970s, Kocks and Mecking (1979) [155] proposed one of the first attempts of linking plasticity to microstructure (population of dislocations). Their model was physically-based and derived from the total dislocation density stored in a material. The associated assumptions include a unidirectional model, a homogeneous deformation state, and, if being a polycrystal, all of the grains must be oriented along the same direction to have a homogenous plastic deformation. Other experimental studies have revealed that material properties change as a function of grain size. For example, Fleck et al. [156] showed in

torsion of thin polycrystalline copper wires that the normalized yield shear stress increases by a factor of 3 as the wire diameter decreases from 100 to 12.5 μm . One of the first works on gathering all these theories and on the multiscale approach was done by Tadmor et al. (1996) [157] for an atomistic-based analysis of dislocations and hardening plasticity of polycrystalline metals. They studied the structural failure being due to necking, which is caused by nonlinear geometric effects of finite strain.

This methodology is a bridging approach, which typically is performed as an upscaling approach. There are two different general bridging methodologies: hierarchical and concurrent [158]. In the hierarchical method, the calculations run at disparate length scale and independently. After calculating each scale, one of the several methods in a bridging methodology such as statistical analysis methods, homogenization techniques, or optimization methods is used to differentiate the relevant causes.

In concurrent bridging method, schematically shown in **Fig. 2.18**, the main focus is on combining different scale algorithms together with matching procedures raised in some overlapping domain in order to resolve the important multiscale physics. A review of this method and the associated challenges can be found by Phillips (2001) [159] and Liu et al. (2006) [160].

The study in this method begins with electronic scale simulations, using different approaches such as Density Functional Theory (DFT), see Annex F. Going to the next scale using **bridge 1** in Fig. 2.18, which is probably the most active area of research in this bridging method, the atomistic level calculations should be done. Atomistic level and coupling of this level simulations to continuum level simulations concurrently with different information being shared between the two is the main part of this scale calculation [159]. Kohlhoff and his team (1989) [161, 162] were probably the first to join atomistic level simulation capabilities within a finite element code. The next important contribution to the atomistic scale was made by Tadmor et al. (2012) [140] by joining the physics community's EMBEDDED ATOM METHOD (EAM) molecular statics code (see Annex E).

By the year 2000, the concept of concurrent multiscale modeling had diffused into the greater solid mechanics' community at different length scales besides the continuum level. Many researchers, such as Shilkrot et al. (2002) [163, 164] and Shiari et al. (2005) [165] started connecting the atomistic scale simulations with the DISLOCATION DYNAMICS (DD, microscale simulations). This connection is shown in Fig. 2.18 as **bridge 2**. A considerable contribution was done by Zbib and Diaz de la Rubia (2002) [166], who joined dislocation dynamic methods with finite element methods.

Using **bridge 3** in Fig. 2.18, mesoscale simulations with the Crystal Plasticity (CP) approach was involved. Although the CP modeling community focused on several length scales in their simulations, the term concurrent multiscale modeling was not historically used. CP models became popular during the 1980s as a tool to study deformation and texture behavior of metals during material processing [167, 168] and shear localization [169]. The basic elements of the theory comprise:

- (i) Kinetics related to slip system hardening laws to reflect intragranular work hardening, including self and latent hardening components [170];
- (ii) Kinematics in which the concept of the plastic spin plays an important role and,
- (iii) Intergranular constraint laws to govern interactions among crystals or grains.

The theory is commonly acknowledged for providing realistic prediction/correlation of texture development and stress – strain behavior at large strains as it joins the continuum theory with discretized crystal activity (see Annex B). Finally, the mesoscale is connected to the structural scale simulation, as shown as **bridge 4** in **Fig. 2.18**.

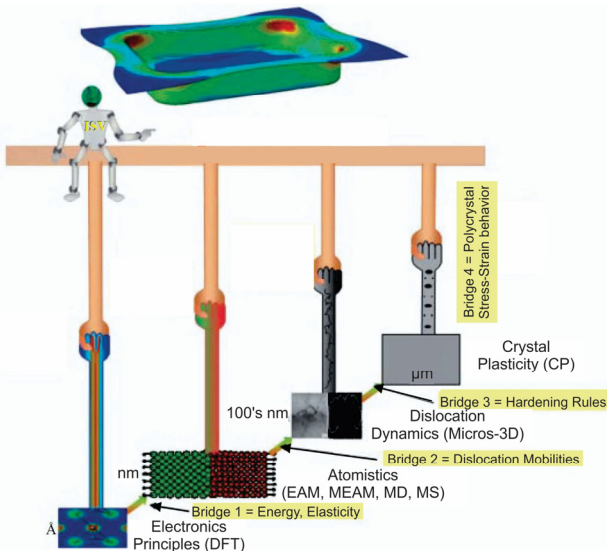


Fig. 2.18 Schematic of concurrent bridging method, showing the bridges for downscaling and upscaling [142].

2.6.2 Macroscale analysis

Macroscale models can include ordinary, partial, and integro-differential equations, where categories and flows between the categories determine the dynamics or may involve only algebraic equations. At this scale two important aspects are existing; kinematics of deformation and continuum theory constitutive equations.

Based on the deformation kinematic, presented in detail in Annex B, when a body is changed, the parameter defining the relative position of any two points is the strain. Instead, if the distance between every pair of points in the body remains constant, this body will be called as rigid body. General speaking, the strain tensor (which causes the change of the body) is nonlinear and leads to a complex analysis. Hence, in case of having a small deformation (say less than 2%), a linear and more simple strain tensor will be used. However, if the deformation is large, then the rotations become important and texture needs to be analyzed. Since in this work large strain deformations (caused by tube drawing) are involved and the rotation of crystals is an important parameter, initially the deformation gradient will be discussed, and the strain tensor will arise.

In continuum theory constitute equations, the internal constitution of metal defines what the response of metal will be when an external stimulus happens to it. Hence, a constitutive equation is then the mathematical representation of the inner “value” system of the material. In another word, the constitutive equations describe the macroscopic behavior resulting from internal constitution of the materials. This is a foundational point to the theory of the multiscale modeling idea. The constitutive equations relating to each theory will be presented in the relevant section.

2.6.3 Mesoscale analysis

Different researchers give different interpretations from mesoscale analyses. In this thesis, mesoscale relates to the intermediate scale, for which starts at the scale of the grain or crystal with CP being a good starting point for this scale. Basically, the basis of CP formulation is the continuum theory, which makes it a mesoscale analysis. However, the details of the equations start at the scale of the crystal or grain. Therefore, the main features of CP are texture evolution arising from the natural plastic spin, the direct modelling of slip systems on the crystalline axes, and anisotropy of single crystals. With respect to downscaling, CP includes prescribed hardening rules so that lower length scale formulations - such as DD formulations - can be used to help defining the hardening rule constants. Apart from the very brief discussion in following two sections on these two formulations - CP and DD, they are discussed in Annex C and D, respectively, as far as necessary for understanding.

2.6.3.1 Elasticity and crystal rotation

Depending on the type of the crystalline lattice of the materials (*fcc*, *bcc*, or *hcp*), the elastic moduli and the slip system vectors (\underline{s}_i^0 and \underline{m}_i^0) will have different values [171]. For *fcc* materials, twelve $\{111\} \langle 100 \rangle$ slip systems are considered and the anisotropic elasticity tensor $\underline{\underline{C}}$ is presented as shown in Eq. (2.24). As can be seen, using three main elastic constants the elasticity tensor can be defined.

$$\underline{\underline{C}} = \begin{bmatrix} C_{11} & C_{12} & C_{12} & 0 & 0 & 0 \\ C_{12} & C_{11} & C_{12} & 0 & 0 & 0 \\ C_{12} & C_{12} & C_{11} & 0 & 0 & 0 \\ 0 & 0 & 0 & C_{44} & 0 & 0 \\ 0 & 0 & 0 & 0 & C_{44} & 0 \\ 0 & 0 & 0 & 0 & 0 & C_{44} \end{bmatrix} \quad (2.24)$$

The anisotropy level of a material can be described by the Zener factor as given in Eq. (2.25). $Z = 1$ describes the situation when the elastic properties are isotropic, values greater than 1 represent an anisotropic behavior of the elastic properties [172]:

$$Z = \frac{2C_{44}}{C_{11} - C_{12}} \quad (2.25)$$

If the lattice is rotated with respect to the global system of coordinates, then the components of the vectors \underline{s}_i^0 and \underline{m}_i^0 must be rotated accordingly with the rotation matrix \underline{R} :

$$\underline{s}_i = \underline{R} \cdot \underline{s}_i^0 \quad (2.26)$$

$$\underline{m}_i = \underline{R} \cdot \underline{m}_i^0 \quad (2.27)$$

where \underline{s}_i^0 and \underline{m}_i^0 are the slip direction vector and unit normal vector to the slip plane, representative of the Schmid tensor.

There are many representations of the crystal orientation. One of the most common is Bunge convention that uses three Euler angles φ_1 , Φ and φ_2 . The rotation matrix in Bunge convention is written as the following [173]:

$$R = \begin{bmatrix} \cos \varphi_1 \cos \varphi_2 - \sin \varphi_1 \sin \varphi_2 \cos \Phi & \sin \varphi_1 \cos \varphi_2 + \cos \varphi_1 \sin \varphi_2 \cos \Phi & \sin \varphi_2 \sin \Phi \\ -\cos \varphi_1 \sin \varphi_2 - \sin \varphi_1 \cos \varphi_2 \cos \Phi & -\sin \varphi_1 \sin \varphi_2 + \cos \varphi_1 \cos \varphi_2 \cos \Phi & \cos \varphi_2 \sin \Phi \\ \sin \varphi_1 \sin \Phi & -\cos \varphi_1 \sin \Phi & \cos \Phi \end{bmatrix} \quad (2.28)$$

Depending on the active slip systems or what are the plastic slip increments, or how the selection of the set of active slip systems are determined, two different implementations of crystal plasticity models can be chosen: rate-dependent and rate-independent algorithms. In rate-dependent integration, the above mentioned parameters are not considered and therefore this integration algorithm deals with less issues than the rate-independent plasticity one [171].

2.6.3.2 Dislocation dynamics

In general, crystalline materials contain various forms of defects, such as point defects (e.g. vacancies or interstitials), line defects (dislocations), planar defects (e.g. microcracks), grain boundaries and heterogeneous interfaces, or volume defects as twins or precipitates. The major part of the mechanical behavior and strength of the materials are determined by these defects. So, dislocations define plastic yield and flow behavior, either as the dominant plasticity carriers or through their interactions with the other strain-producing defects [174]. Dislocation dynamics is discussed shortly in 0.

Considering Eq. (2.29) and also assuming the fact that the total plastic shear strain rates for the 12 slip systems are constant, the hardening rate equation can be written as indicated below [155],

$$\dot{\kappa} = h_0 \left(\frac{\kappa_s - \kappa}{\kappa_s - \kappa} \right) C, \quad (2.29)$$

where C is the constant plastic shear strain rate calculated by DD, h_0 is the initial hardening rate and κ_s is the saturation strength. A closed-form solution for the hardening as a function of the time can be obtained by integrating Eq. (2.29) with respect to time, which corresponds to the strength values of κ_0 and κ , respectively. The Palm-Voce equation is then recovered [140]:

$$\kappa = \kappa_s - (\kappa_s - \kappa_0) \exp\left(-\frac{h_0}{\kappa_s - \kappa_0} Ct\right). \quad (2.30)$$

with the initial slip system strength κ_0 . By correlating this equation with the predicted hardening by DD, κ_s , h_0 , and κ_0 can be obtained [175].

2.6.4 Atomistic modeling method

Speaking of atomistic simulations refers to calculations of material properties based on explicit treatment of the atomic degrees of freedom within classical mechanics. As discussed in the prior section, the mechanical behavior of materials is mostly determined by dislocations. To describe these defects it is necessary to involve their atomistic scale structure [176].

Different techniques exist in atomistic scale to study the properties of varied materials; however, for metals the Embedded Atom Method (EAM, see Annex E) and Modified Embedded Atom Method (MEAM) are the preferred ones. Using these formalisms, the total energy of the system can be calculated. Hence, in EAM or MEAM calculations, initially the potential model calibration should be done using experimental results or electronic scale calculations (e.g. DFT), then, these calibrated potentials can be used to determine mechanisms or phenomena to be used for higher length scale analyses [140].

In calibrating the EAM/MEAM potentials, reliability and flexibility are two different constraints on developing these semi-empirical potentials, because they will be used for practical engineering applications, and they need to be computationally efficient. A reliable interatomic potential would accurately reproduce various fundamental physical characteristics of the relevant element or alloy such as elastic, structural, and thermal properties [177]. EAM potentials will not be discussed here. Brenner [178] summarized the class of bond order formalism that has proven valuable for covalently bonded systems. Mishin (2005) [179] reviewed different interatomic potentials for metals.

2.6.4.1 Modified embedded atom method

MEAM was developed by Baskes and his colleagues [180]. It is based on potentials of the EAM which are extended to include angular forces. Nowadays, it is one of the most widely used methods calculating semi-empirical atomic potentials. The free surfaces are better addressed on MEAM potentials than on EAM ones, which is one of the advantages of MEAM. It makes this method more attractive for fatigue, fracture, and damage simulations [140]. The relevant potentials required for MEAM are determined for different elements and alloys and available in literature. An effort has been made by Lee et al. (2003) [181] to create the MEAM potentials for Cu, Ag, Au, Ni, Pd, Pt, Al, and Pb based on the first and the second nearest - neighbor. Jelinek et al. (2012) also studied the MEAM potentials for Cu, Al, Si, Mg, and Fe alloys [182]. The National Institute of Standards and Technology (*NIST*) is a good source to get the potentials and also relevant software for evaluation to judge the quality of the simulations [183].

To develop an MEAM potential, a two-step iterative process is considered; initially: a single crystal structure designated as the reference structure is chosen and the MEAM parameters are calibrated to experimental data and DFT results. After this step, the calculated potential will be applied to atoms under conditions not used during its calibration phase to validate the accuracy of the new potential. These systems include different crystal structures, surfaces, stacking faults, and point defects. If the validation is not satisfactory, one needs to go back to the first step and has to recalibrate the parameters in a way that

improves the overall quality of the potential. Although this iterative method does work eventually, in many cases, it is very tedious and time – consuming [184].

The potentials classically require the lattice constant, the elastic constants [see Eq. (2.24)] and the cohesive energy. Mostly, the Generalized Stacking Fault Curve (*GSFC*) is used for validation. The cohesive energy is calculated as the differences between the energy of bulk atoms and the free atoms, which is defined as the heat of formation per atom when all of the atoms are assembled into a crystal structure [185] as given in Eq. (2.31):

$$E_{coh} = -\left(\frac{E_{tot} - NE_{atom}}{N}\right). \quad (2.31)$$

where E_{tot} is the total energy of the system, N is the number of atoms in the system, and E_{atom} is the total energy of an isolated atom. Plotting the cohesive energy versus the lattice parameter, the minimum of the cohesive energy curve determines the equilibrium lattice constant a_0 [185]. Another energy which is calculated by MEAM is the stacking fault formation energy:

$$E_{sf} = \frac{E_{tot} - N\Omega}{A}. \quad (2.32)$$

where Ω is the total energy per atom in the bulk, and A is the unit cell area that is perpendicular to the stacking fault [140].

Using MEAM calculation, one can numerically calculate the elastic constants of the material by applying small strains to the lattice. For small deformations, the relationship between the deformation strain and the elastic energy can be quantified. Mehl et al. (1994) [186] introduced a procedure in order to calculate these constants.

One of important parameters in upscaling MEAM simulations to the mesoscale simulations, is the mobility of dislocations, which can be calculated by the dislocation mobility law written:

$$v = \frac{\tau b}{B}. \quad (2.33)$$

where B is the drag coefficient to be determined from atomistic level simulations. The coefficient B essentially accounts for the electron and phonon drag [140].

2.6.5 Electronic scale calculation

In recent years, the way that the theoretical and componential research is done, is changing dramatically due to the electronic-structure approaches and their capabilities. Success of the electronic scale calculations is because of its ability to derive many materials properties from first-principles. The calculations are also with an accuracy that complements or even augments experimental observations. Measuring such properties is highly time-consuming and/or cost-intensive. The availability of computers together with the different theories, such as Density Functional Theory (DFT, Annex F), has been instrumental to this success, made it possible to deal with realistic problems [187].

It is rather interesting that the origin of all the good properties of solids is not more than the interaction between electrons in the outer shells of the atoms and it has been found so far that neglecting the core electrons, which are bound tightly to the core/nucleus of the atoms, and considering only the valence electrons have reasonable agreement on predicting material properties [188]. The general understanding so far of the electronic structure of matter is based on the theoretical methods of quantum mechanics and statistical mechanics. However, this part is not going to be discussed in this context. A nice review of different aspects of quantum mechanics is presented by Greiner and Walter in "Quantum Mechanics, An Introduction" [189].

2.6.6 Structure scale simulation; FEM

As stated by Roters et al. in "*Crystal Plasticity Finite Element Methods*" [190] "*The Finite Element Method (FEM) is nowadays the most popular simulation tool in structural scale simulations*". FEM is a tool to solve nonlinear partial differential equations, which means the FEM is only the solver and has to be combined with some physics to make a model, which could have different parts, mechanical and/or physical boundary condition and material model. It is worth mentioning, along with FEM there are different other numerical methods to solve such nonlinear equations, e.g. meshless methods and the boundary element method [190]. The work published by Zienkiewicz (1967) [191] with the title of "The Finite Element Method in Structural and Continuum Mechanics", made a huge contribution to the FEM.

The basic of FEM is to discretize the region of calculation into several smaller areas (called finite elements) and each element consists of certain points, named nodes. The general procedure in FEM is that initially the variables which are going to be calculated, for example displacement (as primary parameter) in solid mechanics, are approximated using piecewise continuous functions that are continuous inside the elements. The solver tries to minimize the error by changing the solution parameters. After getting the solution for the primary parameter, it is post-processed to calculate the secondary parameters like

strain, stress etc. [192]. Summarized, the FEM needs to perform the following steps: (i) Pre-processing, (ii) Developing elementary equations, (iii) Assembling equations, (iv) Applying boundary conditions, (v) Solving the system of equations, and (v) Post-processing [193]. A brief description of these steps is given in Annex G.

The advantage of FEM analysis is its ability to model complex forming processes. The effect of each process variable and their coupling effects can be investigated, and the results used to design the proper forming process. The disadvantage of the FEM analysis is the complexity in preparing input data, selecting proper output variables, and interpreting analysis results.

Different researchers studied tubes and tube drawing processes in different aspects. Tekkaya et al. (1985) [194] studied RS in some manufacturing processes such as rod and tube extrusion using FEM. They also performed experimental studies and compared simulation and experimental results achieving a good agreement. Rigaut et al. (1988) [195] used a FEM approach to simulate the floating plug in steel tubes to achieve an optimum design of drawing scheme in a quick way. They compared the results of FEM with the KEM (Kinematic Element Method) and SEM (Static Element Method) approaches. Pietrzyk and Sadok (1990) [196] studied the tube sinking process with the aim of validating their FEM model. Their study intended at validation of the flow approximation for steady-state analyses of the tube drawing process. The predictions of their model were very close to the measured values. Sawamiphakdi et al. (1991) [197] developed a pre- and post-processing model considering some tube drawing processing parameters to calculate the dimensions, mechanical properties and required drawing forces. The pre-processing program generated the FEM mesh for an Abaqus software and the post-processing program calculates the aforementioned drawn tube information from the analysis results.

Sadok et al. (1991) [198] studied the strains in tube sinking for copper tubes. They developed an FEM model and validated the model by using experimental data and also presented a brief description of the model. Mulot et al. (1996) [199] numerically studied the cold pilgering process using FEM. The main purpose of their work was to demonstrate the feasibility of the FEM analysis for tube pilgering. They showed that a number of variables and phenomena can be examined numerically. Some are in agreement, qualitatively or even quantitatively with known values or tendencies, while others still need to be checked experimentally. Mackerle (1996) [200] presented a comprehensive bibliography on published papers from 1976 to the 1996 on the application of FEM usage in the analysis of tubing. Ruminski et al (1998) [201] studied the influence of the geometry of the deformation zone on the distribution of strains in the deformed material and on the distribution of mechanical properties in the final product. The analysis of strain distribution was performed using a FEM

simulation as well as the experimental technique based on hardness measurements.

Yoshida and Ruruya (2004) [202] examined processing conditions, the improvement of dimensional accuracy and reduction of the roughness of the inner tube surface in mandrel and plug drawings using FEM and experimental methods. They stated an optimal shape for the plug, with which breakage frequency during plug drawing is suppressed to as low as possible using FEM. Based on the calculated optimal shapes plugs were fabricated and used for experiments. Neves et al. (2005) [203] studied tube drawing with a fixed plug using FEM and the commercial software MSC Superform to find the best die and plug geometry aiming at the reduction of the drawing forces. The numerical analysis helped determine the reactions of the die and the plug, the stresses in the tube, the drawing force and the final dimensions of the product. The results of the FEM model were compared with the results from analytical models and used to design the tools. Different lubricants and different drawing speeds to optimize the drawing force were analyzed. Palkowski et al. (2013) [204] investigated the RS state of drawn copper tubes by numerical simulation and neutron diffraction in standard drawn tubes with and without a plug. They developed a symmetrical model in order to be able to predict the RS state in cold drawn tubes. Despite the good agreement between the results of drawn tubes without a plug with the experimental data, there were still discrepancies for radial RS.

Chapter 3

Experimental and simulation procedures

3.1 Introduction

In this chapter, the experimental procedures used for the investigations, as well as the simulation software are presented. After introducing the drawing machine and the used materials, the laboratorial and industrial tools are introduced. The experiments and the used devices on performing the eccentricity, RSs, and texture measurements are presented and discussed. In case of the model developments, the different simulation software packages and codes used for the different length scale simulations are presented.

3.2 Tube drawing and materials

3.2.1 Drawing machine

The tube drawing was performed with a laboratory size 2500 kN hydraulic tube drawing machine [205], which is shown in **Fig. 3.1**. The drawing process was performed with a fixed plug and during drawing, plug and drawing forces were recorded using a data acquisition device. The drawing speed used changed for the different materials, ranging from 5-30 m/min. The drawings of the copper, aluminum, and brass tubes were done using an inner clamping system [205]. However, the steel tubes were pointed by a swaging process, prior to the drawing.

3.2.2 Materials

Eccentricity and RSs were measured for all tubes of different material using ultrasonic and hole-drilling methods, respectively. The further investigations such as studying the RSs using neutron diffraction, the measurements of texture evolution as well as the multiscale simulations were done only for the copper tubes.

Two different series (G-I and G-II) of annealed phosphorus deoxidized copper tubes (ISO named Cu-DHP – ASTM B75 [206]) with the dimensions of $65.0 \times 5.5 \text{ mm}^2$ and $64.0 \times 3.1 \text{ mm}^2$ (outer diameter \times wall-thickness) were used. These tubes were produced by continuous casting of the billets, hot extruding them to pre-tubes followed by one cold drawing step before recrystallization heat treatment [207]. This was the as-received condition of the tubes, used in this work. Their chemical composition is given in **Table 3.1**.

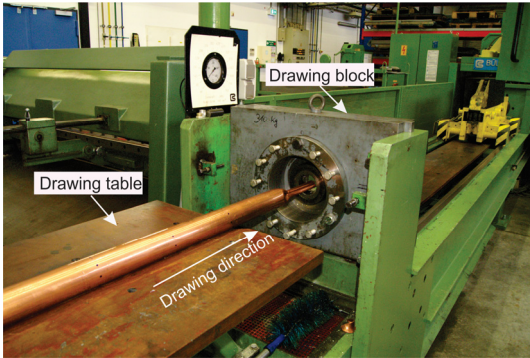


Fig. 3.1
The tube drawing
facility [205].

Table 3.1 The chemical composition of the Cu-DHP tubes.

wt. %	Zn	Fe	Si	Mg	Te	P	Sb	Al	C	Cu
Cu-DHP	0.05	0.02	0.02	0.01	0.02	0.01	0.01	0.01	0.01	99.84

Two drawing steps were performed on the Cu-tubes as listed in **Table 3.2**. The geometrical data of the tools used as well as the final dimension of the tubes and the reductions performed can be found there, too. The strain in wall-thickness and in diameter (also called reduction value or deformation) can be calculated using Eqs. (2.1) and (2.3). The Q -value is defined as ratio of the strain in wall-thickness (ϵ_s) to strain in diameter (ϵ_d) as $Q = \epsilon_s / \epsilon_d$ [12]. The microstructure at the thickest wall-thickness – in this context for the sake of easiness the maximum (minimum) wall-thickness will be called *Max* (*Min*) – of the as-received tubes is shown in **Fig. 3.2**. The average grain size of the *Max* and *Min* were $(47.05 \pm 4.0) \mu\text{m}$ and $(48.30 \pm 6.1) \mu\text{m}$, respectively.

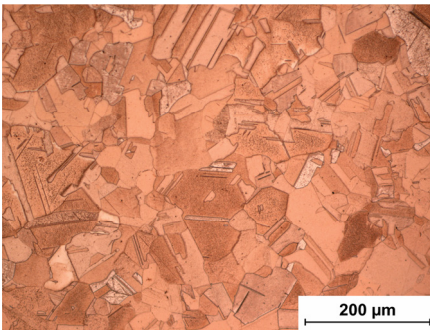


Fig. 3.2
The micrograph of the as-received sample at *Max* side of the tube.

Table 3.2 Drawing steps for Cu-DHP tubes of sizes 65.0 × 5.5 mm and 64.0 × 3.1 mm.

Group	Step	Initial size, mm	Die, \varnothing , mm	Plug \varnothing , mm	Thickness reduction, ϵ_s	Diameter reduction, ϵ_d	Q value	Final size, $\varnothing \times t$ mm
G-I	first	65.0 × 5.5	60.0	51.0	0.20	0.08	2.5	60.0 × 4.5
	second	60.0 × 4.5	50.0	44.0	0.22	0.11	2.0	50.0 × 4.0
G-II	first	64.0 × 3.1	60.0	55.0	0.21	0.06	3.5	60.0 × 2.5
	second	60.0 × 2.5	50.0	46.0	0.22	0.18	1.2	50.0 × 2.0

The chemical composition and the drawing steps for the aluminum, brass, and steel tubes are given in **Table 3.3** and **Table 3.4**, respectively. It should be mentioned that all the drawing steps are chosen based on the steps, which tubes were supposed to be drawn industrially.

Table 3.3 Chemical compositions of the aluminum, brass and steel tubes.

wt. %	Zn	Fe	Si	Mg	Te	P	Sb	C	Cu
Aluminum	0.05	0.02	0.02	0.01	0.02	0.01	0.01	0.01	99.84
wt. %	Fe	Ni	Al	Pb	Sn	Zn	Cu		
Brass	0.04	0.30	0.02	0.05	0.10	36.00	63.50		
wt. %	Si	Mn	P	S	Al	C	Fe		
Steel	0.55	1.60	0.02	0.01	0.02	0.22	97.58		

Table 3.4 Drawing steps for aluminum, brass and steel tubes.

Material	Initial size mm	Die \varnothing , mm	Plug \varnothing , mm	Thickness reduction ϵ_s	Diameter reduction ϵ_d	Q	Final size $\varnothing \times t$ mm
Aluminum	60.0 × 5.0	55.0	46.0	0.10	0.09	1.1	55 × 4.5
Brass	50.0 × 4.0	45.0	38.0	0.13	0.10	1.3	45 × 3.5
Steel	46.0 × 4.4	42.0	34.4	0.17	0.10	1.7	42 × 3.7

3.3 Eccentricity

In order to follow the changes of the eccentricity before and after the tube drawing, a pattern was applied on the outer surface of the tube using an electrical pen (schematically shown in **Fig. 3.3-a**). This pattern was made in different cross sections over the length of the tube with a distance of 80 mm (which are called rings), each ring comprising eight measuring points with an angular distance of 45° over the circumference of the tube (**Fig. 3.3-b**). The wall-thicknesses were measured using an ultrasonic device (Krautkramer CL 400 [208]). Based on the measured wall-thicknesses, the eccentricity of the tubes was calculated using Eq. (2.13).

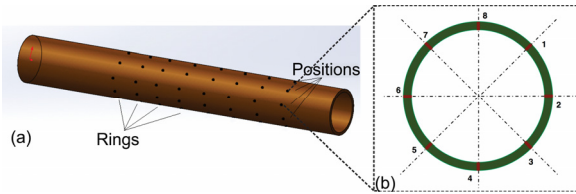


Fig. 3.3 (a) Schematic of the created pattern on the surface of the tube with different rings and measure points and (b) the measure points on each ring.

3.4 Tilting and offset principles

For tilting, a die holder was used. The simple principle of tilting is shown in **Fig. 3.4-a**. Offset was done by using a second die. Same as tilting, shifting of the die creates a change between the center line of the tube and the drawing line of the machine. **Fig. 3.4-b** shows its principle. To apply tilting and/or offset in the drawing process, a laboratory and an industrial solution were designed and explained below.

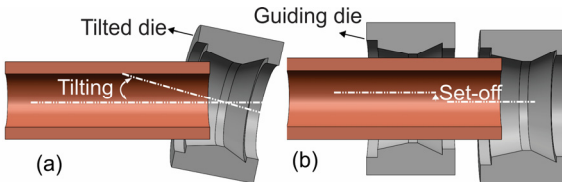


Fig. 3.4 Sketch of the (a) tilting and (b) offset principle.

3.4.1 Laboratory solution

To investigate the influence of the tilting and offset in a laboratory scale, tools for a static tilting and offset were prepared. Static tilting and offset mean that to change any parameters regarding tilting or shifting, one has to stop the drawing process to change any drawing parameter such as changing the die or the plug. After applying the desired parameters, the drawing process could go on.

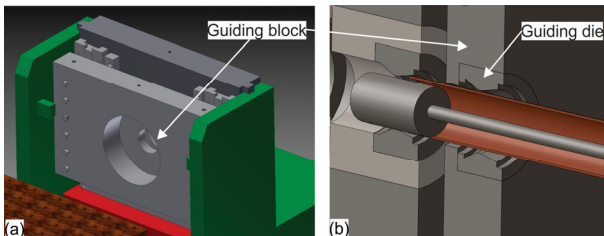


Fig. 3.5 (a) Placing the guiding block before the main die. (b) The guiding die inside the guiding block, with the same diameter as the tube.

To facilitate tube shifting (applying offset), a guiding block with a guiding die was built and placed at the feeding side of the main block (**Fig. 3.5**). This guiding die had the same diameter as the entering tube, making it possible to shift the tube without any deformation.

Considering tubes with eccentricity, it is important to specify the position of *Max* and *Min* regarding the tilting/offset direction. For this reason, two types of arrangements were defined regarding tilting and/or offset: a positive setup (+) is given, when, *Max* is in the same direction as the tilting/offset and vice versa, if *Min* (-) is placed in this direction. **Fig. 3.6** shows schematically the tilting process: *Max* is in the same direction as the tilting angle, hence it is called a “positive tilting” (+). If the tilting is kept fixed and the tube is rotated about 180° to have *Min* on top, then it will be called “negative tilting” (-).

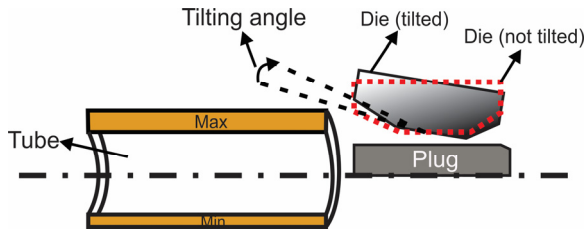


Fig. 3.6 Definition of the “positive tilting”: positioning the *Max* on top in the same direction of the tilting angle.

The used tilting angles and offset values are shown in **Table 3.5**. Furthermore, the combination of tilting and offset – performed only on copper tubes - are shown in this table as well.

Table 3.5 Tilting angle, offset value, and combination of tilting/offset

Tilting (°)	Negative tilting	0	Positive tilting	0
		-1		+1
		-2		+2
		-5		+5
Offset (mm)	Negative offset	0	Positive offset	0
		-2		+2
		-3		+3
		-4		+4
		-6		+6
Combination of tilting (°)/ offset (mm)	0	0	0	0
	±2	-1	±2	+1
	±4	-2	±4	+2
	±6	-5	±6	+5

3.4.2 Industrial solution

Along the laboratory solution, the design for an industrial solution was performed in this work, as well. The idea of this type of solution was to make the parameter change (changing the tilting angle/offset value) possible during the drawing process without the need to stop the process, in other words, perform the tilting/offset dynamically. Thus, a new block was designed using Autodesk® Inventor LT™ software in the framework of a bachelor's thesis [209].

The most important criterion for this solution was the integration of the construction into the overall structure from the aspect of the existing space in the drawing machine. Additionally, in the design of this new block the possibility for an easy and quick adjustment of the tilting and shifting as well as changing of the die without moving the guiding die were considered. Relevant calculations regarding the drawing force were done in the critical points in the new construction - most importantly was the main drawing die. **Fig. 3.7** shows the final designed main block which makes the changing of the die and tilting angle setting easier and dynamic. All material selections and calculations regarding the new design could be found in the bachelor's thesis in [209].

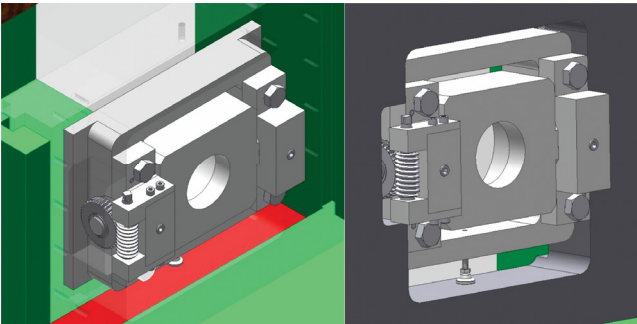


Fig. 3.7 The new designed block with the possibility of tilting the die from outlet [209].

3.5 Evaluation of RSs

3.5.1 Residual strain measurement by hole drilling

The residual strains were measured using the hole drilling method of Stresstech [210]. **Fig. 3.8** shows the basic components of the device. The measurements were done at *Max*, *Min*, and between these two points (which is called 90° position). Drills with a diameter of 0.80 mm were used and the residual strains on the surface of the tubes were measured up to 0.70 mm which is the measurable depth normally suggested to be equal to the hole diameter [84]. Measurements were performed in 12 steps and between each step, there were 45 s of waiting for stress relief before taking the value.

The evaluation of RSs from the measured strains was performed by Prism software [210]. This software uses the taken pictures during the drilling and calculates the residual strains based on the changes by hole drilling.

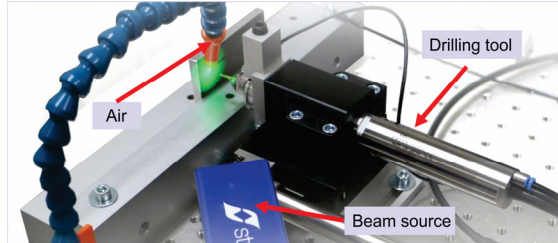


Fig. 3.8 Stresstech hole drilling device.

3.5.2 Residual strain measurement by neutron diffraction

SALSA instrument (Stress Analyzer for Large Scaled Engineering Applications), is an instrument to measure residual strains based on the neutron (diffraction) strain scanning method. SALSA is at the high flux research reactor of the Institut Laue-Langevin (ILL) in Grenoble, France.

The instrument provides low background, a well-defined gage volume [whether $2 \times 2 \times 2 \text{ mm}^3$ or $0.6 \times 0.6 \times 2 \text{ mm}^3$ ($fwhm^1$)], high neutron flux, and - thanks to the available Hexapod - enough space for scanning. It provides the ability to scan in all three orthogonal directions through the beam [211]. The schematic of the SALSA instrument is shown in Fig. 3.9 [212].

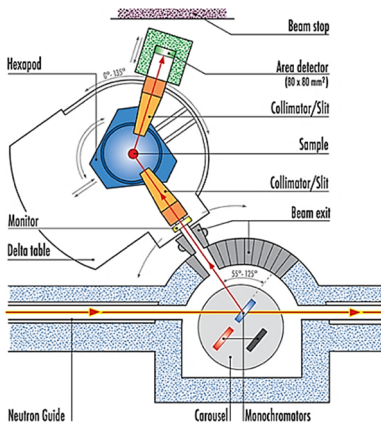


Fig. 3.9 Schematic of the SALSA instrument at ILL in Grenoble, France [212].

¹ $fwhm$: Full width at half maximum

Assuming the principal axes correspond to the sample symmetry, axial, radial, and hoop (also called tangential) as pointed out in **Fig. 3.10**, the measurements were done in three orthogonal directions. For the evaluation of Cu-DHP, (311) – Bragg peak was used, which has a wavelength of $\lambda = 0.165 \text{ nm}$ and a diffraction angles at 98° . Stress balancing was used to find out the reference lattice parameter d_0 . As for hole drilling, RSs were measured at the same three parts of the tube – *Max*, *Min*, and 90° . Table 3.6 summarizes the experimental parameters for RS determination.

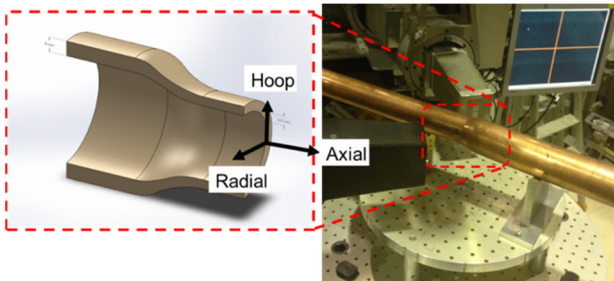


Fig. 3.10 Sample geometry for the neutron measurement of strains at the SALSAs strain imager.

Table 3.6 Experimental parameters and conditions for RS measurement using SALSAs.

Equipment	SALSAs
Method	Tri-axial
Monochromator	Double focusing, bent Si crystals
Wavelength (nm)	0.165
Detector	Two-dimensional position sensitive microstrip detector
Beam shaping optics	Radial focusing collimator,
Gauge volume (mm^3)	$0.6 \times 0.6 \times 2$
Lateral resolution (mm):	
radial	1.07
axial and tangential	1.23
Diffraction planes	{311}
Acquisition time (min)	10
E_{macro} (GPa)	116
V_{macro}	0.343

To analyze the evolution of the RSs during the drawing and also to understand the RSs developments during deformation, a so called Interrupted Drawn Tube (IDT) was prepared. These IDTs were not-completely drawn tubes having three main zones as shown in **Fig. 3.11**: As the as-received zone, the deformation zone, and the drawn zone. This geometry has some advantages: (1) the possibility to measure all three important parts at one single measurement time and therefore no need to apply for several beamtime, (2) possible to measure the RSs inside the die (deformation zone), which has not been studied so far, and (3) if some further processes must be done on the tube, the measurements

could be done on the same tube. The IDT was prepared for the first drawing step as well as the second drawing step. For this goal, after preparing IDT for step 1 and analyzing at SALSA instrument, the same tube was drawn one more step and an IDT for the second step was prepared making possible to see the changes of the RSs for one exact point. **Fig. 3.12-a** and **b** show the IDT for the first and second drawing steps.

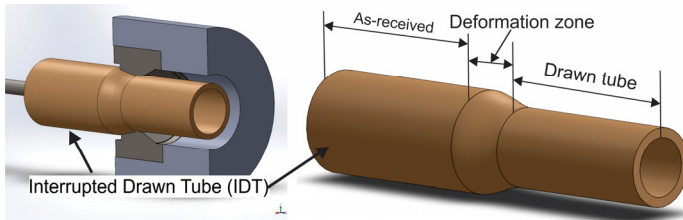


Fig. 3.11 Sketch of the Interrupted Drawn Tube (IDT).

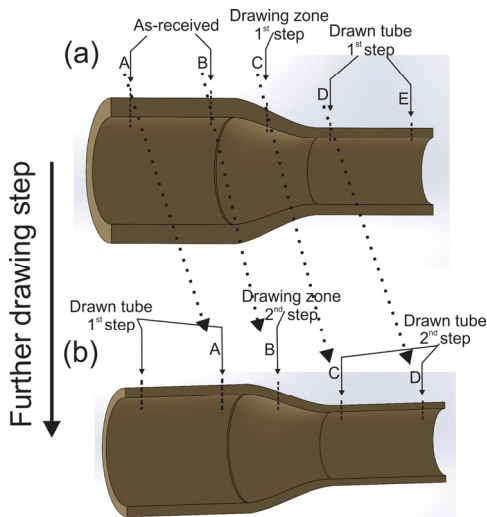


Fig. 3.12 Two different IDTs after (a) first and (b) second drawing steps.

As an example, the measuring points at the IDT after first drawing step are shown in **Fig. 3.13**. At each of these positions penetration and through thickness scans were performed. Depending on the wall-thickness, between 16 and 21 measuring points were taken in 0.25 mm steps for each measurement point. During the through thickness scans, the SGV successively increases until it reaches the full size of the IGV. This matter is discussed in more detail in “5.3.2 – After first drawing step”.

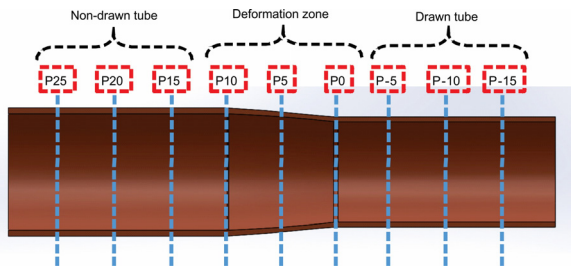


Fig. 3.13 Measurement points in an IDT.

3.6 Analysis of texture development

Neutron and synchrotron diffraction methods were used to measure the global texture of the copper tubes, which is shown schematically in **Fig. 3.14**. The main reason for using two different methods was the different grain sizes of the as-received and drawn tubes. Since the as-received tubes had a quite coarse grain size, measuring these tubes with synchrotron diffraction method was not suitable as not being a sufficient number of grains in SGV. For this reason, the global texture of the as-received samples was measured using neutron diffraction method (see 3.6.1). After deformation, the grains became fine enough to be able to measure texture by synchrotron. So, the deformation zone and drawn tubes were measured using synchrotron methods (see 3.6.2). The local texture was measured using synchrotron and electron diffraction methods (as shown in Fig. 3.14). Using the electron diffraction method (see 3.6.3) gave the possibility to measure the micro-texture of the sample.

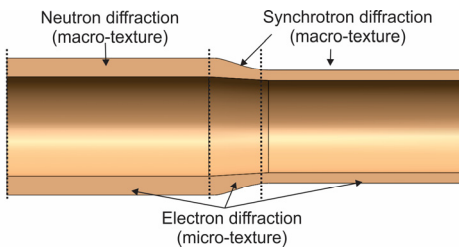


Fig. 3.14
Texture measurements performed on the IDT.

3.6.1 Texture measurements by neutron diffraction

Analysis by neutron diffraction was done at the STRESS-SPEC instrument at Heinz Maier-Leibnitz (*FRM II*) in Garching/Germany [213]. Basic information about the STRESS-SPEC instrument can be found in [214]. Since in texture measurement, tilting and rotation of the sample is of importance, measurements were performed using an Eulerian cradle type Huber 512 with an asymmetric table arrangement to gain more space. Cubic samples with dimensions of

$10 \times 10 \times WT^1$ were cut. To have enough thickness for the neutron measurements, three same samples were glued together. A neutron wavelength of 1.565 \AA , which was obtained from $Ge (311)$ monochromator, was used for the measurements.

3.6.2 Texture measurements by synchrotron diffraction

Texture measurements by synchrotron have been performed ex-situ at the instrument HEMS-P07B at Petra III/Hasylab of the German Electron Synchrotron (DESY²) in Hamburg, Germany. Synchrotron has a high penetration depth, excellent brilliance, and high photon flux, which allows the measurement of global and local texture [32]. Complete PFs could be obtained by using an area detector in case of texture measurements [173]. Nevertheless, the destructive procedure of this method in most of the cases is one of the disadvantages of this method. [215]. The texture measurements in this work were carried out all in transition with a monochromatic beam.

Fig. 3.15 shows schematically the basic beam line setup at HEMS-P07B [173]. The sample is positioned on the ω -rotation stages, which is mounted on an XZ -stage allowing the translation of the sample in sample-height (Z) and perpendicular to the incident beam (X) direction. At a stationary sample position, only the lattice planes (hkl) that are inclined by an angle of 90° to the incident beam satisfy the Bragg's condition [Eq. (2.15)], and the corresponding Debye-Scherrer rings are generated with an opening angle of 2θ [214].

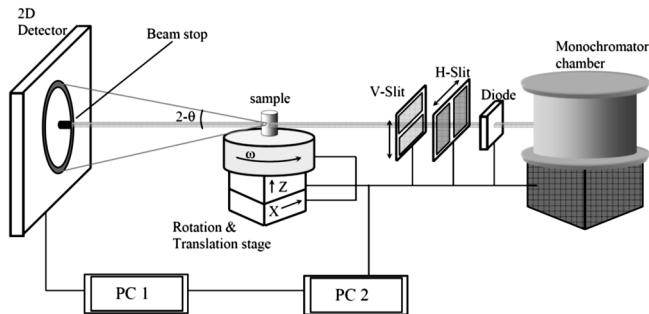


Fig. 3.15 Beamline set-up for texture measurement at HEMS-P07 [173].

Samples were taken from the area of the as-received tube, the deformation zone, and the drawn tube of the IDT. Same as residual strain measurements, texture was measured at Max , Min , and 90° . Tubes were drawn without tilting and with tilting angles ± 5 . The samples were fixed on a pin and mounted on the

¹ Wall-thickness

² Deutsche Elektron Synchrotron

ω -rotation stage so the drawing direction was pointed in the direction of the detector. An X-ray beam with a wavelength of 0.142441 Å with a size of $0.5 \times 0.5 \text{ mm}^2$ was used for local texture measurements. The distance between the sample and the two-dimensional Perkin Elmer (PE) detector was 1123 mm. The PE detector has a resolution of 0.2 mm and diameter of 416 mm [173]. The azimuthal rotation (phi motor) was driven from -90° to 90° in steps of 5° with an exposure time of 3 s for every phi step. Debye-Scherrer rings for several reflections were recorded.

The treatment of the data was done using an intern software developed at Institute of Material Science of Clausthal University of Technology [173]. For the correction of the data, LaB_6 was used, which is a texture free material. The global texture variation was calculated by averaging the measured data for the various positions. Three PFs {111}, {200} and {220} were achieved and used for ODF calculations with the degree of series expansion $L_{max} = 23$. Due to the fact of lower sample symmetry, the ODF-calculation was done with triclinic sample symmetry.

3.6.3 Texture measurements by electron diffraction

Beside macro-texture measurements using synchrotron and neutron diffraction methods, micro-textures of the copper samples were measured as well, using the electron diffraction method with EBSD technique. The samples of *Min* and *Max* sides of as-received tubes, as well as the drawn ones without and with -5° tilting after first and second drawing were taken from the axial-radial plane. *Tescan Vega II XMU* Scanning Electron Microscope with an EBSD camera of *Digiview III* with Forward Scattered Detector (FSD) was used. The scan dimension was $800 \times 550 \mu\text{m}^2$ with a step size of $0.3 \mu\text{m}$ and each scan had about 5644981 number of points, which took about 26 h for each sample for a complete scan. The voltage of scan was 30 kV and probe size was about $0.3 \mu\text{m}$ and with a probe current of 127 pA. A low vacuum mode pressure (about 10 Pa) was used for these tests. Data treatment was done with OIM¹ Data Collection software V5.31 and OIM Analysis software V5.31 [216] as well as MTEX [217] software.

3.7 Multiscale simulation

As shown in Fig. 1.2, one aim of this work was to develop an FEM model for the tube drawing process, which can get the required and/or desired parameters – in case of this work: Eccentricity, RSs, and texture of the tube - as input and analyze the desired parameters in the tube drawing process, which can be performed with or without tilting/offset. Furthermore, it should be possible to use

¹ Orientation Imaging Microscopy

this model in other forming processes, as well. For this reason, the multiscale simulation approach was used. Based on this methodology, it was possible to get all the necessary parameters and desirable input data for the structural scale simulation (FEM) – this methodology is already discussed in “2.6 - Multiscale simulation”. **Fig. 3.16**, which is a more relevant form of the Fig. 2.18 for this work, shows the different approaches used in different simulation length-scales and the bridging between these scales.

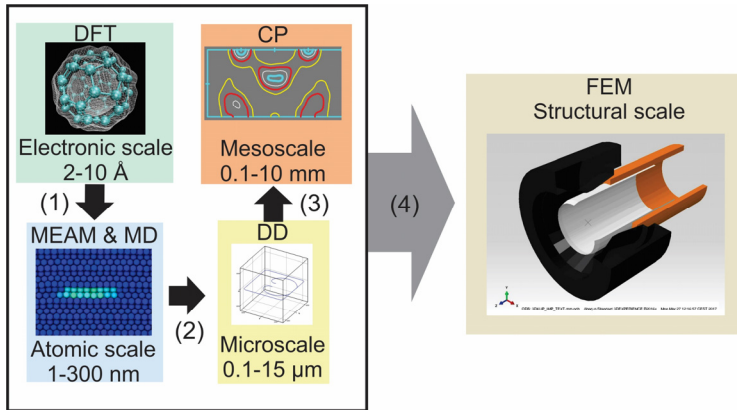


Fig. 3.16 Schematic of the multiscale simulation, showing the bridges for upscaling related to the plasticity information for forming finite element simulations.

The bridges, which were used in this work - as illustrated in Fig. 3.16 - are explained briefly in the following. Based on the aim of each simulation approach, these bridges can be performed with different software and solvers. The solvers used in this work at each simulation scale are discussed as well.

Bridge 1: Using DFT calculations, the lattice parameter, bulk modulus, energy variation and *GSFE* were calculated for copper. These parameters were upscaled for the bridge 2.

Bridge 2: Calculating the elastic constants and developing required potentials for MD using the calculated parameters in bridge 1, with MEAM calculations. After garnering the required potential, the dislocation mobility and drag coefficient were calculated by MD.

Bridge 3: Gaining the hardening parameters from DD calculations with the calculated dislocation mobility achieved in the previous scale.

Bridge 4: Importing the CP theory and all the calculated parameters into the FEM simulations, using a subroutine and developing the FEM model for the simulation of the tube drawing.

3.7.1 Bridge 1, DFT calculation

DFT calculations were done using Quantum Espresso software [218], which is an open-source computer codes based on DFT and pseudopotentials. It is used for electronic-structure calculations and materials modeling. For the DFT calculations, three main files were needed: (1) the input file, which is defining the type of calculation, the atomic positions and potential, and the K -points (consider it as mesh), (2) the executable from Quantum Espresso, and (3) the pseudopotential file - defining the electronic potential used for the material. The used pseudopotential for copper was achieved from the Quantum Espresso's databank [219].

3.7.2 Bridge 2, MEAM and MD calibration

To get the elastic constants of copper for the anisotropic elasticity tensor [Eq. (2.24)], MEAM calculations were used. For this reason, MPCv4 software (MEAM Parameter Calibration) was used, which is executed as a library inside the MATLAB workspace [220]. Using MPCv4, the G_{SFE} , energy changes by changing the lattice parameter for different crystal structures (fcc , bcc , and hcp) and elastic constants were calculated and calibrated using the already calculated values by DFT. After successful calibration, atomic potentials were exported for the MD simulations in form of "**.library.meam*" and "**.parameter.meam*".

To acquire the dislocation mobility and the drag coefficient of copper, MD simulations were done using Large-scale Atomistic/Molecular Massively Parallel Simulator (LAMMPS) [221]. Moreover, it was necessary to create the atom positions and atomistic dislocation. A simulation cell with a size of $100 \times 60 \times 2$ Burgers vector was produced for simulation, containing almost 70,000 atoms for an fcc structure. The visualizations of the results were done using OVITO (Open Visualization Tool) [222]. The main output of this scale simulation was the dislocation mobility of an edge dislocation which is an input value for the DD simulations.

3.7.3 Bridge 3, DD simulation

The DD simulations were done by Multiscale Dislocation Dynamics Plasticity (MDDP), developed by Hussein M. Zbib and colleagues [223]. MDDP is a model for crystalline materials coupled with finite element analysis. One of the key inputs is the dislocation mobility (calculated from MD simulations) and the

calculated stress-strain curve data can be used to upscale to the mesoscale CP and calculate the Palm-Voce hardening parameters [see Eq. (2.30)]. Other inputs for the MDDP simulations were as follow:

- Density
- Crystal structure, which was fcc
- Shear modulus
- Poisson's ratio
- Dislocation source and number of dislocation, Frank-read sources were used, for more information see chapter 5 of "*Physical Metallurgy Principles*" published by Abbaschian et al. [224])
- Burger's vector (B_a)
- $GSFE$

3.7.4 Bridge 4, CPFEM simulation

For the structural scale simulation, Abaqus FEM software package was used [225]. To incorporate the CP into the FEM, UMAT user subroutine, which defines a material's mechanical behavior, was used [226] In UMAT was possible to insert the anisotropic elastic constants (calculated by MEAM), hardening parameters (calculated by DD), and measured texture (Euler angles - measured by neutron diffraction) into the FEM simulations.

Chapter 4 Eccentricity

4.1 Introduction

As discussed in Chapter 1, to find a general rule for the tubes' behavior concerning eccentricity, different drawing steps and materials (copper, aluminum, brass, and steel) with different tube dimensions were investigated varying the tilting angles, offset values, or a combination of tilting and offset. Initially, the eccentricity results regarding copper tubes after first and second drawing steps are discussed. Subsequently, the effects of the tilting on the eccentricity of the other three materials - aluminum, brass, and steel – are discussed.

4.2 Copper

4.2.1 Tilting

The eccentricity of some of the as-received Cu-tubes for both series of copper (G-I and G-II) are shown in **Fig. 4.1**. Each point in this diagram gives the average eccentricity for all rings measured in the tube. As can be seen, the eccentricity of the G-I series varies between 2.5 and 8%, and the G-II series between 1 and 5%. As the error bar of each average value shows, most of the tubes exhibited a quite homogenous eccentricity along the tube.

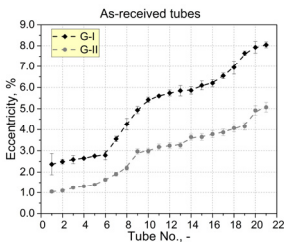


Fig. 4.1
The eccentricity of the as-received copper tubes of G-I and G-II series.

So, these as-received tubes were categorized into three main groups: Tubes with low, medium, and high eccentricities. Since the minimum number of tubes tested each time for each tilting angle/offset value was three, categorization was necessary to have at least one tube from each category.

Fig. 4.2 shows the change of eccentricity for some numbers of tubes (chosen from G-I), having the same as-received eccentricity, but been drawn with

different tilting angles. The black lines with square symbols show the eccentricities in the as-received state. The other lines present the results for the eccentricity after drawing with different tilting angles; 0° (standard drawing), -5° and $+5^\circ$. Looking at the results of -5° tilting - *Min* in the direction of tilting – shows that drawing with -5° tilting results in a higher reduction of the eccentricity, compared to the standard drawing. Rotating the tube 180° - therewith positioning the *Max* in the direction of tilting $+5^\circ$ - a significant increase of eccentricity occurred. These results demonstrate that, by introducing tilting to the tube drawing process and taking the position of *Max* and *Min* into the account, it is possible to influence and control the eccentricity during drawing. This influence can be either a reduction or an increase of the eccentricity.

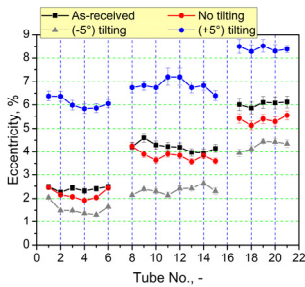


Fig. 4.2
Variation of eccentricity after drawing without (0°) and with $\pm 5^\circ$ tilting angles.

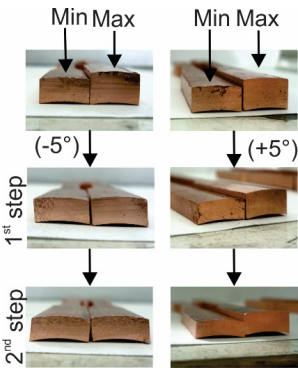


Fig. 4.3
Variations of *Max* and *Min* after each drawing steps and changes in the eccentricity of the tubes drawn with -5° (left column) and $+5^\circ$ (right column).

To show the discussed increase and decrease of the eccentricity visually, the cross-section of two tubes, having almost the same as-received eccentricity, were cut after each drawing step. One tube was drawn with a tilting angle of -5° , the other one with $+5^\circ$. The results are presented in **Fig. 4.3**: After the second drawing with -5° , the eccentricity of the tube was reduced significantly. In contrary, the difference between *Max* and *Min* in tube drawn with $+5^\circ$ tilting was

augmented, i.e. the wall-thickness difference relatively was increased for this tube.

To be able to discuss the effects of different tilting angles on the eccentricity and to present a general behavior, the variation of the eccentricity (before and after drawing) was relativized by dividing the changes of the eccentricity by the eccentricity of the as-received tube (E_0), as given in Eq. (4.1).

$$\Delta E = \frac{E_0 - E_1}{E_0} \times 100\%. \quad (4.1)$$

where ΔE is the relative change of the eccentricity, and E_0 and E_1 are the eccentricities of the tube before and after drawing, respectively. Positive values for ΔE mean that the eccentricity of the drawn tube is less than the one of the as-received tube, and vice versa. **Fig. 4.5-a** and **b** illustrate the relative changes of eccentricity after the first drawing step for G-I and G-II series, respectively. Before discussing this diagram and avoiding any misunderstanding regarding high deviations between the measurements in this diagram, the way the results were achieved for this diagram was explained in beforehand. **Fig. 4.4-a** shows the average results of the eccentricities for a number of tubes before (red line) and after (black line) drawing with -5° tilting (left y-axis). For the same tubes, the relative change of eccentricity is plotted as a second y-axis in the same diagram. As can be seen, even though the eccentricity after drawing is almost the same for all seven example tubes, concerning the eccentricity of the as-received tubes, the relative change of eccentricity could be high or low. Comparing tube 4 with tube 7 (one having a higher as-received eccentricity than the other one), ΔE varies about 20%, nevertheless, the final eccentricity for both is almost 1%. For this reason, the results in Fig. 4.4-b show a high difference, which does not mean any high deviation between end results.

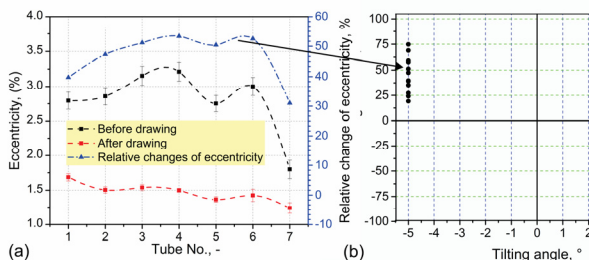


Fig. 4.4 (a) The absolute (left y-axis) and relative (right y-axis) changes of eccentricity for some tubes drawn with a tilting angle of -5° . (b) Plotting the relative change of eccentricity in the ΔE vs. the tilting angle diagram.

In Fig. 4.5 the average of the results for each tilting angle was calculated and plotted and fitted using a linear fit. Based on the slope of this linear fit, a general dependency of the eccentricity variation to the tilting angle can be presented. Eqs. (4.1) and (4.2) show this equation for both series of tubes. In these equations, θ is the tilting angle. The as-received tubes were in heat-treated condition for these drawing steps.

$$\Delta E = 0.04 - 0.10\theta, \quad (4.1)$$

$$\Delta E = 0.09 - 0.11\theta. \quad (4.2)$$

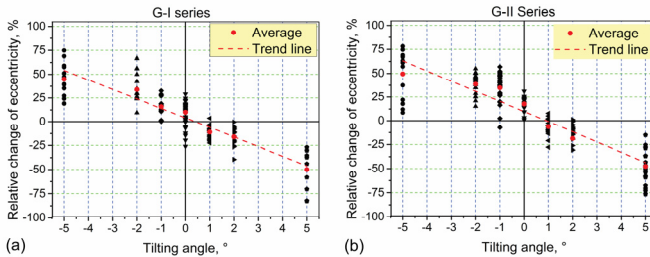


Fig. 4.5 Relative change of the eccentricity for different tilting angles for two different series of copper tubes after first drawing step; (a) G-I and (b) G-II.

The main phenomenon which results in getting different eccentricities after drawing with different tilting angles, is the inhomogeneous mass flow, which is induced by the tilting of the die and therewith superposing an inhomogeneous momentum to the tube.

In the case of negative tilting (see Fig. 4.6), the *Max* side (lower side) initially contacts the die and starts to get deformed. As the upper side of the tube up to then is not under deformation condition, the material starts to flow in circumferential direction dominantly, which is approved by RSs and simulation results to be discussed in Chapter 5 and Chapter 7, respectively. This circumferential mass flow from the thickest part of the tube (*Max*) to the thinnest one (*Min*) decreases the differences between *Max* and *Min* and successively the eccentricity.

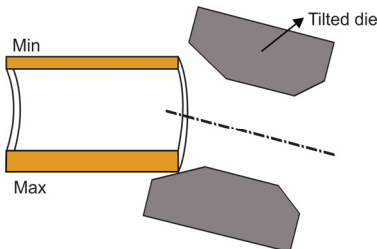


Fig. 4.6 Initial contact between the tube and the tilted die (negative tilting), *Max* reaches the die first.

In the case of positive tilting, initially *Min* reaches the die and starts to flow toward *Max* side, therewith increasing this part of the tube with decreasing the thinnest part. Consequently, the difference between *Max* and *Min* (and the eccentricity) increases, therewith a local thickening is achieved.

Another difference between drawing with tilting is the positioning of the plug. In the standard drawing process, since the tube has eccentricity, during the drawing, the plug moves from the thickest part in direction of the thinnest part, which results in keeping the differences between *Max* and *Min* almost constant or sometimes with a slight reduction. In tilting, however, this matter is avoided. Further difference is the friction condition in tilting/shifting compared to the standard drawing. This different friction creates different forces on the tubes, which affect the mass flow during the drawing.

The results of eccentricity variation as a function of the tilting angle (the results shown in Fig. 4.5) are compared to the results of performed simulations, as shown in "7.5.3.3 - Eccentricity".

To study the influence of work hardening on the effectiveness of tilting, a further drawing step was performed. The results after the second drawing step are given in Fig. 4.7-a and b. The equations for the trend lines for both series are given in (4.3) and (4.4), showing a slight change compared to the ones after the first pass. These dependencies and their description are not in the focus of this thesis.

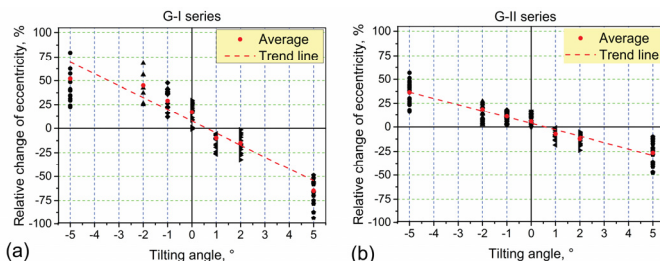


Fig. 4.7 Relative changes of the eccentricity after second drawing step of copper tubes; (a) G-I series and (b)-II series.

$$\Delta E = 0.075 - 0.11\theta, \quad (4.3)$$

$$\Delta E = 0.03 - 0.08\theta. \quad (4.4)$$

The drawing forces needed for the tube drawing with different tilting angles are exemplarily shown in Fig. 4.8. Two maxima are visible: the first one occurs when the tube contacts the die and the latter one occurs when the plug reaches its correct position. Generally, what is used to define the drawing force, is the

linear part of the plot. Apart from very small differences between these curves, one can state that tilting does not affect the drawing force significantly. Nevertheless, they are slightly increased compared to the standard (0°) condition. The values for positive tilting angles were in the range of the negative ones.

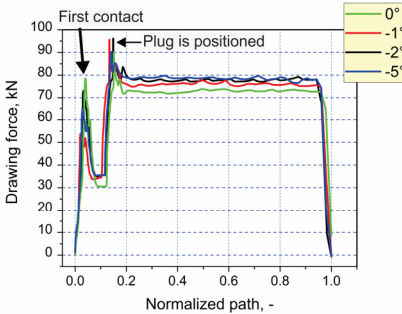


Fig. 4.8
Drawing forces measured for tube drawing with different tilting angles.

4.2.2 Offset

Same as tilting, shifting of the tube was performed on the G-I series. The eccentricity of the tube after first drawing step is shown in Fig. 4.9. Same as tilting, by applying a negative value of offset, the eccentricity was reduced and in the case of using positive values, the eccentricity increased. Comparing the slope of the trend line in shifting with tilting, see Eq. (4.5), it can be seen that with shifting the same behavior as with tilting results. However, the effect is less intensive.

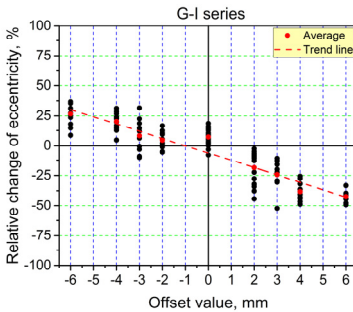


Fig. 4.9
Relative change of eccentricity in G-I series after the first step of drawing with different offset values.

$$\Delta E = -0.063 - 0.06\theta.$$

(4.5)

4.2.3 Combination of tilting/offset

As mentioned in “3.3 - Eccentricity”, the combination of tilting and shifting was also performed on the copper tubes to see whether the change of eccentricity could be amplified by combining both technologies. For this reason and as shown in Table 3.5, G-I series was chosen and only negative tilting angles (-1° , -2° , and -5°) were selected and combined with positive and negative shifting values (± 2 , ± 4 , ± 6 mm). To compare the combination effect with the case of pure tilting, 0 mm of shifting was also performed.

Fig. 4.10 shows the combination of the negative shifting value - four distinct categories, each presenting one value of shifting - with negative tilting angles. In the case of no shifting in addition to tilting, the same trend as Fig. 4.5-a was achieved. In the case of combining tilting with shifting, the results look a bit different, and this statement “the higher the tilting angle is, the more the eccentricity change is” is not valid any more. As can be seen, the highest relative changes of eccentricity (decrease of eccentricity) were achieved mostly for -2° tilting, whereas, -5° tilting has even some contrary effect on the eccentricity.

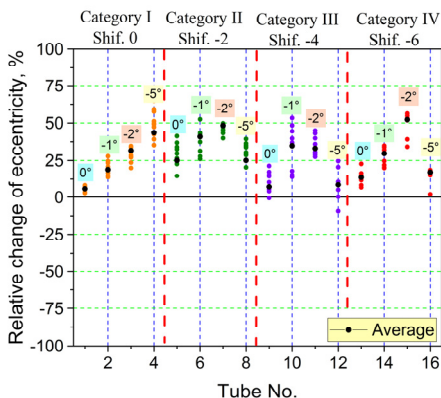


Fig. 4.10 Relative change of eccentricity in the combination of negative tilting angles with negative shifting values for Cu-tubes.

In the case of using positive shifting with negative tilting, as shown in **Fig. 4.11**, the increase of the eccentricity is more intensive than with pure tilting or shifting. Therefore, for applications with the aim of increasing the differences between *Max* and *Min* as strong as possible, this kind of combination could be used.

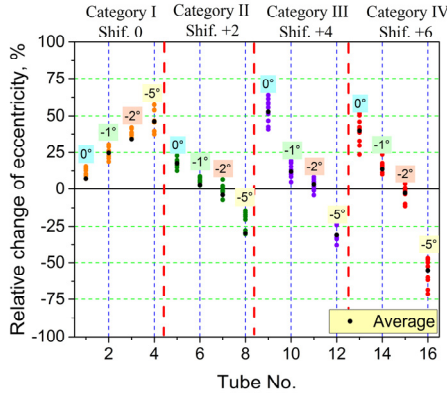


Fig. 4.11 Relative change of eccentricity for the combination of negative tilting angles with positive shifting values for Cu-tubes.

4.3 Other materials

Since the main experimental focus of the work was on tilting and understanding the behavior under different conditions (material and process), the eccentricity changes of other three materials were analyzed just by changing the tilting angles. Shifting is not yet investigated for these materials.

The representative eccentricities of the as-received aluminum, brass, and steel tubes are shown in **Fig. 4.12**, changing for aluminum from 2 - 3.5%, for steel from 1.8 - 5%, and for brass 2 to almost 7%, respectively. These tubes were, like the copper tubes, classified into three main groups and were drawn with one relevant drawing step (Table 3.4).

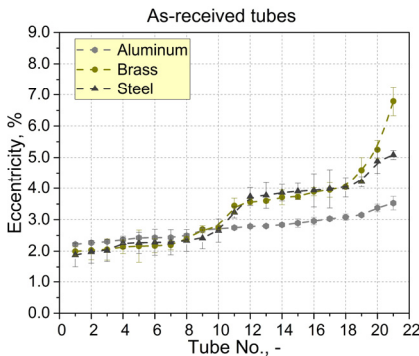


Fig. 4.12 Eccentricity of as-received aluminum, brass, and steel tubes.

After the drawing step, the relative changes of eccentricity for all drawn tubes and tilting angles were calculated. Using the average value for each tilting angle, the trend line was calculated with a linear fit for all three types of materials, see Fig. 4.13-a to c:

$$\Delta E = 0.08 - 0.09\theta, \quad (4.6)$$

$$\Delta E = -0.01 - 0.10\theta, \quad (4.7)$$

$$\Delta E = 0.07 - 0.03\theta. \quad (4.8)$$

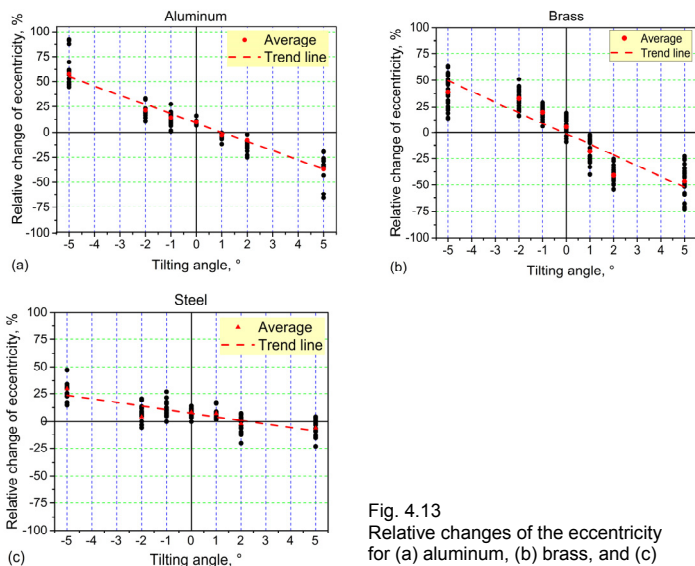


Fig. 4.13
Relative changes of the eccentricity for (a) aluminum, (b) brass, and (c) steel tubes.

The results of the relative change of eccentricity for aluminum and brass tubes exhibit almost same behavior as copper for different tilting angles. In contrary, steel shows a bit different behavior. It seems that the tilting has less effect on the eccentricity in steel tubes. Moreover, in steel tubes, for the tilting angles of -1° , 0° , and $+1^\circ$, almost same behavior was observed, showing that tilting about 1° (either negative or positive), has no significant effect on the eccentricity of steel tubes. One main reason for such a different behavior is different mechanical properties, which creates different mass flow. Different crystallographic structure is another reason for this different behavior. Comparing the fit line equations for these three materials [Eqs. (4.6) to (4.8)] with the one for copper [Eqs. (4.1) and (4.2)], it can be seen, the trend line of aluminum, brass, and copper are almost identical. But, steel trend line varies significantly from the other three materials. These trend lines are plotted in Fig. 4.14, as well.

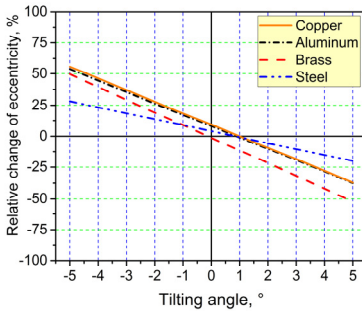


Fig. 4.14
Comparison of the trend lines of all four materials after drawing with different tilting angles.

4.4 Conclusion

The effects of tilting, offset, and combination of these two on the eccentricity evolutions in tubes were investigated. It has shown that, the tilting and offset affect the final eccentricity of the tubes and this method makes it possible to control the eccentricity of the tubes – either increase or decrease of the eccentricity. It can be stated for all investigated materials that with increasing tilting angle the eccentricity variations were stronger.

In case of copper tubes, by introducing -5° tilting to the die (*Min* in the direction of the tilting), the eccentricity of the drawn tubes was significantly reduced. The average reduction achieved by this tilting angle was about 48%, which was higher than the eccentricity reduction achieved by the standard drawing, which was about 18%. Nevertheless, by using $+5^\circ$ tilting, the eccentricity was considerably increased, which is interesting for applications in which the local thickening is required. The average eccentricity increase achieved by this tilting angle was about 50%. These results were tested for two different dimensions going through different wall-thickness and diameter reduction.

A further drawing step was also performed, to investigate the influence of work hardening on the effectiveness of tilting. The achieved results showed a same behavior as the first drawing step.

Drawing forces needed for tube drawing with different tilting were compared to the standard drawing. There was no notable change in case of drawing with tilting.

Applying offset to the copper tubes during the drawing resulted in controlling the eccentricity, as well. Shifting the tube about -6 mm resulted in a 35% eccentricity reduction (as average). However, $+6$ mm offset increased the eccentricity about 46%. Comparing the trend line slope of the offset results with

the tilting ones shows that tilting affects the eccentricity slightly more than the shifting.

After analyzing the tilting and offset influences on the eccentricity in copper tubes, tilting was studied for other three materials, to analyze the material dependency of the results. Aluminum and brass tubes showed very similar results to copper ones. The eccentricity reduction as well as the increase of it were more or less same in these tubes. Steel tubes have shown, however, a slightly different behavior. Although the reduction and increase of eccentricity were achieved by applying -5° and $+5^\circ$ tilting to die, respectively, which were same as results of other materials, however, the results of other tilting angles were different. This different behavior could have been because of the different mechanical properties of steel.

As final conclusion in case of eccentricity, it could be stated that, introducing tilting/shifting to the tube drawing process, made it possible to control the eccentricity. In next chapter, it is shown that, how this introduced tilting affects the RSs and whether it can influence the RSs in a destructive way.

Chapter 5 Residual stresses

5.1 Introduction

The tensile nature of RSs existing on the outer surface of the drawn tubes is one of the factors, which can lead to an early failure during each application. If modifying a process results in increasing of the tensile nature of the RSs, the life time of the component will be affected in a significant way. As shown in the previous chapter, it is possible to control the eccentricity of the tubes during the drawing process by introducing tilting and/or shifting. In this regard, it was important to investigate the evolution of RSs of the tubes, which were drawn with different tilting angles – only variation of RSs in tilting was studied. The main aim of these investigations was to analyze the evolution of RSs and to find out whether the tilting affects the RSs in a destructive way.

In this chapter, firstly, the measured surface-near residual strains using hole drilling method are presented and discussed for all four materials drawn under the different tilting angles. The measurements were performed before and after drawing over the circumference of the tubes in three positions; *Max*, *Min*, and between these two. However, since with hole drilling method, only the RSs can be measured, which are near to the outer surface of the tubes, to study the RSs through the whole wall-thickness, neutron diffraction method was chosen. In this method, apart from the possibility of determining the RSs through the whole wall-thickness of the tubes, the measurements were also performed non-destructively. This latter made it possible to use the tube after the neutron diffraction measurements and draw it one further step and analyze the same tube. These measurements are presented and discussed in this chapter, as well. The achieved RSs by the neutron were used in the FEM simulations; the measured RSs of the as-received tubes were used as input and the RSs of the drawn tubes were used for validation of the simulation results.

5.2 Hole drilling

5.2.1 Copper

Fig. 5.1-a and **b** show the axial and hoop RSs of the as-received G-I series measured over the circumference of the tubes - in *Max*, *Min*, and 90° positions - respectively. RSs were measured in at least 5 tubes, having same condition. To get statistical results, in each tube, at least 3 measurements were done at each position. Since the as-received tubes were in heat-treated condition, the

measured RSs show only moderate values. Moreover, there is no significant difference between the RSs in different positions over the circumference of the tube.

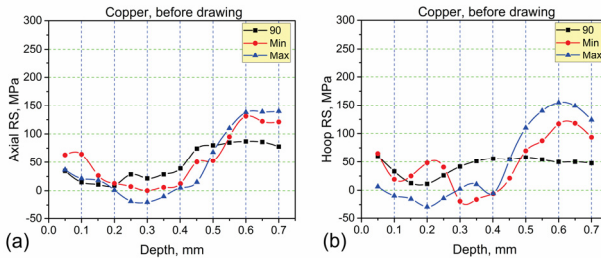


Fig. 5.1 (a) Axial and (b) hoop RSs in three different positions measured in a copper pre-tube.

Drawing these tubes using standard drawing method (0° tilting), results in different RSs after drawing, as shown in **Fig. 5.2**. In this figure, the axial (Fig. 5.2-a) and hoop (Fig. 5.2-b) RSs are compared after drawing in three different positions; *Max*, *Min*, and 90° . As expected, the axial and hoop RSs are increased in all three positions. However, the increase happened in the axial direction is more significant than the hoop direction, showing that the mass flow during the standard drawing is dominant to the one in circumference of the tube. Moreover, comparing the RSs at *Max*, *Min*, and 90° shows no considerable differences between the RSs over the circumference of the tube.

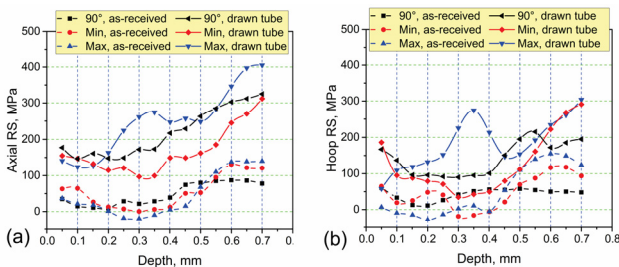


Fig. 5.2 (a) Axial and (b) hoop RSs at three positions over the circumference of the tube, *Max*, *Min*, and 90° , measured after first drawing step with no tilting.

Same comparison as above is made for the drawn tubes with -5° tilting angle, which are shown in **Fig. 5.3-a** and **b**. Looking at the axial RSs at *Min* and comparing them to the *Max* and 90° positions, shows, unlike the standard drawn tubes, there is a considerable difference between RSs over the circumference of the tube in axial direction. In hoop direction, nevertheless, the RSs are almost same. Other interesting point is the direct comparison of the RSs in drawn tube

with 0° (standard drawing) with the drawn tubes with -5° tilting, which is shown in **Fig. 5.4**. This comparison is done for all three positions. As can be seen, in all these positions, the RSs for drawn tubes with -5° tilting is less than the standard drawn tubes.

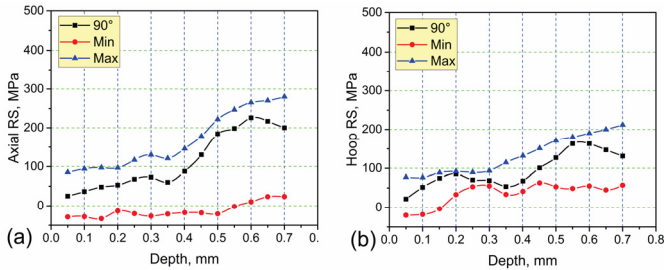


Fig. 5.3 (a) Axial and (b) hoop RSs at three positions over the circumference of the tube; *Max*, *Min*, and 90° , measured after first drawing step with -5° tilting.

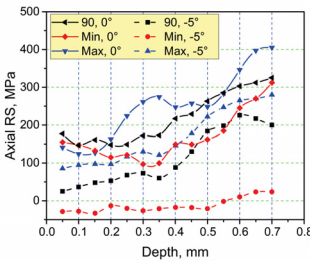


Fig. 5.4 Comparison of the RSs in axial direction in three positions over the circumference of the tube.

Comparison of the axial RSs at *Max* and *Min* sides of the drawn tubes with different tilting angles are shown in **Fig. 5.5-a** and **b**, respectively. As can be seen, drawing the tube with standard method results in a higher RSs either at *Max* and *Min* sides. Interestingly, the side of the tube, which stands in direction of the tilting – e.g. in case of $+5^\circ$ tilting angle, the *Max* side – has always the lower RSs. This could be because of the higher mass flow existing in the other side of the tube - due to the initial contact with the die.

Fig. 5.6-a and **b** show the adequate results as Fig. 5.5, but the hoop RSs. It can be concluded that the side of the tube positioned in the direction of tilting, has lower RSs compared to the opposite side of the tube, as e.g. presented in **Fig. 5.7-a** for the case of -5° tilting at *Max* and *Min* side of the drawn tube. RSs of drawn tubes with different tilting angles after step 1 of drawing (Fig. 5.7-b) show that, unlike the eccentricity's results, there is no specific trend regarding RSs. However, at *Max* side of the tube, the drawn tube with $+5^\circ$ tilting angle has the lowest RS and at *Min*, the -5° drawn tube has the lowest RS. Generally,

both sides have clearly less RSs values compared to the standard drawing condition.

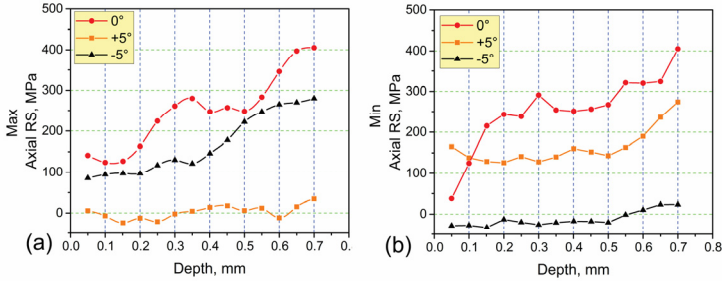


Fig. 5.5 Axial RSs at (a) *Max* and (b) *Min* sides of the tubes drawn under 0°, -5°, and +5° tilting angles.

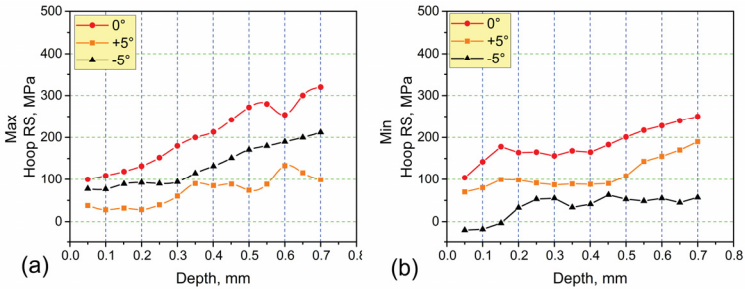


Fig. 5.6 Hoop RSs at (a) *Max* and (b) *Min* sides measured after drawing with three different tilting angles; 0, -5, and +5°.

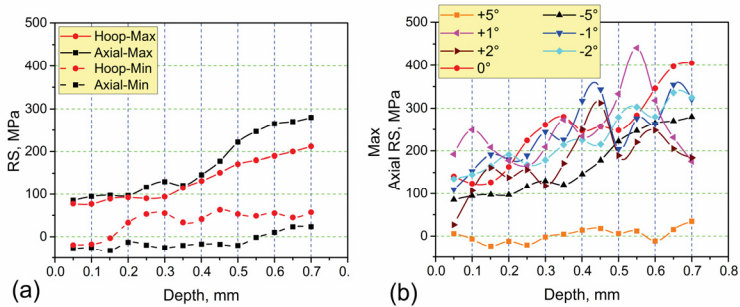


Fig. 5.7 (a) Axial and hoop RSs at *Max* and *Min* side of the drawn tube with -5° tilting. (b) RSs of different tubes after first drawing step with different tilting angles.

Averaging all the measured axial RSs at *Max* and *Min* sides of the tube for tubes drawn with 0° and $\pm 5^\circ$ describes how tilting affects the RSs, which is shown in Fig. 5.8-a and b, respectively. Generally speaking, the drawn tubes with 0° tilting - standard drawing - have higher RSs than the tubes drawn with -5° tilting, either in *Max* or *Min* side. Tubes drawn with $+5^\circ$ tilting angle show the lowest RSs at *Max* side of the tube and tubes drawn with -5° tilting angle has lower RSs at *Min* side. However, the difference of the RSs in case of $\pm 5^\circ$ tilting is not significant. In another word, superposing tilting not only makes it possible to control the eccentricity, it gives also the possibility to reduce the tensile RS level on the surface of the tube.

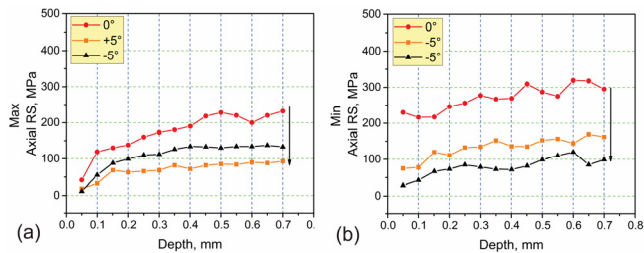


Fig. 5.8 Average axial RSs at *Max* side of the tube measured in tubes drawn with 0° and $\pm 5^\circ$ tilting.

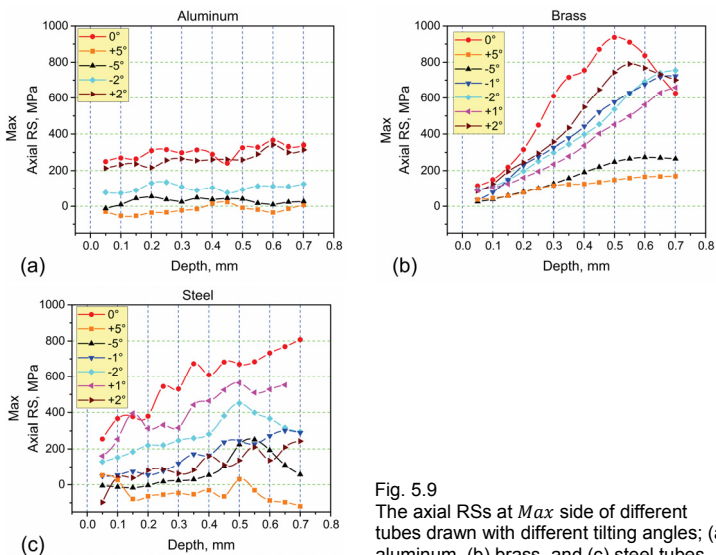


Fig. 5.9 The axial RSs at *Max* side of different tubes drawn with different tilting angles; (a) aluminum, (b) brass, and (c) steel tubes.

5.2.2 Other materials

The axial RSs at *Max* side of the aluminum, brass, and steel tubes are shown in Fig. 5.9-a to c, respectively. As for the copper tubes, the general trend is that the standard drawing condition has always the highest axial RSs at *Max* and the +5° tilting results in the lowest ones. Tubes drawn with -5° tilting have RSs lower than for all the other tilting angles, except the +5° one. The results of the axial RSs at *Min* side of the tubes present exactly same behavior; however, the lowest RS at *Min* side of the tube has been observed for the -5° tilting angle, same as for copper tubes. Generally and same as copper, not only tilting does not increase the RSs, but also reduces the RSs – in both “+” and “-” cases.

5.3 Neutron diffraction

Even though the RS measurements using hole drilling is a fast and relatively inexpensive method and it is a practical method to investigate the RSs on the surface of the tubes, RSs through the whole wall-thickness of the tube cannot be analyzed. For this reason, the neutron diffraction method was used for copper tubes. The measurement parameters and the method of performance of the experiments are already discussed in “3.5.2 – Residual strain measurement by neutron diffraction”. As mentioned there, to be able to understand the behavior of the RSs during drawing also to measure the as-received and the drawn tubes in one shot, IDT samples were prepared and analyzed for two drawing steps (Fig. 5.10).

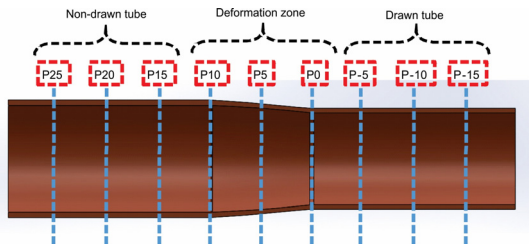


Fig. 5.10 Schematic of measurement positions on the IDT after first drawing step.

5.3.2 After first drawing step

For neutron measurements, a tube from G-I series with a tilting angle of -5° was chosen. The measurements were done through the wall-thickness of the tube at each measurement position in *Max*, *Min*, and 90° position. “P0” describes the first position after the deformation, “P-5” the position 5 mm behind this point in the final deformed zone, “P5”, “P10”, etc. the position 5 mm, 10 mm, etc. before the P0-position. Depending on the wall-thickness of the tube, 15-25 scans were done for each measuring point to correctly describe the RS profile

through the wall-thickness. As an example, **Fig. 5.11**-a and b, shows a 3D and 2D presentation of the scans for one measurement through the wall-thickness. Fig. 5.11-a shows the intensity variation as a function of 2-theta through the wall-thickness and Fig. 5.11-b shows a blue to red contour of the scans – red being higher.

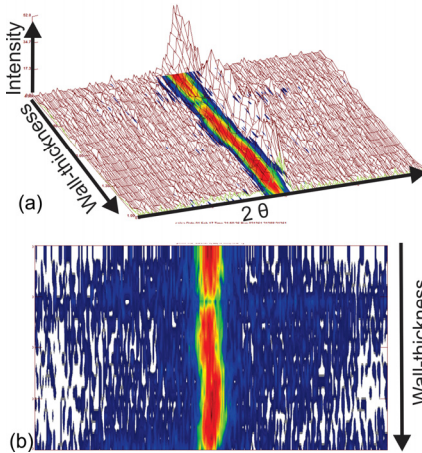


Fig. 5.11
(a) 3D and (b) 2D demonstrations of scans performed through the wall-thickness at a measurement points.

One advantage of neutron diffraction is its possibility to measure the RSs at surface or the interfaces with a higher lateral resolution than the instrument measurement volume permits by default, by allowing the measurement volume to penetrate only partially into the sample. **Fig. 5.12** shows the procedure with this kind penetration scan, which was performed in this work as well. The information about the strain or stress is achieved from this SGV as an average value, which has a center of gravity, assumed to be the real measurement point.

Nevertheless, in such measurements, as the center of gravity of the scattering volume shifts with different penetration depths, there is a displacement of the diffraction reflexes, called “pseudo peak shift” for these measurement points. The resulting strain values are called pseudo strain and require correction. Since the determination of the diffraction angle is related to the geometric center of the IGV, a misinterpretation of the angles can occur. This error is called geometric error. In addition, the monochromator generates a wavelength gradient in the primary beam. If the center of gravity of the SGV is not at the center of the IGV, the wavelength deviates from the mean wavelength at which the instrument is calibrated.

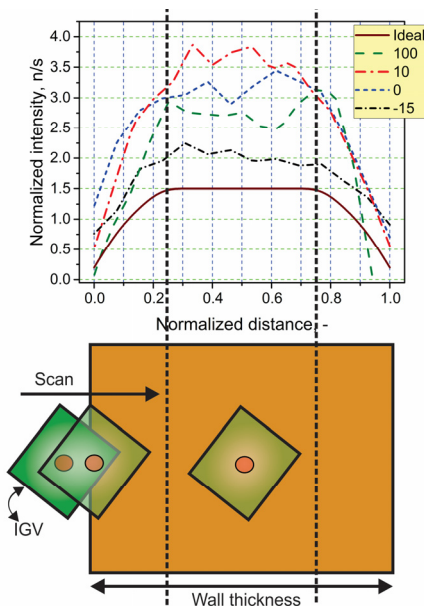


Fig. 5.12 Intensity profile in different depth positions at Max of the drawn tube with -5° tilting; first drawing step.

For SALSA instrument a process has been developed, which corrects these faults or deviations. For this reason, before starting the main measurements, the IGV is measured using a reference sample and with that the geometrical and wavelength-dependent reflex shifts are determined. The parameters obtained are used to make the corresponding corrections to the measured data using an analytical model of the instrument configuration. For this purpose, the program first measures the intensity profile to determine the coordinate of the measuring point relative to the reference point of the instrument and the sample coordinate system. The pseudo peak shift to be corrected is calculated and subtracted from the measured data. At the same time, the instrument coordinates (= motor positions) are converted into sample coordinates. That is, the distance of the measurement points from the surface is calculated.

The normalized intensities of the measured positions in as-received position (P100), beginning of deformation zone (P10), beginning of the bearing zone (P0), and the drawn tube (P-15) are shown in Fig. 5.12. The ideal intensity profile of the thickness of the tube is shown in Fig. 5.12, as well. Without having any texture in materials and/or different grain sizes, by entering of the IGV to the sample, the intensity of the diffracted beam increases and from the moment that the IGV is completely inside the wall-thickness, the intensity will be

constant. This phenomenon will be repeated on the other side of the tube (inner side), where the IGV goes out of the sample. Looking at the profiles of the mentioned positions, the first thing coming to attention is that the intensity should have been constant, which is not for the measured points, that is because of texture and grain size effects. P-15 (the drawn part) and P10 (the beginning of the deformation zone) has the lowest and highest intensities, respectively.

Fig. 5.13-a shows the peak center (position) of the as-received tube (P100), the beginning of the deformation zone (P10), the beginning of the bearing zone (P0), and the drawn tube (P-15) position. The peak positions are related to the lattice and their change relates to the lattice. There are two main reasons for the variation of peak positions: Either scaling of the lattice happens, which does shift all peaks into the same direction – which can be due to the induced strain - or a change of the lattice parameter ratio can be the reason. As shown in Eq. (2.16), peak center is used to calculate the strain, and therefore, exact determination of diffraction peak positions is of particular importance for the evaluation of residual strains [227]. As can be seen, for positions P100 and P10 the peak centers are almost constant, nevertheless, the peak position starts to change significantly by entering the bearing zone and also after the drawing, the final tube, which correlates with the RSs developments in the tube.

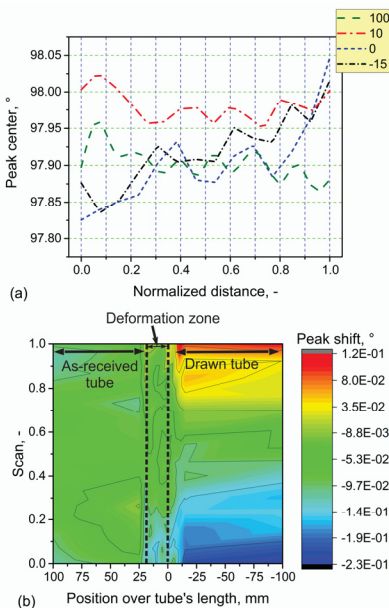


Fig. 5.13
 (a) The variation of the peak center for four different positions in the -5° drawn tube at *Max* at the as-received position (P100), beginning of deformation zone (P10), beginning of the bearing zone (P0), and the drawn tube (P-15). (b) Peak shift from the ideal 2θ for the whole IDT.

As shown in Eq. (2.16), the strain is linear a function of the peak shift (Δd) - the amount of the shift which happened to a diffraction at each measurement points - and therefore the higher the peak shift is, the higher the strain will be. The peak shift represents the distance of the stressed hkl plane from the unstressed one [228]. Fig. 5.13-b shows different scans through the wall-thicknesses (y -axis) for different measurement positions (x -axis). This measurement positions are the same ones shown in Fig. 5.10, starting from the as-received part (100 mm) going to the finally drawn tube (-100 mm).

With the measured peak position and peak shifts and using the Bragg law [see Eq. (2.15)], the strains in all three directions were calculated, which are shown in Fig. 5.14-a to c. Using these calculated strains and Hooke's law [Eqs. (2.17) - (2.19)], the RSs could be calculated.

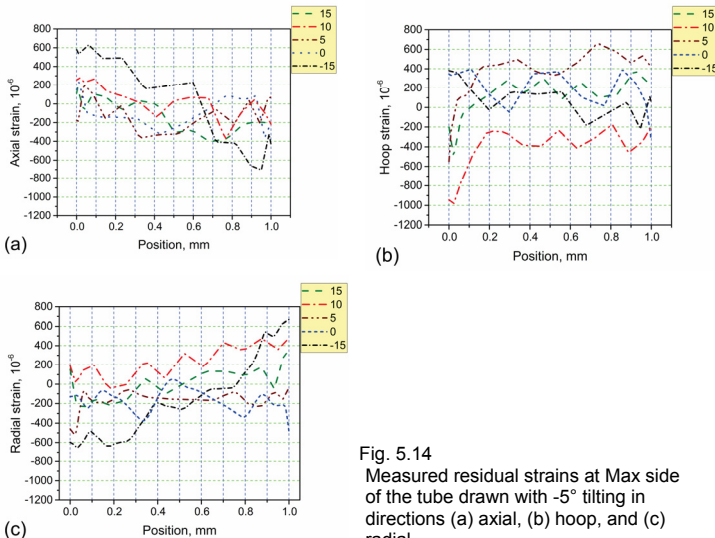


Fig. 5.14
Measured residual strains at Max side of the tube drawn with -5° tilting in directions (a) axial, (b) hoop, and (c) radial.

Fig. 5.15-a to d show the results of the measured RSs using neutron diffraction for different points in the IDT in three different directions. These results are achieved at *Max* side of an IDT sample, which were after first drawing step with -5° tilting angle. As can be seen from the measured point P10 (Fig. 5.15-a), the tube has a compression RS state in hoop direction, with a higher level on the surface than the inner side. The radial RS starts from a zero state and shifts slightly to tensile RS at the inner tube surface. Axial RS keeps its level more or less constant over the wall-thickness.

By entering the deformation zone (P5), there is a strong change in hoop RS. This change - compared to the change of axial and radial RS - can be explained by the inhomogeneous material flow during tube drawing with a tilted die. The RSs in all three directions have a compression state on the tube's surface, caused by the reduction in diameter.

However, after leaving the die (P0) all three components of RS on the surface change to the tensile state with the same trend over the thickness. This change of RS on the surface of the tube can be explained with the springback effect after leaving the die.

The measured RSs at the as-received tube (P10) were used in the simulation as input RSs in the developed simulation model (see 7.5.3.4). Other measured RSs were used to validate the simulation results.

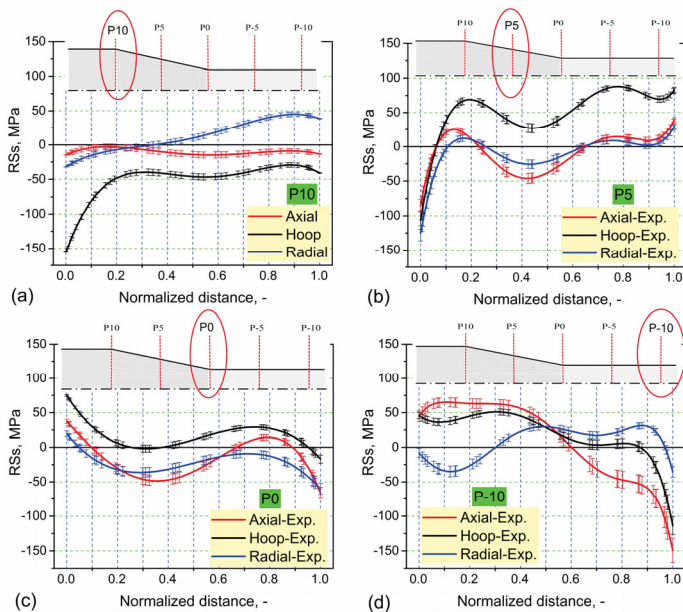


Fig. 5.15 Measured RSs in an IDT of first drawing step drawn with -5° tilting angle at *Max* side in axial, hoop, and radial directions for positions (a) P10, (b) P5, (c) P0, and (d) P-10

The results for P-10 are given in Fig. 5.15-d. As can be seen, the RS trends for axial and hoop directions are of tensile state on the outer surface turning to compression in the inner side of the tube. The radial RS, however, are very low because of the almost thin wall-thickness of the tube. Comparing the axial and

hoop RSs in the as-received tube (P10) and in deformation zone (P5) shows that the changes in axial RS towards the deformation zone is less than in the hoop RSs, which is shown in Fig. 5.16-a. This shows that the mass flow which happens in the circumference of the tube is higher than what is in the axial direction in the deformation zone. This is in a good agreement with what eccentricity changes have shown in -5° and $+5^\circ$ tilting.

Like the hole drilling, comparing the RSs measured by neutron diffraction shows also that the RSs in drawn tubes without tilting has a higher level of RSs compared to the RSs in tubes with -5° tilting. This matter is shown in Fig. 5.16-b. The RSs in drawn tubes without tilting was measured by Pirling et al. [229] on the same tube. The results show that the RSs in all three directions are lower in case of the -5° drawn tube.

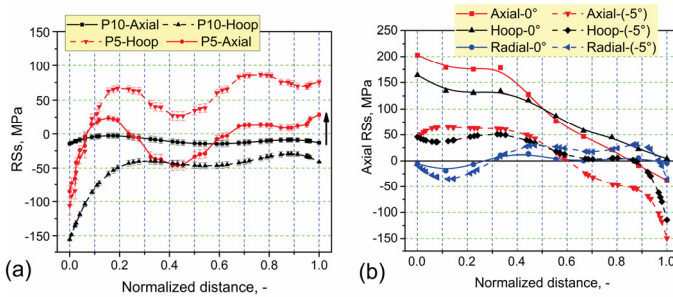


Fig. 5.16 (a) Change of axial and hoop RSs at *Max* side of the tube with -5° tilting going from the as-received tube (P10) to the deformation zone (P5). (b) Comparison of the axial RSs at *Max* side of tubes drawn with -5° and 0° [229].

5.3.3 After second drawing step

Comparing the peak center at *Min* in the axial direction after drawing with -5° tilting after first and second drawing steps, as presented in Fig. 5.17, shows that after the second drawing step the peak center on the surface of the tube changes considerably. This means that the residual strains in the tubes after the second drawing are higher compared to the ones after the first one. The calculated RSs for the *Max* side of the tube after second drawing step with -5° tilting in three axial, hoop, and radial directions are shown in Fig. 5.18. Along with these stresses, the RSs after the first drawing step are presented in this figure as well. The results show a tensile RSs on the outer surface of the tube and compression RS in the inner side, which results in the typical “S” shape of the RSs in drawn tubes. Comparing these results shows that, after drawing the RSs are higher than the first drawing step. Same as first drawing step, the RSs in axial and hoop direction have more or less same value. Unlike the first

drawing step, which has less radial RSs, the radial RSs after second drawing step were higher.

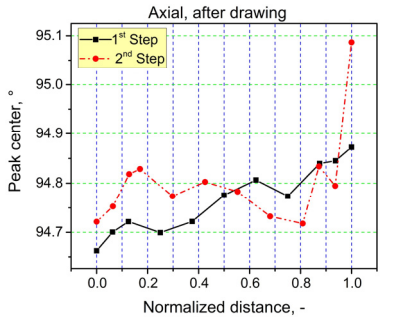


Fig. 5.17

(a) Peak center in axial direction after first and second drawing at Min side of the tube drawn with -5° tilting. (b) Peak shifts in the IDT of second step starting in the as-received tube and going to the drawn one.

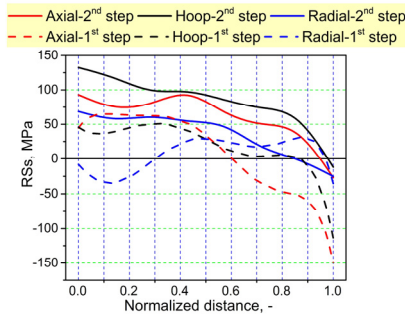


Fig. 5.18

Variation of the RSs at *Max* side of the tube after first and second drawing step with -5° tilting.

5.4 Conclusion

After studying the effects of tilting on the eccentricity of the drawn tubes, which were presented in “Chapter 4 - Eccentricity”, the effects of tilting on the RSs were investigated to know whether tilting can influence the RSs in a destructive way.

For this reason, two different methods were used: Hole drilling method, thereby the RSs in all four materials in two axial and hoop directions were measured. The measurements were done before and after drawing over the circumference of the tubes – *Max*, *Min*, and 90° positions. The measurements with hole drilling, however, was done only on the surface of the tubes (up to 0.7 mm), therefore, another method was used to be able to measure the RSs over the whole thickness. These measurements were done using neutron diffraction method. The measured RSs with neutron diffraction were used in the FEM simulations, as well.

In case of copper tubes, the RSs, which were measured by hole drilling method, showed that introducing tilting to the process, not only does not increase the developed RSs after the tube drawing, but even decreases the RSs. Tubes drawn with either $+5^\circ$ or -5° tilting angles, had over the whole circumference less RSs than the standard drawn tubes.

This matter was also observed in case of the RSs measurements in aluminum, brass, and steel tubes. The RSs of these tubes were significantly reduced (both in *Max* and *Min* sides) after being drawn with either $+5^\circ$ or -5° tilting angle.

Interrupted Drawn Tubes (IDT) were prepared for the neutron diffraction methods, in which all three desired zones were existing; undeformed (as-received tube), deformation zone, and the drawn tubes. Using neutron measurements, it was possible to measure the RSs through the whole wall-thickness. Beside this benefit, the measured RSs were used to be compared to the ones measured by hole drilling method. Moreover, the results of the as-received tubes were used as input in the developed simulations. The results of the other zones were used to validate the simulation results.

The measured results by neutron diffraction have shown that the RSs in the as-received tube were mainly in the compressive state at the surface due to the heat-treatment they underwent before. By entering to the deformation zone, RSs in all three directions started to change significantly. However, the changes in hoop direction in the deformation zone were considerably higher than in the axial one. After drawing, the RSs showed the typical "S" shape of the RS profile, nevertheless, their level is below that one of the non-tilted tubes. Comparing the RSs of the tilted tubes with the standard drawn tubes has shown, that the tilted drawn tubes have less RSs in all three directions. The results of the RSs after second drawing step confirms this matter as well.

Finally, it can be concluded, introducing tilting not only makes it possible to control the eccentricity of the drawn tubes, but also it decreases the developed RSs on the surface and also through the wall-thickness of the tubes. In next chapter, it is discussed, how the tilting affects the crystallographic behavior of the drawn tubes, whether different texture (crystallographic orientations) are developed due to the tilting.

Chapter 6 Texture development

6.1 Introduction

So far it has been shown that the eccentricity can be controlled by using a tilted die in tube drawing process, which is not affecting the RSs in the drawn tubes. As discussed in Chapter 1, in order to understand the anisotropic behavior of the tubes during drawing with tilted die, and in order to study the creation of the new crystallographical orientations during drawing with tilting, their crystallographical evolution – the texture - were investigated. Beside the anisotropic behavior, the mass flow in the tubes and its behavior in the drawing process with and without tilting, was another interesting point. In this regard, it was decided to analyze the texture evolution of the tubes before and after drawing with tilting, to understand whether tilting can create different texture (crystallographical orientations) and/or affect the mass flow in a detectable way. Additionally, investigating the texture evolution was important to prepare sufficient input data for the multiscale simulation model (see Chapter 7 “Multiscale simulation”) and for validation of the simulation model. After validation of the model, using the model, the texture evolution in the standard drawing was compared with the tube drawing with tilting.

To do so, same as strain measurements, the same IDT samples were used to analyze the texture in the as-received tubes as well as in the deformation zone and after the drawing steps. To study these parameters, the macro- and micro-texture of the tubes were investigated. Using macro-texture, different crystallographical orientations can be compared before and after drawing and it can be investigated, whether the tilting creates different texture. Micro-texture was studied to be able to detect the possible texture inhomogeneity through the wall-thickness of the tubes.

Three methods for texture analysis were used in this work: Neutron and synchrotron diffraction methods for macro-texture measurements, and electron diffraction method for micro-texture measurement. Since the as-received tubes had a coarse grain size, the macro-texture of the as-received samples were measured using the neutron diffraction method. The drawn tubes were measured by the synchrotron method. Micro-texture measurements were performed by electron diffraction method (EBSD).

6.2 Macro-texture data

6.2.1 As-received tube and tubes after the first drawing step

In the neutron diffraction techniques, the initial output of the investigation is the diffracted intensity or a profile of diffracted intensities, which characterize a sufficient volume of the sample. $\{111\}$, $\{200\}$ and $\{220\}$ Pole Figures (PFs) at *Max* and *Min* sides of the as-received tube are shown in **Fig. 6.1-a** and **b**, respectively. It should be mentioned that these PFs are plotted after volume and anisotropic absorption corrections (for more information see [214]) and they represent the global texture of the samples. As can be seen in Fig. 6.1-a, the PFs exhibit on both sides of the as-received tube the same shape and almost the same PF density.

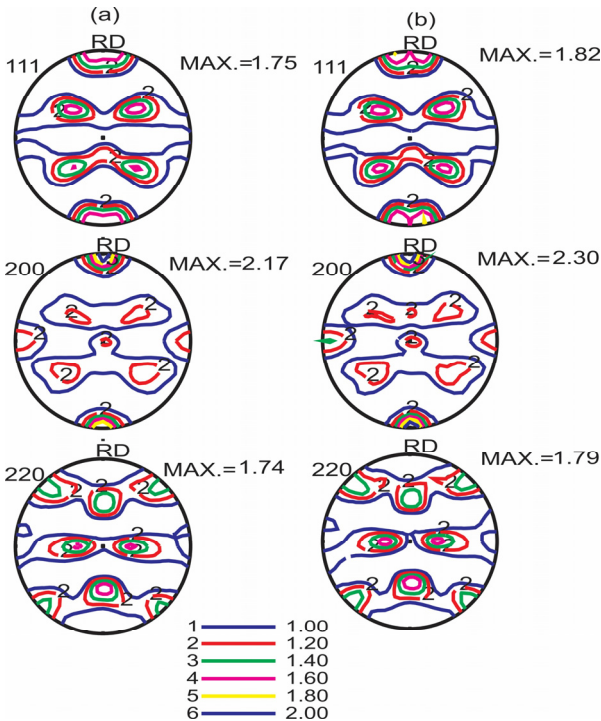


Fig. 6.1 $\{111\}$, $\{200\}$, and $\{220\}$ PFs at (a) *Max* and (b) *Min* side of the as-received tubes.

Comparing $\{111\}$ PFs at *Max* and *Min* sides of the as-received tube with the results of heat-treated copper samples at 400°C , done by Suwas et al. (2002) [230], **Fig. 6.2**, it can be seen that the shape of the PFs are the same and in

both figures, the cube component (also called cube texture or cube orientation) $\{001\} \langle 100 \rangle$, is the most dominant one (Fig. 6.2-b), which is the characteristic of a recrystallization texture in materials with a medium to high Stacking Fault Energy (*SFE*), such as Al, Ni, and Cu [231]. The shown deformed and heat-treated PF, which demonstrates a cube texture, is due to the cube-oriented nuclei from the bandlike structure, which are mainly deformed grains with retained cube orientation. These orientations mainly will be prevailed during the subsequent deformation process, due to their optimum growth conditions into the deformation texture [232].

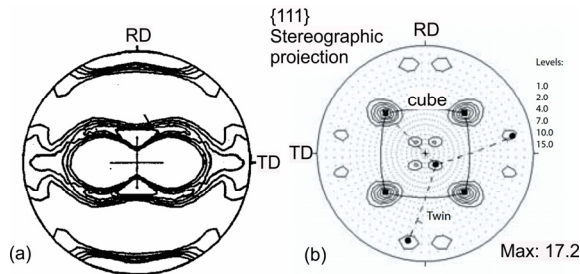


Fig. 6.2 (a) $\{111\}$ PF of Cu after heat treatment at 400 °C [230]. (b) Cube component in recrystallization texture of Cu [231].

Twin orientations can be seen in PFs of the as-received tube, as well. These twinning are also visible by microstructural investigation done on these samples (already presented in Fig. 3.2). However, this twin orientation is not strong as the cube orientation, which is mainly due to the alloying elements in Cu-DHP. These alloying elements reduce the *SFE* which interfere with the formation of twin component [233].

Al-Hamndany has also studied the PFs in heat-treated copper tubes. **Fig. 6.3** shows the $\{111\}$, $\{200\}$ and $\{220\}$ PFs after heat-treatment of the tubes, exhibiting the same PF shape for all three directions [214].

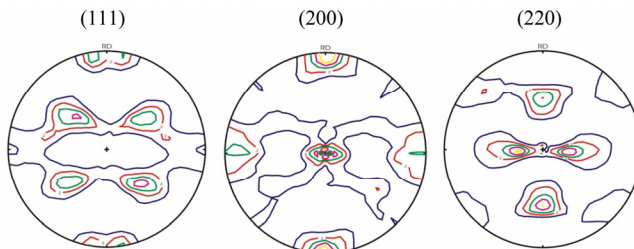


Fig. 6.3 $\{111\}$, $\{200\}$, and $\{220\}$ PFs of heat-treated copper tube after volume and anisotropic absorption corrections [214].

Using the three PFs $\{111\}$, $\{200\}$ and $\{220\}$ the ODF φ_2 sections of the as-received samples at *Max* and *Min* sides were calculated. The iterative series expansion method was used with $L_{Max} = 23$. Fig. 6.4-a and b show the calculated ODF sections for different φ_2 angles at *Max* and *Min* sides, respectively. Due to the lower sample symmetry, triclinic sample symmetry was used for calculations. Normally, the ODF density is presented as mrd^1 , which is in respect to the distribution expected in a material with uniformly distributed orientations. In deformation processes, the most important components, which are *cube*, copper (*Cu*), and brass (*Bs*), are visible in sections 0° and 45° . Therefore, mainly in most of cases only these two sections are discussed.

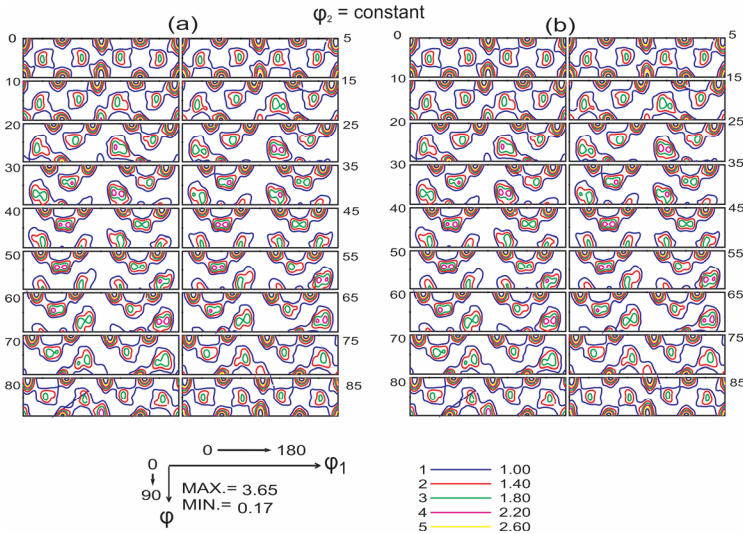


Fig. 6.4 The ODF sections of the as-received tube at (a) *Max* and (b) *Min* sides for different φ_2 angles. (c) ODF section 0° and 45° Sections of ODFs, which mostly are discussed in deformation processes.

Since the biggest effort was made to investigate the texture in rolled samples and the most analyzed material was copper and its alloys, the type of deformation texture is normally defined by terms such as rolling texture and copper-type and alloy-type. This categorization is due to the *SFE* and its effects on the deformation mechanisms, most importantly the deformation twinning. Pure metals, such as aluminum, copper, nickel, with a medium to high *SFE* mostly show a copper-type texture (which is also called pure-type). Having alloying elements, such as in brass or austenitic steel, the *SFE* will be lower, and this reveals an alloy-type texture. In these materials, deformation twinning

¹ multiples of random distribution

exists and causes subsequent massive shear band formation changing the deformation texture evolution [234]. The ODFs of pure copper and brass (Cu-37%Zn) are shown in **Fig. 6.5-a** and **b**, respectively. To describe the ODFs, most researchers use the ideal components (or orientations), such as *Cu* orientation $\{112\} \langle 111 \rangle$, brass orientation (*Bs*) $\{011\} \langle 211 \rangle$, and *S* orientation $\{123\} \langle 634 \rangle$. These orientations are given with their Euler angles in **Table 6.1** [231].

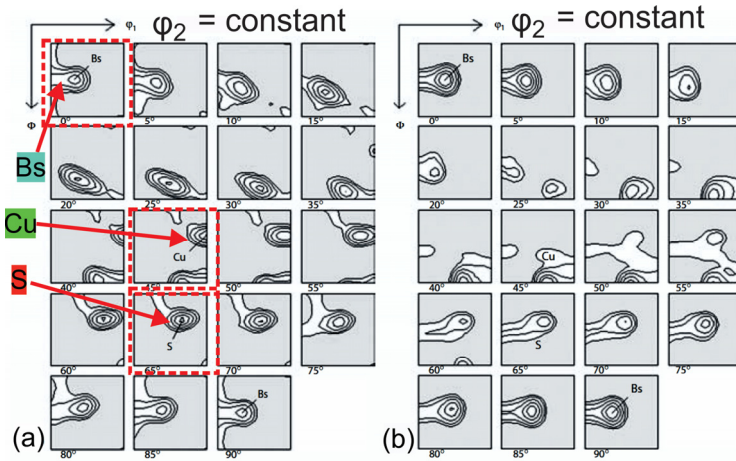


Fig. 6.5 Rolling texture of (a) pure copper, showing metal-type or pure-type ODF and (b) brass (Cu-37%Zn) showing alloy-type ODF [235].

Table 6.1 The most important orientations of Cu and Cu alloys after deformation with their Euler Angles and Miller indices [231].

Orientation	Miller indices {hkl}<uvw>	Euler angles φ_1, Φ_2	
		first var.	second var.
<i>Goss</i>	$\{011\} \langle 100 \rangle$	first var.	$0^\circ 45^\circ 0^\circ$
		second var.	$90^\circ 90^\circ 45^\circ$
		3 rd var.	$0^\circ 45^\circ 90^\circ$
<i>S</i>	$\{123\} \langle 634 \rangle$	$59^\circ 34^\circ 65^\circ$	
<i>Bs</i>	$\{011\} \langle 211 \rangle$	first var.	$35^\circ 45^\circ 0^\circ$
		second var.	$55^\circ 90^\circ 45^\circ$
		3 rd var.	$35^\circ 45^\circ 90^\circ$
<i>Cu</i>	$\{112\} \langle 111 \rangle$	first var.	$90^\circ 30^\circ 45^\circ$
<i>Cube</i>	$\{001\} \langle 100 \rangle$	first var.	$45^\circ 0^\circ 45^\circ$
		second var.	$135^\circ 0^\circ 45^\circ$
		3 rd var.	$225^\circ 0^\circ 45^\circ$
		5 th var.	$270^\circ 0^\circ 45^\circ$
		6 th var.	$315^\circ 0^\circ 45^\circ$

The 0° and 45° section of the achieved ODF are shown in **Fig. 6.6-a** and **b** for *Max* and *Min* sides, respectively. At the 0° section of the ODF of the as-received tube at both *Max* or *Min* sides, ten *cube* and four *Bs* components can be detected. The 45° section - Fig. 6.6-b - presents the *Cu* and *Bs* orientations. The *Bs* component in the 0° section and *Cu* component in the 45° section can be found also in the rolling texture of pure copper, which is illustrated in Fig. 6.5-a. The *S* component could be found in the 65° section (Fig. 6.4-a and b), which is almost in the same visual position as the *Cu* component in the 45° section [235].

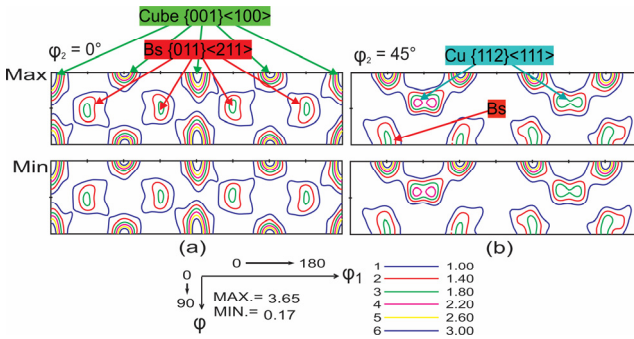


Fig. 6.6 The (a) 0° and (b) 45° ODF sections of the as-received tube at *Max* and *Min* sides of the as-received tube.

The $\{111\}$, $\{200\}$ and $\{220\}$ PFs of the samples drawn with -5° tilting angle at *Max* side of the tube are shown in **Fig. 6.7-a** to **c**. Comparing these PFs with the as-received tubes shows that the *cube* orientation, which was the dominant orientation in the as-received tube, almost disappeared due to their optimum growth conditions into the deformation texture. Moreover, it can be seen that, the *Cu* orientation has become the main orientation.

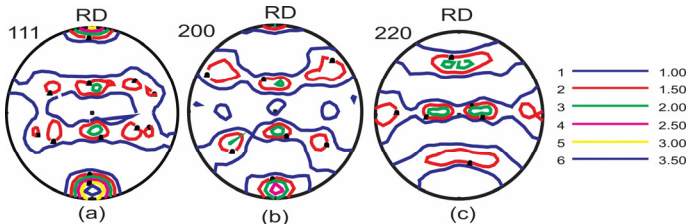


Fig. 6.7 The $\{111\}$, $\{200\}$ and $\{220\}$ PFs of the *Max* side of the tube drawn with -5° tilting angle.

Comparing the $\{111\}$, $\{200\}$ and $\{220\}$ PFs at the *Max* and *Min* sides of the same tube, which is presented in **Fig. 6.8**, shows that both sides have almost same PFs in all three planes. The only minor difference between these two

sides is that the *cube* component at *Min* side disappeared completely, nevertheless, at *Max* side there is still some cube components. This matter is because of different amount of deformation at these two sides. The PF densities of both sides are almost same.

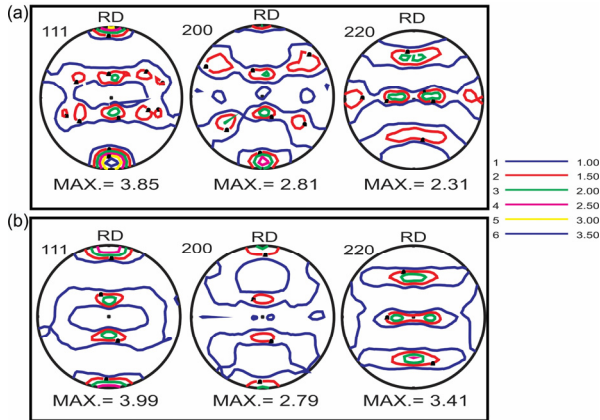


Fig. 6.8 The $\{111\}$, $\{200\}$ and $\{220\}$ PFs at the *Max* and *Min* sides of the tube drawn with -5° tilting angle.

Same comparison between *Max* and *Min* sides are done for tubes drawn with $+5^\circ$ tilting angle, see Fig. 6.9-a and b. As above, no significant difference observed between the both sides of the tube. One can see the same components as the tube drawn with -5° tilting.

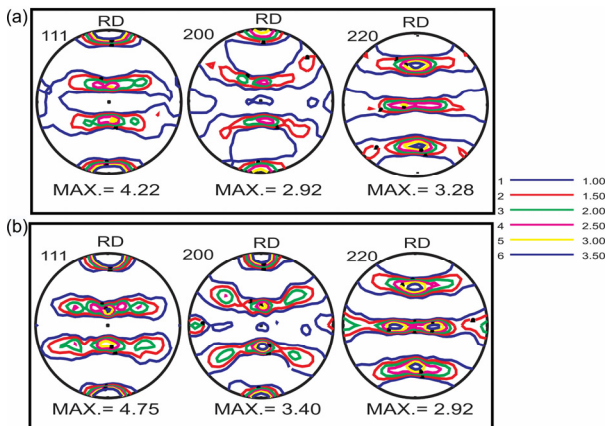


Fig. 6.9 The $\{111\}$, $\{200\}$ and $\{220\}$ PFs at the *Max* side of the tubes with (a) -5° and (b) $+5^\circ$ tilting angle.

The $\varphi_2 = 45^\circ$ ODF sections at *Max* and *Min* sides of the drawn tube with -5° tilting angle are shown in **Fig. 6.10-a** and **b**, respectively. These ODFs show the dissipation of the *cube* component, same as PF results. The *Cu* orientation is major one with a *cube* orientation being weaker compared to the as-received tube. The ODF densities at *Max* and *Min* sides, however, are slightly different, being at *Max* higher.

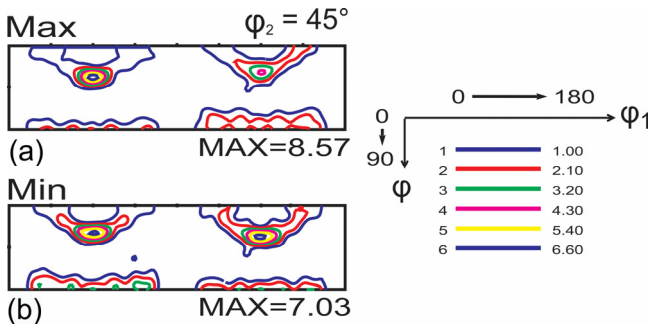


Fig. 6.10 45° ODF of (a) *Max* and (b) *Min* sides of the tube drawn with -5° tilting angle

The texture gradient in the samples itself is another parameter which causes inhomogeneity through the wall-thickness, and therefore it is interesting to analyze. Using the synchrotron method, it was possible to measure different points through the thickness of each sample and investigate the variation of the ODF density through the thickness. **Fig. 6.11-a** presents the measurement points through the wall-thickness of the tube starting from the outer surface to the inner surface.

Looking at *Cu* and *cube* components through the wall-thickness of the *Max* and *Min* sides of the as-received tube (**Fig. 6.11-b**), shows that, same as PF results, the *cube* component is the most dominant component in the as-received tube. However, it varies over the thickness. The highest density of the *cube* component can be found on the outer surface. Nevertheless, the density of this component is at *Max* and *Min* sides almost the same. The *Cu* component, on the other hand, is almost constant through the wall-thickness, having same density at *Max* and *Min*, same as the *cube* component.

Together with the *Cu* and *cube* components, the *Bs* and Goss components vary slightly over the thickness. **Fig. 6.11-c** and **d** show the variation of four different components over the thickness for the *Max* and *Min* sides of the tube, respectively. The Goss component has the lowest ODF density and the *cube* one the highest. The *Cu* and *Bs* components do not change significantly over the wall-thickness.

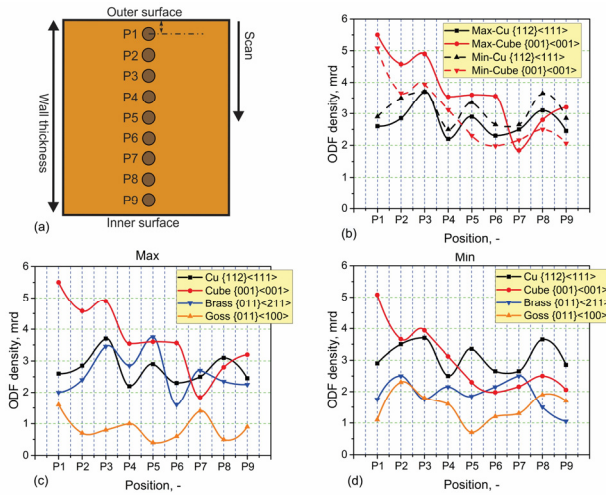


Fig. 6.11 (a) Measurement points through wall-thickness of the tube. (b) Comparison of the *Cu* and cube components at *Max* and *Min* sides of the as-received tube. (c) and (d) Variation of four main components at *Max* and *Min* sides of the as-received tube.

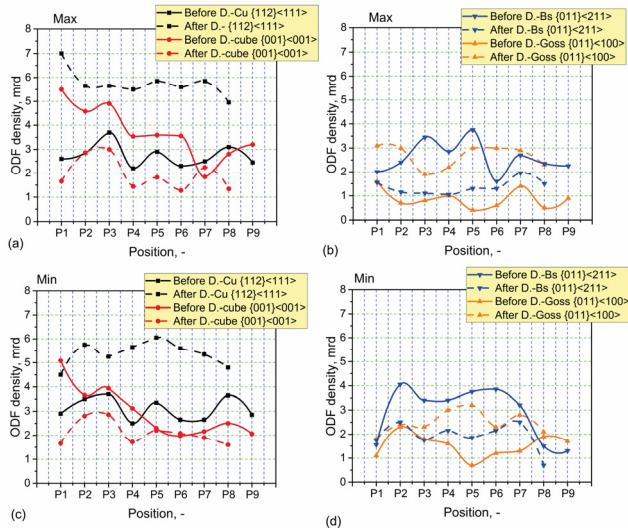


Fig. 6.12 Variation of the main components *Cu*, cube, Goss, and *Bs* before and after drawing at (a and b) *Max* and (c and d) *Min* side of the tube. P1 to P9 are the measurement points, which are shown in Fig. 6.11.

Comparing the ODF density of the four main components before and after drawing with -5° tilting at *Max side* of the tube, see **Fig. 6.12**, shows that the *Cu* component has significantly increased (Fig. 6.12-a), but the *cube* component has decreased after drawing. These components do not vary significantly over the wall-thickness. Variation of the *Bs* and Goss components are shown in Fig. 6.12-b. The *Bs* component has decreased after drawing, but the Goss component has increased. Same comparison for the *Min* side of the tube is presented in Fig. 6.12-c, which compares the *Cu* and *cube* components variations. Fig. 6.12-d shows the variation of the *Bs* and Goss components. It can be concluded, apart from some minor differences between *Max* and *Min* sides, after drawing there is no significant texture gradient through the wall-thickness.

6.2.2 After second drawing step

The macro-textures of the tubes were studied after the second drawing step, as well. **Fig. 6.13-a** and **b** show the $\{111\}$ PFs at *Max* and *Min* position of the tubes drawn with -5° tilting angle, respectively. As can be seen, at *Max* the PF density was considerably increased, which is due to the higher deformation happening. On the other hand, tilting causes a directional mass flow from one side of the tube to the other side creating an asymmetrical texture development comparing *Max* and *Min*.

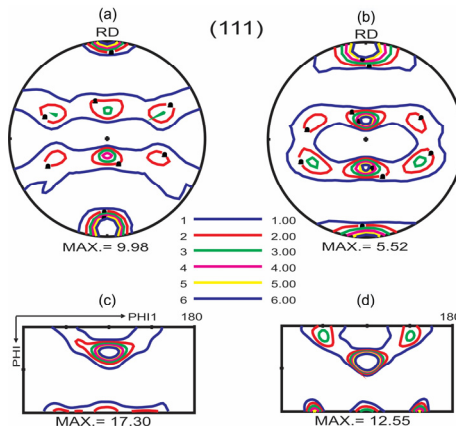


Fig. 6.13 $\{111\}$ PFs of drawn tube after second drawing step at (a) *Max* and (b) *Min* sides of the tube. 45° section of ODF in the same sample at (c) *Max* and (d) *Min*. Because of the symmetry in the ODF, only $0 < \phi_1 < 180$ is presented.

As for first drawing step, the *Cu* component is the dominant one. Comparing the ODFs of *Max* and *Min* - because of symmetry only $0 < \phi_1 < 180$ is

presented - shows that the same behavior as after the first drawing step and also for the PFs after the second drawing step, the Cu orientation is the dominant one. Moreover, the ODF density is significantly increased compared to the as-received tube as well as after the first drawing step.

Fig. 6.14-a to **c** show the variation of the ODF density for different components in the as-received tube, after the first, and after the second drawing step through the wall-thickness at Max side of the tube drawn with -5° tilting. As discussed above, after each drawing step the Cu component changes significantly and its density increases, see Fig. 6.14-a. The cube and Bs components decreased after the second drawing step (Fig. 6.14-b and c), nevertheless, the Goss component increased (Fig. 6.14-d), same as in the first drawing step.

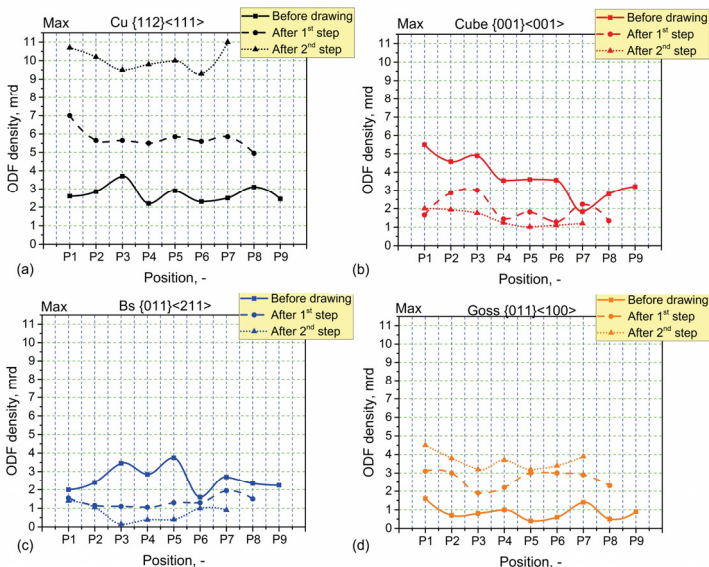


Fig. 6.14 Different components through the wall-thickness of the tube at Max side before and after drawing; (a) Cu , (b) cube, (c) Bs , and (d) Goss components.

6.3 Micro-texture

A major difference between macro-texture techniques (mainly synchrotron and neutron diffraction methods) and micro-texture techniques is the scale of the investigation, which influences the nature of the achieved results. As stated by Wilkinson and Hirsch (1977), who reviewed the electron diffraction based techniques by SEM of bulk materials [236], to characterize the local micro-texture (local crystallography) of materials, SEM is a powerful instrument and

among three main SEM based techniques - electron channeling patterns, electron channeling contrast imaging, and electron backscatter diffraction -, the last one is one of the mostly used methods. It has become a universal method to measure the micro-texture in materials [237]. In micro-texture techniques, a diffraction pattern is analyzed, which for a majority of techniques this pattern is Kikuchi diffraction pattern. These patterns represent a complete information about the crystallographic structure of materials, including their orientations [236].

A Kikuchi pattern could be achieved by different techniques, such as [238]:

- SAD¹ (also called SAC²) in SEM and TEM
- EBSD in SEM
- CBED³ in TEM

Analyzing the Kikuchi pattern is a time-consuming task, which nowadays is done by commercially available software packages, being a huge advantage for this technique. The formation Kikuchi pattern is well described by Engler and Randle in [237].

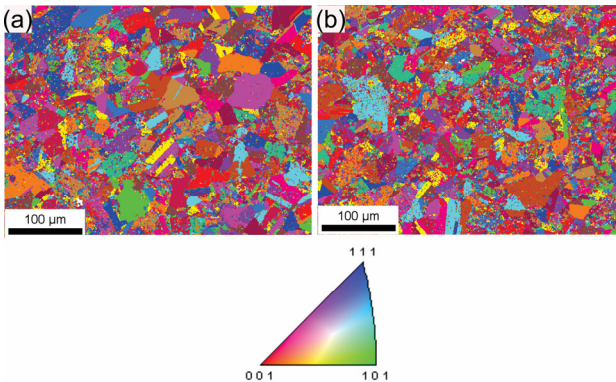


Fig. 6.15 Micrograph of the *Max* (a) and *Min* (b) sides of the as-received tube.

Fig. 6.15-a and **b** show the micrographs of the *Max* and *Min* sides of the tube before drawing, respectively. One can see the grains and different orientations of various grains. No significant difference is notable between *Max* and *Min* sides of the as-received tube. The color pattern of the micrographs shows that there is no dominant orientation and different grains have diverse orientations. These tubes were drawn with tilting angles of 0° and -5°. The micrographs of

¹ Selected Area Diffraction

² Selected Area Channeling

³ Convergent Beam Electron Diffraction

the drawn tubes at the *Max* side after the first drawing step are shown **Fig. 6.16-a** and **b**, respectively. No significant effect on the micro-texture could be stated for the two conditions of drawing.

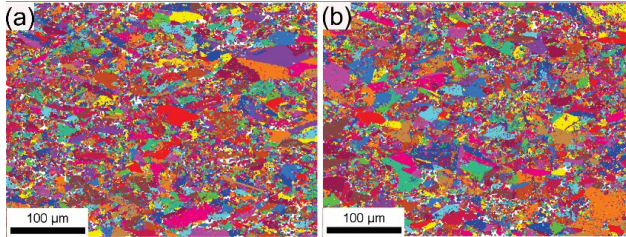


Fig. 6.16 Micro-textures of the drawn tubes at *Max* side with (a) 0° tilting and (b) -5° tilting angle. The legend of these micrographs is same as Fig. 6.15.

The $\{111\}$, $\{100\}$, and $\{110\}$ PFs of the as-received tube at *Min* side is shown in **Fig. 6.17-a** to **c**, respectively. The *cube* component is the only dominant component to be detected in these PFs. The maximum intensity of these PFs was about 1.78, which is a quite weak density.

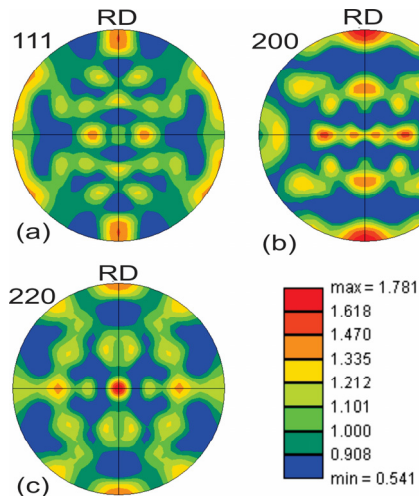


Fig. 6.17 (a) $\{111\}$, (b) $\{100\}$, and (c) $\{110\}$ PFs of the as-received tubes at *Min* side. The maximum intensity of PFs is approx. 1.78.

Comparing the $\{111\}$, $\{100\}$, and $\{110\}$ PFs of the drawn tubes after second drawing step with 0° and -5° tilting angles at *Min* side of the tube, which are shown in **Fig. 6.18** and **Fig. 6.19**, respectively, shows also no remarkable difference between tilting and standard drawing. The only noticeable difference

is the maximum intensity of the PFs, which is increased in case of -5° tilting compared to the standard drawn tubes. As macro-texture, no major differences was detected in case of micro-texture, either.

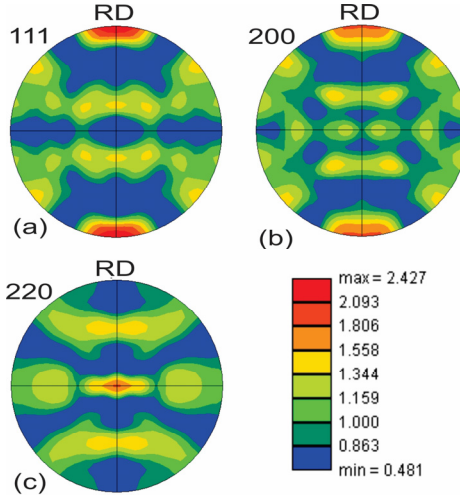


Fig. 6.18 (a) $\{111\}$, (b) $\{100\}$, and (c) $\{110\}$ PFs of the standard drawn tubes after second drawing step at Min . The maximum intensity of PFs is approx. 2.42.

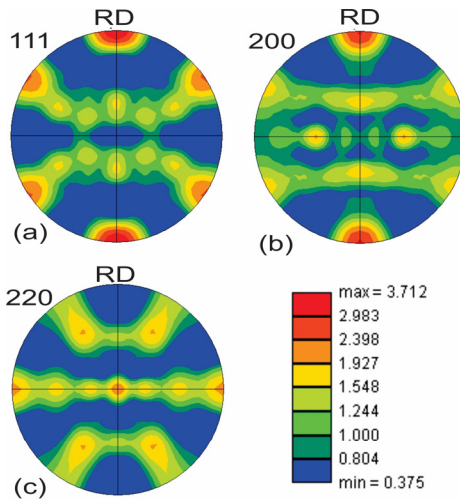


Fig. 6.19 (a) $\{111\}$, (b) $\{100\}$, and (c) $\{110\}$ PFs of the drawn tubes with -5° tilting angle after second drawing step at Min . The maximum intensity of PFs is approx. 3.71.

6.4 Conclusion

In this chapter, the evolutions of the macro- and micro-texture of the copper tubes, which were drawn with -5° tilting angles, were presented and discussed. The main aim of texture measurement was to understand how the tilting affects the texture evolution of the tubes, and whether there is a significant difference in texture of the drawn tubes with and without tilting. Macro-texture of the tubes – before and after drawings – were analyzed using neutron and synchrotron diffraction methods. The micro-texture of the samples, however, was studied by electron diffraction method. Texture was analyzed in both *Max* and *Min* sides of the tubes.

Comparing the {111}, {200} and {220} PFs at *Max* and *Min* side shows no significant difference between them. The PF density of these two sides are also almost same. The most dominant orientation in the as-received tube was the *cube* orientation, which is due to the performed heat-treatment on the as-received copper tubes. The $\varphi_2 = 0^\circ$ ODF section of the as-received tube has shown the *cube* orientation as well as the *Bs* one. The $\varphi_2 = 45^\circ$ section, however, exhibited the *Cu* orientation as well. The *S* orientation was also visible in the $\varphi_2 = 65^\circ$ section.

After drawing with -5° tilting, *cube* component almost disappeared, which is due to its optimum growth condition into the deformation texture. On the other hand, the *Cu* component has increased significantly. At both *Max* and *Min* sides of the tube. The {111}, {200} and {220} PFs of the drawn tubes with -5° tilting at *Max* and *Min* sides, showed no major difference. The only minor difference between these two sides is that the *cube* component at *Min* side disappeared completely, nevertheless, at *Max* side there are still some cube components.

Concerning the gradient of different components over the wall-thickness in the as-received tube, the cube component was the most dominant one at both *Max* and *Min* sides of the as-received, varying strongly through the wall-thickness of the tube. However, there was no significant difference between the *Max* and *Min* sides through the wall-thickness and cube component's variation through the wall-thickness was same for both sides. The *Cu*, Goss and *Bs* components were more or less constant through the wall-thickness of the *Max* and *Min* sides of the as-received tube.

After first drawing step with -5° tilting angle, the ODF intensity of the cube and *Bs* components were reduced, however, this reduction was in the case of the *cube* component very significant. *Cu* and Goss components were increased, *Cu* being strongly affected. Same as for the first drawing, the second drawing showed the same tendencies.

Micro-textures of the as-received and drawn tubes were studied using the EBSD method. Results of EBSD analyses of the as-received tubes has shown no significant difference between the micro-texture of the *Max* and *Min* sides. EBSD results of the drawn tubes with -5° and 0° tilting showed no significant difference in micro-texture of the tubes after drawing with different tilting angles. The only difference in their micro-texture was the higher PF density in case of the drawn tubes with -5° tilting, which was about 3.71, compared to the 2.42 for the standard drawn tube.

It can be finally concluded that, except some minor differences between the texture evolution of the drawn tubes with and without tilting, there is no significant differences between them and no additional orientation is created because of the introduction of tilting. The measured textures of the as-received tubes are used as input for the developed simulation model and the experimentally measured results of the drawn tubes (with -5°) used for the validation of the simulation results, which are discussed in next chapter.

Chapter 7 Multiscale simulation

7.1 Introduction

As discussed in Chapter 1, tube drawing investigations with different tilting/offset values on materials of different qualities with different starting RSs and initial textures are time and cost intensive. Moreover, not all combination can be studied experimentally. To overcome this problem and also to have a better understanding of the process, it was decided to develop a simulation model containing all relevant properties of the as-received materials – such as eccentricity, RSs, initial texture, mechanical properties – and therewith analyzing more complex situations. Moreover, using the developed model, it was possible to compare the texture evolution of the drawn tubes with and without titling, without performing time consuming neutron, synchrotron, or electron measurements. For this reason, a multiscale simulation approach based on the Integrated Computational Material Engineering (ICME) was used.

In this chapter, the results of the developed multiscale simulation are introduced and discussed. This methodology starts with electronic scale calculations, which is done using the Density Function Theory (DFT) approach using the Quantum Espresso software. The most important parameter in this simulation length is the *GSE*. After achieving the required data, these data are bridged to the next simulation scale, the atomic scale calculation, using the Modified Embedded Atom Method (MEAM), and Molecular Dynamics (MD): the anisotropic elastic constants of copper and dislocation mobility are calculated. The DD approach is used in the next simulation scale, i.e. microscale simulations, and hardening parameters in Palm-Voce hardening equation are computed. These parameters along with the measured texture are used in Crystal Plasticity (CP) simulations to be imported in the FEM model, which was created for the tube drawing process. RSs, measured by neutron diffraction, are also imported to the FEM model. The simulation results are validated using the measured RSs, texture, and mechanical properties gained by tension testing. This methodology to achieve all the necessary parameters for the final FEM simulations is sketched in **Fig. 7.1**.

In this chapter, the development of the model is described starting from the electronic scale going up to structural scale simulation (FEM). At each scale, initially the simulation setup is introduced and then the achieved results are presented. Finally, at each scale, the upscaled results to the upper – next - simulation scale are introduced.

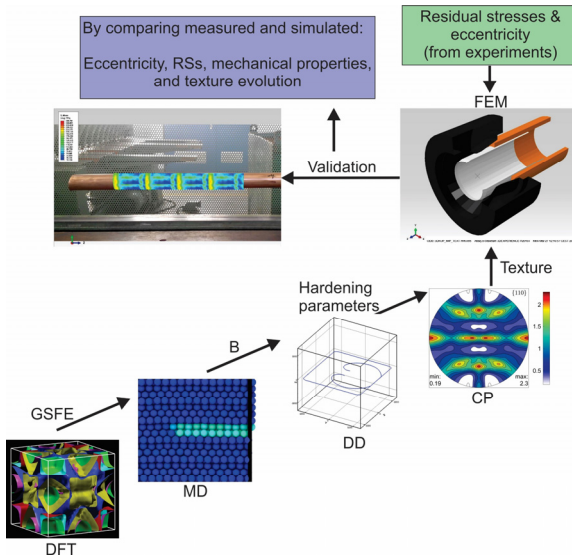


Fig. 7.1 Schematic presentation of the multiscale methodology which was used in this work to simulate the tube drawing process.

7.2 Electronic scale simulations

7.2.1 Simulation setup at the electronic scale

As mentioned in “3.7.1 - *Bridge 1, DFT calculation*”, the electronic scale simulation was done using the DFT approach by Quantum Espresso software. The main parameters calculated in this simulation scale were: The lattice parameter, the energy of crystal lattice by variation of the lattice parameter, the bulk modulus, and, most importantly, the *GSFE*. The setup, which has been chosen for the simulation, was an *fcc* structure with an initial guess for the lattice parameter of copper, which was 6.824 Bohr or 3.61 Å. The method used for electrons' occupation was the electron smearing method. This technique allows for electrons to have a fractional occupation number by creating an energy window [239]. Another important parameter was the *K*-point, which can be considered as mesh, and controls the “good sampling” of the occupied manifold. To find the optimum *K*-point value, different *K*-points were used, and the results were compared. The parameters used are listed in **Table 7.1**.

7.2.2 Electronic scale simulation results

The variation of the lattice parameter and bulk modulus of copper as a function of the *K*-point is shown in **Fig. 7.2-a**. As can be seen, by increasing the *K*-point value, the lattice parameter and bulk modulus vary up to a point from where

they remain constant. By increasing the K -point, the simulation time increases as well. For this reason, the smallest K -point giving a stable result was chosen. This K -point was used for energy variation and $GSFE$ calculations. Fig. 7.2-b shows the variation of the energy of fcc copper crystal structure by variation of the lattice parameter. The minimum energy is achieved for a lattice parameter of 3.607 Å.

Table 7.1 Input parameter used for electronic scale simulation.

Parameter	Value	Source
Crystal structure	fcc	-
Cell dimension	6.824 Bohr / 3.61 Å	[240]
E_{cut}	30 Ry ¹ / 408 eV ²	[241]
Occupation	Smearing	[239]
Atomic weight	63.54 g/mol	[240]
Pseudopotential ³	-	[219]
K -point	2 - 20	-
Cohesive energy	3.49 eV/atom	[242]

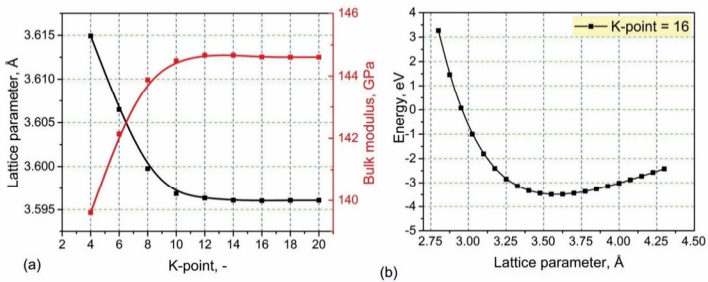


Fig. 7.2 (a) Variations of lattice parameter and bulk modulus of copper as a function of k -point mesh. (b) Energy changes by changing the lattice parameter of copper.

Before presenting the calculated $GSFE$, it is worth talking about the perfect and partial dislocations in fcc crystal. In fcc metals, $1/2 < 110 >$ and $< 001 >$ vectors are the shortest lattice vector, and therefore the best fitting Burgers vector for dislocation. The energy of the dislocation is a function of the Burgers vector, which itself is a function of the vector length. Since the energy of the $1/2 < 110 >$ dislocation is less than the one of the $< 001 >$, the $< 001 >$ is much less favored energetically and rarely observed. $1/2 < 110 >$ is a translation vector and if a dislocation glides with this Burgers vector, it will leave a perfect crystal and the dislocation will be a perfect dislocation [see Eq. (7.1)] [174]. As an example, the $1/2[110]$ edge dislocation is shown in **Fig. 7.3-a**, in

¹ Rydberg constant (1 Ry = 13.605 eV)

² Electronvolt

³ Cu.pbcsol-dn-kjpaw_psl.0.2.UPF

which the (110) planes are perpendicular to the Burgers vector and have a $ABAB \dots$ stacking sequence. However, an imperfect crystal containing a stacking fault could be developed by the motion of a dislocation whose Burgers vector is not a lattice vector. When this stacking fault ends in the crystal, it creates a partial dislocation which is the boundary between the faulted and the perfect regions. This partial dislocation is due to the splitting of a perfect dislocation into two dislocations, which is called dissociation of the dislocation; it is according to Eq. (7.3). In fcc materials, Shockley [see Eq. (7.2)] and Frank are two most recognized partial dislocations [243].

$$\text{Perfect} \left(b = \frac{1}{2} \langle 110 \rangle \right) : b^2 = \frac{a^2}{4} (1^2 + 1^2 + 0^2) = \frac{a^2}{4}. \quad (7.1)$$

$$\text{Shockley} \left(b = \frac{1}{6} \langle 112 \rangle \right) : b^2 = \frac{a^2}{36} (1^2 + 1^2 + 2^2) = \frac{a^2}{6}, \quad (7.2)$$

$$\frac{1}{2} \langle 110 \rangle \rightarrow \frac{1}{6} \langle 211 \rangle + \frac{1}{6} \langle 1\bar{2}\bar{1} \rangle. \quad (7.3)$$

The formation of a Shockley dislocation is shown in Fig. 7.3-b, which represents the position of atoms in a $(10\bar{1})$ plane. In this figure, the filled circles show the position of atoms in the $(10\bar{1})$ plane and filled circle the atoms in the $(10\bar{1})$ planes, directly above and below the plane of the diagram. The right side of the diagram shows a perfect lattice with a $ABCAB \dots$ stacking sequence, while, on the left side, a B layer was created from the slipping of the A layer of atoms above LM in the $[1\bar{2}1]$ direction. In the same manner, the B atoms slipped to C and C to A , which has produced a stacking fault and a partial dislocation [244].

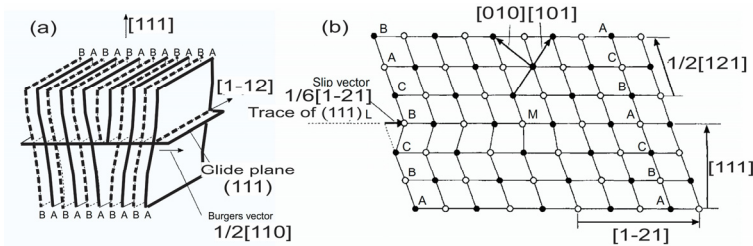


Fig. 7.3 Edge dislocation in a fcc crystal [174], (b) formation of stacking fault and partial Shockley dislocation [244].

The calculated $GSFE$ of copper along with a perfect dislocation - along $(111)[110]$ - is shown in Fig. 7.4-a. The optimum K -point, achieved in the previous step, was used for these calculations. Other parameters were the same as used in the energy calculation. Calculated $GSFE$ s of copper along the same direction by other researchers are shown in the same graph. For a perfect stacking the $GSFE$ is zero, while for an intrinsic stacking fault the $GSFE$ will reach

a maximum. Considering the dislocation processes in copper and their atomistic simulation, this matter was discussed by Vegge and Jacobsen (2002) [245]. Their calculated values for copper for these three components of SFE are shown in **Fig. 7.5**. Crampin et al (1990) [246] calculated the contribution of the intrinsic, extrinsic and twin fault energy in the whole stacking fault energy for some ideal close packed metals.

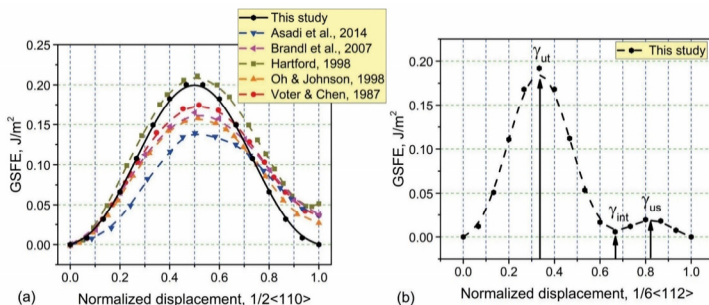


Fig. 7.4 Variation of $GSFE$ along the (a) $\langle 110 \rangle$ and (b) $\langle 112 \rangle$ directions. γ_{ut} is the unstable twinning stacking fault energy, γ_{int} is the intrinsic stacking fault energy, and the γ_{us} is the extrinsic or unstable stacking fault energy.

Back to our results (Fig. 7.4-a), the calculated values in this work are in good agreement with the results of Hartford (1998) [247]. Calculated values by Asadi et al. (2014) [248], Brandl et al. (2007) [249], Oh and Johnson (1998) [250], and Voter and Chen (1987) [251] are also shown in Fig. 7.4-a, which have some deviations with the values calculated in this work. Fig. 7.4-b shows the variation of the $GFSE$ along $(111)[112]$ with three main points: γ_{ut} , which is the unstable twinning stacking fault energy, γ_{int} , the intrinsic SFE, and γ_{us} , the unstable stacking fault energy (also known as extrinsic SFE).

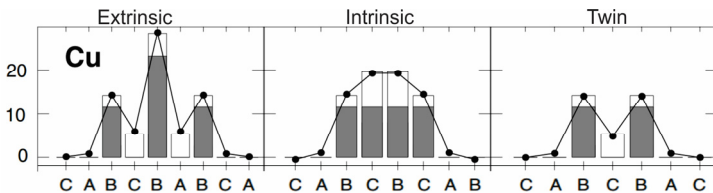


Fig. 7.5 Layer-by-layer energy contributions to the extrinsic, intrinsic, and twin stacking fault energies [245].

7.2.3 Electronic scale to atomic scale bridging

After calculating the above-mentioned parameters, they were used for atomic scale simulations. The energy variation as a function of lattice parameter as well

as the partial and perfect *GSFEs* were bridged to the next level and used as calibration parameters.

7.3 Atomic scale simulations

At this simulation scale, the MEAM and MD approaches were used. MEAM, to calculate the elastic constants and to develop the necessary potentials for the MD calculations, and MD, to calculate the drag coefficient (dislocation mobility), bridged to the microscale simulations (DD).

7.3.1 Material parameters at atomic scale

As mentioned in "2.6.4.1 - *Modified embedded atom method*", MEAM has an advantage to EAM calculations due to considering the angular force dependency. As stated by Jelinek et al. (2007) [182], the calculated SFE and elastic constants with MEAM potentials are in better agreement with the experimental results. A dissociation of a perfect dislocation into the partial dislocations (Shockley dislocations) is significantly controlled by these two parameters.

Peierls stress (also called Peierls-Nabarro stress) is the applied shear stress, required to make a dislocation glide without having the temperature (at 0 K). The Peierls stress is different to the yield stress and gives rise to micro-plasticity under stresses much smaller than the yield stress [252]. In metals, which has a low Peierls stress, such as *Al* and *Cu*, the drag is the main mechanism controlling the movement of the screw and edge dislocation [253]. In MD calculations, the most important simplifying factor assumed was that the edge and screw dislocation move with the same velocity (mobility). There are some studies, nevertheless, showing that the edge dislocation has a smaller mobility (or drag coefficient) than the screw dislocation – e.g. Olmsted et al. (2005) [254].

In our work, the MD simulation was done at 300 K and a simulation box was created for copper with the *fcc* crystal structure and a size of 100 x 60 x 2 lattice vectors having an edge dislocation. The lattice parameter of copper was taken from the DFT calculations. The simulation box contained almost 70,000 copper atoms, the smallest box possible, where the simulation results became independent of the size. This simulation box was oriented along the [100], [010], and [001] directions. Different shear stresses, starting from 20 MPa going up to 350 MPa, were applied on the top and the bottom surfaces of this simulation box. Dislocation was created after a time step of 0.01 s, which the energy minimization of the system happened. The centrosymmetry value was used to locate the dislocation core. The dislocation mobility was obtained by slip plane gliding. The centrosymmetry value, which was defined by Kelchner et al (1998) [255] is zero for centrosymmetric materials (such as *fcc* materials) when the

material experiences any homogenous elastic deformation, and it is nonzero when any plastic (nonelastic) deformation happens to the material. In solid-state systems, the centrosymmetry parameter is a useful measure of the local lattice disorder around an atom. It can be used to characterize whether the atom is part of a perfect lattice, a local defect (e.g. a dislocation or stacking fault), or at a surface [222]. In our work, only the steady state velocity of dislocation was considered and the other two parts, transient stage and acceleration, were not taken into account. **Fig. 7.6** shows the created dislocation in the simulation box of MD calculations.

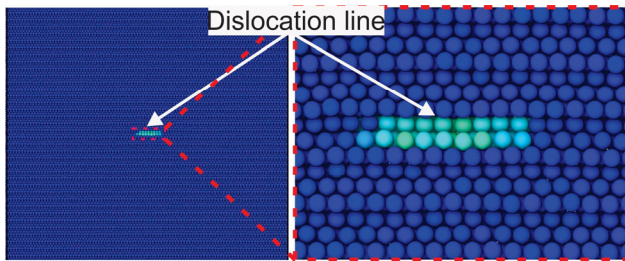


Fig. 7.6 Dislocation in the simulation box, which was created for MD simulations.

7.3.2 Results of atomic simulations

7.3.2.1 Modified embedded atom method

Using the *MPC* routine [256, 257], the initial energy variation as a function of lattice parameter was calculated for a copper atom, having *fcc*, *bcc*, and *hcp* crystal structures. Since a dislocation is the part of the crystal having other crystal structure, it was necessary to have energy variations of the *bcc* and *hcp* crystal structures, as well. *GSFE* as well as elastic constants for copper were calculated using MEAM.

Before creating the required potential for MD calculations, the results were calibrated. The calculated energy of different crystal structures by MEAM is shown in **Fig. 7.7-a**. The E_{fcc} was calibrated using the calculated energy by DFT. *GSFE* calculated by MEAM was also calibrated using DFT results, shown in **Fig. 7.7-b**. The calculated three elastic constants; C_{11} , C_{12} , and C_{44} , by MEAM are presented in **Table 7.2** and compared to values calculated by Ledbetter and Naimon (1974) [258], Chandra et al (2015) [259], and Zahedi et al. [260]. The calibration was done also using the elastic constants. The anisotropic elasticity tensor for copper based on the calculated elastic constants can be written as Eq. (7.4).

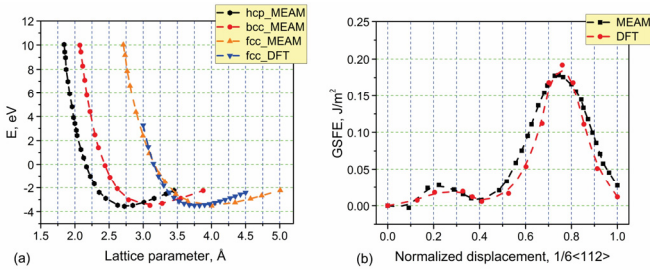


Fig. 7.7 (a) Energy versus lattice parameters of copper with different lattice structures calculated by MEAM and calibrated using DFT results. (b) Partial GSFE (along $\langle 112 \rangle$) calculated by MEAM and DFT.

Table 7.2 C_{11} , C_{12} , and C_{44} elastic constants calculated by MEAM at this work, compared with values from the literature.

	C_{11}	C_{12}	C_{44}	Ref.
This work	169.20	123.19	77.20	-
Chandra et al., 2015	168.15	125.60	78.80	[259]
Zahedi et al., 2013	168.00	121.40	75.40	[260]
Ledbetter & Naimon, 1974	168.40	121.40	75.4	[258]

$$C = \begin{bmatrix} 169.20 & 123.19 & 123.19 & 0 & 0 & 0 \\ 123.19 & 169.20 & 123.19 & 0 & 0 & 0 \\ 123.19 & 127.19 & 169.20 & 0 & 0 & 0 \\ 0 & 0 & 0 & 77.20 & 0 & 0 \\ 0 & 0 & 0 & 0 & 77.20 & 0 \\ 0 & 0 & 0 & 0 & 0 & 77.20 \end{bmatrix} \quad (7.4)$$

7.3.2.2 Molecular dynamics

After calibrating the MEAM calculations, the required potentials were created for MD simulations. The applied shear stress - on the simulation box in MD simulations - made the edge perfect dislocation (Burgers vector of $[\bar{1}01]$) to glide and created a step between the upper and lower half-part of the simulation box, shown in Fig. 7.8.

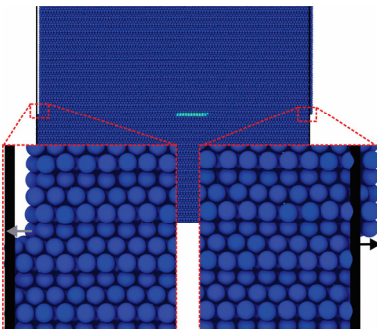


Fig. 7.8 Creation of step due to the movement of the simulation box, which is because of the applied shear stress.

For each applied shear stress, the displacement of the dislocation was measured as a function of time as shown in **Fig. 7.9-a**. Having the displacement results as a function of time helps to calculate the velocity of the dislocation at each applied shear stress, see Fig. 7.9-b, up to 50 MPa, the velocity of the dislocation is low and does not change significantly. However, the dislocation velocity increases with increasing shear stresses above 50 MPa. The drag coefficient, which was bridged to the upper scales, was $2.56 \times 10^{-5} \text{ Pa}\cdot\text{s}$. This value was reported to be $5 \times 10^{-5} \text{ Pa}\cdot\text{s}$ by Fusenig and Nembach (1993) [261].

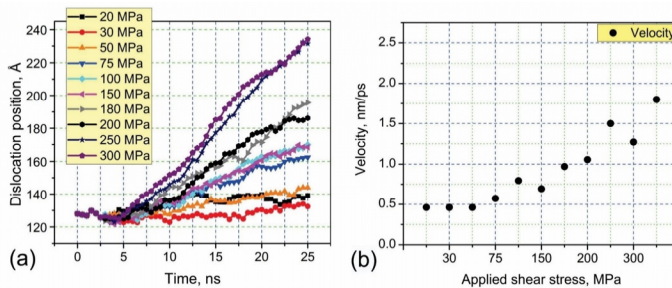


Fig. 7.9 (a) Position of the dislocation as a function of time, (b) Dislocation mobility (velocity) calculated for each applied shear stress.

With the above velocity results as function of the shear stresses and Eq. (2.33), the drag coefficient was calculated for each shear stress, see **Fig. 7.10-a**. The drag coefficient was calculated at 300 K. Nevertheless, the drag coefficient varies with the temperature and if during the process, the temperature changes, it should be considered. Jassby and Vreeland (1970) [262] have calculated the variation of the drag coefficient between 66 K and 373 K by means of torsion technique, which is shown in Fig. 7.10-b.

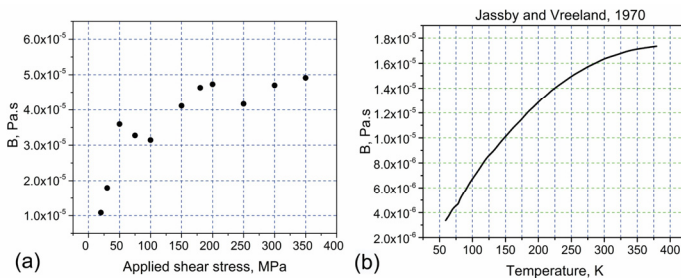


Fig. 7.10 (a) Drag coefficient calculated for different applied shear stresses. (b) Variation of drag coefficient as function of temperature, calculated by Jassby and Vreeland (1970) [262].

7.3.2.3 Bridging to the next microscale simulation scale

The three calculated elastic constants of copper using MEAM were imported directly to the FEM simulations. The developed potentials by MEAM were used at the same simulation scale, i.e. MD simulations. After simulating different simulation boxes under different shear stresses, the mobility of an edge dislocation was calculated for a certain temperature and shear stress. The calculated velocities were used in DD simulations at the microscale simulations to study the hardening behavior of copper, as well as the calculated drag coefficient imported to the FEM simulation.

7.4 Microscale simulations

7.4.1 Material parameter at microscale

DD simulations were done using an existing MDDP code, solving Eq. (2.29). The initial prismatic simulation box (also called DD-cell) consists of randomly distributed Frank-Read loops over all existing slip systems of a *fcc* crystal structure (12 slip systems). The initial dislocation density was chosen to $10^{12}m^{-2}$, to which a relaxation was applied to represent the annealed condition of the as-received copper tubes investigated. The deformation of the dislocation box was achieved by applying a $20 s^{-1}$ strain rate. As described by Groh et al. (2009) [253], the equilibrium of the simulation cell is achieved by applying a periodic boundary condition to have the same value of dislocation density leaving and entering the cell. The cell was a cubic one with $5.5 \mu m$ side with *x*- and *y*-axis in directions of $[\bar{2}11]$ and $[0\bar{1}1]$, respectively. A constant plastic strain rate of $10^{-2} s^{-1}$ along the $[111]$ axis was given. The *SFE*, bulk modulus, and dislocation mobility, calculated in the previous scales, were used as input data for the next calculations. The time step and temperature were $10^{-7}s$ and 300 K, respectively.

7.4.2 Results

The key parameters, which were calculated at this simulation scale, were the Palm-Voce hardening parameters (see 2.6.3.2 “Dislocation dynamics”); κ_s , h_0 , and κ_0 . The Palm-Voce hardening equation was introduced in Eq. (2.30), which for the sake of easiness, is presented here again in Eq. (7.5). To define these three parameters, results of DD calculation were used and different sets of these three parameters were fitted, to find the best suitable results, which are shown in Fig. 7.12.

$$\kappa = \kappa_s - (\kappa_s - \kappa_0) \exp\left(-\frac{h_0}{\kappa_s - \kappa_0} Ct\right). \quad (7.5)$$

The above Palm-Voce hardening equation is achieved by using the following equation:

$$\dot{\kappa} = h_0 \left(\frac{\kappa_s - \kappa}{\kappa_s - \kappa_0} \right) \sum_i |\dot{\gamma}_i|, \quad (7.6)$$

in which the $\sum_i |\dot{\gamma}_i|$ is taken as constant C (see [263], for more details).

Using the above equation and the results of DD simulation, the C value can be calculated and taking this value as a constant, the other three hardening parameters κ_s , h_0 , and κ_0 can be calculated, too. **Fig. 7.11-a** shows the variation of $\sum_i |\dot{\gamma}_i|$ as a function of time and the fitted line to this diagram, which defines the C value in Eq. (7.6). The evolution of the dislocation density with applying the plastic strain to the simulation box is shown in Fig. 7.11-b. As can be seen, initially the dislocation density changes with a high slope, however, increasing the plastic strain, it turns to a slower one, finally reaching a plateau.

The variation of κ in function of the plastic strain is presented in **Fig. 7.12-a**. As can be deduced in **Table 7.3**, 4 different sets of κ_s , h_0 , and κ_0 were used to fit to the $\kappa - \varepsilon$ diagram. As reported by Groh et al. [253], for aluminum alloy, the highest sensitivity of κ is to h_0 . Moreover, κ is not very sensitive to the changes of κ_0 and κ_s , in aluminum they caused almost variations of only 2% and 5%, while h_0 caused approx. 35% of variations. For this reason, the sets were chosen in a way that highest changes were firstly on h_0 and κ_s and κ_0 was kept constant. As can be seen in Fig. 7.12-b, set No. 1 is in a good agreement with the result of DD simulation. These values have been chosen as hardening parameters.

These values are in a good agreement with the ones calculated by Wang et al. (2004) [264] and also Zahedi and Silberschmidt (2013) [260], see Table 7.3.

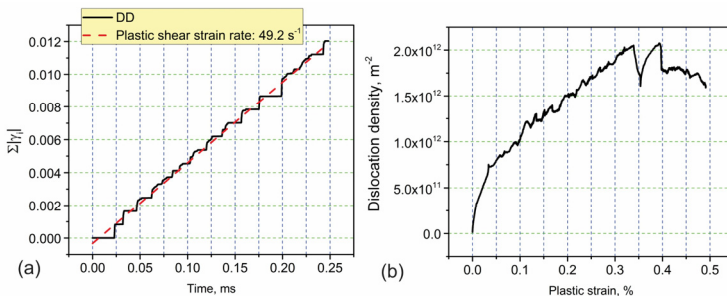


Fig. 7.11 (a) Variation of $\sum_i |\dot{\gamma}_i|$ as a function of time calculated by DD simulation to find out the C value, which is equals to 49.2. (b) Evolution of dislocation density in DD simulations.

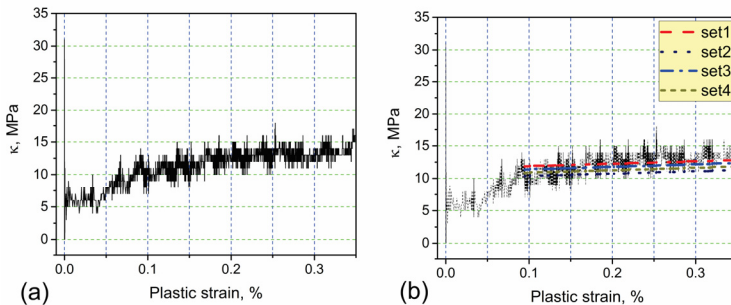


Fig. 7.12 (a) Variation of κ by changing the plastic strain. (b) Fitting the different hardening parameters in different sets used to calculate most suitable parameters.

Table 7.3 Sets of hardening parameters used to correlate the DD results, compared to other researchers' results.

Set No.	h_0	κ_s	κ_0	Source
1	180	148	16	This study
2	175	150	16	This study
3	185	152	16	This study
4	180	154	16	This study
Wang et al. (2004)	180	148	16	[264]
Zaafarani et al. (2006)	200	75	8	[265]
Zahedi & Silberschmidt (2013)	180	149	16	[260]

7.4.3 Bridging to the CPFEM

The most important parameters, which were calculated at this simulation level, were κ_s , h_0 , and κ_0 . These Palm-Voce hardening parameters were used in the next simulation scale to simulate the plastic behavior of copper in tube drawing process.

7.5 Meso- and structural scale (CPFEM)

Meso- and structural scales are discussed here as CPFEM (Crystal Plasticity Finite Element Method) level embracing both scales. The simulation at mesoscale uses the CP theory. To include this approach in the FEM simulations, a UMAT subroutine was used. The flow rule values in the CP model (m, γ_0) were taken from literature, however, a sensitivity study was done on these parameters to see their effects on the final results. The necessary elastic and plastic parameters were calculated at atomic and micro scales level, respectively, and were imported to the FEM calculations. The measured macrotexture was also an input to the FEM through the CP theory.

7.5.1 CPFEM, first drawing step

Different tubes with different measured-eccentricity were created for the FEM simulations in Solidworks software. The used die and plug were generated with real dimensions in the FEM software and considered as rigid bodies. The experimentally analyzed RSs by neutron diffraction were also imported into the software using a Sigin subroutine. Initially, drawing without tilting (standard drawing) was modeled and after successful validation the model was used for studying tube drawing with tilting. The assembly of the created FEM model is shown in **Fig. 7.13-a**, consisting of the tube (G-I series), the die and the plug. The drawing direction is in z -direction. The mesh type *C3D8R* with one integration point was used. To increase the simulations' efficiency, a sub-modeling technique was used. Sub-modeling is a technique for studying a local part of a model with a refined mesh, based on interpolation of the solution from an initial, global model onto appropriate parts of the boundary of the sub-model [266]. For this reason, initially a global model was developed and simulated by a normal to coarse mesh size.

The results of this model were validated using measured RSs, eccentricity, and stress-strain diagram. After validating the results, a sub-model based on the global model was created at *Max*, *Min*, and 90° using a very fine mesh and the experimental results achieved at the same positions (**Fig. 7.13-b**). Use of such a sub-model increases the calculation time without effecting the exactness of the simulation results.

The results of the sub-model along the measured macrotexture at *Max*, *Min*, and 90° , were used to validate the simulated texture. A dynamic implicit step with full Newton solution technique was chosen. The friction formulation was as penalty with the friction coefficient of 0.05, which was based on Coulomb's law of friction [267]. The boundary conditions of the tube, die, and plug were chosen in a way that the exact same condition as reality was applied to the simulations. The drawing velocity was 0.33 m/s (20 m/min). Table 7.4 summarizes all the parameters and inputs used in FEM simulations.

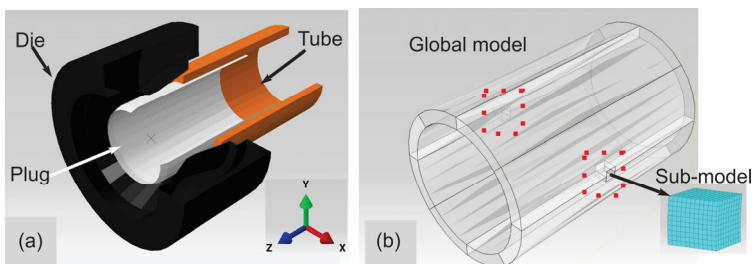


Fig. 7.13 (a) Assembly of the first drawing step, showing tube, die, and plug. (b) Global and submodel.

Table 7.4 Parameters used in FEM simulations.

Tube properties	Diameter		Experimentally measured
	Eccentricity		Experimentally measured
	Residual stresses		Experimentally measured
	Texture		Experimentally measured
	Elastic parameters		Calculated atomic scale
	Plastic parameters		Calculated microscale
	Parameters of slipping rate		Literature
Die and plug	Dimensions	Experimentally measured	
	Behavior	Rigid body	
Step	Dynamic, implicit		
Interaction	Penalty		
Friction coefficient	0.05		
Element type	C3DR8		
Drawing velocity	0.33 m/s = 20 m/min		

7.5.2 CPFEM, second drawing step

After simulating and validating the model for the first drawing step, the second one was simulated. In this regard, the results of the first drawing step - geometry, eccentricity, RSs, and texture - were imported as input data for the model as shown in **Fig. 7.14**. The simulated mesh was converted to a 3D geometry and re-meshed. The simulation of the 2nd drawing step was done globally and with a sub-model. The results were validated using the experimentally measured eccentricities, RSs, mechanical properties, and macro-texture.

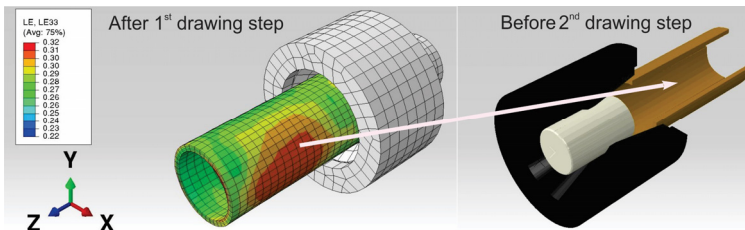


Fig. 7.14 The simulated tube after a drawing step imported as the input for the next drawing step.

7.5.3 Results of CPFEM simulations

In the following sections, a brief description of the mesh modeling and mesh convergence study, which was done in this work, is given. Then, to validate the models, the results of the CPFEM simulations are presented separately. In addition to the validation of the model using the experimental results, the energy assessment of the system was another way employed in this work.

7.5.3.1 Mesh modeling and mesh convergence study

For the global model with a complete geometry, the use of the uniform hexahedron mesh is appropriate because it provides an optimum of calculation quality and computation time. Initially, a coarse mesh with the size of 0.005 m was selected; (Fig. 7.15-a) the simulation could be done in a relatively short time (48 min) but the results of the eccentricity had a quite big deviation compared to the experimental ones.

Then, the mesh was reduced to an edge length of 0.0036 m to increase the mesh strength on the wall-thickness of the tube in radial direction by one node, as shown in Fig. 7.15-b. The simulation was about 3:50 h and the results, which are presented later, were in a very good agreement with the experimental ones. A further decrease in the edge length to 0.0021 m (Fig. 7.15-c) did not lead to any improvement but increased the computation time strongly (19 h). The eccentricity (see 7.5.3.3 "Eccentricity") results were not plausible. So, an edge length of 0.0036 m was selected for the complete simulation of the global model.

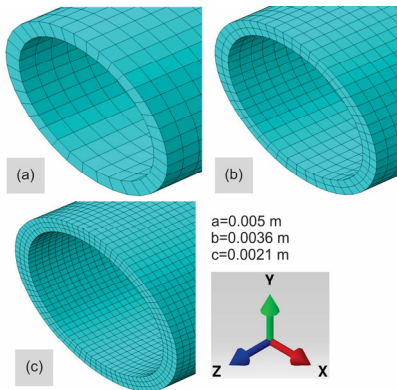


Fig. 7.15
Different mesh sizes, used in simulations to get the most proper mesh size: (a) 5 mm, (b) 3.6 mm, and (c) 2.1 mm.

7.5.3.2 Energy validation

The energy assessment of the system is an alternative way to validate the CPFEM model. In principle, the energy balance of external and internal energy must be zero or near zero. The energy balance is as follows (the parameters are introduced in Table 7.5):

$$|E_I| + |E_{FD}| + |E_{PW}| + |E_{KE}| + |E_{VD}| - |E_W| = -1.41 J \quad (7.7)$$

As an example, the calculated energy for the simulation with a tilting angle of -2° is listed in Table 7.5. The above energy balance corresponds to $-1.41 J$ is almost the same as the total energy of the simulation system.

Table 7.5 Different energies of the simulation model for tube drawing with -2° tilting angle.

Type of energy	Symbol	Value (J)
External work	E_W	166101
Frictional dissipation	E_{ED}	66977,80
Internal energy	E_I	90906,80
Internal work by penalty contact	E_{PW}	- 8161,13
Kinetic energy	E_{KE}	0,52
Viscous dissipation	E_{VD}	53,29
Total energy	E_{TOT}	-1,61

7.5.3.3 Eccentricity

The same G-I series tubes - see Table 3.2 - were simulated using the developed model with different tilting angles. As an example, the eccentricity of tubes before (the measured eccentricity of as-received tubes) and after drawing (simulated eccentricities) without tilting and with -5° tilting are shown in **Fig. 7.16**. In order to validate these results, they were compared directly to the measured values, which is shown in Fig. 7.16. Regarding the eccentricity, the results of simulations are in a good agreement with the measured ones, proving that the model is valid describing the drawing without and with tilting.

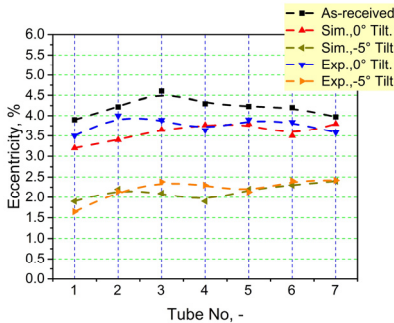


Fig. 7.16
Variation of the simulated eccentricity, before and after drawing for 7 different tubes drawn with 0° and -5° tilting angles and their comparison with the experimental results.

To compare all tilting angles, the relative change of eccentricity is presented in **Fig. 7.17-a**. As for the experimental results, the simulated ones show that by using negative tilting angles, the eccentricity diminishes and vice versa. The equations of the trend line are calculated and given in Eq. (7.8) and Eq. (7.9) for simulated and experimental results, respectively. For the investigated Cu-tubes the simulated and measured averages for the relative change of eccentricity for each tilting angle and the trend line achieved by simulation and experiment are presented in Fig. 7.17-b.

$$\Delta E (Sim.) = 0.05 - 0.10\theta, \quad (7.8)$$

$$\Delta E (Exp.) = 0.04 - 0.10\theta. \quad (7.9)$$

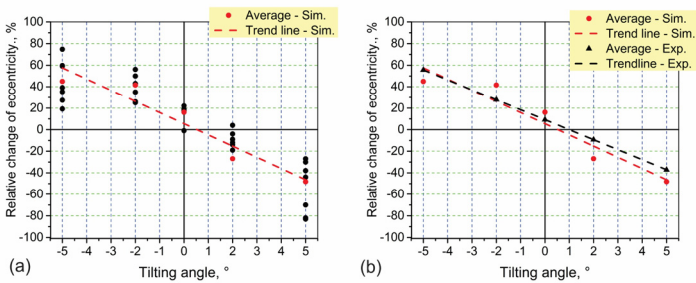


Fig. 7.17 (a) Simulated relative change of eccentricity, showing the effect of tilting on the variation of eccentricity. (b) Comparison of the average relative change of eccentricity and the trend line of simulated and measured values for Cu-tubes.

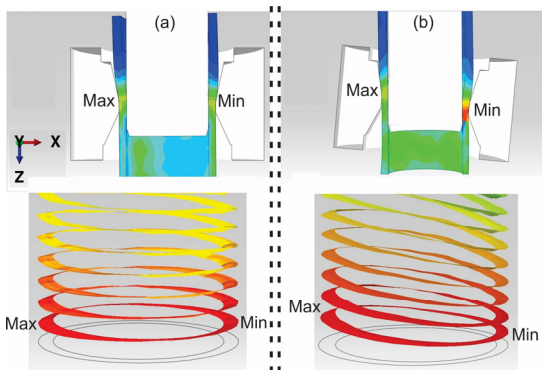


Fig. 7.18 Iso-surface for the mass flow during tube drawing (a) without tilting and (b) with -5° tilting.

As discussed in Chapter 4, the different mass flow, created due to the tilting of the die, was the main reason for the variation of eccentricity using different tilting angles. The iso-surface of the mass flow in tube drawing without and with -5° tilting is shown in Fig. 7.18. In standard tube drawing (Fig. 7.18-a) there is a homogenous – symmetrical - mass flow in opposite to tube drawing with -5° tilting (Fig. 7.18-b), where is a preferred mass flow from *Max* to the *Min*, causing an additional reduction of the eccentricity.

7.5.3.4 RSs and stress-strain diagram

The simulated RSs in axial, hoop, and radial directions at three positions: deformation zone (P5), the beginning of the bearing zone (P0) and the drawn tube (P-10) - with -5° tilting angle at *Max*, are displayed in Fig. 7.19-a to -c. To compare these results with the measured RSs at the same tube and same

positions, the measured RSs are shown in the same diagrams. The solid and dashed lines depict the experimentally measured and simulated RSs, respectively. As it can be clearly seen, the results in all three directions and positions are close to each other, showing that the model is valid in respect to the RSs.

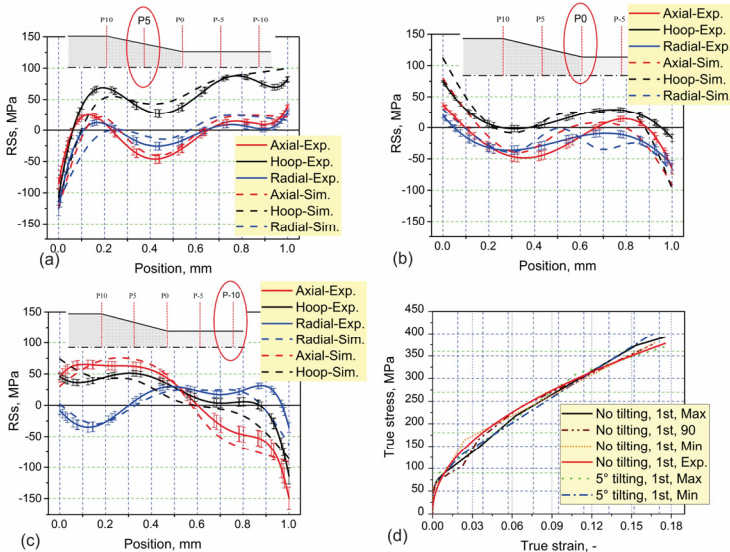


Fig. 7.19 Simulated and measured RSs in axial, hoop, and radial directions at *Max* side of the tube in (a) P5, deformation zone, (b) P0, beginning of the bearing zone, (c) P-10, after drawing. (d) Simulated and measured stress-strain diagrams of drawn tube with 0° and -5° tilting angles.

The stress-strain diagrams of the tubes after drawing, simulated by the global model as well as the sub-models at *Max*, *Min*, and 90° positions for tubes with 0° and -5° tilting angles are shown in Fig. 7.19-d. There is no significant difference between the stress-strain diagrams, showing that the *Max* and *Min* side of the tubes present roughly the same mechanical properties after drawing. Moreover, comparing the drawn tubes without and with tilting, shows the same behavior, having same mechanical property after drawing. Moreover, the results of the simulation are in good agreement with the experimentally measured stress-strain diagram, which is another validation proof.

7.5.3.5 Sensitivity study of m and $\dot{\gamma}_0$

As presented in “Annex C - *Crystal plasticity*”, in kinetic of crystal plasticity m and $\dot{\gamma}_0$, are two parameters which are affecting the exactness of the simulation

results. For this reason, a sensitivity study on these two parameters was done. For this matter, beside the chosen m and $\dot{\gamma}_0$ for the performed simulations, which were achieved from literature, four additional combination sets, as presented in **Table 7.6** were used to perform the simulations and as comparison value, the stress-strain diagrams were investigated and compared.

Table 7.6 Different sets used for sensitivity study of m and $\dot{\gamma}_0$. Set 1 was the so far used values.

	m	$\dot{\gamma}_0$
Set 1 - chosen values so far	0.05	0.001
Set 2	0.01	0.001
Set 3	0.5	0.001
Set 4	0.05	0.0001
Set 5	0.05	0.01

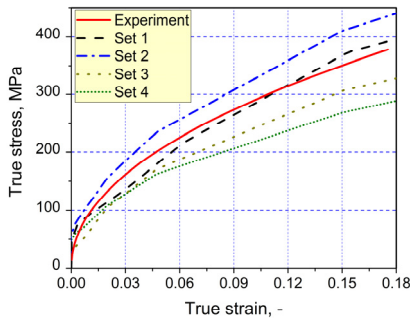


Fig. 7.20 Comparison of the experimentally measured stress-strain diagram of a drawn copper tube with standard drawing (0° tilting) at *Max* side of the tube with the simulated values for different sets, presented in Table 7.6.

Fig. 7.20 depicts the comparison of the stress-strain diagram of a standard drawn tube (0° tilting) at *Max* side of the tube using the different sets in Table 7.5 as well as the experimentally measured stress-strain. As to be pointed out that the result of set 5 was not converged and therefore has not been presented. Set 1 displays the most fitting result, which were chosen from beginning on. Therefore, simulations of texture were done by this combination, as well.

7.5.3.6 Texture

Texture measurement using diffraction methods is an expensive process, which can be also time consuming. Therefore, having a model, which is able to simulate the texture evolution is very useful. Thus, after developing and verifying the model using eccentricity, RSs, and stress-strain diagrams, the simulation of texture was done by importing the experimentally measured macro-texture as input texture into the sub-models of *Max*, *Min*, and 90° . The $\{111\}$, $\{200\}$, and $\{220\}$ PFs and $\varphi_2 = 0^\circ$, 45° , and 65° ODF sections of input are shown in **Fig. 7.21**, which is a re-presentation of the measured texture shown

in Fig. 6.1 and Fig. 6.4. As discussed in “6.2 - *Macro-texture data*“, the as-received tubes had four main components: *Cube*, *Cu*, *Bs*, and Goss components, which all were imported in to the simulations. The maximum PF and ODF intensities were 1.8 and 2.5, respectively.

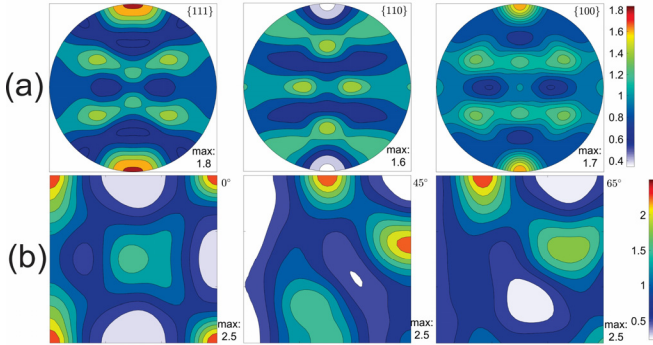


Fig. 7.21 The (a) {111}, {100}, and {110} PFs and (b) 0°, 45°, and 65° sections of ODF of the input texture, representing the texture of the as-received tube.

Using these orientations (texture), the simulation of a tube without tilting was performed. **Fig. 7.22** shows the simulated {111}, {200}, and {220} PFs as well as 0°, 45°, and 65° sections of ODF for the *Max* sub-model. These results show that, {111} PF has the highest PF intensity. Which is almost 1.5 times higher than the 100} PF. The most dominant orientation is *Cu* (can be seen by 45° ODF section). Same as experimental results, the cube orientation was significantly reduced. The maximum PF and ODF intensities were 2.9 and 3.7, respectively.

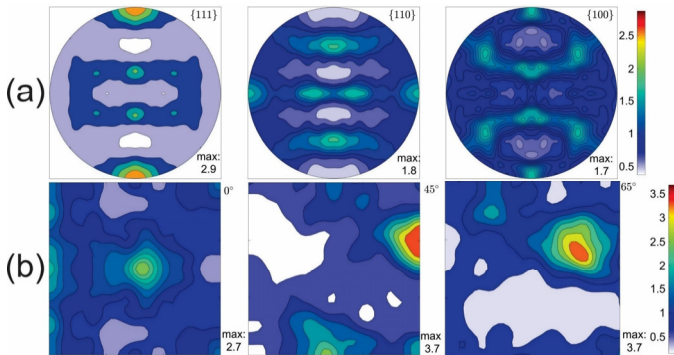


Fig. 7.22 The simulated (a) {111}, {100}, and {110} PFs and (b) $\varphi_2 = 0^\circ, 45^\circ,$ and 65° sections of ODF of the drawn tube without tilting after the first drawing step at *Max* side of the tube.

These simulated textures were used as input texture for the second drawing step. The simulations were performed on the tubes having same eccentricity and RSs, as the experimental tubes. **Fig. 7.23**-a and b illustrate a comparison of simulated $\{111\}$, $\{100\}$, and $\{110\}$ PFs of a drawn tube with -5° tilting at *Max* and *Min* sides of the tube after the second drawing, respectively. These results show almost same simulated PF density for the *Max* and *Min* sides of the tube. As simulation results for the standard drawn tube, simulated tube with -5° tilting has shown also a higher PF density in $\{111\}$ than the other PFs – almost 2 times higher.

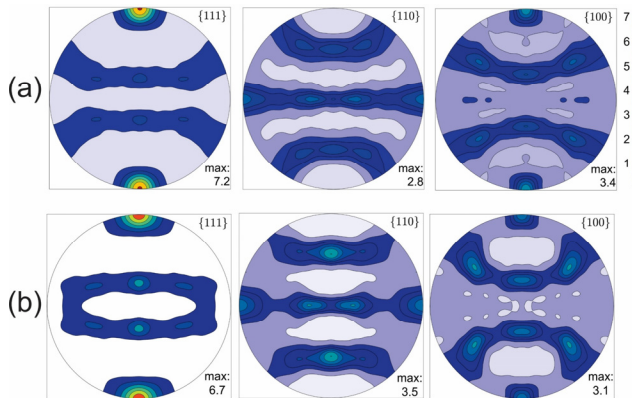


Fig. 7.23 The $\{111\}$, $\{100\}$, and $\{110\}$ PFs of drawn tube with -5° tilting after second drawing step at (a) *Max* and (b) *Min* side of the tube.

To validate the simulation results, the simulated and experimentally achieved PFs and ODF were compared. **Fig. 7.24**-a to d present a comparison of the simulated and experimentally measured $\{111\}$ PFs after second step drawing with -5° tilting at *Max* and *Min* sides. Both simulation and experimental PFs show developments of same orientations. Moreover, the shape of the PFs are same in both cases at both *Max* and *Min* sides. The simulated ODF sections were compared to the experimental results as well and used to validate the simulation results.

The simulated 45° ODF at *Max* side is compared in **Fig. 7.25** with the measured one, showing same Cu component in both simulated and experimentally measured results. In both cases the cube component is reduced strongly.

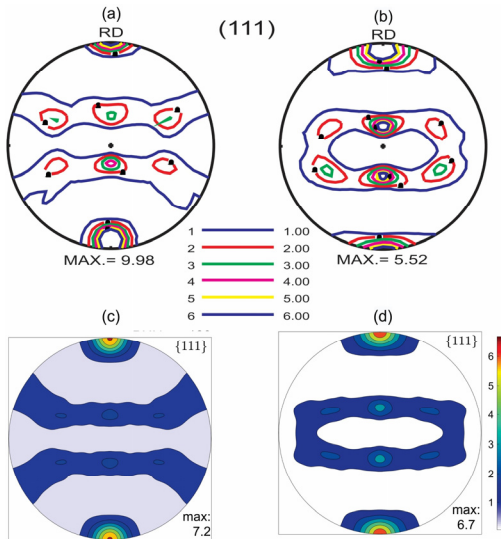


Fig. 7.24 Comparison of experimentally measured (a and b) and simulated (c and d) $\{111\}$ PFs at *Max* and *Min* sides of the tubes after second drawing step, drawn with -5° .

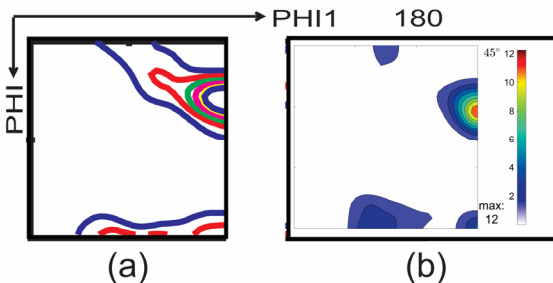


Fig. 7.25 The (a) experimentally measured and (b) simulated $\varphi_2 = 45^\circ$ ODF section at *Max* side of the tubes after second drawing step, drawn with -5° .

Using the validated model, it is possible to simulate the texture developments in tubes drawn with different tilting angles under different amount of reduction. As an example, a comparison of the texture evolution of the tubes drawn -5° and 0° tilting after the second drawing step is shown in **Fig. 7.26**-a and b. This comparison shows that ODF intensity of the drawn tubes with -5° tilting is higher compared to the standard drawn tube. However, in both tubes, the evolution of the texture was same.

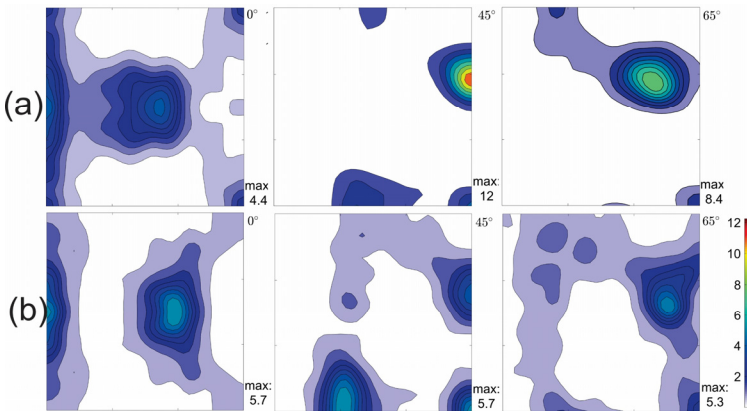


Fig. 7.26 The $\varphi_2 = 0^\circ, 45^\circ,$ and 65° ODF sections of drawn tube with (a) -5° and (b) 0° tilting angle after second drawing step at *Max* side of the tube.

7.6 Conclusion

In this chapter, the method for the development of the multiscale simulation model using ICME approach was discussed. The aim was to develop a model, which is able to simulate the eccentricity, RSs, and texture variations for tubes having same properties as the as-received tubes. The results of the simulation were validated using eccentricity, RSs, stress-strain diagrams, and texture of the drawn tubes.

By electronic scale simulation, DFT approach was used and the atomic lattice parameters of an *fcc* crystal structure, the bulk modulus of copper, and the energy variation of an *fcc* structure as a function of the lattice parameters were calculated. Additionally, the *GSFE* was calculated in this simulation scale. All these parameters were bridged to the next simulation level, which was the atomic scale simulations. In this simulation level, initially the three elastic constants of copper; namely C_{11} , C_{12} , and C_{44} were calculated using the MEAM approach. Moreover, the *GSFE* and energy variations of *fcc*, *bcc*, and *hcp* crystal structures were calculated. The achieved results were calibrated using the results of DFT calculations and the potentials were created using MEAM formalism.

The next method used at atomic scale simulations was MD method. The created potentials by MEAM were used as an input to calculate the dislocation mobility. For this reason, using LAMMPS software, a simulation box with approx. 70,000 Cu atoms was created and an edge dislocation line was placed in this box. Different shear stresses were applied, and the movement of the dislocation was calculated and, subsequently, the dislocation velocity was

calculated for each applied shear stress. Using these values, the drag coefficient could be calculated, being a direct input to the *FEM* simulations.

Elastic constants as well as drag coefficient were bridged directly to the structural scale simulation. The dislocation mobility was bridged to the next simulation scale, which was the microscale simulation using *DD* method. At this level, a simulation box with a specific dislocation density was created and this box was deformed with a specific strain rate and the achieved mechanical properties were used to get the hardening parameters - the Palm-Voce hardening. These parameters were bridged to upper simulation level. Mesoscale simulations were done using *CP* method and a *UMAT* subroutine was used to implement this method into the *FEM* simulations. Finally, a model for tube drawing with and without tilting angle could be created using Abaqus *FEM* software package. The inputs for the *FEM* model were as follow:

- Measured outer diameter of the tubes
- Measured wall-thickness of the tube (eccentricity)
- Measured RSs by neutron diffraction
- Measured global macro-texture by neutron diffraction
- Anisotropic elastic tensor of copper, calculated by *MEAM* (atomic scale simulation)
- Drag coefficient, calculate by *MD* (atomic scale simulation)
- Hardening parameters, calculated by *DD* (microscale simulation)
- Parameters of slipping rate, from literature

The results of the *FEM* simulations were validated using eccentricity, RSs, stress-strain diagrams, and texture. Using the developed model, it is possible to study the tube drawing process having different parameters, such as different materials, different amount of reduction, and various tilting/offset values.

Chapter 8 Summary and outlook

The key aim of this work was to optimize the standard tube drawing process in a way that the wall-thickness variation (eccentricity) of the drawn tubes can be controlled during the tube drawing process, either reducing or increasing of the eccentricity. To be able to control the eccentricity, the standard drawing method was optimized and tilting and/or offset was introduced to the die and/or tube.

To perform the tube drawing with tilting/offset, initially the required tools were built for the existing tube drawing machine in the Institute of Metallurgy at Clausthal University of Technology and all tests were performed on this machine in a laboratorial scale. Beside laboratory experiments, the industrial usage of this method was considered from the beginning on and for this reason, an industrially suitable construction of the new drawing block (including the tilting and offset tools) was designed.

To find a general rule for the tubes' behavior concerning eccentricity different drawing steps and materials (copper, aluminum, brass, and steel) with different tube dimensions were investigated varying the tilting angles, offset values, or a combination of tilting and offset. Measurements of the wall-thickness of the tubes were performed prior to each experiment. The as-received copper tubes were in a recrystallized state, therefore, different drawing steps were performed to consider the work hardening effect on the eccentricity. Tilting results of copper tubes have shown that it is not only possible to affect the eccentricity, it is also possible to control it, whether for reduction or targeted thickening of the tube. Using -5° tilting angle resulted in ca. 50% reduction after the first drawing step, where the standard drawing (0°) resulted only in 18% reduction of eccentricity. Using positive tilting angles, the eccentricity was increased about 50% (for $+5^\circ$ tilting) and a local thickening of the *Max* position resulted. Although most producers want to decrease the eccentricity because of material costs and product's weight, some applications favor thickening of the tube. Introducing tilting to the tube drawing process, however, did not change the force needed for drawing.

The same effect can be reached by applying offset to the tube. Shifting the tube about -6 mm resulted in 25% eccentricity reduction. The combination of tilting and shifting was performed, as well. However, in the case of combining negative shifting with negative tilting (where a maximum reduction of the eccentricity was expected), the -5° tilting angle did not deliver the highest decrease in the eccentricity, but -2° . Moreover, the reduction achieved by such

combinations was not significantly different compared to pure tilting. Interestingly, combining the positive shifting with negative tilting resulted in completely different results. For example, using a -5° tilting angle with $+4$ mm shifting, resulted in ca. 30% thickening (the increase of eccentricity).

Same as copper tubes, the other three materials were tested in tube drawing with tilting (shifting was not performed). Aluminum and brass showed a very close behavior to the copper tubes, however, steel differed clearly in comparison, which is mainly due to the different mechanical properties, which creates different mass flow.

After analyzing the effect of tilting/offset on the eccentricity of the drawn tubes, to know whether the tilting and/or offset can influence the developed RSs in a destructive way, the evolution of the RSs due to the introduced tilting and/or offset was investigated. Two different methods were chosen; hole drilling and neutron diffraction methods. Hole drilling results, which were measured on the surface of the tubes, showed that in the case of using a 5° tilting (both, negative or positive) the achieved RSs are less than the result of the standard drawn tube. In another word, using $+5^\circ$ tilting angle resulted in reduction of the RSs. Same exact behavior has been seen by the three other materials investigated, as well.

Hole drilling is a fast and quite inexpensive method but limited to the surface of the tube. In contrary using the neutron diffraction method, the whole wall-thickness of the tube can be measured (the measurements were done using SALSA instrument at ILL in Grenoble/France); however, it is an expensive method. The measurements done with neutron diffraction method were used also to prepare required data (input as well as validation data) for the simulation. To be able to follow the development of the RSs during deformation and to be able to investigate the RSs inside the die, special samples were prepared. For this reason, the drawing process was interrupted, and IDT samples were prepared, which all three main zones were existing in these tubes. The benefit of such sample was that the as-received sample, the part of the tube which is inside the die, and the drawn tube could be measured in one shot. Considering the deformation zone of the -5° tilting condition, it can be stated that the hoop RSs changes significantly compared to the axial ones, which shows that in the deformation zone, there is mass flow from *Max* side of the tube to the *Min* side.

Along eccentricity and RSs, the anisotropic behavior and the crystallographical evolution of the tubes drawn with tilting were investigated to make sure that their final properties are not being significantly directionally dependent of the crystallographical directions. Considering anisotropy and mass flow, it was decided to analyze the texture evolution of the tubes before and after drawing with tilting, to state whether tilting creates significant different textures (crystallographical orientations) and/or affect the mass flow in a detectable way.

To study these parameters, the macro- and micro-texture of the tubes were investigated. Using macro-texture, different crystallographic orientations were compared before and after drawing and texture was analyzed. Micro-texture was studied for through-wall-thickness analyses.

For macrotexture analyses, two methods were chosen; synchrotron and neutron diffraction methods. The reason for having two different methods, was the coarse grain size of the as-received tubes, which was not possible to be measured by synchrotron method, and therefore, neutron method was used. The main orientations were analyzed by discussing PF and ODF results. As-received tubes exhibited the *Cu*, *cube*, *Bs*, and Goss components as main components. After drawing, the cube component diminished and the intensity of the *Cu* component increased, same as ODF and PF densities. However, there was no significant difference between the drawn tubes with and without tilting angles.

The micro-texture of the tubes was measured by electron diffraction method, using EBSD technique. The $\{111\}$, $\{200\}$ and $\{220\}$ PFs were analyzed and compared, as well. However, no significant differences in the micro-texture of the drawn tubes with and without tilting could be stated. The only difference between the drawn tubes with and without tilting was the minor difference between their PF intensities.

Tube drawing investigations with different tilting/offset values on materials of different qualities with different starting RSs and initial textures are time and cost intensive. Moreover, not all combination can be studied experimentally. To overcome this problem and also to have a better understanding of the process, it was decided to develop a simulation model containing all relevant properties of the as-received materials – such as eccentricity, RSs, initial texture, mechanical properties – and therewith analyzing more complex situations (as described in Fig. 1.1-f). Moreover, using the developed model, it was possible to compare the texture evolution of the drawn tubes with and without tilting, without performing time consuming neutron, synchrotron, or electron measurements. For this goal, a multiscale simulation approach based on Integrated Computational Material Engineering (ICME) was used.

At electronic scale simulation, DFT was used and the lattice parameter and bulk modulus were calculated. Calculating these two parameters gave the possibility to find out the optimum *K*-point (mesh) for DFT simulations. The optimum *k*-point has been calculated to be 16. Using this *K*-point, the energy variation of a *fcc* crystal structure for copper was calculated as a function of the lattice parameters. Since dislocations are a very important parameter in defining the hardening behavior of the material, partial and perfect *GSFEs* were calculated as well. All these parameters were bridged to the atomic scale simulations. MEAM was used to create the needed potentials for MD

calculations. Moreover, by MEAM calculations, the elastic constants of copper were calculated. C_{11} , C_{12} , and C_{44} were found to be 169.20, 123.19 and 77.20 GPa, respectively. MEAM calculations were calibrated by results of DFT. After calibration of MEAM results, the potential of copper was created and imported for the MD calculations. Using MD calculations, the dislocation mobility for different applied shear stress was computed and for each velocity the drag coefficient was calculated, as well, which was equal to 2.56×10^{-5} Pa s.

Elastic constants and the drag coefficient were bridged directly to the FEM simulations, whereas the dislocation mobility was bridged to upper scale, which was micro-scale simulations using DD. Using DD simulations, the hardening parameters for Palm-Voce hardening were determined. κ_s , h_0 , and κ_0 were calculated to be 148, 180, 16 MPa, respectively. In the mesoscale simulation, a CP approach was used in form of a UMAT subroutine. The FEM model was developed using Abaqus software and following parameters were imported to this model:

- Measured outer diameter of the tubes
- Measured wall-thickness of the tube (eccentricity)
- Measured RSs by neutron diffraction
- Measured global macro-texture by neutron diffraction
- Anisotropic elastic tensor of copper, calculated by MEAM (atomic scale simulation)
- Drag coefficient, calculate by MD (atomic scale simulation)
- Hardening parameters, calculated by DD (microscale simulation)
- Parameters of slipping rate, from literature

After verifying the effects of tilting and offset on the eccentricity and RSs of tubes during drawing, which was performed statically, the performance of such a tilting/offset in a dynamic way is of interest for the industrial establishment of this method. In the frame work of an AiF¹ project, this establishment is going to take place. In this project

- The tube drawing is going to be performed using a floating plug and effects of tilting/offset is going to be studied.
- The wall-thickness of the die is going to be measured dynamically using the ultra-sonic device and before the die, to be able to characterize the eccentricity and also define the position of *Max* and *Min* position.
- The dynamic adjustment of the die based on the position of *Max* and *Min*.

¹ The German Federation of Industrial Research Associations

Within the framework of the planned project, the knowledge to be developed will enable the small and medium-sized enterprises of the above-mentioned industrial branches to supply market-oriented, optimized solutions for the plant, pipeline construction, and automotive areas by exploiting the possible material gain and ensuring narrower and more homogeneous material properties. In addition, new product fields with strong demand potential, such as heat exchanger tubes as well as bearings, high-precision bushes and guide tubes for the automotive industry, are developed. This results in an effective increase in the performance and competitiveness of these companies in the German market. The economic importance of the planned research project is confirmed by the great interest of various companies who have actively supported the project. Moreover, the developed simulation methodology will be used to study other metal forming processes, to be able to generalize the existing model.

Chapter 9 Résumé de thèse en Français

Les tubes de précision sans soudure sont utilisés pour diverses applications mécaniques telles que la plomberie, l'automobile, l'architecture... et généralement sont produites par extrusion, suivie de plusieurs étapes d'étréage à froid pour atteindre les dimensions finales. Dans le processus d'étréage des tubes, la déformation s'effectue par une combinaison de contraintes de traction et de compression - créées par la force de traction appliquée à la sortie de la matrice et par sa configuration géométrique.

Les tubes étréés présentent des contraintes résiduelles qui sont souvent un point négatif pour leur utilisation finale. De plus, à cause des vibrations du mandrin il peut se produire des tolérances de positionnement de la matrice ainsi que des différences de température potentielles dans le tube, des variations d'épaisseur sur la longueur et la circonférence causant l'excentricité (E) et l'ovalité. Ces dernières sont généralement causées par un fluage non symétrique du matériau et, celui-ci étant présent pendant le processus d'étréage à froid, provoque une déformation non homogène sur la circonférence.

Les contraintes résiduelles (CR) sont des contraintes multiaxiales statiques autoéquilibrées existant dans un système isolé de température uniforme et en l'absence de tout chargement extérieur. Si des parties du corps (morceaux pris dans la masse) sont enlevées, par exemple par usinage, l'état d'équilibre est généralement perturbé et le corps réagit en se déformant. Les CR développées lors de l'étréage du tube influencent le comportement mécanique et la durabilité des tubes utilisés pour les structures sous contrainte, et en particulier la forme de la courbe contrainte-déformation.

Différentes techniques non destructives pour évaluer les CR par la diffraction des rayons X et des neutrons et par rayonnement synchrotron ont été développées, ainsi que des techniques destructives telles que la nano indentation et le « sectioning method ». D'autre part, il est bien établi que le développement des CR dépend de l'inhomogénéité de la microstructure et des orientations cristallographiques des grains. En effet, la texture initiale influence l'évolution microstructurale lors de la déformation plastique (évolution de la texture, contrainte résiduelle, précision des dimensions) et, pour cette raison, il est important d'étudier les effets de l'orientation cristallographique sur les CR et l'excentricité.

La production des tubes avec différentes lignes de passage (inclinaison et décalage visibles sur les **Fig. 9.1** et **Fig. 9.2** et l'étude de différentes propriétés et paramètres sont significativement lourdes en termes de temps et de coût.

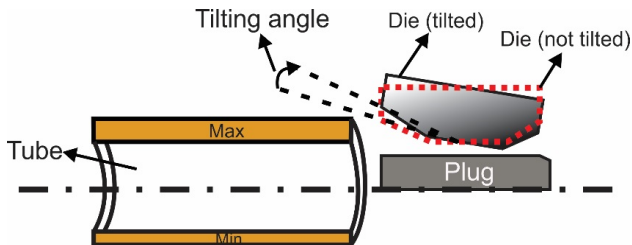


Fig. 9.1 Schéma de basculement (tilting).

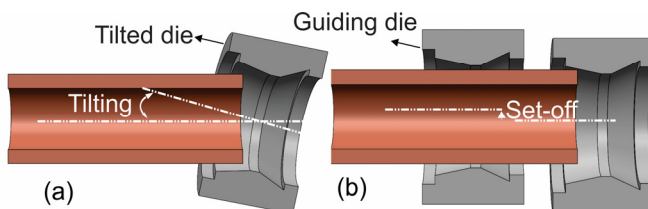


Fig. 9.2 Schéma de décalage (offset)

Au cours des dernières années, un développement rapide des techniques informatiques et l'application de la théorie de la plasticité ont permis d'appliquer une approche plus complexe de la formabilité des métaux et des problèmes de plasticité. L'avantage de l'analyse par méthode des éléments finis (FEM) est sa capacité à modéliser les processus complexes de mise en forme. L'effet de chaque variable du processus et leurs effets de couplage peuvent être étudiés puis les résultats utilisés pour concevoir le processus de formage approprié. L'inconvénient de l'analyse FEM est la complexité de la préparation des données d'entrée, la sélection des variables de sortie appropriées et l'interprétation des résultats de l'analyse. Les travaux réalisés au cours des dernières années dans le domaine de la mesure et de la simulation des CR et de la texture dans les produits étirés à froid ont montré qu'il était possible d'obtenir des résultats quantitatifs fiables.

L'objectif de cette thèse de doctorat a été d'analyser la variation de l'excentricité, des CR et de la texture lors de l'étréage de différents tubes avec différents angles basculants (**Fig. 9.1** et **Fig. 9.2**) et ainsi de comprendre le comportement d'écoulement des matériaux lors de l'étréage des tubes en cuivre, aluminium, laiton et acier (**Figure 3**, Aim 1). Parallèlement, un modèle

de simulation FEM basé sur l'approche de simulation multi échelle a été développé pour analyser ces mêmes paramètres (Fig. 9.3, Aim 2).

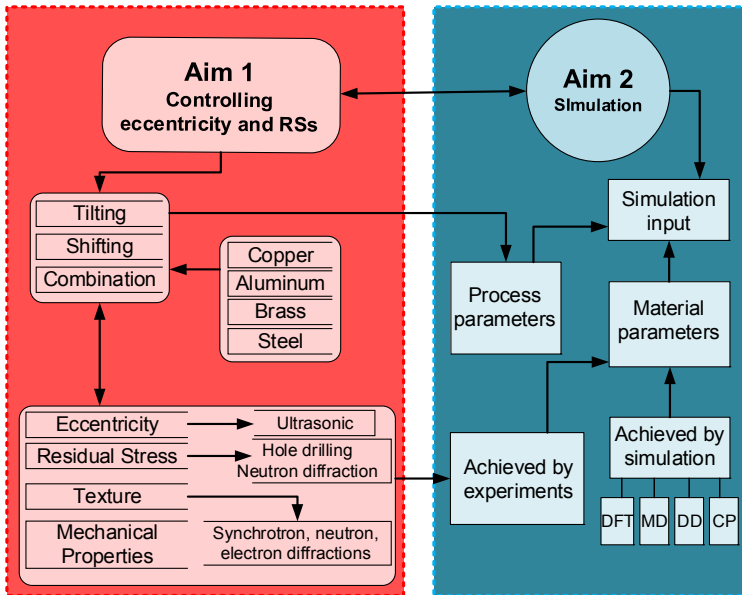


Fig. 9.3 Les objectifs de cette thèse de doctorat.

Dans ce travail de thèse, une nouvelle méthode a été développée, dans laquelle une valeur spécifique d'inclinaison et / ou de décalage (l'inclinaison et le décalage (décrit dans le chapitre 3) a été introduite dans la matrice et / ou le tube. L'élaboration des tubes a été réalisée à la TUC avec un nouveau procédé (développé dans l'Institut de métallurgie dirigé par M. Palkowski) pour influencer l'excentricité des tubes en inclinant la matrice dans le processus de tirage ou en déplaçant un couple de matrices l'une contre l'autre pour contrôler le fluage du matériau pendant le processus et contrôler les variations d'épaisseur des parois.

Différents tubes de matériaux différents tels que le cuivre, l'aluminium, le laiton et l'acier, avec différentes dimensions ont été étudiés en utilisant cette méthode. En plus d'influencer et de contrôler l'excentricité, il était crucial de prendre en compte ces paramètres pour comprendre l'évolution des contraintes résiduelles à la surface et à travers l'épaisseur de la paroi du tube dans cette méthode. La modification du processus d'étirage de tube et l'introduction de l'inclinaison et / ou du décalage ont fortement influencé le flux du matériau, et pour comprendre ce phénomène dans le processus, les développements des orientations

cristallographiques tels que la texture cristallographique sont également nécessaires. Ainsi ce travail a été concentré sur l'étude de l'excentricité, des CR et des évolutions de la texture lors du processus d'étrirage de tube avec des matrices inclinées et / ou décalées. Pour calculer l'excentricité, les épaisseurs des parois des tubes reçus ont été mesurées le long de leur longueur et sur leur circonférence à l'aide d'un dispositif à ultrasons. Les déformations résiduelles et le gradient de texture ont été mesurés en utilisant les diffractomètres SALSA à l'ILL (Institute Laue Langevin) de Grenoble et Petra III à DESY (Deutsches Elektronen-Synchrotron) à Hamburg (sous la supervision de Mme Carradò, UNISTRA).

Parallèlement aux travaux expérimentaux, un modèle FEM avec une approche de simulation multi-échelle a été développé en vue de mieux comprendre le processus afin d'obtenir l'excentricité, les contraintes résiduelles et la texture des tubes avant le processus d'étrirage et de simuler les mêmes paramètres et leurs variations pendant l'étrirage avec et sans inclinaison / décalage. Tous les paramètres nécessaires pour les simulations, tels que les valeurs de la dureté, les constantes élastiques, ... ont été calculés à différentes échelles de simulation.

La simulation a été effectuée à l'aide d'une démarche de simulation multi-échelle (**Fig. 9.4**). Cette méthodologie démarre par des calculs à l'échelle électronique, qui sont réalisés par approche DFT (Density Function Theory, par le logiciel Quantum Espresso). La donnée la plus importante issue de la simulation est le GSFÉ (Generalized Stacking Fault Energy). Après avoir obtenu les données requises, ces données sont reliées à la prochaine échelle de simulation, qui est le calcul au niveau atomistique, en utilisant la MEAM (Modified Embedded Atom Method) et la MD (Dynamique Moléculaire). Les constantes élastiques du cuivre et la densité de dislocations ont ainsi été calculées. L'approche DD (Dynamique de dislocations discrète) a été utilisée à l'échelle de simulation suivante, c'est-à-dire les simulations à échelle microscopique et les paramètres de durcissement dans l'équation de durcissement de Palm-Voce ont ainsi été calculées. Ces paramètres, ainsi que la texture mesurée, ont été utilisés dans les simulations CP (Crystal plasticity) pour être importés dans le modèle FEM, qui a été utilisé pour le processus d'étrirage du tube. Les CR mesurées par diffraction neutronique ont également été importées dans le modèle FEM.

Les principales étapes de ce travail sont schématisées sur la **Fig. 9.5**. Le chapitre 1 présente les principaux objectifs et chapitre 2 fournit un bref aperçu des bases théoriques et des travaux existants sur les procédés de production des tubes, le CR, la texture et les méthodes de simulation. Le chapitre 3 décrit les matériaux utilisés. Les résultats des variations d'excentricité pour différents types de matériaux sont présentés en chapitre 4. Le chapitre 5 et le chapitre 6 fournissent les résultats expérimentaux des CR et les développements de

texture tandis que la simulation à grande échelle est discutée dans le chapitre 7. Les conclusions sont présentées dans le chapitre 8.

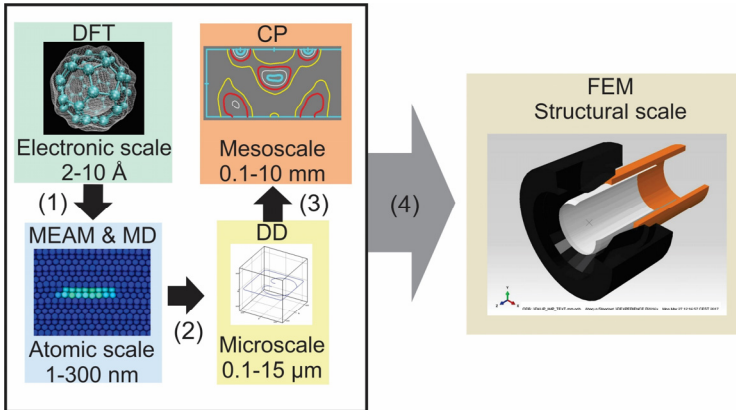


Fig. 9.4 Méthodologie multi échelle.

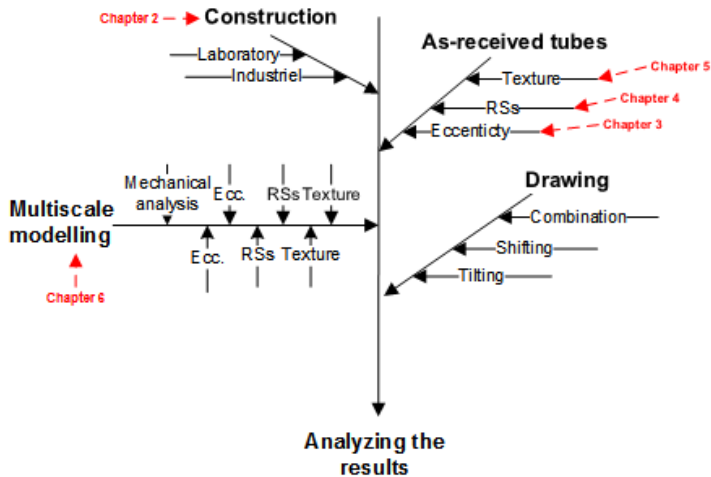


Fig. 9.5 Principales étapes de ce travail.

Une nouvelle géométrie du tube (IDT) a été choisie pour comprendre l'évolution des contraintes dans le tube (Fig. 9.6). Le tube a été préparé en interrompant l'étrépage et trois différentes régions ont été mises en évidence et

étudiées : la zone initiale (no-drawn), la zone de déformation (déformation) et la zone finale (drawn) (Fig. 9.7).

Les mesures des CR et leurs profils complets à travers l'épaisseur de la paroi ont été obtenus par diffraction neutronique (Fig. 9.6). En outre, un modèle par éléments finis non symétrique pour la simulation des contraintes résiduelles a été développé.

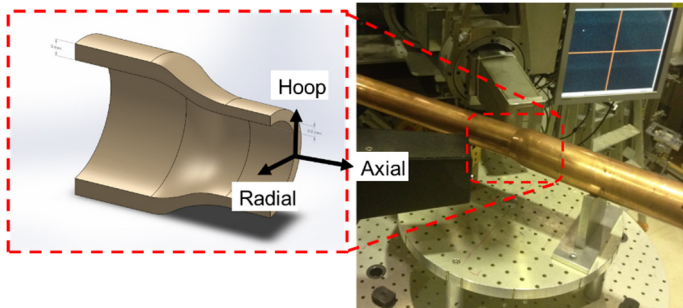


Fig. 9.6 Géométrie d'un échantillon pour la mesure par neutrons de la déformation à l'imageur de tension SALSA

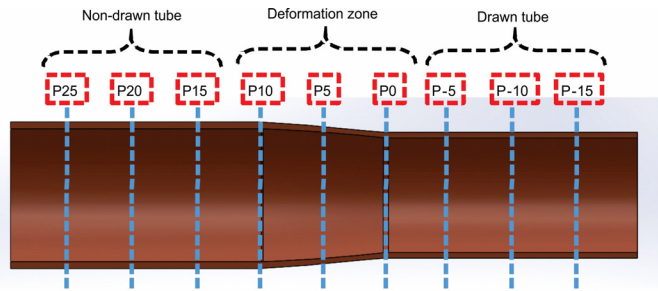


Fig. 9.7 Points de mesure en mm et étapes d'interruption de l'étréage (IDT).

Le modèle par FEM permet de considérer comme paramètres d'entrée : l'excentricité et les CR initiales avant étréage du tube. Les résultats obtenus ont été comparés aux mesures neutroniques. L'utilisation du gradient de texture comme paramètre d'entrée peut aussi être considérée. La simulation des CR a été effectuée en utilisant le logiciel Abaqus FEM. Le tube excentrique et l'inclinaison de la matrice ont été préparés sur Solidworks et importés sur Abaqus. L'inclinaison a été effectuée sur une plage de $+5^\circ$ à -5° (la définition de l'inclinaison positive et négative est illustrée en Fig. 9.8).

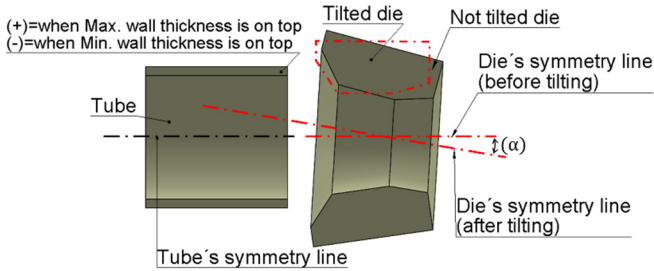


Fig. 9.8 Définition des configurations de l'inclinaison positive et négative.

Les résultats sont présentés en **Fig. 9.9** pour la première et la deuxième étape de l'étréage. Un changement relatif positif de l'excentricité indique une réduction absolue par rapport à l'état initial du tube. Un changement négatif implique une augmentation de l'excentricité. Une relation fonctionnelle a été trouvée entre l'angle d'inclinaison et son effet sur E. Sur la base de ces résultats (**Fig. 9.9**), l'angle d'inclinaison négatif le plus élevé choisi (-5°) semble avoir le meilleur effet en diminuant E, et E peut être augmenté en utilisant des angles d'inclinaison positifs. Les équations de courbes de tendance linéaire pour la première étape [Eq. (9.1)] et la deuxième étape [Eq. (9.2)] d'étréage sont données ci-dessous :

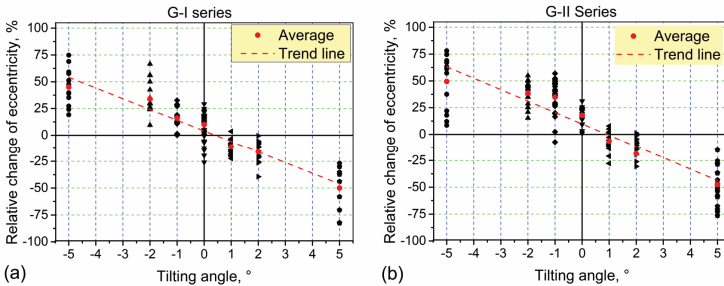


Fig. 9.9 (a) Modifications relatives de l'excentricité pour la première et (b) deuxième étape de l'étréage.

$$\Delta E = 0.10 - 0.09\theta, \quad (9.1)$$

$$\Delta E = 0.04 - 0.09\theta. \quad (9.2)$$

Où E est l'excentricité (%) et θ est l'angle d'inclinaison ($^\circ$). Pour les deux étapes d'étréage, ce comportement semble être cohérent tout au long du programme de test.

Les résultats de la simulation multi-échelle (Fig. 9.4 et Fig. 9.10) ont été validés en utilisant les CR mesurées, la texture et les propriétés mécaniques (diagramme contrainte-déformation).

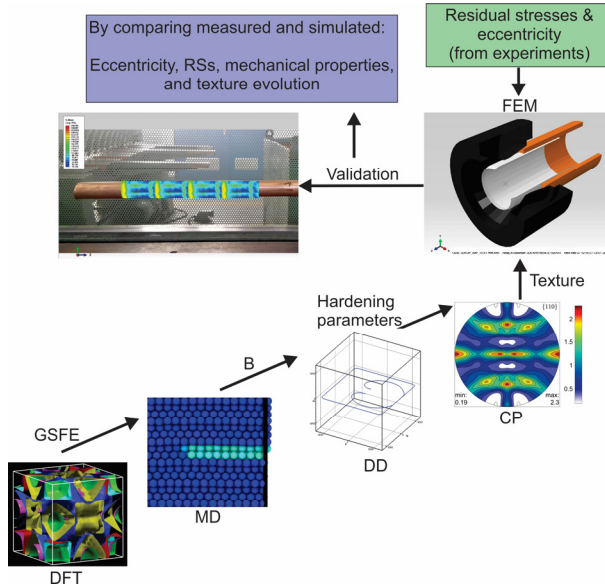


Fig. 9.10 Méthodologie multi-échelle.

Les mesures de l'épaisseur de paroi des tubes et le calcul de l'excentricité avec différents matériaux, ont été effectuées avant chaque expérience. Différents angles d'inclinaison et valeurs de déplacement ont été testés. Les tubes fournis par le fabricant ont été traités thermiquement, des étapes d'étréage différentes ont été effectuées pour pouvoir considérer l'effet de durcissement du travail sur la variation de l'excentricité. Les résultats d'inclinaison des tubes ont montré que, même s'il est possible d'affecter l'excentricité, il est également possible de la contrôler, qu'il s'agisse de réduction ou d'épaississement ciblé du tube.

À l'aide d'une inclinaison de -5° , l'inclinaison négative signifie que le côté Min du tube était en direction de l'inclinaison, ce qui a entraîné environ une réduction de 50% de l'excentricité après la première étape d'étréage, alors que l'étréage standard (0°) n'a eu qu'une réduction de l'excentricité de 18%.

En utilisant des angles d'inclinaison positifs, par exemple $+5^\circ$, l'excentricité augmente d'environ 50 % et un épaississement du tube s'est produit (le Max est devenu plus épais et le Min plus mince). Bien que la plupart des producteurs souhaitent diminuer l'excentricité pour pouvoir diminuer les coûts de production

(poids du produit), on pourrait envisager des applications où l'épaississement du tube présente un intérêt.

En introduisant une inclinaison vers le processus d'étirage du tube, sans changer la force d'étirage, le même effet a été observé par le décalage du tube. Le décalage du tube d'environ -6 mm a entraîné une réduction de l'excentricité de 25 %. La combinaison de l'inclinaison et du décalage a également été effectuée. En cas de combinaison de décalage négatif avec valeurs d'inclinaisons négatives (avec laquelle une réduction de l'excentricité était attendue), et contrairement à l'inclinaison pure, l'angle d'inclinaison de -5° n'a pas produit la diminution plus importante d'excentricité. Par contre avec un angle de -2° la réduction la plus importante a été obtenue. De plus, la réduction obtenue par combinaison n'était pas significativement différente de celle obtenue avec l'inclinaison pure. Il est intéressant de noter que la combinaison du décalage positif avec l'inclinaison négative a abouti à des résultats complètement différents. Par exemple, l'utilisation d'un angle d'inclinaison de -5° avec un décalage de +4 mm a produit un épaississement (augmentation de l'excentricité) de 30 %. Un comportement identique a été obtenu pour l'aluminium et le laiton testés par étirage du tube avec inclinaison (le décalage n'a pas été effectué contrairement à l'acier).

Les contraintes résiduelles des tubes étirés ont été étudiées par perçage (hole drilling, méthodes destructives) et par diffraction neutronique (non destructive). Les résultats de perçage ont montré que, pour l'inclinaison à $\pm 5^\circ$, les contraintes résiduelles atteintes sont inférieures au résultat du tube étiré standard. En d'autres termes, l'utilisation d'un angle d'inclinaison de 5° a entraîné une réduction des CR. Le même comportement a également été observé pour les trois autres matériaux.

Pour pouvoir suivre le développement des contraintes résiduelles pendant le processus d'étirage du tube à l'intérieur de la matrice, un échantillon IDT (**Figure 6**) a été préparé et étudié par diffraction neutronique à l'instrument SALSA à Grenoble, en France. Les résultats du tube reçu ont également été utilisés comme valeurs pour les simulations. Compte tenu de la zone de déformation de l'inclinaison à -5°, nous avons constaté que les contraintes résiduelles changent considérablement par rapport aux axes (radial, axial et longitudinal), ce qui montre que dans la zone de déformation, il y a un débit massique du côté « Max » du tube par rapport au côté « Min ». Ce flux massique est un comportement clé dans le contrôle de l'excentricité des tubes étirés (**Fig. 9.11**).

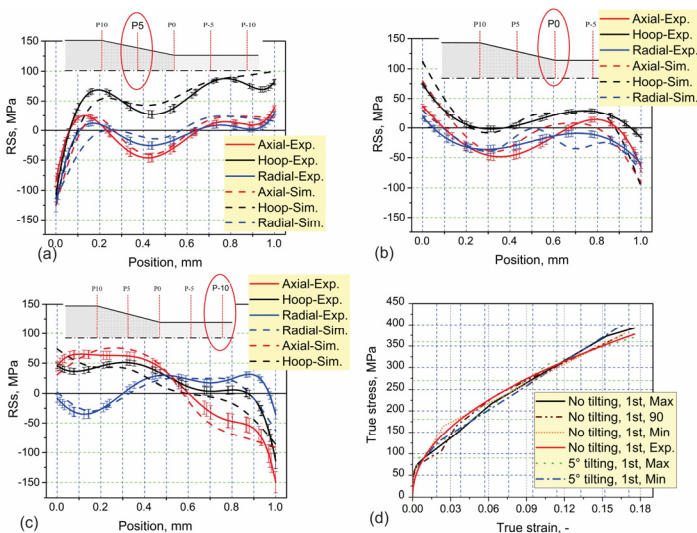


Fig. 9.11 Calculs et mesures des CR en directions axiale, longitudinale, et radiale en (a) P10, (b) P5, (c) P0, et (d) P-10 pour étirer le tube avec -5° d'inclinaison.

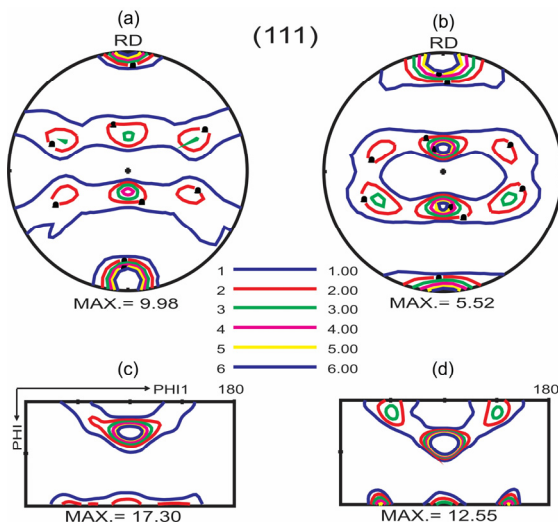


Fig. 9.12 {111} PF du tube étiré après la 2ème étape d'étréage à (a) Max et (b) Côtés Min. Du tube. Section de 45° de ODF dans le même échantillon à (c) Max et (d) Min. En raison de la symétrie dans l'ODF, seulement $0 < \varphi_1 < 180$ est présenté.

La microtexture dans l'échantillon IDT a été mesurée par diffraction neutronique (@ STRESS-SPEC) et rayonnement (@ HEMS). Les principales orientations ont été analysées en observant les résultats des PF (Pole figure) et ODF (Orientation distribution function). Les tubes reçus ont montré que les composants Cuivre et Cube

Étaient les composants principaux avant l'étréage. Après l'étréage, le composant Cube réduit lorsque le composant Cuivre augmente ainsi que les densités ODF et PF. Cependant, nous n'avons observé aucune différence significative entre les tubes étréés avec et sans angles d'inclinaison (**Fig. 9.12**).

La microtexture des tubes a été mesurée par une méthode de diffraction électronique, en utilisant la technique EBSD. Les graphiques de la **Fig. 9.13** et **Fig. 9.14** n'ont montré aucune différence significative dans la microtexture des tubes étréés avec et sans basculement. De plus, leurs $\{111\}$, $\{200\}$ et $\{220\}$ PF ont également été analysés et comparés. Les tubes étréés avec une inclinaison de -5° ont une intensité maximale de PF maximale (3.71, **Fig. 9.14**) par rapport à l'intensité maximale du tube de dessin standard (2.42, **Fig. 9.13**).

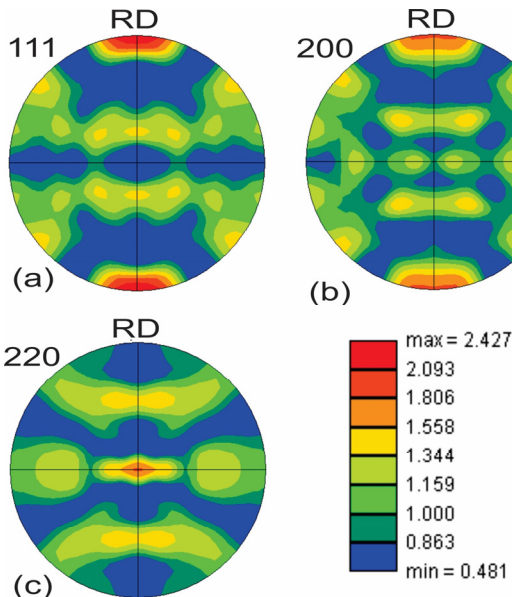


Fig. 9.13 $\{111\}$, $\{100\}$, and $\{110\}$ PFs du tube standard après la deuxième étape de l'étréage au *Min*.

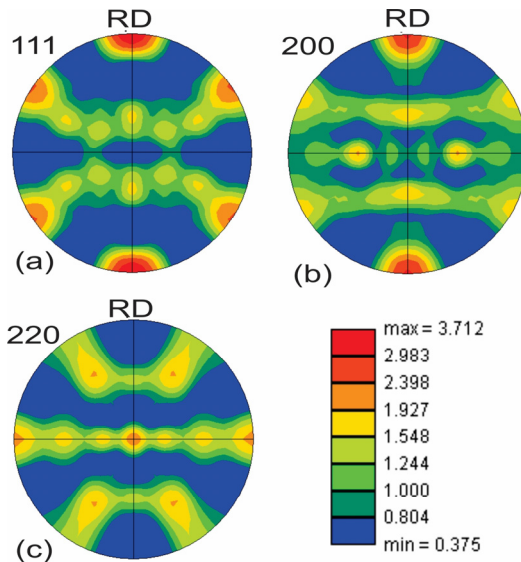


Fig. 9.14 {111}, {100}, and {110} PFs du tube standard après la deuxième étape de l'étréage avec un angle d'inclinaison de -5° au *Min*.

Le modèle de simulation a été développé à l'aide d'une méthode de simulation multi-échelle avec l'approche ICME. Différents temps de simulation ont été utilisés pour obtenir tous les paramètres requis pour les simulations. À la simulation d'échelle électronique, on a utilisé la DFT et on a calculé le paramètre de réseau et le module de compressibilité. Le calcul de ces deux paramètres a permis de trouver le point k optimal (maillage) pour les simulations DFT. Le nombre de points k optimal calculé est de 16. En utilisant ce nombre de points k , la variation d'énergie d'une structure cristalline FCC pour le cuivre a été calculée en fonction du paramètre réseau. Comme les dislocations sont un paramètre très important dans la définition du comportement de durcissement du matériau, les GSFÉ partielles et totales ont également été calculés. Tous ces paramètres ont été utilisés pour faire « une passerelle » entre les simulations à l'échelle atomique (**Figure 4**). MEAM a été utilisé pour créer les potentiels nécessaires pour les calculs de MD. De plus, selon les calculs MEAM, les constantes élastiques du cuivre ont été calculées. C_{11} , C_{12} et C_{44} ont été calculées comme étant respectivement de 169,20, 123,19 et 77,20 GPa. Les calculs MEAM ont été étalonnés d'après les résultats de DFT. Après l'étalonnage des résultats MEAM, le potentiel du cuivre a été créé et importé pour les calculs MD. À l'aide de simulation par MD, nous avons calculé la mobilité de la dislocation pour les différentes contraintes de cisaillement

appliquées et, pour chaque vitesse, le « Drag coefficient » a également été calculé, celui-ci étant trouvé égal à $2,56 \times 10^{-5}$ Pa s.

Les constantes élastiques et le « Drag coefficient » ont été reliés directement aux simulations FEM, tandis que la mobilité de la dislocation a été incluse dans les simulations à l'échelle supérieure, soit une simulation à l'échelle microscopique en utilisant la DD. Les paramètres de durcissement pour le durcissement Palm-Voce (K_s , h_0 et κ_0) ont été calculés par simulations DD. K_s , h_0 et κ_0 ont été calculés et donnent respectivement les valeurs de 148, 180, 16 MPa. Dans la simulation à l'échelle mésoscopique, l'approche CP a été utilisée sous la forme d'un sous-programme UMAT.

Le modèle FEM a été développé à l'aide du logiciel Abaqus et les paramètres suivants ont été importés dans ce modèle :

- Diamètre extérieur mesuré des tubes
- Épaisseur de paroi mesurée du tube (excentricité)
- Contraintes résiduelles mesurées par diffraction neutronique ;
- Macrotexture globale mesurée par diffraction neutronique ;
- Tenseur élastique anisotrope du cuivre, calculé par MEAM (simulation à échelle atomique) ;
- Coefficient de glissement, calculé par MD (simulation à l'échelle atomique) ;
- Paramètres de durcissement, calculés par DD (simulation à l'échelle microscopique) ;
- Paramètres du taux de glissement, provenant de la littérature ;
- À l'aide de l'excentricité calculée et mesurée, des contraintes résiduelles, du diagramme contrainte-fatigue et de la texture, les résultats du modèle FEM ont été validés avec succès.

Les résultats obtenus ont montré la possibilité de contrôler l'excentricité pendant l'étirage de la même manière pour le cuivre, l'aluminium et le laiton. Selon l'application, il est possible de produire le tube avec une excentricité contrôlée. Pour l'acier, le comportement n'était pas identique aux trois autres matériaux. Dans le cas du cuivre, l'inclinaison de la matrice d'environ 5° et la fixation du côté minimum du tube dans le sens de l'inclinaison ont conduit à une réduction de l'excentricité moyenne du 40 % (par rapport à l'amélioration de l'excentricité moyenne de 18 % par étirement standard). Le décalage du tube d'environ 3 mm et le placement du côté minimum du tube dans le sens de décalage améliorent l'excentricité d'environ 30 %.

La comparaison des résultats de contraintes résiduelles pour les tubes étirés standard et inclinés montre aussi la possibilité d'influencer les contraintes résiduelles.

La texture des échantillons de cuivre a été mesurée avec succès en utilisant les trois méthodes de diffraction. L'approche de simulation multi-échelle a été développée avec succès et tous les paramètres nécessaires ont été importés dans le modèle FEM à l'aide d'un sous-programme UMAT.

Le modèle développé est capable d'obtenir et de simuler l'excentricité, les contraintes résiduelles, le comportement mécanique et les évolutions de la texture du processus d'étirage pour les étirages standard ou incliné / décalé.

En conclusion, les compétences scientifiques complémentaires et technologiques des deux laboratoires ont permis : (i) l'évaluation par techniques non destructives et (ii) le développement de calculs multi-échelle pour la caractérisation des propriétés mécaniques.

Chapter 10 Annexes

Annex A Pole figure

Typically, a rolled sheet of cubic materials is considered to illustrate the principle of a PF. Such a sample is associated with three mutually perpendicular specimen directions, namely the normal direction (ND), which is perpendicular to the sheet plane, the rolling direction (RD), and the transverse direction (TD). Considering the specimen to be very small placing it at the center of a big reference sphere (Fig. 10.1-a), then there is a projection (parallel to the sheet surface), where ND will be at the center and RD and TD will be on the periphery of the projection, as shown in Fig. 10.1-b. Assuming three mutually perpendicular planes (100), (010), and (001) of a rectangular specimen, as shown in Fig. 10.1-c and letting the normals to these three planes be extended to intersect the reference sphere at the three x-marked points (Fig. 10.1-c) - obviously, these three plane normals will be mutually perpendicular to one another. The points 100, 010, and 001 in Fig. 10.1-c are nothing but the poles of the planes with these three sets of indices - makes it possible to project these poles on a projection plane which is parallel to the surface of the specimen, as shown in Fig. 10.1-d. This diagram is a stereographic projection showing both the specimen parameters ND-RD-TD and the crystallographic parameters 100-010-001 [113].

Fig. 10.1-e shows a material which is textured. This PF is plotted considering all the 100, 010, and 001 poles from the different grains in the sheet specimen and drawing the projections of those poles on the given projection plane. In this case, most of the projected poles are clustered together and therefore it shows a textured material. If, on the other hand, the projected poles are distributed rather uniformly, then it will indicate that the material is without texture or random. Normally, the pole densities in a PF are represented not as discrete points, but by way of some contour lines, as shown in Fig. 10.1-f. The number against each contour line represents the density of poles relative to that which would be expected for a specimen which is without texture or random. Whereas, contour lines greater than one time random will signify a concentration of poles; contour lines less than one time random will imply a depletion of poles. In a real-life situation, the number of grains in a specimen, generally, will be rather large and, therefore, the determination of individual orientations will be impractical. The normal practice these days is to collect orientation data from many grains simultaneously (using synchrotron or neutron diffraction, sections 2.5.2.1 and

2.5.2.3) or collect the individual grain orientation data (using electron diffraction, section 2.5.2.2) and combine them to present in the form of density contours on the PF.

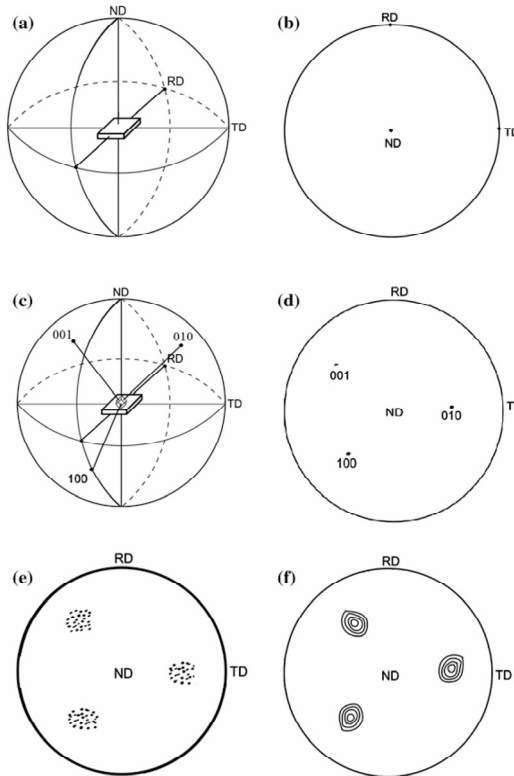


Fig. 10.1 (a) Projection plane and reference sphere with a rolled sheet at the center. (b) Projection of the poles RD, TD, and ND on the reference plane constituting the sample reference frame of a pole figure. (c) The points of intersection of the normal to the plane (100), (010), and (001) of the specimen on the reference sphere. (d) The three poles 100, 010, and 001, as projected on the basic circle. (e) Clustering of projected poles of (100), (010), and (001) planes from the different grains of the specimen. (f) Pole densities are shown as contour lines [99].

Annex B Kinematics of deformation and strain

Let a deformation gradient tensor \underline{F} represent the uniform deformation of the system, with:

$$\underline{F} = \frac{\partial \underline{x}}{\partial \underline{X}} \quad (10.1)$$

The deformation gradient represents a motion (\underline{x}), mapping a particle from its initial position (\underline{X}) in the reference configuration (R_0) to its position in the current configuration (R_3) as shown in Fig. 10.2 [268].

The deformation gradient \underline{F} assumes a sufficient continuity, where the local deformation at \underline{X} is characterized as the gradient of the motion, which is a second-order, two-point tensor. From here, the Green elastic strain tensor \underline{E} or Lagrangian strain tensor falls out naturally with respect to the reference coordinates as (10.2) [269].

$$\underline{E} = \frac{1}{2}(\underline{F}^T \underline{F} - 1), \quad (10.2)$$

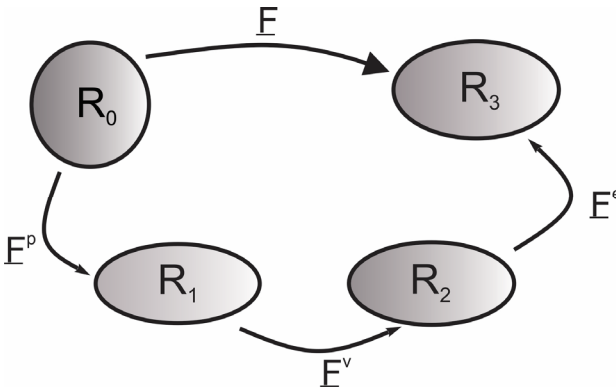


Fig. 10.2 The deformation gradient \underline{F} is multiplicatively decomposed into elastic \underline{F}^e , volumetric \underline{F}^v , and plastic \underline{F}^p components [268]. In this work only the \underline{F}^e and \underline{F}^p components are considered.

The deformation gradient could have decomposed into different components, depending on the way by which the material accomplishes the shape change and possibly rotation from the reference. As illustrated by the multiplicative decomposition of the deformation gradient shown in Fig. 10.2, the kinematics of motion combines elastic straining, inelastic flow, and formation and growth of damage. Since in this work, no damage is studied, this component of deformation gradient will be ignored. Therefore, the deformation gradient \underline{F} can be decomposed into the plastic (\underline{F}^p) and elastic parts (\underline{F}^e) given by (10.3). This

decomposition is based on the elastoplastic decomposition introduced by Kröner (1959) [270] and Lee (1969) [271].

$$\underline{F} = \underline{F}^p \underline{F}^e. \quad (10.3)$$

where the plastic deformation gradient (\underline{F}^p) represents a continuous distribution of dislocations and the elastic deformation gradient (\underline{F}^e) characterizes the lattice displacements from equilibrium [270].

The Jacobian of Eq. (10.3) is related to the change in volume or change in density for a constant mass as (10.4) and must be positive. In another word, J is the ratio of the current volume to the volume at the undeformed state, and it is assumed that all volumetric changes result from elastic stretches in the lattice. The change in volume from the reference configuration (State 0) to the intermediate configuration (State 2) is $V_2 = V_0 + V_v$ assuming that the volume in State 0 equals that in State 1, because of inelastic incompressibility [140].

$$J = \det \underline{F}^p = \frac{V_2}{V_0} = \frac{\rho_0}{\rho_2}. \quad (10.4)$$

A time-dependent displacement, or motion, of a body entails a nonzero velocity field, given by the time derivative of the corresponding displacement field. Its spatial gradient is termed velocity gradient (L) and quantifies the relative velocity between two positions in the current configuration. The relation between the velocity gradient and the rate of change, $\dot{\underline{F}}$, of the corresponding deformation gradient can be inferred from the equivalence of the relative change in the velocity of two points separated by dy and the rate of change of their relative position:

$$L dy = \frac{\partial v}{\partial y} dy \equiv \frac{d}{dt} dy = \frac{d}{dt} F dx = \dot{F} dx = \dot{\underline{F}} \underline{F}^{-1} dy. \quad (10.5)$$

$$L = \dot{\underline{F}} \underline{F}^{-1}. \quad (10.6)$$

where the superscript -1 denotes the tensor inverse, and a superposed dot denotes the material-time derivative. This velocity gradient is also could be decomposed into elastic $\underline{L}^e = \dot{\underline{F}}^e \underline{F}^{e-1}$ and plastic $\underline{L}^p = \dot{\underline{F}}^p \underline{F}^{p-1}$ components, as deformation gradient [172].

Annex C Crystal plasticity

In recent years continuum slip polycrystal plasticity models, a tool to study the deformation and texture behavior of metals during processing and shear localization, have become very popular [272]. The basic elements of the theory comprise three items [140]:

1. **Kinematics** which deals with the plastic spin.
2. **Kinetics** which considers the slip system hardening laws to reflect intragranular- work hardening, that can be derived from lower length scale results [5]; and
3. **Intergranular** constraint laws to gain interactions among crystals or grains for upscaling to the macroscale level.

Some researchers focused on the current configuration formulations such as Rashid and Nemat-Nasser (1992) [273], while some developed formulations, called the intermediate stress configuration, for example Anand and Kothari (1996) [274]. In most of the published works, elasticity effects were ignored [275], though there are some having included it in their formulations, e.g. Groh et al. (2009) [253]. It is worth mentioning that the texture and stress-strain responses are essentially the same and differences lie within the assumptions related to the kinetics of slip [172].

Historically, dislocation glide on slip planes, i.e. crystallographic slip, is caused by plastic deformation. Taylor and Elam (1923) were the first, who presented the relationship between the tensile test axis and the orientation of one crystallographic slip axis, which were not necessarily coincident. They speculated that perhaps two slip systems were involved [276]. Schmid (1926) determined that the magnitude of crystallographic slip on the glide planes was related to the resolved shear stress [277]. The next major historical work was related to that of Taylor (1938) founding the “principle of minimum shears”, in which the elastic strains were disregarded and only five independent slip systems were assumed to be necessary to describe three-dimensional polycrystalline behavior [278]. Using this assumption, Bishop and Hill (1951) determined the three-dimensional stress state resulting from all the slip possibilities in a face-centered cubic (*fcc*) lattice with twelve slip systems (three possible $\{110\}$ slip directions on four $\{111\}$ planes) [279]. A review by Gil Sevillano et al. (1981) [280] and also book written by Kocks et al. [281] provide a nice review of the history and the relevant issues associated to the kinetics, kinematics, and intergranular constraints of crystal plasticity.

a. Kinematic of crystal plasticity

In this section, the equations (10.1) to (10.4) which are related to the deformation and velocity gradients and their decomposition to the elastic and plastic parts, will be used. The velocity gradient in Eq. (10.4) however, can be rewritten as follows (see [282]):

$$L = \dot{F}F^{-1} = L^e + F^e L^p F^{e-1}, \quad (10.7)$$

The plastic flow (plastic strain) L^p is presumed to be given by the superposition of crystallographic slips on different slip systems [169], such that

$$L^p = \sum_{i=1}^N \dot{\gamma}_i (\underline{s}_i^0 \otimes \underline{m}_i^0), \quad (10.8)$$

where $\dot{\gamma}_i$ is the plastic slip (shearing) rate on i th slip system, and \underline{s}_i^0 and \underline{m}_i^0 are the slip direction vector and unit normal vector to the slip plane, representative of the Schmid tensor. Since \underline{s}_i^0 and \underline{m}_i^0 are fixed in space according to the classical assumption of Taylor (material flows through the lattice), the so-called intermediate configuration is specified; hence, material plastically flows from the reference to the intermediate configuration. Substituting Eq. (10.8) into (10.7) gives [283]:

$$L = L^e + \sum_{i=1}^N \dot{\gamma}_i (F^e \underline{s}_i^0 \otimes \underline{m}_i^0 F^{e-1}) = L^e + \sum_{i=1}^N \dot{\gamma}_i \bar{s}_i^0 \otimes \bar{m}_i^0, \quad (10.9)$$

with

$$\bar{s}_i^0 = F^e \underline{s}_i^0, \quad \bar{m}_i^0 = \underline{m}_i^0 F^{e-1} = F^{e-T} \underline{m}_i^0. \quad (10.10)$$

Here, \bar{s}_i^0 and \bar{m}_i^0 are viewed as \underline{s}_i^0 and \underline{m}_i^0 , respectively, pushed forward from the lattice space to the deformed configuration, and the superscript T denotes the transpose of a tensor.

b. Kinetic of crystal plasticity

To include kinetics relations to the already discussed kinematics and constitutive relations, the thermally activated dislocation motion theory will be used. A good review on this theory is presented by Kocks et al. in [284] and also by Meyers et al. in [285]. In this theory, it is assumed that the resolved shear stress on the i - slip system can be additively decomposed into thermal and athermal parts. In another word, the resolved shear stress can be written as $|\tau_i| = \tau_i^a + \tau_i^t$, where τ_i^a and τ_i^t are the applied shear stresses needed to overcome the athermal (long range) and thermal (short range) barriers to

dislocation motion, respectively. Similarly, the slip resistance (also called slip system strength) is partitioned as $|R_i| = R_i^a + R_i^t$, where R_i^a and R_i^t represent the resistance of the athermal and thermal obstacles to dislocations gliding on the i -slip plane (R is chosen being the designator for isotropic hardening on the slip system and the associated isotropic hardening, which are the thermodynamic displacements, are κ_i , κ_i^a and κ_i^t). One can assume that the athermal components are the same, so $\tau_i^a = R_i^a$, while the thermal components, τ_i^t and R_i^t with $0 \leq \tau_i^t \leq R_i^a$ define the slip system plastic shear strain rate as following [286]:

$$\dot{\gamma} = \dot{\gamma}_i \exp \left[-\frac{\Delta F}{kT} \left\{ 1 - \left(\frac{\tau_i^t}{R_i^t} \right)^p \right\}^q \right] \text{sign}(\tau_i), \quad (10.11)$$

A common viscoplastic flow rule modified by Horstemeyer et al. [140] taking into account kinematic hardening is given by:

$$\dot{\gamma} = \dot{\gamma}_0 \text{sgn}(\tau_i - \alpha_i) \left| \frac{\tau_i - \alpha_i}{R_i} \right|, \quad (10.12)$$

where m is the rate sensitivity, and α_i representing kinematic hardening effects resulting from backstress at the slip system level [140]. The connection between Eqs. (10.11) and (10.12) can be established with the strain rate sensitivity parameter m as follows:

$$m = \frac{\partial \ln|\tau_i|}{\partial \ln|\dot{\gamma}_i|} = \frac{kT}{\Delta F} \frac{1}{pq} \left(\frac{T}{T_c} \right)^{\frac{1}{q}-1} \left[1 - \left(\frac{T}{T_c} \right)^{\frac{1}{q}} \right]^{-1}. \quad (10.13)$$

The proposed evolution equation for dislocation density (ρ_i) by Kocks and Mecking [287] is used to formulate a dislocation-based hardening rule. In this theory, the competition of storage and annihilation of dislocations controls the hardening. The mean free path ($\propto 1/\sqrt{\rho_i}$) the dislocations travel before being immobilized is used to describe the (athermal) storage rate. However, the annihilation (dynamic recovery) follows a first-order kinetics; linear in ρ_i . Hence

$$\dot{\rho}_i = \left(\frac{C_h}{A_i} - C_r \rho_i \right), \quad (10.14)$$

where C_h and C_r are the hardening and recovery constants. The above equation can be transformed into a rate equation as the thermodynamic displacement (an internal elastic strain κ_i) using $\kappa_i = b\sqrt{\rho_i}$ (b is burgers vector) and relating the constants C_h and C_r to meaningful physical quantities as $C_h = 2h_i^0/(c_\kappa \mu b)$ and $C_r = 2h_i^0/(c_\kappa \mu \kappa_{i,s})$ [140]. Here, h_i^0 is the initial hardening rate due to dislocation accumulation, $\kappa_{i,s}$ is a saturation internal strain-like quantity, which,

in general, is a function of strain rate and temperature, and μ is the bulk modulus. Eq. (10.14) then can be written as [171]:

$$\dot{\kappa}_i = \frac{h_i^0}{c_{\kappa} \mu_E} \left(1 - \frac{\kappa_i}{\kappa_{i,s}} \right) |\dot{\gamma}_i|, \quad (10.15)$$

The above relationship can be given in terms of the slip system strength R_i (which is the thermodynamic force related to κ_i), an expression that can be obtained using (10.15) when one assumes an elastic constitutive relationship:

$$R_i = \mu_E c_{\kappa} \kappa_i. \quad (10.16)$$

The internal thermodynamic force rate equation is given by:

$$\dot{R}_i = h_i |\dot{\gamma}_i|. \quad (10.17)$$

Arising from the hardening moduli with the internal thermodynamic displacement (strain - like) quantity as

$$h_i = h_i^0 \left(1 - \frac{\kappa_i - \kappa_i^0}{\kappa_{i,s} - \kappa_i^0} \right). \quad (10.18)$$

By assuming that all the slip systems harden at the same rate, the following simplification for the crystalline isotropic hardening rate can be realized:

$$\dot{R} = h^0 \left(1 - \frac{\kappa_{s,s} - \kappa_s}{\kappa_{s,s} - \kappa^0} \right). \quad (10.19)$$

where the saturation strength $\kappa_{s,s}$ is given [171]

$$\kappa_{s,s} = \kappa_{s,s}^0 \left(\frac{\sum_i |\dot{\gamma}_i|}{\dot{\gamma}_s^0} \right)^{kT/\mu_E b^3 A}. \quad (10.20)$$

Finally, equation (10.20) can be written as:

$$\dot{\kappa} = h_0 \left(\frac{\kappa_s - \kappa}{\kappa_s - \kappa_0} \right) \sum_i |\dot{\gamma}_i| \quad (10.21)$$

Annex D Dislocation dynamics

A dislocation can be easily understood by considering that a crystal can deform irreversibly by slip, i.e., offset or sliding along one of its atomic planes. If the slip displacement is equal to a lattice vector, the material across the slip plane will preserve its lattice structure and the change of shape will become permanent. However, rather than simultaneous sliding of two half crystals, slip displacement proceeds sequentially, starting from one crystal surface and propagating along the slip plane until it reaches the other surface. The boundary between the slipped and still unslipped crystal is a dislocation, and its motion is equivalent to slip propagation. In this picture, crystal plasticity by slip is a net result of the motion of a large number of dislocation lines, in response to the applied stress. [288]

As mentioned, the macroscopic properties of a crystalline materials depend highly on the behavior of their defects. Yet, this issue is not involved in continuum theory of crystal plasticity. However, the complexity of the dislocation motion and its interactions makes it hard to develop a quantitative analytical approach. This difficulty of the dislocation-based one on one hand, and the developing needs of material engineering at the nano and micro length scales on the other hand, have created the current situation that equations of crystal plasticity used for continuum modeling are phenomenological and somewhat disconnected from all of the degrees of freedom related to the underlying dislocation behavior. However, with the advancement in computational technology with larger and faster computers, making this connection between dislocation physics and continuum crystal plasticity has become possible [289].

In the following, the principles of DD analysis will be presented by giving a brief description of dislocation motions and plastic strain and also the upscaling method for work hardening. The basic definition of dislocations and dislocation motion will not be discussed here. For a more elaborate discussion of dislocations, their motions and mechanics refer with the books by Hull and Bacon [174] or Weertman and Weertman [290] for a comprehensive introductory presentation and the book by Hirth and Lothe [291] for a more advanced presentation.

a. Dislocation motion and plastic strain

The slip due to dislocation motion at the microscopic level defines the tensor of plastic strain tensor to be calculated using Eq. (10.18) [292]. Gliding dislocations can collide with each other resulting is special types of interactions (short - range interactions) that are very complicated in nature and depend strongly on the dislocations' slip systems, line senses, and approach trajectory. The main interactions include annihilation, jog formation, junction formation, and dipole formation. Furthermore, dislocations can also be trapped by: (i) short

-range interactions leaving them locked, (ii) long-range effects like pileups against obstacles, and/or (iii) the occurrence of regions in the material where the stress field is not high enough to move dislocations [174].

b. Modeling discrete dislocations

Kinematics and kinetics of dislocation motion and their interactions all are considered in the framework of DD. In addition to the fundamental of the dislocation theory, a few dislocation properties and dislocation reaction rules are necessary for DD, which are derived either from experiments or from molecular dynamics (MD) simulations (as done in this work). For example, dislocation mobility is a critical property that determines the reliability of the DD simulation.

Mostly, a Representative Volume Element (RVE) of a larger specimen is chosen as the simulation box in DD. The usual simulation time in DD is in the range of nano- to microseconds and the simulation cell is on the order of a few microns. The cell includes an elastic medium with dislocations, which are represented as lines. After creating an initial dislocation structure, which is generally based on a random number of dislocation sources, the boundary conditions and the desired loading are applied. The dislocations will be forced to move because of the resulting stresses from applied forces also other dislocations. This movement calculation is based on the dislocation mobility equations (10.22) and (10.23), calculated at each time step for the velocity. The dislocation lines are discretized into small segments connected by nodes. The mesh size, which in DD is the length of the segment can be refined to obtain the desired accuracy in representing curved dislocation lines and their dynamics. The above sequence of calculations is repeated as time marches in appropriately chosen time steps to the desired point of evolution of the dislocation system or the overall stress or strain levels [140].

The motion of a straight dislocation with a segment of s can be calculated by the following equation, which is based on the theory of dislocations [293]:

$$m_s \dot{v}_s + \frac{1}{M_s} v = F_s. \quad (10.22)$$

The dislocation segment with the effective mass m_s moves in a viscous medium with a drag coefficient, defined in Eq. (10.23), of $1/m_s$ under the effect of a net force F_s . In general, the force due to a general stress field σ is given by [292]

$$F_s = l_s \sigma \cdot b_s \times \xi_s. \quad (10.23)$$

where l_s is the segment length, σ is the stress field created by the dislocation segment, while b_s and ξ_s are the Burgers vector and the line sense, of the dislocation segment, respectively.

Annex E Embedded atom method

In metals EAM uses a potential supplemented by a function of a pairwise sum, which was developed by Daw and Baskes (1984) [294]. The idea of developing a function is based on attraction and repulsion of atoms, that is presented in **Fig. 10.3** [294]. Essentially, EAM includes a cohesive energy¹ [see (2.31)] of an atom determined by the local electron density into which that atom is placed. Within the EAM approach, the total energy E of a system of atoms is written as the sum of the atomic energies:

$$E = \sum_i E_i. \quad (10.24)$$

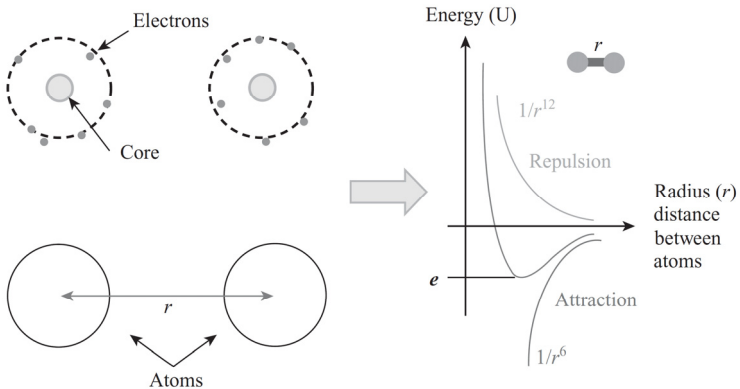


Fig. 10.3 The correlation of the atoms and the potential which is developed: there are regions where the atoms will attract each other when far apart but will repel when they are too close.

¹ Cohesive energy, is the energy which is needed to rip a sample apart into widely separated atoms [295].

Annex F Density functional theory

The idea of DFT, which not only includes bulk materials but also ones such as biological materials, is to study a body of electrons, which includes interacting electrons and use their density for calculations. For N electrons in a solid, which obey the Pauli principle (see [296]) and repulse each other via the Coulomb potential, this means that the basic variable of the system depends only on three spatial coordinates, x , y , and z , rather than $3 * N$ degrees of freedom [297].

The lattice parameter and bulk modulus are two main parameters in DFT calculations. The bulk modulus can be calculated using eq. (10.25), where G is the bulk modulus and δ is the differential energy change for which the differential volume change occurred. The last part of this equation is specially meant for the f_{cc} crystallographic system [298]:

$$G = V \frac{\partial^2 E}{\partial^2 V} = \left(\frac{4}{9a} \right) \frac{\partial^2 E}{\partial^2 a}. \quad (10.25)$$

As mentioned before, the lattice parameter and bulk modulus are two main quantities in DFT calculations. The bulk modulus can be calculated using eq. (10.25), where G is the bulk modulus and δ is the differential energy change for which the differential volume change occurred.

Considering dislocations, the energy change of the system due to stacking sequence when is changed from the perfect bulk lattice can be calculated by DFT, which is another purpose of this method. This energy, called Stacking Fault Energy (SFE), is a variable material quantity in metals and their alloys [299]. The SFE , which controls the slip and the dislocations motion, is a key property in defining the deformation mechanisms in crystal structures. In materials with a low SFE , such as gold (45 mJ/m^2) and silver ($19\text{--}22 \text{ mJ/m}^2$), cross slip of dislocations is hard, and the dislocations are limited to move in a more planar fashion and their mobility decreases. However, in materials with a high SFE , such as aluminum (167.5 mJ/m^2), nickel (128 mJ/m^2) and copper (78 mJ/m^2) dislocations can go through a cross slip easily around obstacles. In metals with a low SFE along slip during plastic deformation, mechanical twinning can also happen [300]. In metals with a medium to high SFE slip is the main deformation mechanism. When the SFE of metals is lowered, the twinning mechanism becomes more significant and some noticeable texture transitions take place [301].

The nature of the slip in metals cannot be presented by only one absolute SFE value. For a correct interpretation, generalized stacking fault energy ($GSFE$) curves, which include both stable and unstable SFE, are used. To calculate this parameter, a supercell with three directions should be defined; in an f_{cc}

material, since (111) and [110] are the glide plane and direction, respectively, normally a supercell will be created, in which the Z axis is aligned along the [111] direction, and X and Y along the [1 - 10] and [11 - 2] directions. Now consider, like the SFE calculations, 12 layers of atoms along the Z direction. The lower block with six atomic layers will be labeled as A and the upper block with another six layers as B . Then the A layer will be shifted along the Y direction as this is the gliding direction. In order to get the $GSFE$ surface plateau, one needs to shift block A along both the X and Y directions. For a convenient description, define a relative translation vector in the (111) plane

$$\vec{f} = x \frac{1}{2} [1\bar{1}0] + y \frac{1}{2[11\bar{2}]} \quad (10.26)$$

By using the above equations, the $GSFE$ surface can be obtained [140].

Annex G Finite element method

Pre-processing. In this step, the elements are defined/created for the part(s). The elements can be of different shapes and sizes. Considering only a one-dimensional problem, this element has only one shape i.e., a line, as shown in Fig. 10.4-a, with two nodal points at the corners of the element. With this element, one can approximate a primary variable u by the following interpolation function:

$$u = a + bx. \quad (10.27)$$

The task is to find the two a and b constants. If the coordinates of two nodes are x_1 and x_2 , then the values at the nodes are

$$u_1 = a + bx_1. \quad (10.28)$$

$$u_2 = a + bx_2, \quad (10.29)$$

Solving these two equations for a and b , and substituting these values in Eq. (10.27), u can be written as

$$u = \frac{x_2 - x}{x_2 - x_1} u_1 + \frac{x - x_1}{x_2 - x_1} u_2 \equiv N_1 u_1 + N_2 u_2. \quad (10.30)$$

where N_1 and N_2 are called shape functions, because they give an idea of the shape of the approximating function u . With this, the task of solution gets transformed into finding the nodal values of the primary variable u , which has the advantage, that the nodal variables convey physical meanings, whereas the constants a and b , in Eq. (10.27), do not represent any physical quantity [302].



Fig. 10.4 (a) A two-noded Lagrangian element. (b) A three-noded Lagrangian element [302].

The two-noded element can provide only a linear approximation. If a quadratic approximation is required, a three-noded element as shown in Fig. 10.4-b can be used. It can easily be shown that the approximating polynomial u can be expressed in terms of the nodal variables as

$$u \equiv N_1 u_1 + N_2 u_2 + N_3 u_3. \quad (10.31)$$

These shape functions are basically Lagrangian interpolation functions and are therefore called Lagrangian shape functions [302]. Other dimensions (2D and

3D) also could be shown the similar relations between the displacement components and polynomials.

Assembly procedure. It is not possible to obtain the nodal values of an element by just solving the elemental equations, because internal load vectors are undetermined due to unknown heat flux at the boundaries of the element. The simple way to assemble the equations is to express the elemental matrices and vectors in a global form and then add them. Supposing the total number of nodal values (degrees of freedom), which equals the primary variables per node times the number of node is N , it is possible to write for each element N equations in n -unknown variables. The elemental equations for a particular element i can be expressed as

$$[K]^i\{\Delta\} = \{R\}^i + \{F\}^i, \quad (10.32)$$

where $\{\Delta\}$ is the global vector of nodal variables and $[K]^i$ is the coefficient matrix of the element expressed in the global form and $\{R\}^i$ and $\{F\}^i$ together are the elemental right-hand side vector expressed in the global form. All the elements of vector $\{R\}^i$ are known, whereas in general, the elements of vector $\{F\}^i$ contain the derivatives of primary variables and are unknown. In the process of summation, elements of $\{F\}^i$ will add up to give 0 at all nodes except the boundary nodes. Thus, there is no need to calculate the vectors $\{F\}^i$ for the interior elements. The final assembled system of equations is

$$[K]\{\Delta\} = \{R\}. \quad (10.33)$$

where $[K]$ is called the global stiffness matrix and $\{R\}$ is the global right side vector [193].

Solving the system of equations. Gauss-elimination is the method in which $[K]$ is converted into an upper triangular form by a number of row operations. At the k -th step of this method, the elements of the k -th column from $(k+1)$ -th row to the n -th row are made zero by multiplying the elements of the k -th row by K_{ik}/K_{kk} , $i = (k+1, k+2, \dots, N)$ and subtracting them from rows $k+1, \dots, n$ to produce zeros in position $(k+1, k), \dots, (n, k)$. The entry K_{kk} is called the pivot and it should not be very small. Therefore, at the k -th step, it is better to interchange the rows to make the magnitude of the pivot large. This is called partial pivoting. To complete pivoting, both rows and columns are interchanged [302].

Post-processing. Once the nodal values of the solution are found, they can be post-processed to provide the derivatives of the primary variables.

Indices

Figure captions

Chapter 1	Introduction	1
Fig. 1.1	(a) Motivation of this work along with the aim. (b) to (f) Different methodologies used in this work.	3
Fig. 1.2	Main aims of this work.	6
Chapter 2	Theoretical background	7
Fig. 2.1	Tube drawing processes: (a) tube sinking, (b) drawing with a fixed plug, (c) floating plug, and (d) drawing on a mandrel [14].	8
Fig. 2.2	Schematic of the wall-thickness and diameter of the tube before and after drawing.	9
Fig. 2.3	Deviating of wall-thickness from an ideal form (eccentricity).....	12
Fig. 2.4	Distribution of eccentricity in extruded and drawn copper tubes [46].	14
Fig. 2.5	Various sources of RSs in metals [58].	15
Fig. 2.6	Measurement penetration vs. spatial resolution for various residual stress measurement methods [82].	17
Fig. 2.7	Schematic cross-sections around a hole drilled into tensile RSs. (a) Before and (b) after hole drilling [84].	18
Fig. 2.8	Monochromatic beam diffractometer showing diffraction from the monochromator to the right and diffraction from the sample to the left resulting in focusing [95].	19
Fig. 2.9	Three-dimensional description of the anisotropy of elastic modulus in crystals of (a) gold, (b) aluminum, (c) magnesium and (d) zinc [101].	21
Fig. 2.10	Schematic of the differences in local or microtexture and global or macrotexture [99].	22
Fig. 2.11	Orientation g of the crystal coordinate system KB with respect to the sample coordinate system KA [100].	24
Fig. 2.12	Euler's angle: (a) Coordinate system is presented as Z -axis and its X - Y plane for the sample; Z' and $X' - Y'$ plane for crystal [116].	24
Fig. 2.13	Schematic representation of a microstructure consisting of different grains i of volume V_i with different orientations. Similar	

	orientations g within an orientation range dg are coded with the same gray value [103].	25
Fig. 2.14	Texture analysis by the Debye–Scherrer method with monochromatic synchrotron radiation. Schematic view of the experimental setup. 2θ is the scattering angle, ω describes the sample rotation, and ϕ denotes the angle along the Debye–Scherrer ring [128].	26
Fig. 2.15	Schematic of Kikuchi pattern formation in SEM-based EBSD technique. (a) Schematic of SEM-EBSD set-up, (b) incidence of electron beam on a polycrystalline material, (c) interaction of incident electron beam and generation of Kikuchi lines, (d) schematic showing diffraction of electron beam from atomic planes [99].	27
Fig. 2.16	The specimen-beam interaction volume in a specimen tilted for EBSD [130].	28
Fig. 2.17	Computational and experimental techniques for a variety of length and time scales [137].	30
Fig. 2.18	Schematic of concurrent bridging method, showing the bridges for downscaling and upscaling [142].	32
Chapter 3	Experimental and simulation procedures	41
Fig. 3.1	The tube drawing facility [205].	42
Fig. 3.2	The micrograph of the as-received sample at <i>Max</i> side of the tube.	42
Fig. 3.3	(a) Schematic of the created pattern on the surface of the tube with different rings and measure points and (b) the measure points on each ring.	44
Fig. 3.4	Sketch of the (a) tilting and (b) offset principle.	44
Fig. 3.5	(a) Placing the guiding block before the main die. (b) The guiding die inside the guiding block, with the same diameter as the tube.	44
Fig. 3.6	Definition of the “positive tilting”: positioning the <i>Max</i> on top in the same direction of the tilting angle.	45
Fig. 3.7	The new designed block with the possibility of tilting the die from outlet [209].	46
Fig. 3.8	Stresstech hole drilling device.	47
Fig. 3.9	Schematic of the SALSA instrument at ILL in Grenoble, France [212].	47
Fig. 3.10	Sample geometry for the neutron measurement of strains at the SALSA strain imager.	48
Fig. 3.11	Sketch of the Interrupted Drawn Tube (IDT).	49
Fig. 3.12	Two different IDTs after (a) first and (b) second drawing steps.	49

Fig. 3.13	Measurement points in an IDT.	50
Fig. 3.14	Texture measurements performed on the IDT.	50
Fig. 3.15	Beamline set-up for texture measurement at HEMS-P07 [173].51	
Fig. 3.16	Schematic of the multiscale simulation, showing the bridges for upscaling related to garnering the plasticity information for forming finite element simulations.	53
Chapter 4 Eccentricity		57
Fig. 4.1	The eccentricity of the as-received copper tubes of G-I and G-II series.	57
Fig. 4.2	Variation of eccentricity after drawing without (0°) and with ±5° tilting angles.	58
Fig. 4.3	Variations of <i>Max</i> and <i>Min</i> after each drawing steps and changes in the eccentricity of the tubes drawn with -5° (left column) and +5° (right column).	58
Fig. 4.4	(a) The absolute (left y-axis) and relative (right y-axis) changes of eccentricity for some tubes drawn with a tilting angle of -5°. (b) Plotting the relative change of eccentricity in the ΔE vs. the tilting angle diagram.	59
Fig. 4.5	Relative change of the eccentricity for different tilting angles for two different series of copper tubes after first drawing step; (a) G-I and (b) G-II.	60
Fig. 4.6	Initial contact between the tube and the tilted die (negative tilting), <i>Max</i> reaches the die first.	60
Fig. 4.7	Relative changes of the eccentricity after second drawing step of copper tubes; (a) G-I series and (b)-II series.	61
Fig. 4.8	Drawing forces measured for tube drawing with different tilting angles.	62
Fig. 4.9	Relative change of eccentricity in G-I series after the first step of drawing with different offset values.	62
Fig. 4.10	Relative change of eccentricity in the combination of negative tilting angles with negative shifting values for Cu-tubes.	63
Fig. 4.11	Relative change of eccentricity for the combination of negative tilting angles with positive shifting values for Cu-tubes.	64
Fig. 4.12	Eccentricity of as-received aluminum, brass, and steel tubes...64	
Fig. 4.13	Relative changes of the eccentricity for (a) aluminum, (b) brass, and (c) steel tubes.	65
Fig. 4.14	Comparison of the trend lines of all four materials after drawing with different tilting angles.	66
Chapter 5 Residual stresses		69

- Fig. 5.1 (a) Axial and (b) hoop RSs in three different positions measured in a copper pre-tube. 70
- Fig. 5.2 (a) Axial and (b) hoop RSs at three positions over the circumference of the tube; *Max*, *Min*, and 90° , measured after first drawing step with no tilting. 70
- Fig. 5.3 (a) Axial and (b) hoop RSs at three positions over the circumference of the tube; *Max*, *Min*, and 90° , measured after first drawing step with -5° tilting. 71
- Fig. 5.4 Comparison of the RSs in axial direction in three positions over the circumference of the tube. 71
- Fig. 5.5 Axial RSs at (a) *Max* and (b) *Min* sides of the tubes drawn under 0° , -5° , and $+5^\circ$ tilting angles. 72
- Fig. 5.6 Hoop RSs at (a) *Max* and (b) *Min* sides measured after drawing with three different tilting angles; 0 , -5 , and $+5^\circ$ 72
- Fig. 5.7 (a) Axial and hoop RSs at *Max* and *Min* side of the drawn tube with -5° tilting. (b) RSs of different tubes after first drawing step with different tilting angles. 72
- Fig. 5.8 Average axial RSs at *Max* side of the tube measured in tubes drawn with 0° and $\pm 5^\circ$ tilting. 73
- Fig. 5.9 The axial RSs at *Max* side of different tubes drawn with different tilting angles; (a) aluminum, (b) brass, and (c) steel tubes. 73
- Fig. 5.10 Schematic of measurement positions on the IDT after first drawing step. 74
- Fig. 5.11 (a) 3D and (b) 2D demonstrations of scans performed through the wall-thickness at a measurement points. 75
- Fig. 5.12 Intensity profile in different depth positions at *Max* of the drawn tube with -5° tilting; first drawing step. 76
- Fig. 5.13 (a) The variation of the peak center for four different positions in the -5° drawn tube at *Max* at the as-received position (P100), beginning of deformation zone (P10), beginning of the bearing zone (P0), and the drawn tube (P-15). (b) Peak shift from the ideal 2θ for the whole IDT. 77
- Fig. 5.14 Measured residual strains at *Max* side of the tube drawn with -5° tilting in directions (a) axial, (b) hoop, and (c) radial. 78
- Fig. 5.15 Measured RSs in an IDT of first drawing step drawn with -5° tilting angle at *Max* side in axial, hoop, and radial directions for positions (a) P10, (b) P5, (c) P0, and (d) P-10. 79
- Fig. 5.16 (a) Change of axial and hoop RSs at *Max* side of the tube with -5° tilting going from the as-received tube (P10) to the deformation zone (P5). (b) Comparison of the axial RSs at *Max* side of tubes drawn with -5° and 0° [229]. 80
- Fig. 5.17 (a) Peak center in axial direction after first and second drawing at *Min* side of the tube drawn with -5° tilting. (b) Peak shifts in the

	IDT of second step starting in the as-received tube and going to the drawn one.....	81
Fig. 5.18	Variation of the RSs at <i>Max</i> side of the tube after first and second drawing step with -5° tilting.....	81
Chapter 6 Texture development		83
Fig. 6.1	{111}, {200}, and {220} PFs at (a) <i>Max</i> and (b) <i>Min</i> side of the as-received tubes.	84
Fig. 6.2	(a) {111} PF of Cu after heat treatment at 400°C [230]. (b) Cube component in recrystallization texture of Cu [231].	85
Fig. 6.3	{111}, {200}, and {220} PFs of heat-treated copper tube after volume and anisotropic absorption corrections [214].	85
Fig. 6.4	The ODF sections of the as-received tube at (a) <i>Max</i> and (b) <i>Min</i> sides for different φ_2 angles. (c) ODF section 0° and 45° Sections of ODFs, which mostly are discussed in deformation processes.	86
Fig. 6.5	Rolling texture of (a) pure copper, showing metal-type or pure-type ODF and (b) brass (Cu-37%Zn) showing alloy-type ODF [235].	87
Fig. 6.6	The (a) 0° and (b) 45° ODF sections of the as-received tube at <i>Max</i> and <i>Min</i> sides of the as-received tube.	88
Fig. 6.7	The {111}, {200} and {220} PFs of the <i>Max</i> side of the tube drawn with -5° tilting angle.	88
Fig. 6.8	The {111}, {200} and {220} PFs at the <i>Max</i> and <i>Min</i> sides of the tube drawn with -5° tilting angle.	89
Fig. 6.9	The {111}, {200} and {220} PFs at the <i>Max</i> side of the tubes with (a) -5° and (b) $+5^\circ$ tilting angle.	89
Fig. 6.10	45° ODF of (a) <i>Max</i> and (b) <i>Min</i> sides of the tube drawn with -5° tilting angle	90
Fig. 6.11	(a) Measurement points through wall-thickness of the tube. (b) Comparison of the <i>Cu</i> and cube components at <i>Max</i> and <i>Min</i> sides of the as-received tube. (c) and (d) Variation of four main components at <i>Max</i> and <i>Min</i> sides of the as-received tube.	91
Fig. 6.12	Variation of the main components <i>Cu</i> , cube, Goss, and <i>Bs</i> before and after drawing at (a and b) <i>Max</i> and (c and d) <i>Min</i> side of the tube. P1 to P9 are the measurement points, which are shown in Fig. 6.11.	91
Fig. 6.13	{111} PFs of drawn tube after second drawing step at (a) <i>Max</i> and (b) <i>Min</i> sides of the tube. 45° section of ODF in the same sample at (c) <i>Max</i> and (d) <i>Min</i> . Because of the symmetry in the ODF, only $0 < \varphi_1 < 180$ is presented.	92

Fig. 6.14	Different components through the wall-thickness of the tube at <i>Max</i> side before and after drawing; (a) <i>Cu</i> , (b) cube, (c) <i>Bs</i> , and (d) Goss components.	93
Fig. 6.15	Micrograph of the <i>Max</i> (a) and <i>Min</i> (b) sides of the as-received tube.	94
Fig. 6.16	Micro-textures of the drawn tubes at <i>Max</i> side with (a) 0° tilting and (b) -5° tilting angle. The legend of these micrographs is same as Fig. 6.15.	95
Fig. 6.17	(a) {111}, (b) {100}, and (c) {110} PFs of the as-received tubes at <i>Min</i> side. The maximum intensity of PFs is approx. 1.78.	95
Fig. 6.18	(a) {111}, (b) {100}, and (c) {110} PFs of the standard drawn tubes after second drawing step at <i>Min</i> . The maximum intensity of PFs is approx. 2.42.	96
Fig. 6.19	(a) {111}, (b) {100}, and (c) {110} PFs of the drawn tubes with -5° tilting angle after second drawing step at <i>Min</i> . The maximum intensity of PFs is approx. 3.71.	96
Chapter 7 Multiscale simulation		99
Fig. 7.1	Schematic presentation of the multiscale methodology which was used in this work to simulate the tube drawing process.	100
Fig. 7.2	(a) Variations of lattice parameter and bulk modulus of copper as a function of <i>k</i> -point mesh. (b) Energy changes by changing the lattice parameter of copper.	101
Fig. 7.3	Edge dislocation in a <i>fcc</i> crystal [174], (b) formation of stacking fault and partial Shockley dislocation [244].	102
Fig. 7.4	Variation of <i>GSFE</i> along the (a) <110> and (b) <112> directions. γ_{ut} is the unstable twinning stacking fault energy, γ_{int} is the intrinsic stacking fault energy, and the γ_{us} is the extrinsic or unstable stacking fault energy.	103
Fig. 7.5	Layer-by-layer energy contributions to the extrinsic, intrinsic, and twin stacking fault energies [245].	103
Fig. 7.6	Dislocation in the simulation box, which was created for MD simulations.	105
Fig. 7.7	(a) Energy versus lattice parameters of copper with different lattice structures calculated by MEAM and calibrated using DFT results. (b) Partial <i>GSFE</i> (along < 112 >) calculated by MEAM and DFT.	106
Fig. 7.8	Creation of step due to the movement of the simulation box, which is because of the applied shear stress.	106
Fig. 7.9	(a) Position of the dislocation as a function of time, (b) Dislocation mobility (velocity) calculated for each applied shear stress.	107

- Fig. 7.10 (a) Drag coefficient calculated for different applied shear stresses. (b) Variation of drag coefficient as function of temperature, calculated by Jassby and Vreeland (1970) [262]. 107
- Fig. 7.11 (a) Variation of $\gamma\dot{\gamma}$ as a function of time calculated by DD simulation to find out the C value, which is equals to 49.2. (b) Evolution of dislocation density in DD simulations. 109
- Fig. 7.12 (a) Variation of κ by changing the plastic strain. (b) Fitting the different hardening parameters in different sets used to calculate most suitable parameters. 110
- Fig. 7.13 (a) Assembly of the first drawing step, showing tube, die, and plug. (b) Global and submodel. 111
- Fig. 7.14 The simulated tube after a drawing step imported as the input for the next drawing step. 112
- Fig. 7.15 Different mesh sizes, used in simulations to get the most proper mesh size: (a) 5 mm, (b) 3.6 mm, and (c) 2.1 mm. 113
- Fig. 7.16 Variation of the simulated eccentricity, before and after drawing for 7 different tubes drawn with 0° and -5° tilting angles and their comparison with the experimental results. 114
- Fig. 7.17 (a) Simulated relative change of eccentricity, showing the effect of tilting on the variation of eccentricity. (b) Comparison of the average relative change of eccentricity and the trend line of simulated and measured values for Cu-tubes. 115
- Fig. 7.18 Iso-surface for the mass flow during tube drawing (a) without tilting and (b) with -5° tilting. 115
- Fig. 7.19 Simulated and measured RSs in axial, hoop, and radial directions at *Max* side of the tube in (a) P5, deformation zone, (b) P0, beginning of the bearing zone, (c) P-10, after drawing. (d) Simulated and measured stress-strain diagrams of drawn tube with 0° and -5° tilting angles. 116
- Fig. 7.20 Comparison of the experimentally measured stress-strain diagram of a drawn copper tube with standard drawing (0° tilting) at *Max* side of the tube with the simulated values for different sets, presented in Table 7.6. 117
- Fig. 7.21 The (a) $\{111\}$, $\{100\}$, and $\{110\}$ PFs and (b) 0° , 45° , and 65° sections of ODF of the input texture, representing the texture of the as-received tube. 118
- Fig. 7.22 The simulated (a) $\{111\}$, $\{100\}$, and $\{110\}$ PFs and (b) $\varphi_2 = 0^\circ$, 45° , and 65° sections of ODF of the drawn tube without tilting after the first drawing step at *Max* side of the tube. 118
- Fig. 7.23 The $\{111\}$, $\{100\}$, and $\{110\}$ PFs of drawn tube with -5° tilting after second drawing step at (a) *Max* and (b) *Min* side of the tube. 119
- Fig. 7.24 Comparison of experimentally measured (a and b) and simulated (c and d) $\{111\}$ PFs at *Max* and *Min* sides of the tubes after second drawing step, drawn with -5° 120

Fig. 7.25	The (a) experimentally measured and (b) simulated $\varphi_2 = 45^\circ$ ODF section at <i>Max</i> side of the tubes after second drawing step, drawn with -5°	120
Fig. 7.26	The $\varphi_2 = 0^\circ, 45^\circ,$ and 65° ODF sections of drawn tube with (a) -5° and (b) 0° tilting angle after second drawing step at <i>Max</i> side of the tube.	121
Chapter 9	Résumé de thèse en Français.....	128
Fig. 9.1	Schéma de basculement (tilting).....	129
Fig. 9.2	Schéma de décalage (offset)z	129
Fig. 9.3	Les objectifs de cette thèse de doctorat.....	130
Fig. 9.4	Méthodologie multi échelle.....	132
Fig. 9.5	Principales étapes de ce travail	132
Fig. 9.6	Géométrie d'un échantillon pour la mesure par neutrons de la déformation à l'imageur de tension SALSA	133
Fig. 9.7	Points de mesure en mm et étapes d'interruption de l'étirage (IDT).....	133
Fig. 9.8	Définition des configurations de l'inclinaison positive et négative.	134
Fig. 9.9	(a) Modifications relatives de l'excentricité pour la première et (b) deuxième étape de l'étirage.	134
Fig. 9.10	Méthodologie multi-échelle.	135
Fig. 9.11	Calculs et mesures des CR en directions axiale, longitudinale, et radiale en (a) P10, (b) P5, (c) P0, et (d) P-10 pour étirer le tube avec -5° d'inclinaison.	137
Fig. 9.12	{111} PF du tube étiré après la 2ème étape d'étirage à (a) Max et (b) Côtés <i>Min.</i> Du tube. Section de 45° de ODF dans le même échantillon à (c) <i>Max</i> et (d) <i>Min.</i> En raison de la symétrie dans l'ODF, seulement $0 < \varphi_1 < 180$ est présenté.	137
Fig. 9.13	{111}, {100}, and {110} PFs du tube standard après la deuxième étape de l'étirage au <i>Min.</i>	138
Fig. 9.14	{111}, {100}, and {110} PFs du tube standard après la deuxième étape de l'étirage avec un angle d'inclinaison de -5° au <i>Min.</i> 139	
Chapter 10	Annexes	142
Fig. 10.1	(a) Projection plane and reference sphere with a rolled sheet at the center. (b) Projection of the poles RD, TD, and ND on the reference plane constituting the sample reference frame of a pole figure. (c) The points of intersection of the normal to the plane (100), (010), and (001) of the specimen on the reference sphere. (d) The three poles 100, 010, and 001, as projected on the basic circle. (e) Clustering of projected poles of (100), (010), and (001)	

	planes from the different grains of the specimen. (f) Pole densities are shown as contour lines [99].....	143
Fig. 10.2	The deformation gradient F is multiplicatively decomposed into elastic F_e , volumetric F_v , and plastic F_p components [268]. In this work only the F_e and F_p components are considered.	144
Fig. 10.3	The correlation of the atoms and the potential which is developed: there are regions where the atoms will attract each other when far apart but will repel when they are too close.	153
Fig. 10.4	(a) A two-noded Lagrangian element. (b) A three-noded Lagrangian element [302].....	156

Table captions

Chapter 2	Theoretical background	7
Table 2.1	Diffraction elastic constant, E_{hkl} (GPa) calculated from using the Kröner model [97].....	20
Table 2.2	Diffraction Poisson's ratio, ν_{hkl} , calculated from the Kröner model [97].	20
Chapter 3	Experimental and simulation procedures.....	41
Table 3.1	The chemical composition of the Cu-DHP tubes.	42
Table 3.2	Drawing steps for Cu-DHP tubes of sizes 65.0 × 5.5 mm and 64.0 × 3.1 mm.	43
Table 3.3	Chemical compositions of the aluminum, brass and steel tubes.	43
Table 3.4	Drawing steps for aluminum, brass and steel tubes.	43
Table 3.5	Tilting angle, offset value, and combination of tilting/offset.....	45
Table 3.6	Experimental parameters and conditions for RS measurement using SALS.	48
Chapter 6	Texture development.....	83
Table 6.1	The most important orientations of Cu and Cu alloys after deformation with their Euler Angles and Miller indices [231].....	87
Chapter 7	Multiscale simulation.....	99
Table 7.1	Input parameter used for electronic scale simulation.....	101
Table 7.2	C_{11} , C_{12} , and C_{44} elastic constants calculated by MEAM at this work, compared with values from the literature.....	106
Table 7.3	Sets of hardening parameters used to correlate the DD results, compared to other researchers' results.....	110
Table 7.4	Parameters used in FEM simulations.	112
Table 7.5	Different energies of the simulation model for tube drawing with - 2° tilting angle.....	114
Table 7.6	Different sets used for sensitivity study of m and γ_0 . Set 1 was the so far used values.	117

Subject indices

Aluminum	.1, 4, 13, 14, 21, 22, 43, 45, 59, 66, 67, 68, 75, 76, 84, 90, 113, 127, 158, 163, 165, 166, 172, 180, 184, 188, 193, 204, 206
Atomic19, 28, 30, 31, 36, 37, 56, 103, 108, 109, 114, 116, 125, 126, 130, 154, 157, 159, 164, 189
Atomistic	32, 36, 187, 188, 193, 194
Brass	..4, 22, 43, 45, 59, 66, 67, 68, 69, 75, 76, 84, 90, 91, 127, 128, 165, 166, 167, 172, 204, 206
Bridging112, 114, 193, 194
Copper1, 2, 4, 5, 13, 14, 23, 26, 31, 40, 41, 43, 47, 52, 54, 55, 56, 59, 62, 64, 65, 66, 68, 69, 72, 75, 76, 84, 88, 89, 90, 91, 92, 101, 103, 104, 105, 106, 108, 109, 110, 112, 114, 121, 125, 126, 127, 128, 129, 130, 158, 163, 165, 166, 167, 168, 169, 179, 184, 192, 193, 194, 197, 204, 205, 206
CP5, 32, 34, 56, 57, 103, 114, 126, 130, 135, 144
CPFEM57, 114, 115, 116, 117
Crystal Plasticity5, 32, 39, 103, 114, 188, 189, 195
DD	5, 32, 34, 36, 55, 56, 57, 103, 108, 112, 113, 114, 126, 130, 135, 144, 154, 155, 169, 172
Density functional theory158, 196
DFT5, 32, 37, 39, 55, 56, 103, 104, 108, 109, 110, 125, 129, 135, 143, 158, 168
Dislocation dynamics	36, 112, 154
Dislocation Dynamics5, 32, 56, 191, 196
Drawing force10
EBSD4, 23, 27, 28, 29, 54, 87, 98, 102, 129, 142, 164, 191, 194
Eccentricity12, 43, 45, 54, 59, 63, 65, 67, 84, 116, 117, 118, 165, 179, 203, 204, 206
Electronic scale5, 32, 36, 38, 103, 104, 105, 125, 129, 172
Electronic scale38, 104, 105, 108
Embedded atom method157
Finite element method160
Hole drilling4, 17, 18, 48, 49, 50, 71, 76, 82, 84, 128, 140, 163, 164
ICME5, 30, 54, 103, 125, 129, 143, 186, 206
Integrated computational material engineering29
Macroscale analysis33
MD5, 55, 56, 103, 108, 109, 110, 112, 125, 130, 135, 143, 144, 155, 168
MEAM	..5, 36, 37, 38, 55, 56, 57, 103, 108, 109, 110, 112, 125, 126, 130, 135, 143, 144, 168, 172, 191, 194
Mesh117
Mesoscale analysis34
Microscale112
Micro-texture4, 52, 87, 97, 100, 101, 102, 129
Modified embedded atom method37, 108, 109, 189
Molecular dynamics110
Multiscale simulation29, 55, 87, 103, 168, 172
Neutron	4, 5, 17, 18, 20, 23, 26, 29, 41, 43, 49, 50, 52, 54, 57, 71, 76, 77, 78, 81, 82, 84, 85, 87, 88, 97, 101, 103, 115, 126, 128, 129, 130, 147, 164, 183, 186
Neutron diffraction19, 76, 183, 186, 203
Offset	2, 4, 46, 47, 48, 54, 59, 60, 64, 65, 68, 69, 103, 126, 127, 128, 129, 130, 133, 154, 164, 165, 170, 172
PETRA III4, 191

Precision Tube	1, 3, 203, 204, 206
Residual strain	48, 49, 76
Residual Stresses	179, 180, 181, 182, 183, 190, 203, 206
RSs ...	2, 4, 5, 7, 12, 15, 16, 17, 18, 21, 23, 43, 48, 49, 50, 54, 63, 69, 71, 72, 73, 74, 75, 76, 78, 79, 80, 81, 82, 83, 84, 85, 87, 103, 115, 116, 119, 120, 121, 123, 125, 126, 128, 129, 130, 163, 166, 167, 169
Steel ..	1, 2, 4, 13, 40, 43, 45, 59, 66, 67, 68, 69, 75, 76, 84, 90, 127, 128, 165, 166, 172, 179, 180, 181, 182, 184, 204, 206
STRESS-SPEC	4, 52, 142, 191
Structure scale	11, 39
Synchrotron ..	4, 5, 17, 19, 23, 26, 27, 29, 52, 53, 54, 87, 94, 97, 101, 103, 129, 132, 147, 164, 183, 185
Texture	2, 4, 5, 7, 20, 21, 22, 23, 24, 26, 29, 32, 33, 34, 43, 52, 53, 54, 57, 79, 85, 87, 88, 89, 90, 91, 92, 94, 96, 97, 99, 100, 101, 102, 103, 115, 116, 121, 122, 123, 124, 125, 126, 128, 129, 130, 132, 133, 135, 137, 139, 144, 145, 146, 150, 158, 165, 167, 169, 177, 179, 183, 185, 191, 192, 194, 197, 205, 206
Tilting	4, 28, 46, 47, 59, 127, 172, 203, 204
Tube drawing ..	2, 4, 5, 7, 9, 10, 11, 12, 16, 34, 40, 41, 43, 44, 45, 54, 56, 60, 64, 69, 81, 84, 87, 103, 104, 114, 115, 118, 119, 126, 127, 128, 130, 164, 165, 168, 169, 172, 178, 179, 181, 190, 204, 206

Chapter 11 References

- [1] Copper Development Association Inc., *Copper Tube Handbook: Industry Standard Guide for the Design and Installation of Copper Piping Systems*. New York: CDA Publication, 2016.
- [2] M.S.J. Hashmi, "Aspects of tube and pipe manufacturing processes: Meter to nanometer diameter," *3rd Brazilian Congress on Manufacturing Engineering*, vol. 179, no. 1–3, pp. 5–10, 2006.
- [3] F. Dohmann and C. Hartl, "Tube hydroforming—research and practical application," *Journal of Materials Processing Technology*, vol. 71, no. 1, pp. 174–186, 1997.
- [4] J. R. Davis, Ed., *Aluminum and Aluminum Alloys*. Materials Park, OH: Asm International, 1993.
- [5] S. N. David Chua, B. J. MacDonald, and M.S.J. Hashmi, "Finite element simulation of slotted tube (stent) with the presence of plaque and artery by balloon expansion," *Journal of Materials Processing Technology*, vol. 155–156, pp. 1772–1779, 2004.
- [6] "Pipe and Tube Manufacturing Processes," in *Mechanics of offshore pipelines*, vol. 1, *Mechanics of offshore pipelines*, S. Kyriakides and E. Corona, Eds., 1st ed., Amsterdam, Boston, London: Elsevier, 2007, pp. 59–89.
- [7] B. S. K.H. Brensing, "Steel Tube and Pipe Manufacturing Process," *Salzgitter Gro-rohre GmbH*.
- [8] "Wrought Copper Materials," in *Copper in the automotive industry*, H. Lipowsky and E. Arpaci, Eds., Weinheim, Brussels, Belgium: Wiley-VCH; In cooperation with ECI—European Copper Institute, 2007, pp. 29–43.
- [9] E. Tenckhoff, *Deformation mechanisms, texture, and anisotropy in zirconium and Zircaloy*. Philadelphia, PA: American Society for Testing and Materials, 1988.
- [10] Joseph R. Davis, S. L. Semiatin, Ed., *ASM Metals Handbook: Forming and Forging*: American Society for Metals, 1989.
- [11] H. A. Youssef, H. El-Hofy, and M. H. Ahmed, *Manufacturing technology: Materials, processes, and equipment*. Boca Raton, London, New York: CRC Press, Taylor & Francis Group, op. 2012.
- [12] H.-J. Gummert, Ed., *Drawing: The production of wires, bars and tubes*. [Viersen, Stauferstraße 15]: H.-J. Gummert, 2006.
- [13] V. Boljanovic, *Metal shaping processes: Casting and molding, particulate processing, deformation processes, and metal removal*. New York: Industrial Press, 2010.

- [14] G. E. Dieter, H. A. Kuhn, and S. L. Semiatin, Eds., *Handbook of Workability and Process Design: Drawing of Wire, Rod, and Tube*. USA: American Society for Metals, 2003.
- [15] H. Tschaetsch, *Metal Forming Practise: Processes - Machines - Tools*. Berlin, Heidelberg: Springer-Verlag Berlin Heidelberg, 2006.
- [16] N. Şandru and G. Camenschi, "A mathematical model of the theory of tube drawing with floating plug," *International Journal of Engineering Science*, vol. 26, no. 6, pp. 569–585, 1988.
- [17] A. Geleji, *Bildsame Formgebung der Metalle: Theorie, Experiment und Anwendung*. Berlin: Akad.-Verl., 1967.
- [18] F. Anke and M. Vater, *Einführung in die technische Verformungskunde: Mit 31 Tafeln*. Düsseldorf: Verl. Stahleisen, 1974.
- [19] K.-H. Grote and E. K. Antonsson, *Springer handbook of mechanical engineering*. New York [New York], Boston, Massachusetts: Springer; Credo Reference, 2014.
- [20] Lippmann, Horst, Mahrenholtz, Oskar, *Plastomechanik der Umformung metallischer Werkstoffe: Erster Band*. Berlin, Heidelberg: Springer Berlin Heidelberg, 1967.
- [21] O. Hoffman and G. Sachs, *Introduction to the theory of plasticity for engineers*. New York [u.a.]: McGraw-Hill, 1953.
- [22] H. W. Swift, "LXXXI. Stresses and strains in tube-drawing," *Philosophical Magazine Series 7*, vol. 40, no. 308, pp. 883–902, 1949.
- [23] R. Hill, "A Theory of the Yielding and Plastic Flow of Anisotropic Metals," *Proceedings of the Royal Society of London A: Mathematical, Physical and Engineering Sciences*, vol. 193, no. 1033, pp. 281–297, <http://rspa.royalsocietypublishing.org/content/royprsa/193/1033/281.full.pdf>, 1948.
- [24] S. Elion and J.M. Alexander, "An industrial investigation of a process for tube drawing," *Engineer*, no. 211, pp. 682–695, 1961.
- [25] A.P. Green, "Plane Strain Theories of Drawing," *Proc Instn Mech Engr*, no. 174, pp. 847–864, 1960.
- [26] T. Z. Blazynski, *Design of Tools for Deformation Processes*, 1st ed. Dordrecht: Springer Netherlands, 1986.
- [27] W. Johnson and P. B. Mellor, *Engineering plasticity*. Chichester, West Sussex, England, New York: E. Horwood; Halsted Press, 1983.
- [28] G. G. Moore and J. F. Wallace, "Theories and Experiments on Tube Sinking through Conical Dies," *Proceedings of the Institution of Mechanical Engineers*, vol. 182, no. 1, pp. 19–32, 1967.
- [29] B. Avitzur, *Handbook of metal-forming processes*. New York: Wiley, 1983.
- [30] K.-K. Um and L. Dong Nyung, "An upper bound solution of tube drawing," *Journal of Materials Processing Technology*, vol. 63, no. 1–3, pp. 43–48, 1997.

- [31] E. M. Rubio, "Analytical methods application to the study of tube drawing processes with fixed conical inner plug: Slab and Upper Bound Methods," *Journal of Achievements in Materials and Manufacturing Engineering of Achievements in Materials and Manufacturing Engineering*, vol. 14, no. 1-2, pp. 119–130, 2006.
- [32] E. M. Rubio, C. González, M. Marcos, and M. A. Sebastián, "Energetic analysis of tube drawing processes with fixed plug by upper bound method," *Journal of Materials Processing Technology*, vol. 177, no. 1–3, pp. 175–178, 2006.
- [33] B.R. Kumar, A.K. Singh, S. Das, and D.K. Bhattacharya, "Cold rolling texture in AISI 304 stainless steel," *Materials Science and Engineering: A*, vol. 364, no. 1-2, pp. 132–139, 2004.
- [34] M. Bauser, G. Sauer, K. Siegert, and A. F. Castle, *Extrusion*, 2nd ed. Materials Park, Ohio: ASM, 2006.
- [35] L. D. Pari, "Numerical Modeling of Copper Tube Extrusion Process and Eccentricity Analysis," *Journal of Manufacturing Science and Engineering*, vol. 134, 2012.
- [36] Robert F. Bennett, Nicholaas L. Brouwer, and David M. Stricker, "System for determining tube eccentricity," US4099418 A US 05/772,529.
- [37] A. Carradò *et al.*, "Development of Residual Stresses and Texture in Drawn Copper Tubes," *Advanced Engineering Materials*, pp. 1–7, 2013.
- [38] H. A. Merki, S. Naegeli, and J. Daleo, "Device for the ultrasound measuring of cylindrical test models," US7140253 B2 US 10/871,276.
- [39] G. Sansoni, P. Bellandi, and F. Docchio, "Design and development of a 3D system for the measurement of tube eccentricity," (en), *Meas. Sci. Technol.*, vol. 22, no. 7, p. 75302, 2011.
- [40] *Copper and copper alloys - Seamless, round tubes for general purposes*, EN 12449:2012, 2012.
- [41] *Seamless steel tubes for oil- and water-hydraulic systems - Calculation rules for pipes and elbows for dynamic loads*, 2413:2011-06, 2011.
- [42] *Aluminium and aluminium alloys - Extruded round, coiled tube for general applications - Specification*, EN 13957:2008, 2009.
- [43] D. Lévesque *et al.*, "Thickness and grain size monitoring in seamless tube-making process using laser ultrasonics," *NDT & E International*, vol. 39, no. 8, pp. 622–626, 2006.
- [44] Hill John R, Sawester Joseph A, "Patent US3167176 - Method of and apparatus for correcting tube eccentricity," US3167176 A.
- [45] S. N. Randall and H. Prieur, "Tubular production in the cold pilger machine," *Iron Steel Eng.*, 109–117., 1967.
- [46] G. Tetley, "Variation of eccentricity during block drawing of tubes," *J. Applied Metalworking*, vol. 1, no. 1, pp. 80–83, 1978.
- [47] W. Xu, K. Wang, P. Wang, and J. Zhou, "A newly developed plug in the drawing process for achieving the high accuracy of aluminum rectangular tube," *Int J Adv Manuf Technol*, vol. 57, no. 1-4, pp. 1–9, 2011.

- [48] P. Huml, R. Fogelholm, and A. Salwén, "Optimization of Cold Rolling of Precision Tubes," *CIRP Annals - Manufacturing Technology*, vol. 42, no. 1, pp. 283–286, 1993.
- [49] H. Abe, T. Iwamoto, Y. Yamamoto, S. Nishida, and R. Komatsu, "Dimensional accuracy of tubes in cold pilgering," *Journal of Materials Processing Technology*, vol. 231, pp. 277–287, 2016.
- [50] R. S. Matos, T. A. Laursen, J.V.C. Vargas, and A. Bejan, "Three-dimensional optimization of staggered finned circular and elliptic tubes in forced convection," *International Journal of Thermal Sciences*, vol. 43, no. 5, pp. 477–487, 2004.
- [51] R. Bihanta *et al.*, "A new method for production of variable thickness aluminium tubes: Numerical and experimental studies," *Journal of Materials Processing Technology*, vol. 211, no. 4, pp. 578–589, <http://www.sciencedirect.com/science/article/pii/S0924013610003523>, 2011.
- [52] Q. H. Bui *et al.*, "Investigation of the formability limit of aluminium tubes drawn with variable wall thickness," *Journal of Materials Processing Technology*, vol. 211, no. 3, pp. 402–414, <http://www.sciencedirect.com/science/article/pii/S0924013610003250>, 2011.
- [53] M. Negendank, U. A. Taparli, S. Gall, S. Müller, and W. Reimers, "Microstructural evolution of indirectly extruded seamless 6xxx aluminum tubes with axial variable wall thickness," *Journal of Materials Processing Technology*, vol. 230, pp. 187–197, 2016.
- [54] M. Negendank, S. Müller, and W. Reimers, "Extrusion of Aluminum Tubes with Axially Graded Wall Thickness and Mechanical Characterization," *Procedia CIRP*, vol. 18, pp. 3–8, 2014.
- [55] R. Bihanta, M. R. Movahhedy, and A. R. Mashreghi, "A numerical study of swage autofrettage of thick-walled tubes," *Materials & Design*, vol. 28, no. 3, pp. 804–815, 2007.
- [56] Bihanta, R., Ameli, A., Movahhedy, M.R., Mashreghi, A.R., "A comparative study on the radial and indentation forging of tubes," *International Journal of Forming*, vol. 10, no. 2, pp. 179–194, 2007.
- [57] H. Reißner, "Eigenspannungen und Eigenspannungsquellen," *Z. angew. Math. Mech.*, vol. 11, no. 1, pp. 1–8, 1931.
- [58] J. O. Almen and P. H. Black, *Residual Stresses and fatigue in metals*. New York: McGraw-Hill, 1963.
- [59] G. E. Totten, M. A. H. Howes, and T. Inoue, Eds., *Handbook of residual stress and deformation of steel*. Materials Park, OH: Asm International, 2002.
- [60] P. J. Withers and Bhadeshia, H. K. D. H., "Residual stress. Part 2; Nature and origins," *Materials Science and Technology*, vol. 17, no. 4, pp. 366–375, 2001.

- [61] E. Macherauch, "INTRODUCTION TO RESIDUAL STRESS," in *Advances in surface treatments*, vol. 4, *Residual stresses*, A. Niku-Lari, Ed., Oxford [u.a.]: Pergamon Press, 1987, pp. 1–36.
- [62] E. Heyn and O. Bauer, "Measurement of Residual Stresses in Cold Drawn Metals," *Internationale Zeitschrift für Metallographie*, vol. 1, pp. 16–50, 1911.
- [63] S. Timoshenko, *Strength of Materials: Part II, Advanced Theory and Problems*. Lancaster: Lancaster Press, 1940.
- [64] S. Timoshenko, *Strength of Materials: Part I, Elementary Theory and Problems*. Lancaster: Lancaster Press, 1940.
- [65] M. I. Hetényi, *Handbook of experimental stress analysis*. New York, NY, USA: Wiley, 1963.
- [66] M. Elices, "Influence of residual stresses in the performance of cold-drawn pearlitic wires," *Journal of Materials Science*, vol. 39, no. 12, pp. 3889–3899, 2004.
- [67] Takashi Nakashima Kouichi Kuroda Kenichi Beppu, "Cold finished seamless steel tubes," USA US11039954.
- [68] T. Kuboki, K. Nishida, T. Sakaki, and M. Murata, "Effect of plug on levelling of residual stress in tube drawing," *Journal of Materials Processing Technology*, vol. 204, no. 1-3, pp. 162–168, 2008.
- [69] P. J. Withers and Bhadeshia, H. K. D. H., "Residual stress. Part 1; Measurement techniques," *Materials Science and Technology*, vol. 17, no. 4, pp. 355–365, 2001.
- [70] E. Brinksmeier *et al.*, "Residual Stresses — Measurement and Causes in Machining Processes," *CIRP Annals - Manufacturing Technology*, vol. 31, no. 2, pp. 491–510, 1982.
- [71] N. Tebedge, G. Alpsten, and L. Tall, "Residual-stress measurement by the sectioning method," *Experimental Mechanics*, vol. 13, no. 2, pp. 88–96, 1973.
- [72] C. W. Bert and G. L. Thompson, "A Method for Measuring Planar Residual Stresses in Rectangularly Orthotropic Materials," *Journal of Composite Materials*, vol. 2, no. 2, pp. 244–253, 1968.
- [73] G. S. Schajer and M. B. Prime, "Use of Inverse Solutions for Residual Stress Measurements," *J. Eng. Mater. Technol.*, vol. 128, no. 3, p. 375, 2006.
- [74] A. T. DeWald and M. R. Hill, "Eigenstrain-based model for prediction of laser peening residual stresses in arbitrary three-dimensional bodies. Part 1: Model description," *The Journal of Strain Analysis for Engineering Design*, vol. 44, no. 1, pp. 1–11, 2009.
- [75] A. T. DeWald and M. R. Hill, "Eigenstrain-based model for prediction of laser peening residual stresses in arbitrary three-dimensional bodies. Part 2: Model verification," *The Journal of Strain Analysis for Engineering Design*, vol. 44, no. 1, pp. 13–27, 2009.

- [76] Gary S. Schajer and Clayton O. Ruud, "Overview of Residual Stresses and Their Measurement," in *Practical Residual Stress Measurement Methods*, G. S. Schajer, Ed., West Sussex: Wiley, 2013, pp. 1–24.
- [77] I. C. Noyan and J. B. Cohen, *Residual Stress: Measurement by Diffraction and Interpretation*. New York, NY: Springer New York, 1987.
- [78] Y. Javadi, M. Akhlaghi, and M. A. Najafabadi, "Using finite element and ultrasonic method to evaluate welding longitudinal residual stress through the thickness in austenitic stainless steel plates," *Materials & Design*, vol. 45, pp. 628–642, 2013.
- [79] V. Hauk and H. Behnken, Eds., *Structural and residual stress analysis by nondestructive methods: Evaluation - application - assessment*. Amsterdam [u.a.]: Elsevier, 2006.
- [80] M. Born, E. Wolf, and A. B. Bhatia, *Principles of optics: Electromagnetic theory of propagation, interference and diffraction of light*, 7th ed. Cambridge [u.a.]: Cambridge Univ. Press, 2016.
- [81] *Residual Stress, Thermomechanics & Infrared Imaging, Hybrid Techniques and Inverse Problems, Volume 9: Proceedings of the 2015 Annual Conference on Experimental and Applied Mechanics*, 1st ed. Cham: Springer International Publishing, 2016.
- [82] G. S. Schajer, Ed., *Practical Residual Stress Measurement Methods*. West Sussex: Wiley, 2013.
- [83] J. Mathar, "Determination of Initial Stresses by Measuring the Deformation Around Drilled Holes," *Transactions of the American Society of Mechanical Engineering*, vol. 56, no. 4, pp. 249–254, 1934.
- [84] Gary S. Schajer and Philip S. Whitehead, "Hole Drilling and Ring Coring," in *Practical Residual Stress Measurement Methods*, G. S. Schajer, Ed., West Sussex: Wiley, 2013, pp. 29–65.
- [85] *Standard Test Method for Determining Residual Stresses by the Hole-Drilling Strain-Gage Method*, ASTM E837-13a.
- [86] M. Steinzig and E. Ponslet, "Residual Stress measurement Using the Hole Drilling Method and Laser Speckle Interferometry: Part I," *Technology Application Series*, pp. 43–46, 2003.
- [87] P. V. Grant, J. D. Lord, and P. S. Whitehead, "The Measurement of Residual Stresses by the Incremental Hole Drilling Technique: Measurement Good Practice Guide No. 53," National Physical Laboratory, Teddington, UK, 2002.
- [88] Vishay Measurements Group, Inc., "Measurement of Residual Stresses by the Hole-Drilling Strain-Gage Method," Raleigh, NC, 1993.
- [89] R. Oettel, "The Determination of Uncertainties in Residual Stress Measurement (using the Hole Drilling Technique): Code of Practice No. 15," Prüf- und Gutachter-Gesellschaft mbH, Dresden, Germany, Standards Measurement & Testing Project No. SMT4-CT97-2165, 2000.

- [90] E. Ponslet and M. Steinzig, "Residual Stress measurement Using the Hole Drilling Method and Laser Speckle Interferometry: Part II Analysis Technique," *Technology Application Series*, pp. 1–5, 2003.
- [91] M. Steinzig and E. Ponslet, "Residual Stress measurement Using the Hole Drilling Method and Laser Speckle Interferometry: Part IV Measurement Accuracy," *Technology Application Series*, pp. 59–63, 2003.
- [92] C. H. D. Novion, "The use of neutrons for materials characterization," in *Analysis of residual stress by diffraction using neutron and synchrotron radiation*, M. E. Fitzpatrick and A. Lodini, Eds., London, New York: Taylor & Francis, 2003, pp. 1–3.
- [93] A. J. Allen, M. T. Hutchings, C. G. Windsor, and C. Andreani, "Neutron diffraction methods for the study of residual stress fields," *Advances in Physics*, vol. 34, no. 4, pp. 445–473, 2006.
- [94] E. Macherauch, "Residual Stresses," in *Application of Fracture Mechanics to Materials and Structures*, G.C. Sih, E. Sommer, and W. Dahl, Eds.: Springer Netherlands, 1984, pp. 157–192.
- [95] Pintschovius L., "Neutron diffraction methods," in *Structural and residual stress analysis by nondestructive methods: Evaluation - application - assessment*, V. Hauk and H. Behnken, Eds., Amsterdam [u.a.]: Elsevier, 2006, pp. 495–521.
- [96] E. Kröner, "Berechnung der elastischen Konstanten des Vielkristalls aus den Konstanten des Einkristalls," *Z. Physik*, vol. 151, no. 4, pp. 504–518, 1958.
- [97] M. T. Hutchings, *Introduction to the characterization of residual stress by neutron diffraction*. Boca Raton, Fla.: Taylor & Francis, 2005.
- [98] G.A. Webster and R. W. Wimpory, "Polycrystalline Materials Determination of Residual Stresses by Neutron Diffraction," European Communities, Italy ISO/TTA 3:2001, 2002.
- [99] S. Suwas and R. K. Ray, *Crystallographic Texture of Materials*. London: Springer London, 2014.
- [100] H. J. Bunge, "Three-dimensional texture analysis," *International Materials Reviews*, vol. 32, no. 1, pp. 265–291, 1987.
- [101] U.F. Kocks, "Anisotropy and Symmetry," in *Texture and anisotropy: Preferred orientations in polycrystals and their effect on materials properties*, U. F. Kocks, C. N. Tomé, H. R. Wenk, A. J. Beaudoin, and H. Mecking, Eds., 2005th ed., Cambridge: Cambridge University Press, 2005, pp. 10–44.
- [102] O. Engler and V. Randle, "Introduction," in *Introduction to Texture Analysis: CRC Press*, 2009, pp. 3–14.
- [103] O. Engler and V. Randle, "Evaluation and Representation of Macrotecture Data," in *Introduction to Texture Analysis: CRC Press*, 2009, pp. 123–172.

- [104] P. S. Mathur and W. A. Backofen, "Mechanical contributions to the plane-strain deformation and recrystallization textures of aluminum-killed steel," *MT*, vol. 4, no. 3, pp. 643–651, 1973.
- [105] W. Truszkowski, J. Krol, and B. Major, "On Penetration of Shear Texture into the Rolled Aluminum and Copper," *MTA*, vol. 13, no. 4, pp. 665–669, 1982.
- [106] D. Schläfer and H. J. Bunge, "The Development of the Rolling Texture of Iron Determined by Neutron-Diffraction," *Texture*, vol. 1, no. 3, pp. 157–171, 1974.
- [107] H.-G. Brokmeier *et al.*, "Texture gradient in a copper tube at maximum and minimum wall thickness," *IOP Conf. Ser.: Mater. Sci. Eng.*, vol. 82, p. 12102, 2015.
- [108] H. G. Brokmeier, R. E. Bolmaro, J. A. Signorelli, and A. Fourty, "Texture development of wire drawn Cu–Fe composites," *Physica B: Condensed Matter*, vol. 276–278, no. 0, pp. 888–889, 2000.
- [109] H. Park and D. N. Lee, "Deformation and annealing textures of drawn Al–Mg–Si alloy tubes," *5th Asia Pacific conference on Materials processing*, vol. 113, no. 1–3, pp. 551–555, <http://www.sciencedirect.com/science/article/pii/S0924013601006586>, 2001.
- [110] J. H. Cho, S. J. Park, S. H. Choi, and K. H. Oh, "Deformation Texture of Cold Drawn Al6063 Tube," *MSF*, vol. 408–412, pp. 565–570, 2002.
- [111] J. Chen, W. Yan, W. Li, J. Miao, and X.-h. Fan, "Texture evolution and its simulation of cold drawing copper wires produced by continuous casting," *Transactions of Nonferrous Metals Society of China*, vol. 21, no. 1, pp. 152–158, 2011.
- [112] N Al-Hamdany, H.-G Brokmeier, B Schwebke, Z Y Zhong, and N Schell, "Texture Inhomogeneity through the Thickness of a Copper Tube," 2012.
- [113] U.F. Kocks, "The Representation of Orientations and Textures," in *Texture and anisotropy: Preferred orientations in polycrystals and their effect on materials properties*, U. F. Kocks, C. N. Tomé, H. R. Wenk, A. J. Beaudoin, and H. Mecking, Eds., 2005th ed., Cambridge: Cambridge University Press, 2005, pp. 44–102.
- [114] C. Hammond, *The basics of crystallography and diffraction*, 3rd ed. Oxford: Oxford University Press, 2013.
- [115] W. Borchardt-Ott, *Crystallography: An Introduction*. Berlin: Springer, 2012.
- [116] H.-J. Bunge and P. R. Morris, *Texture analysis in materials science: Mathematical methods*. London, England: Butterworth, 1982.
- [117] J.S. Kallend, "Determination of the Orientation Distributuion from Pole Figure Data," in *Texture and anisotropy: Preferred orientations in polycrystals and their effect on materials properties*, U. F. Kocks, C. N. Tomé, H. R. Wenk, A. J. Beaudoin, and H. Mecking, Eds., 2005th ed., Cambridge: Cambridge University Press, 2005, pp. 102–126.

- [118] H. Pursey and H. L. Cox, "XXXIV. The correction of elasticity measurements on slightly anisotropic materials," *The London, Edinburgh, and Dublin Philosophical Magazine and Journal of Science*, vol. 45, no. 362, pp. 295–302, 2009.
- [119] G. Wassermann, "H.-J. Bunge. Mathematische Methoden der Texturanalyse Akademie-Verlag Berlin 1969, 330 Seiten Geb. M 68.–," *Krist. Techn.*, vol. 5, no. 3, pp. K23, 1970.
- [120] R.-J. Roe, "Description of Crystallite Orientation in Polycrystalline Materials. III. General Solution to Pole Figure Inversion," *Journal of Applied Physics*, vol. 36, no. 6, pp. 2024–2031, 1965.
- [121] H.-J. Bunge and C. Esling, *Quantitative texture analysis*. Oberursel: DGM Informationsgesellschaft, 1986.
- [122] O. Engler and V. Randle, "Evaluation and Representation of Macrotecture Data," in *Introduction to Texture Analysis*: CRC Press, 2009, pp. 123–172.
- [123] W. Reimers, A. R. Pyzalla, A. K. Schreyer, and H. Clemens, Eds., *Neutrons and Synchrotron Radiation in Engineering Materials Science*. Weinheim, Germany: Wiley-VCH Verlag GmbH & Co. KGaA, 2008.
- [124] H. J. Bunge, L. Wcislak, H. Klein, U. Garbe, and J. R. Schneider, "Texture and Microstructure Analysis with High-Energy Synchrotron Radiation," *Adv. Eng. Mater.*, vol. 4, no. 5, pp. 300–305, 2002.
- [125] *Neutrons and Synchrotron Radiation in Engineering Materials Science*: Wiley-VCH Verlag GmbH & Co. KGaA, 2008.
- [126] H. Abdolvand *et al.*, "On the deformation twinning of Mg AZ31B: A three-dimensional synchrotron X-ray diffraction experiment and crystal plasticity finite element model," *International Journal of Plasticity*, vol. 70, pp. 77–97, 2015.
- [127] H. F. Poulsen and D. Juul Jensen, "From 2D to 3D Microtexture Investigations," *MSF*, vol. 408–412, pp. 49–66, 2002.
- [128] O. Engler and V. Randle, "Synchrotron Radiation, Nondiffraction Techniques, and Comparisons between Methods," in *Introduction to Texture Analysis*: CRC Press, 2009, pp. 351–375.
- [129] H. Weiland, "Microtexture determination and its application to materials science," *JOM*, vol. 46, no. 9, pp. 37–41, 1994.
- [130] O. Engler and V. Randle, "Scanning Electron Microscopy–Based Techniques," in *Introduction to Texture Analysis*: CRC Press, 2009, pp. 203–240.
- [131] J. A. Venables and R. Bin-jaya, "Accurate microcrystallography using electron back-scattering patterns," *Philosophical Magazine*, vol. 35, no. 5, pp. 1317–1332, 2006.
- [132] V. Randle, *Microtexture determination and its applications*, 2nd ed. London: Maney, for the Institute of Materials, Minerals and Mining, 2008.

- [133] H.-G. Brokmeier, "Neutron Diffraction Texture Analysis of Multi-Phase Systems," *Textures and Microstructures*, vol. 10, no. 4, pp. 325–346, 1989.
- [134] J. A. Szipunar, "Texture studies using neutron diffraction," (English), *J Mater Sci*, vol. 19, no. 11, pp. 3467–3476, 1984.
- [135] M. A. Wells, B. Hernandez-Morales, J. H. Root, and E. B. Hawbolt, "Neutron diffraction in the materials science toolbox," *Physica B: Condensed Matter*, vol. 241-243, pp. 1274–1276, 1997.
- [136] S. Yip, Ed., *Handbook of materials modeling*. Dordrecht: Springer, 2005.
- [137] D. M. Kochmann, *Kochmann Research Group - California Institute of Technology*. [Online] Available: http://www.kochmann.caltech.edu/research_QC.html. Accessed on: Jul. 21 2017.
- [138] S. Yip, "Introduction," in *Handbook of materials modeling*, S. Yip, Ed., Dordrecht: Springer, 2005, pp. 1–5.
- [139] D. L. McDowell and G. B. Olson, "Concurrent design of hierarchical materials and structures," *Sci Model Simul*, vol. 15, no. 1-3, pp. 207–240, 2008.
- [140] M. F. Horstemeyer, *Integrated computational materials engineering (ICME) for metals: Using multiscale modeling to invigorate engineering design with science*. Hoboken, N.J.: WILEY-TMS, 2012.
- [141] G. J. Schmitz and U. Prah, Eds., *Handbook of software solutions for ICME*. Weinheim: Wiley-VCH, 2017.
- [142] M. F. Horstemeyer, *Integrated computational materials engineering: Using multiscale modeling to invigorate engineering design with science*. Weinheim: Wiley-VCH, 2011.
- [143] F.R.N. Nabarro, "Mathematical theory of stationary dislocations," *Advances in Physics*, vol. 1, no. 3, pp. 269–394, 1952.
- [144] J. M. Burgers, *Physics. — Some considerations on the fields of stress connected with dislocations in a regular crystal lattice. I* (en): Springer Netherlands. Available: http://link.springer.com/content/pdf/10.1007%2F978-94-011-0195-0_11.pdf.
- [145] L. M. Brown, "The self-stress of dislocations and the shape of extended nodes," *Philosophical Magazine*, vol. 10, no. 105, pp. 441–466, 1964.
- [146] D. J. Bacon, "A Method for Describing a Flexible Dislocation," *physica status solidi (b)*, vol. 23, 1967.
- [147] A. J. E. Foreman, "The bowing of a dislocation segment," *Philosophical Magazine*, vol. 15, no. 137, pp. 1011–1021, 1967.
- [148] E. O. Hall, "The Deformation and Ageing of Mild Steel: III Discussion of Results," *Proceedings of the Physical Society. Section B*, vol. 64, no. 9, p. 747, 1951.
- [149] N. J. Petch, "The Cleavage Strength of Polycrystals," *Journal of the Iron and Steel Institute*, vol. 174, pp. 25–28, 1953.

- [150] M. F. Ashby, "The Deformation of Plasticity Non-Homogeneous Alloys," in *Strengthening methods in crystals*, A. Kelly and R. Nicholson, Eds., New York: Halstead Press Division, Wiley, 1971, pp. 137–193.
- [151] F. C. Frank, "The influence of dislocations on crystal growth," *Discuss. Faraday Soc.*, vol. 5, no. 0, pp. 48–54, <http://pubs.rsc.org/en/content/articlepdf/1949/df/df9490500048>, 1949.
- [152] F. C. Frank, "Crystal dislocations.—Elementary concepts and definitions," *The London, Edinburgh, and Dublin Philosophical Magazine and Journal of Science*, vol. 42, no. 331, pp. 809–819, 1951.
- [153] W. T. Read, "Dislocations and plastic deformation," *Physics Today*, vol. 6, no. 11, pp. 10–13, 1953.
- [154] D. A. Hughes, D. B. Dawson, J. S. Korells, and L. I. Weingarten, "Near surface microstructures developing under large sliding loads," *JMEP*, vol. 3, no. 4, pp. 459–475, 1994.
- [155] H. Mecking and U. F. Kocks, "A Mechanism for Static and Dynamic Recovery," in *International series on the strength and fracture of materials and structures, Strength of metals and alloys: Proceedings of the 5th International Conference, Aachen, Federal Republic of Germany, August 27-31, 1979*, P. Haasen, V. Gerold, and G. Kostorz, Eds., 1st ed., Toronto, New York: Pergamon Press, 1980, ©1979–©1980, pp. 345–350.
- [156] N. A. Fleck, G. M. Muller, M. F. Ashby, and J. W. Hutchinson, "Strain gradient plasticity: Theory and experiment," *Acta Metallurgica et Materialia*, vol. 42, no. 2, pp. 475–487, 1994.
- [157] E. B. Tadmor, M. Ortiz, and R. Phillips, "Quasicontinuum analysis of defects in solids," *Philosophical Magazine A*, vol. 73, no. 6, pp. 1529–1563, 1996.
- [158] E. B. Tadmor, R. Phillips, and M. Ortiz, "Hierarchical modeling in the mechanics of materials," (English (US)), *International Journal of Solids and Structures*, vol. 37, no. 1-2, pp. 379–389, 2000.
- [159] R. Phillips, *Crystals, defects and microstructures: Modeling across scales*. Cambridge, New York: Cambridge University Press, 2001.
- [160] W. K. Liu, E. G. Karpov, and H. S. Park, *Nano mechanics and materials: Theory, multiscale methods and applications*. Chichester, England, Hoboken, NJ: John Wiley, 2006.
- [161] S. Kohlhoff and S. Schmauder, "A New Method for Coupled Elastic-Atomistic Modelling," in *Atomistic Simulation of Materials: Beyond Pair Potentials*, Srolovitz, David J., Vitek, V., Ed., Boston, MA: Springer US, 1989, pp. 411–418.
- [162] S. Kohlhoff, P. Gumbsch, and H. F. Fischmeister, "Crack propagation in b.c.c. crystals studied with a combined finite-element and atomistic model," *Philosophical Magazine A*, vol. 64, no. 4, pp. 851–878, 1991.
- [163] L. E. Shilkrot, R. E. Miller, and W. A. Curtin, "Coupled atomistic and discrete dislocation plasticity," (eng), *Physical review letters*, vol. 89, no. 2, p. 25501, 2002.

- [164] L. E. Shilkrot, R. E. Miller, and W. A. Curtin, "Multiscale plasticity modeling: Coupled atomistics and discrete dislocation mechanics," *Journal of the Mechanics and Physics of Solids*, vol. 52, no. 4, pp. 755–787, 2004.
- [165] B. Shiari, R. E. Miller, and W. A. Curtin, "Coupled Atomistic/Discrete Dislocation Simulations of Nanoindentation at Finite Temperature," *J. Eng. Mater. Technol.*, vol. 127, no. 4, p. 358, 2005.
- [166] D. Raabe, F. Roters, F. Barlat, and L.-Q. Chen, Eds., *Microstructures - Process Applications (eds)*, 2002.
- [167] F. Roters, P. Eisenlohr, T. R. Bieler, and D. Raabe, "Introduction to Crystalline Anisotropy and the Crystal Plasticity Finite Element Method," in *Crystal Plasticity Finite Element Methods*, Dr. Franz Roters, Dr.-Ing. Philip Eisenlohr, Prof. Dr. Thomas R. Bieler, Prof. Dr. Dierk Raabe, Ed.: Wiley-VCH Verlag GmbH & Co. KGaA, 2010, pp. 1–9.
- [168] P. R. Dawson, "On modeling of mechanical property changes during flat rolling of aluminum," *International Journal of Solids and Structures*, vol. 23, no. 7, pp. 947–968, 1987.
- [169] D. Peirce, R. J. Asaro, and A. Needleman, "An analysis of nonuniform and localized deformation in ductile single crystals," *Acta Metallurgica*, vol. 30, no. 6, pp. 1087–1119, 1982.
- [170] U. F. Kocks, C. N. Tomé, H. R. Wenk, A. J. Beaudoin, and H. Mecking, Eds., *Texture and anisotropy: Preferred orientations in polycrystals and their effect on materials properties*, 2005th ed. Cambridge: Cambridge University Press, 2005.
- [171] M.F. Horstemeyer, G.P. Potirniche, and E.B. Marin, "Crystal Plasticity," in *Handbook of materials modeling*, S. Yip, Ed., Dordrecht: Springer, 2005, pp. 1133–1151.
- [172] M.F. Horstemeyer, G.P. Potirniche, and E.B. Marin, "Crystal Plasticity," in *Handbook of materials modeling*, S. Yip, Ed., Dordrecht: Springer, 2005, pp. 1133–1149.
- [173] Sangbong Yi, "Investigation on the Deformation Behavior and the Texture Evolution in Magnesium Wrought Alloy AZ31," Dissertation, Institute of Materials Science and Engineering, Clausthal University of Technology, Clausthal-Zellerfeld, 2005.
- [174] D. Hull and D. J. Bacon, *Introduction to dislocations*, 5th ed. Oxford: Butterworth-Heinemann, 2011.
- [175] G. I. Taylor, "Plastic Strain in Metals," *Journal of the Institute of Metals*, vol. 62, pp. 307–324, 1938.
- [176] Efthimios Kaxiras and Sidney Yip, "Introduction: Atomistic Nature of Materials," in *Handbook of materials modeling*, S. Yip, Ed., Dordrecht: Springer, 2005, pp. 451–459.
- [177] M. Stoneham, J. Harding, and T. Harker, "The Shell Model and Interatomic Potentials for Ceramics," *MRS Bull.*, vol. 21, no. 02, pp. 29–35, 1996.

- [178] D. W. Brenner, "Chemical Dynamics and Bond-Order Potentials," *MRS Bull.*, vol. 21, no. 02, pp. 36–41, 1996.
- [179] Y. Mishin, "Interatomic Potentials for Metals," in *Handbook of materials modeling*, S. Yip, Ed., Dordrecht: Springer, 2005, pp. 459–479.
- [180] M. I. Baskes, "Modified embedded-atom potentials for cubic materials and impurities," *Phys. Rev. B*, vol. 46, no. 5, pp. 2727–2742, 1992.
- [181] B.-J. Lee, J.-H. Shim, and M. I. Baskes, "Semiempirical atomic potentials for the fcc metals Cu, Ag, Au, Ni, Pd, Pt, Al, and Pb based on first and second nearest-neighbor modified embedded atom method," *Phys. Rev. B*, vol. 68, no. 14, 2003.
- [182] B. Jelinek *et al.*, "Modified embedded atom method potential for Al, Si, Mg, Cu, and Fe alloys," *Phys. Rev. B*, vol. 85, no. 24, 2012.
- [183] C. A. Becker, F. Tavazza, Z. T. Trautt, and R. A. Buarque de Macedo, "Considerations for choosing and using force fields and interatomic potentials in materials science and engineering," *Current Opinion in Solid State and Materials Science*, vol. 17, no. 6, pp. 277–283, <https://www.ctcms.nist.gov/potentials>, 2013.
- [184] John R. Ray, "Ensembles and Computer Simulation Calculation of Response Functions," in *Handbook of materials modeling*, S. Yip, Ed., Dordrecht: Springer, 2005, pp. 729–745.
- [185] C. Y. Fong, *Topics in computational materials science*. Singapore, River Edge, N.J.: World Scientific, 1998.
- [186] M. J. Mehl, B. M. Klein and D. A. Papaconstantopoulos, "First - principles calculation of elastic properties of metals," in *Intermetallic compounds: Principles and practice*, J. H. Westbrook and R. L. Fleischer, Eds., Chichester, New York, Brisbane: J. Wiley & Sons, op. 1995-cop. 2002, pp. 195–210.
- [187] Nicola Marzari, "Understand, Predict, and Design," in *Handbook of materials modeling*, S. Yip, Ed., Dordrecht: Springer, 2005, pp. 9–13.
- [188] James R. Chelikowsky, "Electronic Scale," in *Handbook of materials modeling*, S. Yip, Ed., Dordrecht: Springer, 2005, pp. 121–137.
- [189] W. Greiner, *Quantum Mechanics: An Introduction*. Berlin, Heidelberg: Springer Berlin Heidelberg, 2001.
- [190] F. Roters, P. Eisenlohr, T. R. Bieler, and Raabe, *Crystal Plasticity Finite Element Methods: in Materials Science and Enginee*: John Wiley & Sons, 2010.
- [191] O. C. Zienkiewicz, R. L. Taylor, and D. D. Fox, *The finite element method for solid and structural mechanics, seventh edition*, 7th ed. Oxford, Waltham, Mass.: Butterworth-Heinemann, 2014.
- [192] J. N. Reddy, *An introduction to the finite element method*, 3rd ed. New York: McGraw-Hill Higher Education, 2006.
- [193] R. D. Cook, *Concepts and applications of finite element analysis*, 4th ed. Hoboken, New Jersey: John Wiley & Sons, 2002.

- [194] A. E. Tekkaya, J. Gerhardt, and M. Burgdorf, "Residual Stresses in Cold-Formed Workpieces," *CIRP Annals - Manufacturing Technology*, vol. 34, no. 1, pp. 225–230, 1985.
- [195] J.M. Rigaut, D. Locheignies, J. Oudin, J.C. Gelin and Y. Ravalard, "Numerical analysis of cold drawing of tubes," in *Modelling of Metal Forming Processes: Proceedings of the Euromech 233 Colloquium, Sophia Antipolis, France, August 29-31, 1988*, 1988, pp. 261–268.
- [196] M. Pietrzyk and L. Sadok, "Validation of the finite-element model of the tube-sinking process," *Journal of Materials Processing Technology*, vol. 22, no. 1, pp. 65–73, 1990.
- [197] K. Sawamiphakdi, G. D. Lahoti, and P. K. Kropp, "Simulation of a tube drawing process by the finite element method," *Journal of Materials Processing Technology*, vol. 27, no. 1–3, pp. 179–190, 1991.
- [198] L. Sadok, M. Pietrzyk, and M. Pačko, "Strains in the tube-sinking process evaluated by the finite element method and experimental technique," *Steel Research*, vol. 62, no. 6, pp. 255–260, 1991.
- [199] S. Mulot, A. Hacquin, P. Montmitonnet, and J. L. Aubin, "A fully 3D finite element simulation of cold pilgering," *Journal of Materials Processing Technology*, vol. 60, no. 1–4, pp. 505–512, 1996.
- [200] J. Mackerle, "Finite elements in the analysis of pressure vessels and piping—a bibliography (1976–1996)," *International Journal of Pressure Vessels and Piping*, vol. 69, no. 3, pp. 279–339, 1996.
- [201] M. Rumiński, J. Łuksza, J. Kusiak, and M. Pačko, "Analysis of the effect of die shape on the distribution of mechanical properties and strain field in the tube sinking process," *Journal of Materials Processing Technology*, vol. 80–81, pp. 683–689, 1998.
- [202] K. Yoshida and H. Furuya, "Mandrel drawing and plug drawing of shape-memory-alloy fine tubes used in catheters and stents," *Journal of Materials Processing Technology*, vol. 153–154, no. 0, pp. 145–150, 2004.
- [203] F. O. Neves, S. T. Button, C. Caminaga, and F. C. Gentile, "Numerical and experimental analysis of tube drawing with fixed plug," *Journal of the Brazilian Society of Mechanical Sciences and Engineering*, vol. 27, pp. 426–431, 2005.
- [204] H. Palkowski, S. Brück, T. Pirling, and A. Carradó, "Investigation on the Residual Stress State of Drawn Tubes by Numerical Simulation and Neutron Diffraction Analysis," *Materials*, vol. 6, no. 11, pp. 5118–5130, 2013.
- [205] *Bueltmann GmbH*. [Online] Available: <https://www.bueltmann.com/home.html>.
- [206] *Standard Specification for Seamless Copper Tube*, B75.
- [207] *KME AG*. [Online] Available: <http://www.kme.com/de/>.
- [208] *GE Inspection Technologies*. [Online] Available: <http://www.krautkramer.de/>.

- [209] Johann Naumann, "Konstruktion eines Ziehmatrizenhalters für Rohrziehversuche," Bachelor's Thesis, Institute of Metallurgy, Clausthal University of Technology, Clausthal-Zellerfeld, 2014.
- [210] *Stresstech GmbH*. [Online] Available: <http://www.stresstech.de/de/>.
- [211] T. Pirling, G. Bruno, and P. J. Withers, "SALSA—A new instrument for strain imaging in engineering materials and components," *Materials Science and Engineering: A*, vol. 437, no. 1, pp. 139–144, 2006.
- [212] D. J. Hughes, G. Bruno, T. Pirling, and P. J. Withers, "Scientific Review: First Impressions of SALSA: The New Engineering Instrument at ILL," *Neutron News*, vol. 17, no. 3, pp. 28–32, 2006.
- [213] M. Hofmann, W. Gan, and J. Rebelo-Kornmeier, "STRESS-SPEC: Materials science diffractometer," *JLSRF*, vol. 1, 2015.
- [214] Nowfal A. Abdulrazzag Al-Hamdany, "Texture and Stress Characterization of a Copper Tube by Neutron, Synchrotron and Electron Diffraction," Dissertation, Institute of Materials Science and Technology, Clausthal University of Technology, Clausthal-Zellerfeld, 2015.
- [215] N. Schell *et al.*, "The High Energy Materials Science Beamline (HEMS) at PETRA III," *MSF*, vol. 772, pp. 57–61, 2013.
- [216] *OIM™ Analysis for the Visualization and Analysis of EBSD Mapping Data*. [Online] Available: <http://www.edax.com/Products/EBSD/OIM-Analysis.aspx>. Accessed on: May 08 2017.
- [217] D. Mainprice, F. Bachmann, R. Hielscher, and H. Schaeben, "Descriptive tools for the analysis of texture projects with large datasets using MTEX: Strength, symmetry and components," *Geological Society, London, Special Publications*, vol. 409, no. 1, pp. 251–271, 2015.
- [218] P. Giannozzi *et al.*, "QUANTUM ESPRESSO: a modular and open-source software project for quantum simulations of materials," (eng), *Journal of physics. Condensed matter : an Institute of Physics journal*, vol. 21, no. 39, p. 395502, 2009.
- [219] Quantum Espresso, *Pseudopotentials*. [Online] Available: <http://www.quantum-espresso.org/pseudopotentials/>.
- [220] C. D. Barrett and R. L. Carino, "The MEAM parameter calibration tool: An explicit methodology for hierarchical bridging between ab initio and atomistic scales," *Integr Mater Manuf Innov*, vol. 5, no. 1, p. 25, 2016.
- [221] S. Plimpton, "Fast Parallel Algorithms for Short-Range Molecular Dynamics," *Journal of Computational Physics*, vol. 117, no. 1, pp. 1–19, 1995.
- [222] A. Stukowski, "Visualization and analysis of atomistic simulation data with OVITO—the Open Visualization Tool," *Modelling and Simulation in Materials Science and Engineering*, vol. 18, no. 1, p. 15012, 2010.
- [223] H. M. Zbib, M. Hiratani, and M. Shehadeh, "Multiscale Discrete Dislocation Dynamics Plasticity," in *Continuum scale simulation of engineering materials: Fundamentals, microstructures, process applications*, D. Raabe, Ed., Weinheim: Wiley-VCH, 2004, pp. 201–229.

- [224] R. Abbaschian, R. E. Reed-Hill, and L. Abbaschian, *Physical metallurgy principles*, 4th ed. Stamford, Conn.: Cengage Learning, 2009.
- [225] Hibbitt, *Abaqus 2016 Documentation*. USA: Hibbitt, Karlsson, and Sorensen, Inc, 2016.
- [226] Habbitt, *Abaqus User Subroutines Reference Manual*. USA: Hibbitt, Karlsson, and Sorensen, Inc, 2016.
- [227] J. R. Kornmeier, J. Šaroun, J. Gibmeier, and M. Hofmann, "Neutron Residual Strain Surface Scans - Experimental Results and Monte Carlo Simulations," *Materials Science Forum*, vol. 768-769, pp. 52–59, 2013.
- [228] S. Zhang, H. Xie, X. Zeng, and P. Hing, "Residual stress characterization of diamond-like carbon coatings by an X-ray diffraction method," *Surface and Coatings Technology*, vol. 122, no. 2-3, pp. 219–224, 1999.
- [229] T. Pirling, A. Carradò, S. Brück, and H. Palkowski, "Neutron Stress Imaging of Drawn Copper Tube: Comparison with Finite-Element Model," *Metal and Mat Trans A*, vol. 39, no. 13, pp. 3149–3154, 2008.
- [230] S. Suwas, A. K. Singh, K. N. Rao, and T. Singh, "Effect of modes of rolling on evolution of the texture in pure copper and some copper-base alloys," *MEKU*, vol. 93, no. 9, pp. 928–937, 2002.
- [231] O. Engler and V. Randle, "Macrotexture Measurements," in *Introduction to Texture Analysis*: CRC Press, 2009, pp. 75–121.
- [232] A. A. Ridha and W. B. Hutchinson, "Recrystallisation mechanisms and the origin of cube texture in copper," *Acta Metallurgica*, vol. 30, no. 10, pp. 1929–1939, 1982.
- [233] O. Engler, "Deformation and texture of copper–manganese alloys," *Acta Materialia*, vol. 48, no. 20, pp. 4827–4840, 2000.
- [234] M. Hatherley and W.B. Hutchinson, *An introduction to textures in metals*. London: Institution of metallurgists, 1980.
- [235] G. Wassermann and J. Grewen, *Texturen metallischer Werkstoffe*. Goetingen, Heidelberg: Springer Berlin Heidelberg, 1962.
- [236] A. J. Wilkinson and P. B. Hirsch, "Electron diffraction based techniques in scanning electron microscopy of bulk materials," *Micron*, vol. 28, no. 4, pp. 279–308, 1997.
- [237] O. Engler and V. Randle, "Microtexture Analysis," in *Introduction to Texture Analysis*: CRC Press, 2009, p. 173.
- [238] A. J. Schwartz, M. Kumar, B. L. Adams, and D. P. Field, Eds., *Electron backscatter diffraction in materials science*, 2nd ed. New York: Springer, op. 2009.
- [239] M. C. Michelini, R. Pis Diez, and A. H. Jubert, "A density functional study of small nickel clusters," *Int. J. Quant. Chem.*, vol. 70, no. 4-5, pp. 693–701, 1998.
- [240] E. S. Drexler, N. J. Simon, and R. P. Reed, "Properties of copper and copper alloys at cryogenic temperatures," NIST NIST-MN-177, 1996.

- [241] Z. Yang, L. Xie, D. Ma, and G. Wang, "Origin of the High Activity of the Ceria-Supported Copper Catalyst for H₂O Dissociation," *J. Phys. Chem. C*, vol. 115, no. 14, pp. 6730–6740, 2011.
- [242] *Copper | The Periodic Table at KnowledgeDoor.*
- [243] N. F. Mott, "The Mechanical Properties of Metals," (en), *Proc. Phys. Soc. B*, vol. 64, no. 9, p. 729, <http://iopscience.iop.org/article/10.1088/0370-1301/64/9/301/pdf>.
- [244] W. T. Read, "Dislocations in Crystals. New York, 1953. 228 pp. Illus. \$5," *McGraw-Hill*, p. 228, 1953.
- [245] T. Vegge and K. W. Jacobsen, "Atomistic simulations of dislocation processes in copper," (en), *J. Phys.: Condens. Matter*, vol. 14, no. 11, p. 2929, <http://iopscience.iop.org/article/10.1088/0953-8984/14/11/309/pdf>, 2002.
- [246] S. Crampin, K. Hampel, D. D. Vvedensky, and J. M. MacLaren, "The calculation of stacking fault energies in close-packed metals," *J. Mater. Res.*, vol. 5, no. 10, pp. 2107–2119, 1990.
- [247] J. Hartford, B. von Sydow, G. Wahnström, and B. I. Lundqvist, "Peierls barriers and stresses for edge dislocations in Pd and Al calculated from first principles," *Phys. Rev. B*, vol. 58, no. 5, pp. 2487–2496, 1998.
- [248] E. Asadi, M. A. Zaeem, A. Moitra, and M. A. Tschopp, "Effect of vacancy defects on generalized stacking fault energy of fcc metals," (eng), *J. Phys.: Condens. Matter*, vol. 26, no. 11, p. 115404, 2014.
- [249] C. Brandl, P. M. Derlet, and H. van Swygenhoven, "General-stacking-fault energies in highly strained metallic environments: Ab initio calculations," *Phys. Rev. B*, vol. 76, no. 5, 2007.
- [250] D. J. Oh and R. A. Johnson, "Simple embedded atom method model for fcc and hcp metals," *J. Mater. Res.*, vol. 3, no. 03, pp. 471–478, 1988.
- [251] A. F. Voter and S. P. Chen, "Accurate Interatomic Potentials for Ni, Al and Ni₃Al," *MRS Proc.*, vol. 82, 1986.
- [252] J. P. Hirth, Ed., *Dislocations in solids*. Amsterdam [etc.]: Elsevier, 1979-2008.
- [253] S. Groh, E. B. Marin, M. F. Horstemeyer, and H. M. Zbib, "Multiscale modeling of the plasticity in an aluminum single crystal," *International Journal of Plasticity*, vol. 25, no. 8, pp. 1456–1473, 2009.
- [254] D. L. Olmsted, L. G. H. Jr, W. A. Curtin, and R. J. Clifton, "Atomistic simulations of dislocation mobility in Al, Ni and Al/Mg alloys," (en), *Modelling Simul. Mater. Sci. Eng.*, vol. 13, no. 3, p. 371, <http://iopscience.iop.org/article/10.1088/0965-0393/13/3/007/pdf>, 2005.
- [255] C. L. Kelchner, S. J. Plimpton, and J. C. Hamilton, "Dislocation nucleation and defect structure during surface indentation," *Phys. Rev. B*, vol. 58, no. 17, p. 11085, <http://link.aps.org/pdf/10.1103/PhysRevB.58.11085>, 1998.
- [256] M. F. Horstemeyer *et al.*, "Hierarchical Bridging Between Ab Initio and Atomistic Level Computations: Calibrating the Modified Embedded Atom

- Method (MEAM) Potential (Part A)," *JOM*, vol. 67, no. 1, pp. 143–147, 2015.
- [257] J. M. Hughes *et al.*, "Hierarchical Bridging Between Ab Initio and Atomistic Level Computations: Sensitivity and Uncertainty Analysis for the Modified Embedded-Atom Method (MEAM) Potential (Part B)," *JOM*, vol. 67, no. 1, pp. 148–153, 2015.
- [258] H. M. Ledbetter and E. R. Naimon, "Elastic Properties of Metals and Alloys. II. Copper," *Journal of Physical and Chemical Reference Data*, vol. 3, no. 4, pp. 897–935, 1974.
- [259] S. Chandra, M. K. Samal, V. M. Chavan, and R. J. Patel, "Multiscale modeling of plasticity in a copper single crystal deformed at high strain rates," *Plasticity and Mechanics of Defects*, vol. 1, no. 1, <http://www.degruyter.com/downloadpdf/j/pmd.2015.1.issue-1/pmd-2015-0001/pmd-2015-0001.xml>.
- [260] S. A. Zahedi, A. Roy, and V. V. Silberschmidt, "Modeling of Micro-machining Single-crystal f.c.c. Metals," *Procedia CIRP*, vol. 8, pp. 346–350, 2013.
- [261] K.-D. Fusenig and E. Nembach, "Dynamic dislocation effects in precipitation hardened materials," *Acta Metallurgica et Materialia*, vol. 41, no. 11, pp. 3181–3189, 1993.
- [262] K. M. Jassby and T. Vreeland, "An experimental study of the mobility of edge dislocations in pure copper single crystals," *Philosophical Magazine*, vol. 21, no. 174, pp. 1147–1168, 2006.
- [263] E. B. Marin, "On the formulation of a crystal plasticity model," Sandia National Laboratories SAND2006-4170, 2006. [Online] Available: <http://www.osti.gov/scitech/servlets/purl/890604>.
- [264] Y. Wang, D. Raabe, C. Klüber, and F. Roters, "Orientation dependence of nanoindentation pile-up patterns and of nanoindentation microtextures in copper single crystals," *Acta Materialia*, vol. 52, no. 8, pp. 2229–2238, 2004.
- [265] N. Zaafarani, D. Raabe, R. N. Singh, F. Roters, and S. Zaefferer, "Three-dimensional investigation of the texture and microstructure below a nanoindent in a Cu single crystal using 3D EBSD and crystal plasticity finite element simulations," *Acta Materialia*, vol. 54, no. 7, pp. 1863–1876, 2006.
- [266] Habbitt, *Abaqus 2016 Theory Manual*. USA: Hibbitt, Karlsson, and Sorensen, Inc, 2016.
- [267] V. L. Popov, "Coulomb's Law of Friction," in *Contact Mechanics and Friction*: Springer Berlin Heidelberg, 2010, pp. 133–154.
- [268] Shigenobu Ogata, "Ab initio Study of Mechanical Deformation," in *Handbook of materials modeling*, S. Yip, Ed., Dordrecht: Springer, 2005, pp. 439–448.

- [269] L. Davison, A. L. Stevens, and M. E. Kipp, "Theory of spall damage accumulation in ductile metals," *Journal of the Mechanics and Physics of Solids*, vol. 25, no. 1, pp. 11–28, 1977.
- [270] E. Kröner, "Allgemeine Kontinuumstheorie der Versetzungen und Eigenspannungen," *Arch. Rational Mech. Anal.*, vol. 4, no. 1, pp. 273–334, 1959.
- [271] E. H. Lee, "Elastic-Plastic Deformation at Finite Strains," *J. Appl. Mech.*, vol. 36, no. 1, p. 1, 1969.
- [272] R. J. Asaro, "Crystal Plasticity," *J. Appl. Mech.*, vol. 50, no. 4b, p. 921, 1983.
- [273] M. M. Rashid and S. Nemat-Nasser, "A constitutive algorithm for rate-dependent crystal plasticity," *Computer Methods in Applied Mechanics and Engineering*, vol. 94, no. 2, pp. 201–228, 1992.
- [274] L. Anand and M. Kothari, "A computational procedure for rate-independent crystal plasticity," *Journal of the Mechanics and Physics of Solids*, vol. 44, no. 4, pp. 525–558, 1996.
- [275] P. R. Dawson and E. B. Marin, "Computational Mechanics for Metal Deformation Processes Using Polycrystal Plasticity," in *Advances in Applied Mechanics, Advances in applied mechanics*, E. van der Giessen and T. Y. Wu, Eds., San Diego: Academic P, 1999, pp. 77–169.
- [276] G. I. Taylor and C. F. Elam, "The Distortion of an Aluminium Crystal during a Tensile Test," *Proceedings of the Royal Society A: Mathematical, Physical and Engineering Sciences*, vol. 102, no. 719, pp. 643–667, 1923.
- [277] E. Schmid, "Ueber die Schubverfestigung von Einkristallen bei plastischer Deformation," *Z. Physik*, vol. 40, no. 1-2, pp. 54–74, 1926.
- [278] G. I. Taylor, "Plastic strain in metals," *Journal of the Institute of Metals*, vol. 62, pp. 307–324, 1938.
- [279] J.F.W. Bishop and R. Hill, "A theoretical derivation of the plastic properties of a polycrystalline face-centred metal," *Philosophical Magazine*, vol. 42, no. 7, pp. 1298–1307, 1951.
- [280] J. Gil Sevillano, P. van Houtte, and E. Aernoudt, "Large strain work hardening and textures," *Progress in Materials Science*, vol. 25, no. 2-4, pp. 69–134, 1980.
- [281] U. F. Kocks, H.-R. Wenk, and C. N. Tomé, *Texture and anisotropy: Preferred orientations in polycrystals and their effect on materials properties*. Cambridge: Cambridge University Press, 1998.
- [282] F. Roters *et al.*, "Overview of constitutive laws, kinematics, homogenization and multiscale methods in crystal plasticity finite-element modeling: Theory, experiments, applications," *Acta Materialia*, vol. 58, no. 4, pp. 1152–1211, 2010.
- [283] Mitsutoshi Kuroda, "On scale-dependent crystal plasticity models," in *Plasticity and beyond: Microstructures, crystal-plasticity and phase*

- transitions*, J. Schröder and K. Hackl, Eds., Vienna: Springer Vienna; Imprint; Springer, 2014, pp. 305–353.
- [284] U. F. Kocks, A. S. Argon, and M. F. Ashby, *Thermodynamics and kinetics of slip*, 1st ed. Oxford, New York: Pergamon Press, 1975.
- [285] Meyers M. A. *et al.*, “Constitutive description of dynamic deformation: Physically-based mechanisms,” *Materials Science and Engineering: A*, vol. 322, no. 1-2, pp. 194–216, 2002.
- [286] M. Kothari and L. Anand, “Elasto-viscoplastic constitutive equations for polycrystalline metals: Application to tantalum,” *Journal of the Mechanics and Physics of Solids*, vol. 46, no. 1, pp. 51–83, 1998.
- [287] P. Haasen, V. Gerold, and G. Kostorz, Eds., *Strength of metals and alloys: Proceedings of the 5th International Conference, Aachen, Federal Republic of Germany, August 27-31, 1979*, 1st ed. Toronto, New York: Pergamon Press, 1980, ©1979-©1980.
- [288] A. H. Cottrell, “Theory of dislocations,” *Progress in Metal Physics*, vol. 4, pp. 205–264, 1953.
- [289] E. van der Giessen and A. Needleman, “Discrete dislocation plasticity: a simple planar model,” (en), *Modelling Simul. Mater. Sci. Eng.*, vol. 3, no. 5, p. 689, <http://iopscience.iop.org/article/10.1088/0965-0393/3/5/008/pdf>.
- [290] J. Weertman and J. R. Weertman, *Elementary dislocation theory*. New York, Oxford: Oxford University Press, 1992.
- [291] J. P. Hirth and J. Lothe, *Theory of dislocations*, 2nd ed. Malabar, Fla.: Krieger Publishing Company, 1992.
- [292] H.M. Zbib and T.A. Khraishi, “Dislocation Dynamics,” in *Handbook of materials modeling*, S. Yip, Ed., Dordrecht: Springer, 2005, pp. 1097–1114.
- [293] J. P. Hirth, M. Rhee, and H. Zbib, “Modeling of deformation by a 3D simulation of multiple, curved dislocations,” (en), *Journal of Computer-Aided Materials Design*, vol. 3, pp. 164–166, 1996.
- [294] M. S. Daw and M. I. Baskes, “Embedded-atom method: Derivation and application to impurities, surfaces, and other defects in metals,” *Phys. Rev. B*, vol. 29, no. 12, pp. 6443–6453, 1984.
- [295] D. A. Porter and K. E. Easterling, *Phase transformations in metals and alloys*, 2nd ed. London [u.a.]: Chapman & Hall, 1997.
- [296] C. P. Enz and K. v. Meyenn, Eds., *Wolfgang Pauli: Das Gewissen der Physik*. Wiesbaden: Vieweg+Teubner Verlag, 1988.
- [297] D. S. Sholl and J. Steckel, *Density functional theory: A practical introduction*. Hoboken, N.J.: Wiley, op. 2009.
- [298] Paolo Giannozzi and Stefano Baroni, “Density-Functional Perturbation Theory,” in *Handbook of materials modeling*, S. Yip, Ed., Dordrecht: Springer, 2005, pp. 195–215.

-
- [299] I. J. Beyerlein, L. S. Tóth, C. N. Tomé, and S. Suwas, "Role of twinning on texture evolution of silver during equal channel angular extrusion," *Philosophical Magazine*, vol. 87, no. 6, pp. 885–906, 2007.
- [300] S. Li, I. J. Beyerlein, and D. J. Alexander, "Characterization of deformation textures in pure copper processed by equal channel angular extrusion via route A," *Materials Science and Engineering: A*, vol. 431, no. 1–2, pp. 339–345, 2006.
- [301] I. J. Beyerlein and L. S. Tóth, "Texture evolution in equal-channel angular extrusion," *Progress in Materials Science*, vol. 54, no. 4, pp. 427–510, 2009.
- [302] P. M. Dixit and U. S. Dixit, *Modeling of metal forming and machining processes: By finite element and soft computing methods*. London: Springer, 2008.

Curriculum vitae

Persönliche Daten

Name: Farzad Foadian
Geburtsdag: 23.07.1988
Geburtsort: Täbris
Staatsangehörigkeit: Iranisch
Familienstand: Ledig
Wohnort: Leibnizstr. 20-23
38678
Clausthal-Zellerfeld

Telefon: 05323 / 722639
0157 / 52182510



E-Mail: farzad.foadian@tu-claustahl.de

Beruflicher Werdegang

Dezember 2017 – dato

Entwicklungsingenieur – Benteler Steel/Tube

Februar 2013 – November 2017

Wissenschaftlicher Mitarbeiter in den Themengebieten
FEM-Simulation von Umformvorgängen und Rohrziehen
Technische Universität Clausthal, Institut für Metallurgie, Clausthal

November 2011 – Januar 2013

Sachverständiger, Forschungsabteilung, Bearbeitung von
Forschungsprojekten Iran-Aluminium-Forschungszentrum, Teheran /
Iran

Schulischer Werdegang

September 2010 – September 2012

Student der Iranische Universität für Wissenschaft und Technologie,
Teheran / Iran
Materialwissenschaft mit Vertiefung Werkstoffcharakterisierung
Master of Science (GPA: 19,70 von 20)

September 2006 – September 2010

Student der Universität Täbris, Täbris / Iran
Bachelor of Science Materialwissenschaft (GPA: 19,50 von 20)

September 2002 – Juni 2006

Amir – Momenin High-School, Täbris / Iran
Mathematik und Physik (Note 1,3)

Abschluss

Master of Science

Abschlussarbeiten und Praktika*Februar 2012 – August 2012*

Masterarbeit am Institut für Werkstofftechnik und Metallurgie der
Iranische Universität für Wissenschaft und Technologie, Teheran /
Iran

Titel: „A Study on the Formation of Intermetallics during the Heat
Treatment of Explosively Welded Al-Ti Multilayers“

Juli 2011 – September 2011

Forschungspraktikum im Polymerwerkstoffe und Kunststofftechnik
Institut

Technische Universität Clausthal, Clausthal

Titel: „Improving the Tensile Test of Fiber Reinforced Plastic Materials
under the Consideration of Design of Specimen“

April 2010 – August 2010

Bachelorarbeit am Institut für Maschinenbau Abteilung der
Materialwissenschaft

Titel: „Nitrogen Diffusion in Different Microstructures of Plasma
Nitrided CK45 Steel“

Weiterbildungen*September 2015 – dato*

Bilaterale Promotion an der Universitäten TU Clausthal und
Strasbourg Universität

Februar 2013 – dato

Teilnahme an diversen werkstofftechnischen Seminaren und
Arbeitskreisen

Februar 2013 – dato

Diverse Weiterbildungen im Bereich FEM-Simulation, Neutron und
Synchrotron Strahlung

Weitere Kenntnisse*EDV-Kenntnisse*

Grundlagen Fortran, ANSYS, Minitab, Comsol, Mathcad,
Mathematica, CATIA V5 & Autocad

Erweitert: Abaqus, SolidWorks, Linux, MATLAB, MS-Office,
MS-Project & Windows

Fremdsprachen

Deutsch Sehr gute Kenntnisse in Wort und Schrift

Englisch Sehr gute Kenntnisse in Wort und Schrift

Persisch Muttersprache

Fachgremientätigkeit

seit 02.2017 Mitglied TMS „The Minerals, Metals & Materials Society“
seit 02.2014 Mitarbeit im DGM Fachausschuss „Ziehen“ bei DGM“
seit 04.2013 Mitglied Stahlinstitut VDEh „Verein Deutscher Eisenhüttenleute“

Hobbies

Joggen, Schwimmen, Tischtennis

Publication list

Zeitschriften

- 1) F. Foadian, A. Carradó, T. Pirling, H. Palkowski, "Residual stresses evolution in Cu tubes, cold drawn with tilted dies – Neutron diffraction measurements and finite element simulation", *Materials & Design*, Available online 9 June 2016
- 2) F. Foadian, A. Carradó, H. Palkowski*, "Precision Tube Production: Influencing the Eccentricity and Residual Stresses by Tilting and Shifting", *Journal of Materials Processing and Technology*, vol. 222, pp. 155-162
- 3) M. Akdesir, D. Zhou, F. Foadian, H. Palkowski, "Study of Different Surface Pre-treatment Methods on Bonding Strength of Multilayer Aluminium Alloys/Steel Clad Material", *International Journal of Engineering Research & Science*, Vol. 2, January 2016, 169-177
- 4) F. Foadian, M. Soltanieh*, M. Adeli, M. Etminanbakhsh, "A Study on the Formation of Intermetallics during the Heat Treatment of Explosively Welded Al-Ti Multilayers", *Metallurgical and Materials Transactions A*, December 2013
- 5) F. Foadian, M. Soltanieh*, M. Adeli, M. Etminanbakhsh, "The Kinetics of TiAl₃ Formation in Explosively Welded Ti-Al Multilayers during Heat Treatment", *Metallurgical and Materials Transactions B*, May 2016
- 6) F. Foadian, M. Soltanieh*, M. Adeli, M. Etminanbakhsh, "The Formation of TiAl₃ during Heat Treatment in Explosively Welded Ti-Al Multilayers", *Iranian Journal of Materials Science & Engineering*, Vol. 11, Number 4, December 2014, pp 12-19
- 7) F. Foadian*, F. Feyzi, S. Haghighat, H. Aghajani, "Nitrogen Diffusion in Different Microstructures of Plasma Nitrided CK45 Steel", *Materials Science and Technology*, Vol. 30 Issue 1, January 2014, pp. 86-90

*Corresponding author

Bücher

- 8) A. Carradó, F. Foadian, H. Palkowski, book chapter, "Tube Drawing with Tilted and Shifted Die," in *60 Excellent Inventions in Metal Forming: A. E. Tekkaya, W. Homberg, and A. Brosius, Eds. 2015th ed, Berlin: Springer Berlin, 2015, pp. 433–438.*

Konferenzen

- 9) F. Foadian, A. Carradò, H. Palkowski, "Study the eccentricity variations due to the tilting of the die in tube drawing process for aluminum, brass and steel tubes; numerically and experimentally", Advanced Metal Forming Processes in Automotive Industry New Materials for Vehicle Components, 2015, Wroclaw, Poland, 2016.
- 10) F. Foadian, C. P. Antoine, H. Palkowski, "Simulation der Entwicklung von Brammenkantenfehlern in der Brammenstauchpresse und Vorstraße einer Warmbreitbandanlage", XXXV. Verformungskundliches Kolloquium, Zauchensee, Österreich, 2016
- 11) F. Foadian, A. Carradò, H. Palkowski, "Simulation der Kombination von Kippung und Versetzung auf die Exzentrizität und Eigenspannungen von Rohren beim Gleitziehen", Kupfer Symposium, 2015, Berlin, Deutschland, 2015
- 12) F. Foadian, A. Carradò, H. Palkowski, "Kombination von Kippung und Versetzung Einfluss auf die Exzentrizität von Rohren beim Gleitziehen", WerkstoffWoche, 2015, Dresden, Deutschland, 2015
- 13) F. Foadian, A. Carradò, H. Palkowski, "Einfluss der Vorrohr- und Auslaufführung auf die Exzentrizität und Eigenspannungen von Rohren beim Gleitziehen", XXXIII Verformungskundliches Kolloquium, 2015, Zauchensee, Austria, 2015
- 14) F. Foadian, A. Carradò, H. Palkowski, "Precision Tube Production: Influencing the Eccentricity and Residual stresses by Tilting and Shifting", 1. Niedersächsisches Symposium Materialtechnik, 2015, Clausthal-Zellerfeld, Germany
- 15) F. Foadian, A. Carradò, H. Palkowski, "Numerical studies of residual stresses and eccentricity of drawn copper tubes with titled and shifted die", TMS, 2015, Florida, USA
- 16) M. Soltanieh, F. Foadian, Hafez Amani, M. Adeli, M. Etminanbakhsh, "On the kinetics of Intermetallic Phase Formation during the Heat Treatment of Explosively Welded Al/Ti and Al/Cu Bimetals", 9th Aluminum Two Thousand, 12-16 May, 2015, Florence, Italy
- 17) F. Foadian, M. Soltanieh, M. Adeli, "Kinetics of the Formation of Intermetallics during the Heat Treatment of Explosively Welded Al-Ti Multilayers", 15th International Conference on Advances in Materials and Processing Technologies, 2012

- 18) F. Foadian, M. Soltanieh, M. Adeli, "Intermetallic formation by heat treatment of explosively welded Al-Ti layers", second Iran International Aluminum Conference, 15-16 May, 2012, Arak, Iran

Abschlussberichte

- 19) F. Foadian, H. Palkowski, "Einfluss der Vorrohr- und Auslaufführung auf die Exzentrizität und Eigenspannungen von Rohren beim Gleitziehen", AiF 17263 N final report, 2014, Clausthal University of Technology, Germany (auf Deutsch).
- 20) F. Foadian, C.P. Antoine, H. Palkowski, "Grundlegende Simulation des Umformvorgangs in der Brammenstachpresse und Vorstraße", Industriel project, Final report, 2014, Clausthal University of Technology, Germany (auf English und Deutsch).

Forschungsanträge

- 21) F. Foadian, H. Brokmeier, H. Palkowski, "Numerical and Experimental study of texture, residual stresses, and eccentricity evolution in drawn copper tubes", DFG proposal, 2014, Clausthal University of Technology, Germany (auf English).
- 22) F. Foadian, H. Palkowski, "Gezielte Beeinflussung der Exzentrizität und Eigenspannungen beim Gleitziehen von Rohren – Entwicklung einer In-Line-Messung und Regelung", AiF Proposal, 2015, Clausthal University of Technology, Germany (auf Deutsch).
- 23) F. Foadian, H. Palkowski, „Numerical study of eccentricity, ovality, and residual stresses in drawn copper tubes with tilted and shifted die(s)“, SZW Proposal, 2015, Clausthal University of Technology, (auf English).



Precision Tube Production
Influencing the Eccentricity, Residual Stresses and Texture
Developments: Experiments and Multiscale Simulation

Résumé

Le but principal de ce travail était d'optimiser le processus standard d'étrépage des tubes de manière à contrôler l'excentricité, qui peut être la réduction ou l'augmentation de l'excentricité. Pour cette raison, l'inclinaison et / ou le déplacement ont été introduits respectivement dans le matrice et / ou le tube.

Plusieurs tubes de matériaux différents - tels que le cuivre, l'aluminium, le laiton et l'acier - de différentes dimensions ont été étudiés. L'effet sur l'excentricité a été analysé en utilisant divers angles d'inclinaison, valeurs de déplacement ou combinaison d'inclinaison et de décalage. Tout en influençant et en contrôlant l'excentricité, l'évolution des contraintes résiduelles et de la texture due à l'inclinaison et / ou au décalage introduits ont été étudiées.

L'autre objectif de ce travail était de développer un modèle FEM universel, afin d'obtenir les paramètres d'entrée requis, liés au matériau ou au processus ou aux deux. Ce modèle FEM a été utilisé pour accomplir la simulation du processus de formage du métal défini par l'utilisateur et pour analyser des situations plus complexes. À cet égard, un modèle de simulation multi-échelle a été développé à l'aide d'une méthode de simulation multi-échelle avec l'approche Integrated Computational Material Engineering.

Résumé en anglais

The main and foremost aim of this work was to optimize the standard tube drawing process in a way that the eccentricity can be controlled, which can be the reduction or increase of eccentricity. For this reason, tilting and/or shifting was introduced to the die and/or tube, respectively. Different tubes of varied materials, such as copper, aluminum, brass, and steel with different dimensions were investigated by various tilting angles, shifting values, or combination of tilting and shifting and their effect on the eccentricity was analyzed. Along influencing and controlling the eccentricity, the evolution of the residual stresses and texture due to the introduced tilting and/or shifting were investigated. The other aim of this work was to develop a universal FEM model, which can get the required or desired input parameters, which can be material-related or process-related or both, and perform the simulation of the user-defined metal forming process and therewith analyze more complex situations. In this regard, a simulation model was developed using a multiscale simulation method with Integrated Computational Material Engineering approach.